SWIRLING FLOWS IN DIRECT-INJECTION DIESEL ENGINES

ANTONIS HATZIAPOSTOLOU
Dipl.-Ing.

Thesis submitted for the degree of
Doctor of Philosophy
in the University of London
and for the
Diploma of Membership of the Imperial College

Imperial College of Science, Technology and Medicine
Department of Mechanical Engineering

August 1991

To my loved ones

Στους αγαπημενους μου

ABSTRACT

The thesis describes an experimental investigation of the in-cylinder flowfield in Direct Injection (DI) Diesel engines under both motored and firing conditions. The experimental techniques included laser Doppler Velocimetry, laser beam deflection, high speed photography and shadowgraphy. The optical instrumentation and the supporting electronic equipment were evaluated by measuring the flowfield in an optically-accessible constant volume chamber, where propane-air mixtures were ignited by means of a spark plug.

The main investigation started with experiments performed in a steady-flow rig and a low-compression ratio model engine operating at 200rpm. It was found that the centre of the swirling flow pattern performed a helical motion and precessed periodically with a characteristic frequency linearly related to the induction mass flowrate and/or engine speed. An idealized DI diesel engine with variable compression ratio was used to quantify the effect of inlet manifold geometry and induction-air throttling on the swirl velocity flowfield at top-dead-centre of compression.

A purpose-built single-cylinder research engine with geometrical characteristics identical to those of a 4-cylinder production engine (Ford 2.5L) and incorporating a variable swirl inlet port and a unit-injector fuel-injection system was used for a full investigation of the flow, combustion and performance in small DI diesel engines. The in-cylinder flow during induction and compression was characterised in terms of spatially- and temporally-resolved ensemble-averaged axial and swirl velocities obtained at engine speeds between 1000 and 3000 rev/min for three swirl levels. The multi-hole diesel spray was studied in the time domain under non-reacting atmospheric conditions by means of LDV and a two-beam deflection technique. Combustion was visualised by high-speed photography at various loads, engine speeds and swirl levels and correlated with performance measurements. The results showed that the single-cylinder optical engine has poorer performance than the standard engine with identical geometry and the equivalent multi-cylinder production engine. The implication of the results for small HSDI diesel engines is that matching the in-cylinder swirl

levels, as generated by the inlet port and modified by the combustion chamber geometry, with the spray characteristics is a prerequisite for improving the trade-off between particulates and NO_x/noise levels while operating at optimum bsfc throughout the range of speed and load.

Acknowledgments

Doing a PhD in such a field was for me a 'dream-come-true' although some times, under the occasional stresses and strains, it seemed more like a nightmare! In any case it was a fruitful and fascinating period of my life and in these lines I would like to thank a number of people involved in the realisation of this thesis in one way or another.

I would like to express my sincere gratitude to my supervisor Professor J.H.Whitelaw for his constructive criticism during the realisation of this thesis and his patience during the writing-up period.

I am grateful to my other supervisor Dr. C. Arcoumanis for his continuous guidance, support and valuable advice throughout the course of this work and his thorough review of the manuscript.

I also take the opportunity to acknowledge the financial support of the Science and Engineering Research Council.

I am grateful to Dr Costis Vafidis who introduced to the 'art' of LDV measurements in IC engines and helped me to overcome many difficult situations. I am indebted to Mr Andreas Enotiadis for his valuable assistance in the experimental hardware and numerous occasions in the software, as well as useful and ...endless discussions.

I am pleased to acknowledge the assistance of Dr Philippos Begleris during the first stages of my thesis and Dr Elvio Cossali for the injector experiments. I have also benefited from the association with my colleagues, particularly Dr. Alex Taylor, Dr. Yannis Hardalupas and Mr Vagelis Ikonomou. My thanks go also to Mr Bill Crew for listening to all my technical enquiries, Mr. Oscar Vis for his ingenious constructions in optics and Mr. John Laker for the design and construction of the electronic equipment.

At this moment my thoughts are also with my past and present friends in London; to name but a few, Giorgos V., Elias D., Victor K. and Nikos Ch. provided at times the moral support and companionship needed while Athina P., Aurelia T., Mika I. and, certainly, Fanny P. shared variably my good and bad times, my worries and dreams. I thank them all from the bottom of my heart.

TABLE OF CONTENTS

Page

ABSTRACT 3

LIST OF TABLES 11

LIST OF FIGURES 12

LIST OF SYMBOLS 19

CHAPTER 1 INTRODUCTION TO THE THESIS

1.1 DIRECT INJECTION DIESEL ENGINES: PAST AND PRESENT .. 21

1.2 REVIEW OF FLOW AND COMBUSTION IN HSDI DIESEL ENGINES 23

1.2.1. Flow through the inlet manifold/port/valve assembly 24

A. Flow through the inlet manifold 25

B. Flow through the inlet port/valve assembly 25

C. Swirl producing inlet ports 27

1.2.2 In-cylinder flow during induction and compression 29

A.Statistical representation of engine flows 30

B.Flow during induction and compression 32

1.2.3. Fuel injection 35

1.2.4 Combustion and exhaust process 38

A. Combustion phases in HSDI diesel engines 38

B. Noise and pollutant formation 41

1.3 PRESENT CONTRIBUTION 44

1.4 THESIS OUTLINE 46

CHAPTER 2 OPTICAL INSTRUMENTATION

2.1 INTRODUCTION 55

2.2. REQUIREMENTS FOR OPTICAL INSTRUMENTATION IN ENGINES 55

2.3 EVALUATION OF OPTICAL INSTRUMENTATION 57

2.4 LASER-BEAM DEFLECTION 59

2.4.1 Principle and implementation 59

2.4.2 Results and discussion 61

2.5 HIGH SPEED SHADOWGRAPHY 62

2.5.1 Principle and implementation 62

2.5.2 Results and discussion 64

2.6 LASER-DOPPLER VELOCIMETRY 64

2.6.1 Principle 65

2.5.2 Measurement uncertainties 66

2.5.2 Implementation 68

2.5.3 Results and discussion 69

2.6 CONCLUDING REMARKS 70

CHAPTER 3 SWIRLING FLOWS IN IDEALISED DIESEL ENGINES

3.1 INTRODUCTION 84

3.2 SWIRLING FLOWS IN AXISYMMETRIC PORT GEOMETRIES 85

3.2.1 Flow configuration 85

A. Steady flow/open-ended cylinder 85

B. Steady flow/stationary porous piston 86

C. Model engine 86

3.2.2 Measurement systems 87

3.2.3 Results 89

A. Steady flow/open-ended cylinder 90

B. Steady flow/stationary porous piston. 94

C. Model engine. 97

3.2.4 Conclusions 100

3.3 SWIRLING FLOW IN A MOTORED DIESEL ENGINE 101

3.3.1 Flow configuration 102

3.3.2 Measurement systems 104

3.3.3 Results 104

3.3.4. Conclusions 109

CHAPTER 4 FLOW AND COMBUSTION IN A HSDI DIESEL ENGINE

4.1 INTRODUCTION 137

4.2 HYDRA TEST-BED FACILITY 138

4.2.1 Base frame assembly 138

4.2.2 Control console 139

4.2.3 Standard Hydra engine 140

4.2.4 Special Hydra engine 141

4.3 STEADY-FLOW TESTS 144

4.3.1 Results and discussion 145

4.4 MOTORED TESTS 146

4.4.1 Experimental system 146

4.4.2 Results. 149

A. Swirl velocities 149

B. Axial velocities 156

4.5 SPRAY CHARACTERISTICS OF FUEL INJECTOR 157

4.5.1 Experimental system 158

4.5.2 Results 159

A. Initial conditions 160

B. Spray tip velocities 161

C. Axial droplet velocities 162

4.6 COMBUSTION PHOTOGRAPHY 164

4.6.1 Application to the Hydra engine 165

4.6.2 Analysis of films 166

A. Effect of engine load 169

B. Effect of engine speed 169

C. Effect of swirl 170

4.7 PERFORMANCE TESTS 171

4.7.1 Experimental system 171

4.7.2 Results 172

4.7.3 Discussion 174

4.8 CONCLUSIONS 177

CHAPTER 5 CLOSURE TO THE THESIS 39

APPENDIX A DEFINITION OF SWIRL RATIO 244

REFERENCES 245

LIST OF TABLES

Table No.		Page(s)
1.1	Recent investigations in Direct Injection engines.	48-52
2.1	Materials for optical windows in engines.	56
3.1	Characteristics of the model engine.	87
3.2	Characteristics of the research diesel engine.	102
3.3	Summary of in-cylinder swirl and turbulence characteristics.	106
4.1	Operating and geometric characteristics of Hydra engine.	144
4.2	Swirl ratio values.	154
4.3	Unit injector tests	160
4.4	Summary of photographic tests in optical Hydra engine.	167
4.5	Summary of performance tests in optical Hydra engine.	173

LIST OF FIGURES

Fig. No.		Page(s)
1.1	Average fuel consumption according to ECE city cycle (90km/h and 120km/h) of light duty vehicles powered by gasoline, IDI and DI diesel engines (Wojik, 1989).	53
1.2	Examples of (a) directed and (b) helical ports (Bird, 1985).	53
1.3	Typical piston-bowl geometries used in production HSDI diesel engines (Stephenson and Hood, 1987).	53
1.4	Flow patterns set-up in the axial plane in (a) simple and (b) re-entrant cylindrical bowls (Arcoumanis et al, 1983).	54
1.5	(a) Standard (b) and VCO-type nozzles (Greeves et al, 1977).	54
1.6	Typical pressure and heat release diagram for small HSDI diesel engines (Austen and Lynn, 1961).	54
2.1	Schematic of experimental rig.	72
2.2	Constant volume chamber.	73
2.3	Laser beam deflection principle.	74
2.4	Typical signals from (a) two photodiodes (b) pressure transducer and photodiode.	75
2.5	Variation of flame speed with propagating distance (a) and flame speed with equivalence ratio (b).	76
2.6	Variation of maximum chamber pressure and time at which maximum pressure occurs with equivalence ratio.	77
2.7	(a)Principle of laser shadowgraphy and (b) Schematic of focused laser shadowgraphy system.	78
2.8	Photographs of propagating flame obtained by high-speed laser shadowgraphy.	79
2.9	Comparison of data obtained with two laser techniques.	80
2.10	General arrangement of an LDV system	81
2.11	Velocity traces as a function of time from the start of ignition for three locations in the combustion chamber (a) centre of chamber (b) near the spark plug (c) near the wall.	82-83

3.1	Flow configurations (a) steady flow/open ended cylinder (b)steady flow/stationary porous piston (c) model engine.	110
3.2	Steady flow rig.	111
3.3	Ensemble-averaged swirl velocity profiles, steady flow rig/open-ended cylinder at z=0.5D for valve lifts of (a)2mm (b) 4mm (c) 8mm.	112
3.4	Ensemble-averaged swirl velocity profiles, steady flow rig/open-ended cylinder at z=1.0D for valve lifts of (a)2mm (b) 4mm (c) 8mm.	113
3.5	Ensemble-averaged swirl velocity profiles, steady flow rig/open-ended cylinder at z=2.0D for valve lifts of (a)2mm (b) 4mm (c) 8mm.	114
3.6	Centreline swirl velocity distribution for valve lift of 4mm steady-flow rig/open-ended cylinder (two orientations).	115
3.7	(a) Ensemble-averaged axial velocity profiles, steady flow/open ended cylinder at z=0.5D, 1.0D &2.0D (b) Centreline axial velocity distribution.	116
3.8	Instantaneous traces of swirl velocity at z=2.0D, r=0mm, steady flow rig/open ended cylinder at valve lifts of (a)2mm (b) 4mm (c) 8mm.	117
3.9	Frequency spectra of the instantaneous swirl velocity at various locations,steady-flow rig/open ended cylinder.	118
3.10	Ensemble-averaged swirl velocity profiles, steady flow rig/stationary porous piston at (a) z=0.5D (b) z=1.0D and (c) z=2.0D for valve lift of 4mm.	119
3.11	Centreline swirl velocity distribution for valve lift of 4mm steady-flow rig/stationary porous piston (two orientations).	120
3.12	.(a) Ensemble-averaged axial velocity profiles, steady flow/stationary porous piston at z=0.5D, 1.0D &2.0D (b) Centreline axial velocity distribution.	121
3.13	Frequency spectra of the instantaneous swirl velocity at various locations, steady-flow rig/stationary porous piston.	122
3.14	Variation of characteristic frequency of swirl centre precession versus air mass flowrate, steady flow.	123
3.15	Ensemble-averaged swirl velocity profiles, model engine at (a) $\theta=90^o$, z=0.25D (b) $\theta=90^o$, z=0.5D (c) $\theta=180^o$, z=0.25D (d) $\theta=180^o$, z=0.5D.	124-125

3.16	Ensemble-averaged axial velocity profiles, model engine at (a) θ=90°, z=0.25D and z=0.5D (b) θ=180°, z=0.25D and z=0.5D, and centreline distributions at (c) θ=90° and (d) θ=180°.	126
3.17	Instantaneous traces of swirl velocity at z=0.25D, r=0mm, model engine.	127
3.18	Temporal variation of ensemble-averaged mean swirl velocity at z=0.25D, r=0.	128
3.19	Research Diesel engine with detail of the re-entrant extended piston bowl.	129
3.20	Overall view of the experimental rig.	130
3.21	Photograph of the idealised manifold.	131
3.22	Photograph of the Ford manifold.	131
3.23	Variation of peak cylinder pressure at TDC as a function of degree of throttling.	132
3.24	Ensemble-averaged swirl velocity profiles along the mid-plane (z=8mm), at TDC, compression ratio of 8, flat piston, with three inlet manifold configurations.	133
3.25	Ensemble-averaged swirl velocity profiles along the mid-plane (z=8mm), at TDC, compression ratio of 8, flat piston (a) unthrottled intake (b) partially throttled ΔP=100mmHg (c) partially throttled ΔP=300mmHg.	134
3.26	Ensemble-averaged swirl velocity profiles along the mid-plane (z=5mm), at TDC, compression ratio of 12, flat piston (a) partially throttled intake ΔP=200mmHg (b) partially throttled ΔP=400mmHg.	135
3.27	Ensemble-averaged swirl velocity profiles along the mid-plane (z=3mm), at TDC, compression ratio of 19, flat piston, partially throttled intake ΔP=350mmHg.	135
3.28	Ensemble-averaged swirl velocity profiles at TDC, z=10mm, in the re-entrant piston-bowl at compression ratio of 8.5, unthrottled and partially throttled intake ΔP=400mmHg	136
4.1	Hydra base frame assembly.	180
4.2	Cooling module.	180
4.3	Overall view of the Hydra engine. (a) baseline version (b) optical version	181
4.4	Cross-section of the unit injector.	182
4.5	Layout of the fuel circuit.	182

4.6	Variation of (a) discharge coefficient and (b) Ricardo swirl ratio with setting No of the variable swirl mechanism.	183
4.7	Top (a) and front (b) view of the optical engine cylinder showing measurements axis.	184
4.8	Temporal profile of swirl mean and rms velocities at (a) r=35mm and (b) r=15mm (high swirl,2000rpm).	185
4.9	Temporal profiles of swirl mean velocities at different radial locations (medium swirl,2000rpm)	186
4.10	Swirl mean velocities at different engine speeds as a function of (a) crankangle and (b) time (r=20mm, medium swirl).	187
4.11	Temporal profiles of swirl mean velocities at different swirl levels (r=20mm,2000rpm).	188
4.12	Temporal profiles of swirl rms velocities at different swirl levels (r=20mm,2000rpm).	189
4.13	Temporal profiles of swirl rms velocities at different engine speeds (r=20mm, medium swirl).	189
4.14	Spatial profiles of swirl mean and rms velocities at (a)1000 (b)2000 and (c)3000rpm (θ=180° CA, high swirl)	190
4.15	Spatial profiles of swirl mean and rms velocities at (a)1000 (b)2000 and (c)3000rpm (θ=180° CA, medium swirl)	191
4.16	Spatial profiles of swirl mean and rms velocities at (a)1000 (b)2000 and (c)3000rpm (θ=180° CA, low swirl)	192
4.17	Schematic of the engine cylinder showing swirling air flow during induction.	193
4.18	Spatial profiles of swirl mean and rms velocities at (a)1000 (b)2000 and (c)3000rpm (θ=200° CA, high swirl)	194
4.19	Spatial profiles of swirl mean and rms velocities at (a)1000 (b)2000 and (c)3000rpm (θ=200° CA, medium swirl)	195
4.20	Spatial profiles of swirl mean and rms velocities at (a)1000 (b)2000 and (c)3000rpm (θ=200° CA, low swirl)	196
4.21	Spatial profiles of swirl mean and rms velocities at (a)1000 (b)2000 and (c)3000rpm (θ=218° CA, high swirl)	197

4.22	Spatial profiles of swirl mean and rms velocities at (a)1000 (b)2000 and (c)3000rpm (θ=218° CA, medium swirl)	198
4.23	Spatial profiles of swirl mean and rms velocities at (a)1000 (b)2000 and (c)3000rpm (θ=218° CA, low swirl)	199
4.24	Spatial profiles of swirl mean and rms velocities at (a)1000 (b)2000 and (c)3000rpm (θ=270° CA, high swirl)	200
4.25	Spatial profiles of swirl mean and rms velocities at (a)1000 (b)2000 and (c)3000rpm (θ=270° CA, medium swirl)	201
4.26	Spatial profiles of swirl mean and rms velocities at (a)1000 (b)2000 and (c)3000rpm (θ=270° CA, low swirl)	202
4.27	Spatial profiles of swirl mean and rms velocities at (a)1000 (b)2000 and (c)3000rpm (θ=320° CA, high swirl)	203
4.28	Spatial profiles of swirl mean and rms velocities at (a)1000 (b)2000 and (c)3000rpm (θ=320° CA, medium swirl)	204
4.29	Spatial profiles of swirl mean and rms velocities at (a)1000 (b)2000 and (c)3000rpm (θ=320° CA, low swirl)	205
4.30	Temporal variation of equivalent swirl ratios at different engine speeds for (a) high, (b) medium and (c) low swirl.	206
4.31	Temporal variation of the zero swirl velocity position on the measurements axis at (a)1000 (b)2000 and (c)3000rpm (high swirl).	207
4.32	Temporal variation of the zero swirl velocity position on the measurements axis at (a)1000 (b)2000 and (c)3000rpm (medium swirl).	208
4.33	Temporal variation of the zero swirl velocity position on the measurements axis at (a)1000 (b)2000 and (c)3000rpm (low swirl).	209
4.34	Variation of the characteristic frequency derived from Figs.4.31-4.33 with engine speed.	210
4.35	Temporal profiles of axial mean and rms velocities at (a)1000 (b)2000 (c)3000rpm (r=15mm, medium swirl).	211
4.36	Spatial profiles of axial mean and rms velocities at (a)1000 (b)2000 and (c)3000rpm (θ=70° CA, medium swirl)	212

4.37	Spatial profiles of axial mean and rms velocities at (a)1000 (b)2000 and (c)3000rpm (θ=150° CA, medium swirl)	213
4.38	Spatial profiles of axial mean and rms velocities at (a)1000 (b)2000 and (c)3000rpm (θ=180° CA, medium swirl)	214
4.39	Spatial profiles of axial mean and rms velocities at (a)1000 (b)2000 and (c)3000rpm (θ=218° CA, medium swirl)	215
4.40	Spatial profiles of axial mean and rms velocities at (a)1000 (b)2000 and (c)3000rpm (θ=270° CA, medium swirl)	216
4.41	Spatial profiles of axial mean and rms velocities at (a)1000 (b)2000 and (c)3000rpm (θ=320° CA, medium swirl)	217
4.42	Variation of fuel injected volume at different engine speeds with injection duration.	218
4.43	Temporal variations of instantaneous fuel line pressure and needle lift at the four different cases.	219-222
4.44	Variation of spray-tip velocity at (a)1000 and (b)2000 rpm with distance from the unit injector nozzle tip.	221
4.45	Variation of spray penetration at (a)1000 and (b)2000 rpm with time (ms/°CA) from the start of the injection under both atmospheric and engine conditions (using equation from Dent, 1971), compared with high speed photography data.	222
4.46	Temporal profiles of axial droplet velocities along the centreline at (a)r=10mm (b)r=20mm and (c)r=30mm (case A)	223
4.47	Temporal profiles of axial droplet velocities along the centreline at (a)r=10mm (b)r=20mm and (c)r=30mm (case B)	224
4.48	Temporal profiles of axial droplet velocities along the centreline at (a)r=10mm (b)r=20mm and (c)r=30mm (case C)	225
4.49	Temporal profiles of axial droplet velocities along the centreline at (a)r=10mm (b)r=20mm and (c)r=30mm (case D)	226
4.50	In-cylinder view of the Hydra combustion chamber	227
4.51	Sequence from High-speed film case A_1.	228-229
4.52	Sequence from High-speed film case B_1.	230

4.53	Sequence from High-speed film case C_1.	231
4.54	Sequence from High-speed film case D_1.	232
4.55	Sequence from High-speed film case A_2.	233
4.56	Sequence from High-speed film case B_2.	234
4.57	Sequence from High-speed film case C_2.	235
4.58	Variation of motoring mean effective pressure of the 4-cylinder Ford and Hydra engines (in both versions) with engine speed.	236
4.59	Variation of volumetric efficiency of the Hydra engine with engine speed	236
4.60	Variation of brake mean effective pressure of the Hydra engine in both versions with air-to-fuel ratio at (a)1200 (b)2000 and (c)2400rpm	237
4.61	Variation of (a) torque and (b) power of the4-cylinder Ford and Hydra engines (in both versions) with engine speed.	238

LIST OF SYMBOLS

Roman characters

B	bowl-in-piston diameter
D	cylinder bore
$f_1..f_n$	focal lengths of the lenses
G	diffraction grating
I	light intensity
$L_1..L_n$	lengths between lenses
$\dot{m}$	mass flow rate
m_c	mass of the cylinder contents
N	engine speed in revolutions per second
n	refractive index
r	radial coordinate
R_c	cylinder radius
R_s	Ricardo swirl ratio
S	piston stroke
S_p	spray penetration distance
T	torque measured by impulse swirl meter in steady flow tests
T_g	gas temperature
U, V, W	instantaneous or mean axial, radial and tangential (swirl) velocity components
u, v, w	root mean square of the axial, radial and tangential velocity components
V_P	mean piston speed
z	axial coordinate
z_p	instantaneous piston position

Greek characters

ΔP	pressure difference
$\Delta\theta$	crankangle window
ε_x, ε_y	beam deflection angles

θ	crankangle
λ	laser wavelength
ρ	density
ϕ	angle coordinate
ω_{sb}	angular velocity of the in-cylinder air charge equivalent to solid body rotation
Ω_{tot}	total angular momentum of the in-cylinder air charge

Abbreviations

ATDC	after TDC
BDC	bottom-dead-centre
BTDC	before TDC
CR	compression ratio
EVC	exhaust valve closure
EVO	exhaust valve opening
IVC	inlet valve closure
IVO	inlet valve opening
^{o}CA	degrees crankangle
SR	swirl ratio
SR_e	equivalent swirl ratio
TDC	top-dead-centre

CHAPTER 1

INTRODUCTION TO THE THESIS

1.1 DIRECT INJECTION DIESEL ENGINES: PAST AND PRESENT

During the last two decades, the rising cost of energy and the growing concern for the environment urged the automotive industry towards cleaner and more fuel efficient internal combustion engines. The diesel engine can operate with up to 30% better fuel economy than the gasoline engine (Fig.1.1), while diesel fuel production costs are lower than those for gasoline. These are the prime reasons for the world-wide domination of the diesel engine in heavy-duty truck applications, whereas in passenger cars its market share is modest and varies according to the specific area. In the United States, where fuel prices are low, there is no passenger diesel market, whereas in Asia and Europe diesels are finding increasing utilisation and in Western Europe the percentage of diesels sold has grown from around 3% in 1974 to more than 15% in 1989 (Monaghan, 1990). The reasons for the low proportion of diesel cars are lower specific power, poorer driveability, higher particulate emissions and noise (Wojik, 1989) but over the last years continuous development of small high-speed diesel engines has diminished these drawbacks while maintaining the fuel economy advantage and associated lower CO_2 emissions.

Two different combustion chamber configurations are employed in current diesel engines, the indirect injection concept (IDI) where fuel injection takes place in a pre-chamber formed in the cylinder head and the direct injection (DI) concept where fuel is injected inside the engine cylinder and in a cavity formed in the piston crown. The former uses the very high air movement generated inside the pre-chamber at TDC to achieve rated speeds up to 5000rpm, higher specific power, lower combustion-induced noise and better control of gaseous emissions, particularly nitric oxides, with respect to the latter; for these reasons the IDI diesel engines with displacement ranging from 0.35 to 0.75 litres per cylinder, currently dominate the passenger diesel

car market. On the other hand, the DI diesel engine offers 10% to 15% better fuel economy than the IDI (Fig.1.1), due mainly to lower thermal losses associated with the smaller surface-to volume ratio of the combustion chamber and lower pumping losses associated with the absence of a chamber throat, as in the case of the IDIs. The DIs are used for heavy and medium-duty trucks where displacement per cylinder is greater than one litre. The challenge to the current engine researcher is to develop smaller high-speed direct injection (HSDI) diesel engines which deliver better smoke limited power over a wide range of speeds and reduce noise and emissions, so that it satisfies the requirements of the passenger car market; these improvements, coupled with its inherently better fuel economy, will guarantee increased market share and contribute to more efficient and cleaner fuel burning.

The key factors in the operation of the small HSDI are the organized rotation of the air about the cylinder axis, known as swirl, combustion chambers with a bowl-in-piston and small (0.7-1.5mm) TDC clearance and the fuel injection system. Swirl is induced during intake by specially-designed ports and evolves during the induction and most of the compression stroke until about 40° before TDC of compression, when the geometry of the piston forces the air inside the bowl, altering the flowfield. The mean swirl and turbulence levels combined with the injection system characteristics control the mixing process between the air charge and the fuel inside the piston cavity and determine the efficiency of the compression-ignition combustion. Improvements in the overall performance of the HSDI diesel engine, in terms of efficiency and emissions, require detailed knowledge of the pre-combustion flowfield, as determined by the swirl levels and the piston geometry, and in-depth understanding of the fast transient phenomena occurring after the initiation of fuel injection and during the combustion process.

Empirical research methods employed until about 30 years ago provided qualitative information of the in-cylinder processes which, combined with the researchers' abilities and intuition, resulted in rules for the design of improved versions. Current requirements for the HSDI diesel engines can only be satisfied by means of a combined experimental and theoretical research effort. On the experimental side, laser-based techniques such as laser Doppler and phase Doppler velocimetry, Rayleigh scattering,

spontaneous and coherent Raman spectroscopy are complemented by more classical techniques such as piezoelectric transducers, high speed photography and spectroscopy to provide detailed mapping of the unsteady three-dimensional velocity, temperature, pressure and concentration fields inside the cylinder. Computer-based modelling of the gas flow, heat transfer and combustion enables the researcher to predict all in-cylinder quantities and the designer to test new concepts and select the most appropriate for his requirements. Both experiments and calculations have deficiencies. The hostile environment of the production diesel engines dictates the use of research engines with non-realistic operating variables or realistic engines with limited optical access so that measurements by optical methods are either not representative of the real engine or insufficient to describe fully the processes. Multi-dimensional computer codes can provide detailed data in space and time but they need boundary conditions and their accuracy has to be confirmed by comparison with measurements.

The present thesis contributes to the understanding of the in-cylinder flowfield, spray and combustion in small HSDI diesel engines by describing experimental investigations in steady flow rigs, motored and firing research engines. The mechanisms of swirl generation and evolution were studied and quantified by laser Doppler velocimetry in geometries of gradually increasing complexity, with some emphasis on the spatial and temporal variation of the swirl centre. Atmospheric fuel injection through a multi-hole production injector and combustion visualisation provided qualitative and quantitative information on the operation of the small HSDIs allowing recommendations to be made for future designs. The velocity results are also intended to be used for initial conditions and validation of multi-dimensional computer codes.

The remainder of this introductory chapter is divided into three sections. Section 1.2 reviews the different phases of the in-cylinder flow in small HSDI diesels, based on existing literature. The contribution of this thesis is presented in section 1.3, followed by an outline of the main chapters.

1.2 REVIEW OF FLOW AND COMBUSTION IN HSDI DIESEL ENGINES

The operating cycle of small HSDI diesel engines can be divided in four

sections, the flow through the inlet manifold/port/valve assembly, the in-cylinder flow during induction and compression, the fuel injection and the combustion/exhaust process. The first section is particularly important for these engines due to the vital role of swirl and includes investigations under steady flow conditions used to characterise the induction system. The evolution of the in-cylinder flow is examined in the next section together with a brief discussion on the statistical representation of the flow in the handling of velocity data. The third section deals with the principles of diesel fuel injection and particularly those relevant to HSDIs, while the final section describes the different phases of the compression-ignition process and its effect on noise and emissions

1.2.1. Flow through the inlet manifold/port/valve assembly

The role of the induction system in HSDI diesel engines is to introduce the fresh air charge into the cylinder and to generate the swirling motion. Two quantities represent these functions, the volumetric efficiency which is defined as the mass of fresh charge which passes into the cylinder in one suction stroke divided by the mass of charge which would fill the displacement volume at inlet density (Taylor, 1985) and the swirl ratio, which compares the rotational speed of the air charge with the engine rotational speed (the exact definition of the swirl ratio is given in Appendix A). Both quantities refer to the operating engine and have steady flow analogues, the discharge coefficient and the swirl coefficient, which are discussed later. Steady flow tests are used to characterise the performance of intake port/valve assemblies due to difficulties associated with the measurement of its instantaneous flow characteristics during the induction stroke.

The volumetric efficiency in diesel engines depends on the flow resistance imposed by the induction system, the valve timing and the amount of heat picked up by the air during its passage through the induction system (Dicksie, 1940). Since there is no mixture preparation in diesel induction systems, flow resistance occurs in the inlet manifold, port and the valve gap. The absence of throttle and carburettor means that volumetric efficiencies of diesel engines are usually higher than that of petrol engines by 5%-10% (Heywood, 1988).

A. Flow through the inlet manifold

The role of the inlet manifold in multi-cylinder internal combustion engines is to provide uniform distribution of the air charge to the cylinders. Particularly in HSDIs, it has to compensate for the increased flow resistance of the inlet port, therefore is arranged as straight as available space permits. The effect of the inlet manifold shape on the mean and turbulent characteristics of the in-cylinder flow has not been investigated, due to the belief that the latter is completely determined by the flow through the complicated port shape and the annular valve area. However, differences in power output have been observed with and without a manifold, due probably to minor flowfield variations and an attempt to resolve this uncertainty has been made during the course of this study (chapter 3).

Whenever additional charge pressure is required, usually to increase the relatively low specific power output in HSDI diesel engines, a turbocharger or a supercharger is employed. An alternative method is the variable geometry inlet manifolds which take advantage of the pressure waves generated by the unsteady nature of the flow (Winterbone, 1989), and are used in specialised (usually racing) gasoline engines running at very high speeds (>10000rpm). However, a parametric investigation performed in a HSDI research engine motored at 1000-3000rpm (Margary et al, 1990), showed that tuning at a given engine speed can result in around 10% higher volumetric efficiency, albeit using unrealistic duct lengths. This suggests that tuning can be achieved even in HSDI engines and it is common practice to design the inlet manifold so that the induction flow is tuned at the engine speed where maximum torque is required. In addition, in the design of the inlet manifold an effort is made to minimise the differences in length between the various branches in order to achieve similar mass flow temporal distributions of the air entering the engine cylinders.

B. Flow through the inlet port/valve assembly

The flow resistance imposed by the inlet port/valve assembly is characterised in steady flow rigs by the discharge coefficient (or flow coefficient according to some authors) and is defined as the ratio of the mass flow rate through the valve to the (isentropic) mass flow rate through an ideal

nozzle under the same pressure ratio. The main parameters influencing the discharge coefficient are the port shape and the geometry of the valve. The swirl-producing inlet ports are examined separately in the next section, due to their particular importance in HSDI engines.

The main geometrical characteristics of the valve are valve lift, seat angle with respect to the cylinder head and seat width. Annand (1969) found that 45° seat angles are recommended for high lift engines and 30° for low lift engines and that both give better performance than 60° seat angle. Small seat widths give better flow characteristics but the influence of seat width is not significant. The most effective way to improve the discharge coefficient is the rounding of the sharp corners at the valve head and seat (Kastner et al, 1963) but this solution is not always feasible due to production costs.

The unsteady flow of the operating engine is simulated by steady flow tests employing the quasi-steady assumption, according to which flow characteristics at a given crankangle during engine operation remain the same in steady flow tests performed at the valve lift corresponding to this crankangle and constant pressure difference or constant mass flow rate corresponding to the engine speed. (Vafidis, 1985). For discharge coefficient values, the validity of this assumption is limited by the inertia and resonance effects in the induction system. Fukutani and Watanabe (1982) indicated that the mean 'dynamic' discharge coefficient may be up to 20% lower than the corresponding 'static' discharge coefficient at high engine speeds and large pressure drops across the valve.

The volumetric efficiency, usually estimated experimentally, is an overall parameter representing the integral of the instantaneous discharge coefficient over the time when the inlet valve is open and is a function of speed and load for a particular engine. The speed effects comprise non-linear frictional losses, variable heating of the charge inside the manifold due to different residence time, flow chocking in the valve area (i.e. sonic velocities) during part of the intake process, tuning effects in the manifold and the timing of inlet valve closure (Heywood, 1988). The latter is usually set at 30-40° ABDC in HSDIs to take advantage of the higher inertia of air at high engine speeds, which continues the charging process even after the piston passes BDC. This is usually termed as ram effect and can cause an inverse

flow at lower engine speed, resulting in deterioration of volumetric efficiency. Flattening of the volumetric efficiency-vs-speed curve can be achieved by variable valve timing mechanisms which are still at the experimental stage (Gray, 1988). The engine load affects volumetric efficiency through the variable heating of the air inside the inlet manifold.

When comparing induction systems in steady flow rigs it is expected that the variations in discharge coefficients correspond to volumetric efficiencies. The dynamic flow effects described previously suggest that, although the trend remains consistent, differences in volumetric efficiencies do not match exactly. This is particularly relevant to HSDI diesel engines when comparing different ports or a variable-swirl port at different settings such as the Hydra inlet port used in this study (chapter 4). Results obtained in a commercial variable-swirl inlet port show that differences of 23% in flow coefficient values resulted in around 5% variations in volumetric efficiencies, confirming the above observation (Shimada et al, 1986).

C. Swirl producing inlet ports

The inlet port following the inlet manifold forms part of the cylinder head and is responsible for the generation of the rotational motion of the air charge. Swirl-producing inlet ports can be categorised under two basic groups depending on whether swirl is produced downstream (post-valve swirl) or upstream of the inlet valve (pre-valve swirl). The former comprises the 'directed' ports, the latter the 'helical' ports; for research purposes they can be simulated by shroud or masked valves and by guide vanes, located in the port upstream of the valve, respectively.

Directed ports have a rather straight flow passage of varying cross-section arranged at an angle with respect to the cylinder head, in order to produce a non-uniform flow distribution around the circumference of the inlet valve with a preferential direction (Fig.1.2). During induction, the linear momentum of the flow emerging from the port is partly transformed to angular momentum due to its deflection by the cylinder wall. The magnitude of the resulting swirl depends on the inclination of the port axis to the cylinder head (Fitzgeorge and Allison, 1962) and the valve eccentricity from the cylinder axis (Watts and Scott, 1969). The need for a straight passage

combined with other requirements of the cylinder head (e.g. cooling passages, injector position) imposes a small port cross-section resulting in reduced discharge coefficient. The same applies to the masked or shroud valves where part of the valve periphery is covered to simulate the directional port effect; in addition to the reduced discharge coefficient the latter type suffers from valve turning around its axis during engine operation and, therefore, is only used for research purposes (Witze, 1980)

Helical ports produce swirl about the valve axis by the spiral shape of the port, prior to the flow entering the cylinder, and have steep or shallow ramps (Fig.1.2). Results from steady flow tests showed that they offer advantages over the directed ports in that they produce higher swirl levels at low and medium valve lifts , albeit lower at high valve lifts, do not interfere with the head cooling passages (Uzkan et al, 1983) and are less sensitive to the location in the cylinder head (Watts and Scott, 1969), allowing bigger manufacturing tolerances. In addition, they achieve a more ordered bulk flow (Wigley and Hawkins, 1978), higher discharge coefficients at equivalent swirl ratios and better performance over a wide range of speeds (Brandl et al, 1979). For these reasons most current HSDI diesel engines use helical ports, particularly of the shallow ramp type which gives a directional effect, in order to take advantage of the better performance of directional inlet ports at high valve lifts (Uzkan et al, 1983). Pre-valve swirl can be simulated in basic research by guide vanes positioned upstream of the valve in straight ports, offering simplicity of design and flexibility in swirl variation, albeit suffering of high losses. Vane angles of 15° to 60°, with respect to the port axis, have been successfully used in slow-revving model engines where volumetric efficiency is not important (e.g. Morse et al, 1980; Vafidis, 1984).

As already mentioned, the swirl coefficient is used to quantify the swirl capacity of a port; various definitions have been proposed according to the particular steady flow technique and, as a general rule, the swirl coefficient expresses the ratio of the axial fluxes of the angular momentum to the axial momentum, similar to the swirl number used in swirl combustor studies. An early approach was the use of a paddle wheel placed inside the cylinder of a steady flow rig, with its axis along the cylinder axis (Fitzgeorge and Allison, 1962; Tanabe et al, 1978) and measuring its angular velocity; Tindal and Williams (1977) investigated the effect of placing the paddle wheel or vane

anemometer at various distances from the head with or without flow restrictor and observed inconsistencies in the swirl measurement which cast doubt on the accuracy of this approach. Tippelman (1977) introduced the impulse swirl meter which consisted of a honeycomb flow straightener and measured the torque exerted by the swirling flow, which equals the flux of the angular momentum. This technique was found to give more accurate results than the paddle wheel (Monaghan and Pettifer, 1981) and is still used in industry where a fast and simple measuring method is needed, such as quality control in production lines (Bird, 1985). The value of these steady flow 'global' swirl measuring techniques is in comparing port configurations (Wigley and Hawkins, 1978), but they cannot resolve the details of the flow structures generated in the cylinder. Pettifer (1982) revealed that different intake port geometries giving the same swirl coefficient had different performance in a firing engine and this indicates that the full characterisation of the port can only be achieved by measuring the velocity field. Hot wire and more recently laser Doppler velocimetry have been used to measure velocities around the valve circumference and inside the cylinder, sometimes combined with flow visualisation (e.g. Uzkan et al, 1983; Kajiyama et al, 1984; Arcoumanis et al, 1987a). In addition to better characterisation of the ports, these measurements provide the initial conditions for computer codes which are used to predict the in-cylinder flow (Brandstatter et al, 1985; Arcoumanis et al, 1986).

1.2.2 In-cylinder flow during induction and compression

The flow inside the cylinder of reciprocating engines is unsteady, turbulent at all engine speeds and three-dimensional due to the intake port and combustion chamber geometries. The periodic nature of the flow needs other method of statistical representation than time-averaging, as in steady flows, and several methods were proposed in the past; these methods are discussed briefly in sub-section A, particularly in relation to diesel combustion. The next sub-section describes the flow during induction and the evolution of the flow structures during compression until the time of fuel injection, focussing on the particular characteristics of the HSDI diesel engine.

A.Statistical representation of engine flows

In stationary turbulent flows the usual method of representing the flowfield is to decompose each instantaneous velocity component into a time-averaged mean and a fluctuating part (Reynolds decomposition). The periodicity of the engine flowfield makes this procedure inappropriate and, therefore, the corresponding way is to decompose the instantaneous velocity in parts which are a function of crankangle θ and individual cycle i, i.e.

$$U(\theta,i) = \overline{U}(\theta,i) + u(\theta,i) \qquad (1.1)$$

The most common approach is the ensemble-averaging technique where it is assumed that the mean component is only a function of θ

$$U(\theta,i) = \overline{U}_{ea}(\theta) + u_{ea}(\theta,i) \qquad (1.2)$$

The validity of the assumption that there is no variation of the mean velocity flowfield from cycle-to-cycle has been questioned in a number of studies, which observed cyclic variation of the maximum pressure and/or power output in firing spark-ignition engines and attributed them to the pre-combustion velocity flowfield (e.g. Winsor and Patterson, 1973; Cole and Swords, 1980). Gosman (1986) argues that non-repeatabilities are bound to occur in any phenomenon which is triggered by a localised short-duration intermittent process imposed on a random process with large time and length scales. The nature of the compression-ignition combustion (section 1.2.4) differs from the spark-ignition in that, among others, ignition initiates randomly in a number of sites and, consequently, the variations of the pre-combustion flow variations are averaged out over the cylinder volume and maximum pressure variations in diesels are low compared with those in spark-ignition engines. Following these arguments, it can be concluded that ensemble-averaging is physically justified as a data processing method in diesel engines.

The implementation of ensemble-averaging in processing non-continuous velocity data, such as those obtained by laser Doppler velocimetry, requires the use of sampling crankangle intervals or windows (with duration $\Delta\theta$ and centred around θ) so that the ensemble-averaged mean and fluctuating velocities become

$$\overline{U}_{ea}(\theta) = \frac{1}{N_c}\sum_{i=1}^{N_c} U(\theta \pm \frac{\delta\theta}{2}, i) \qquad (1.3)$$

$$u_{ea}(\theta) = \left[\frac{1}{N_c}\sum_{i=1}^{N_c}\left[U(\theta \pm \frac{\delta\theta}{2}, i)^2 - \overline{U}_{ea}(\theta)^2\right]\right]^{\frac{1}{2}} \qquad (1.4)$$

A variation of this method employed in firing engine studies is conditional sampling (Witze et al, 1984), according to which one or more combustion parameters, such as maximum pressure or flame arrival at a point, are selected to identify individual engine cycles that are similar in nature; the velocity data are then ensemble-averaged in groups, according to the particular cycle they belong. This method appears to have both theoretical and physical justification.

Another approach is cycle-resolved analysis where equation (1.1) is fully implemented to derive in-cycle 'mean' velocity traces and 'true' turbulence. According to Liou and Santavicca (1983, 1985), the instantaneous velocity data are averaged within 1° crankangle intervals and fast Fourier analysis is performed to the mean trace, as well as to all individual cycles. The former is used to select a frequency cut-off limit, which is subsequently used as high pass filter to the spectra of the individual cycles; inverse Fourier transform of the resulting spectra yield the in-cycle mean traces, while rms is computed by subtracting the filtered mean velocity from the corresponding instantaneous traces and ensemble-averaging in 1° intervals. A variation of this method is cycle-by-cycle smoothing (Rask, 1981) where before the fast fourier transform the ensemble-averaged mean trace is fitted with a curve using a cubic spline algorithm. Both methods involve considerable computational work and are subject to uncertainties associated with the spectral analysis of finite duration signals (Enotiadis et al, 1990). High-pass filtering results in underestimation of turbulence magnitudes due to removal of the energy content below the cut-off limit and is also subject to arbitrary selection of filtering criteria, which should have a physical justification. In spark-assisted combustion, Bradley et al (1988) showed that the initial kernel growth is only affected by part of the turbulent spectrum, which suggests that filtering techniques may be justified by the concept of 'effective' turbulence.

Following this review, the ensemble-averaging method seems to combine simplicity with better physical justification than cycle-resolved techniques especially for flow studies in diesel engines. Furthermore the multi-dimensional calculations of the isothermal flowfield are not compatible with the cycle-resolved analysis because they solve the ensemble-averaged equations and, therefore, only ensemble-averaged velocity data can be used for validation. For these reasons ensemble-averaging was employed in the present investigation. However there is some experimental evidence that around the cylinder axis in swirling flows, the ensemble-averaging method can lead to local overestimation of turbulence (Vafidis, 1985) and this phenomenon is reviewed in the next sub-section and considered further in chapter 3.

B.Flow during induction and compression

The velocity field during induction is dominated by the annular jet flow generated by the operating valve and the rotational motion of the air charge generated inside the port.

The valve jet issues at an angle similar to that of the valve seat producing shear layers with large velocity gradients, which generate high turbulence levels, far from homogeneous. Arcoumanis et al (1987a) measured the radial and swirl velocity components at the exit plane of the inlet valve in a motored research diesel engine employing a production helical port and found that mean values range from 5 to 15 times the mean piston speed while the rms of the fluctuating components vary widely in space within 1-5V_p. The same study showed that the mean flow around the valve of the operating engine can be simulated with acceptable accuracy by steady flow measurements, confirming the quasi-steady assumption. However subsequent work (Arcoumanis et al, 1987b; El Tahry et al, 1987) showed that, although this is true for most of the valve opening period, there are differences during early and late induction. The mean velocity distributions around the valve circumference are non-uniform reflecting the effect of the helical shape of the port (Brandstatter et al, 1985) and generate a net angular momentum with respect to the cylinder axis, although certain swirl velocities at points around the valve give rise to negative components (Arcoumanis and Tanabe, 1989).

The effect of swirl on the in-cylinder flowfield during induction has been investigated in axisymmetric and eccentric inlet valve geometries. Vafidis (1984) used 30° and 60° swirl vanes positioned in an axisymmetric inlet port upstream of a single valve (serving as both inlet and exhaust) in a model engine motored at 200rpm and employing a 6.7 compression ratio and two piston geometries, flat and re-entrant bowl-in-piston. The swirl velocity distribution during induction was determined by the swirl level and the geometric characteristics of the piston-cylinder assembly, while at IVC axial stratification of swirl was observed reflecting the history of the induction process. The main features of the initial swirl velocity distribution were retained through the intake and compression stroke, indicating that the in-cylinder flow has strong memory in the transverse plane (i.e. parallel to the cylinder head). When swirl is generated by an eccentric helical port (Arcoumanis et al, 1987a) the swirl flowfield becomes more complicated, exhibiting a double vortex pattern rotating in opposite directions. This pattern is characteristic of all helical ports and has also been confirmed by steady-flow measurements (e.g.Tindal and Williams, 1977) and calculations based on multi-dimensional codes (e.g. Begleris and Gosman, 1987). Later in the induction stroke, the swirling motion becomes more organised and at IVC shows signs towards solid-body rotation. In the axial plane the interaction of the jet flow with the pressure field generated by the presence of swirl and the piston movement results in a complicated system of toroidal vortices. However these structures do not survive at IVC in either the low speed model engine with vane-induced swirl or the diesel engine with helical port at 900rpm, which implies that the in-cylinder flow does not have strong memory of the valve jet-flow in terms of mean flow.

The flowfield in the model engine (Vafidis, 1984) revealed that the swirl centre performs a helical motion which is not exactly repeatable from cycle-to-cycle and gives rise to increased rms values around the cylinder axis. Following this observation an investigation was undertaken in the course of this study (described in chapter 3) to identify its nature and assess its validity in both model and production engines rotating at a wide range of speeds.

The high turbulence levels, generated during early induction in the shear layers of the valve jet flow and the wall impingement region, are

gradually transported to the rest of the cylinder by convection and diffusion and decay rapidly. At IVC, the magnitude of the rms of the velocity fluctuations is in the range 0.7-0.9V_P according to experiments performed in model and realistic research engines (Vafidis, 1984; Arcoumanis et al, 1987a). Turbulence levels continue to decay during compression at a slower rate and at TDC of compression in the absence of a piston-bowl are in the range 0.4-0.5V_P showing signs of homogeneity and isotropy, as observed in a variety of engines rotating up to 2000rpm irrespective of the swirl generating mechanism (Bopp et al, 1986; Vafidis et al, 1987).

The angular momentum of the air charge entering the cylinder is subject to losses through the induction and compression strokes. The swirl loss mechanisms are wall friction (i.e cylinder liner, cylinder head and piston crown/bowl) and the pressure and shear drag around the valve which acts as a bluff body protruding into the cylinder (Begleris and Gosman, 1987). The later is the main loss contributor during most of the induction stroke; eventually as BDC is approached and the valve is nearly closed, this mechanism is surpassed by wall friction, which is associated with the surface-to-volume ratio, and increases during compression.

The role of the piston-bowl is to induce an inwards radial motion, termed squish, which enhances the rotational speed of the air charge by forcing it to rotate in a smaller radius of rotation (i.e. angular momentum conservation). Various designs of piston geometries are currently used including simple cylindrical bowls for research purposes, cylindrical bowls with a lip termed as re-entrant bowls and different toroidal or square bowls with shaped bottoms (Fig.1.3). The main geometrical characteristics are the squish area ratio, which is equal to the square of the cylinder bore to the top bowl diameter and the piston-to-head clearance at TDC. Squish velocities increase with increased squish area ratio and reduced bumping clearance. In some cases a factor K is used, representing the ratio of bowl volume to the total clearance volume. The squish area ratio in practical HSDI diesel engine geometries is around 4 but the observed angular momentum increase in the bowl is lower by 30-50% as indicated by experiments and calculations based on multi-dimensional codes (Monaghan and Pettifer, 1981; Gosman, 1986; for more details see section 4.3). The main reasons are wall friction, dissipation in the fluid due to turbulence and velocity gradients (swirl-squish interaction

according to some authors) and the fact that a fraction of fluid remains in the clearance height above the piston crown (effect of K factor). A computational study showed that squish is initiated at 40° to 50° before TDC and peaks at around 10° before TDC (Arcoumanis et al, 1986). Swirl reduces the penetration of the squish jet towards the bowl axis due to the interaction of the radial momentum with centrifugal forces (El Tahry, 1982; Arcoumanis et al, 1983; Vafidis, 1984), resulting, in the axial plane, in a system of toroidal vortices especially in the presence of a bowl-lip, as shown in Fig.1.4. Local turbulence maxima of around $1.0V_P$ are produced in the bowl entrance, further enhanced by the presence of the lip (Fansler and French, 1987). In practical HSDI diesel engines the piston bowl is always eccentric to the cylinder due to the position of the injector imposed by design constraints. This generates asymmetric squish which, in turn, modifies the in-bowl flow structure with possible further loss of angular momentum (Johns, 1985). However, a new type of very slim injectors (Stanadyne) can be positioned centrally in the cylinder head, thus allowing a concentric piston-bowl.

Most of the above description of the in-cylinder flow was based on knowledge of low speed engines (200-1000rpm) employing axisymmetric or modified production geometries. Some recent experimental investigations are reviewed in Table 1.1, where the main engine variables (geometrical characteristics, compression ratio and range of speed) are listed followed by the main conclusions. From these reviews it is clearly evident that few of the research engines have realistic compression ratios (16-22) or running at speeds similar to current HSDI production diesel engines. Chapter 4 describes the in-cylinder development of the swirling flow in a production engine geometry under motored conditions for different swirl levels and for engine speeds covering the practical range of 1000 to 3000rpm.

1.2.3. Fuel injection

The main requirements of a diesel fuel injection system are to supply pre-determined fuel quantities into the cylinder at certain timings (°CA) and at high pressures, typically 100-350bars for IDI engines and up to 1000bars for DIs. These systems can be categorised under two groups:

i) Pump-pipe-nozzle systems are used in both IDI and DI diesel engines for

passenger cars and employ a pump delivering fuel via high pressure lines to the injectors. Two pump types (Bosch, 1986) exist, the in-line type which utilises one plunger-barrel assembly per cylinder and the distributor type which has one plunger-barrel assembly for all cylinders, combining reciprocal and rotational movement.

ii) Unit injector systems were developed the last decade and are mainly used in large and medium DI diesel engines, although lately they have been considered for small size passenger car engines. The main difference from the previous category is that high injection pressure is generated in individual units fitted to the cylinder head, thus eliminating the need for high pressure lines.

Both systems deliver the fuel inside the combustion chamber through a nozzle, comprising the nozzle body and the nozzle needle whose front edge is pressed against the cone seat of the former by a preloaded spring determining the nozzle opening pressure (NOP). There are two types of nozzles, the pintle nozzle which is used in IDIs and produces a hollow cone spray and the multi-hole nozzle which is used in DIs and produces a number of small dense sprays. The number of holes for small HSDIs is typically 4-5 and their diameter 0.11-0.22mm (Herzog, 1989); they are arranged in an asymmetric configuration due to the inclined position of the injector with respect to the bowl and form a 140-160° cone. The fuel-filled volume between the edge of the seat and the nozzle holes (termed as sac volume) is particularly important due to possible fuel dribbling after the end of injection and the associated increase of hydrocarbon emission. This is prevented by a recent nozzle design where the needle covers completely the holes (termed as valve covering orifice or VCO, see Fig.1.5); the Hydra engine employed in the present study (chapter 4) uses a unit injector system with a 4-hole VCO-type nozzle.

At the time of injection air pressure is typically 40-70bars, temperature about 1000K and density within 16-20Kg/m^3. The fuel emerges from the nozzle holes into the combustion chamber in the form of liquid sprays, which are in a time- and space-varying state of disintegration. Evaluation of spray characteristics, as well as understanding of the mechanisms which govern break-up of liquid plumes, atomisation (i.e. droplet formation) and later evaporation, are important to diesel combustion. For this reason numerous

experiments have been performed with pump-pipe-nozzle systems injecting into the atmosphere (e.g. Obokata et al, 1988; Arcoumanis et al, 1990) or into pressurised environments (e.g. Tindal et al, 1987; Durrett et al, 1987; Hiroyasu and Nishida, 1989). Close to the nozzle exit, the jet spreads gradually at an angle as it entrains and mixes with air in its outer surface where the atomisation process is initiated, although the main spray disintegration and atomisation happens further from the nozzle exit, at a distance called break-up length, where the mass of entrainment air is greater. According to Hiroyasu (1985) the break-up length is about 10-30mm at injection pressures of about 200bars. In addition to spray angle and break-up length, the other main spray characteristics are the penetration of the spray tip, the droplet velocity and the droplet size distribution. The tip penetration was studied in the past extensively and many correlations based on experimental data and turbulent gas jet theory have been proposed and are described in the review of Hiroyasu (1985). Hay and Jones (1972) evaluated most of them and concluded that the formula developed by Dent (1971) best predicts the data; this formula was used in the course of this study and is shown in section 4.4. Evaporation affects the tip penetration (Kobayashi et al, 1982) and therefore the air temperature should be considered, although its effect is felt at distances over 30mm. The droplet size distribution is usually characterised by the Sauter mean diameter (SMD) which represents the diameter of the droplet that has the same surface-to-volume ratio as that of the^ total spray. For given air conditions and fuel properties, droplet size is a function of injection pressure and nozzle geometry; higher injection pressure and smaller nozzle hole results in smaller SMD (Arai et al, 1984). Recent studies employing laser techniques reported axial velocities of up to 200m/s obtained along the centreline of the spray and at 10-30mm from the nozzle (Yule and Aval, 1989; Koo and Martin, 1990).

A number of experimental and theoretical studies is concerned with the interaction of the sprays with the swirling air flow employing either special pressurised chambers (e.g. Oren et al, 1987; Hiroyasu and Nishida, 1989) or research engines (e.g. Kato et al, 1989; Espey et al, 1990). There is an inherent problem in trying to draw general conclusions due to the variety of injection characteristics and combustion chamber geometries employed. In a combined theoretical and experimental study Nabert and Reitz (1988) state that swirl has little effect on the spray shape before impingement on the wall

^droplets of the

and that only the smallest droplets are deflected by the gas motion.

In HSDI diesel engines a typical bowl radius is around 18-25mm and NOP is around 250bars or more; considering the values of break-up length mentioned previously it can be concluded that a proportion of the fuel hits the wall in the form of liquid fuel plumes or relatively big droplets (Nabert and Reitz, 1988) and forms a liquid film on the piston-bowl walls. This phenomenon is termed wall wetting and is also affected by wall temperature due to variable vaporisation rate. Wall wetting is a key factor in the operation of HSDI and will be also discussed in the next section. The presence of fuel ligaments or non-spherical droplets in the near-nozzle area is also reported by Yule and Aval (1989) and is confirmed by photographic evidence inside a typical HSDI diesel engine obtained by a recently developed technique, the endoscopic high-speed photography (Werlberger and Cartellieri, 1987).

Following this discussion and considering that no measurements have been reported in the literature for unit injector systems, measurements of spray tip velocity and axial droplet velocity were obtained by means of laser techniques within the near-to-nozzle area, relevant to HSDIs, and are reported in section 4.4.

1.2.4 Combustion and exhaust process

Compression-ignition combustion is a complex, unsteady, heterogeneous, three-dimensional process. While an adequate conceptual understanding of its successive phases has been achieved, quantitative information is limited and requires further investigation. The combustion process in HSDI diesel engines exhibits similarities and differences from the other types of diesel combustion in terms of swirl, combustion chamber geometry and high-pressure fuel injection through multi-hole nozzles, and, within the scope of this review, a brief description of the process is given below, subsection A, with the mechanisms of pollutant formation and the effect of engine variables on the quantities emitted reviewed in subsection B.

A. Combustion phases in HSDI diesel engines.

The traditional tools for investigating diesel combustion are high-speed photography and in-cylinder pressure recording. Both require accurate synchronisation with the engine crankshaft to identify the TDC and during the whole process with a crankangle resolution of 1° or less, due to minor crankshaft acceleration not entirely smoothed by the flywheel.

A number of investigations employing high speed photography at 5,000-22,000 frames per second have been reported with geometries similar to those of production engines and under near typical operating conditions. The early studies of Alcock and Scott (1963) and Scott (1969) used constant volume chambers and modified single-cylinder engines (bore within 100-250mm corresponding to displacements of 0.8-10litres) with optical access provided by large overhead windows; this method is still used (e.g. Arold et al, 1990) due to the unrestricted optical access and despite the unrealistic in-cylinder flowfield imposed by the alternative induction geometry with scavenging through ports in the liner. An alternative method requires optical access through a transparent piston (e.g. Fisher, 1983; Hiroyasu et al, 1986) and this approach is employed here. Another method, recently developed is endoscopic photography which, by utilising fibre optics, provides a three-dimensional view of the combustion chamber imposing only minor geometrical modifications (Werlberger and Cartellieri, 1987; Karimi, 1989).

According to Scott (1969) the following features can be identified in high speed films of diesel engine combustion:

i) Fuel sprays. The fuel reflects light from spot lamps and defines the liquid spray boundaries. Alternatively the sprays are visualised as shadows against the background of the well polished cylinder head illuminated by spot lamps. The vapour phase of the sprays can also be visualised by shadowgraphy, which is difficult to implement since it requires a mirror-like cylinder head and complicated optical setup.

ii) 'Premixed' flames. The luminosity is normally too low to be recorded on the film with the exposure level used and correspond to the first phase of mixture burning (see below). In order to visualise them, Scott (1969) and Fisher (1983) added copper salt to the fuel which gave to these

normally blue flames a brighter greenish colour.

iii) 'Diffusion' flames. These flames involve high-temperature carbon particles and provides more than adequate luminosity, appearing on the film as white. As the flame cools, the particles change colour through orange to red in the manner of normal black body radiation. The temperature range varies from 2300°C, corresponding to the totally white areas, to 1000°C corresponding to the dull red regions.

iv) Over-rich mixture. The appearance of a brown flame, usually surrounded by a white diffusion flame, indicates a very rich mixture which gives rise to clouds of soot particles. This fuel-rich soot-laden cloud burns up rapidly with a bright white flame when it contacts areas consisting of unburnt air.

Investigations based on pressure recordings (e.g. Austen and Lyn, 1961; Lyn, 1962; Gatowski et al, 1984) evaluate the heat release rate and the fuel mass burning rate during combustion using zero-dimensional or single-zone models. The following phases can be identified, as indicated in Fig.1.6, where a typical for a HSDI diesel engine pressure-heat release-vs-crankangle diagram is shown:

i) Ignition delay (ab) is the period between the start of the fuel injection into the combustion chamber and the start of combustion as determined from the change in slope on the pressure-vs-crankangle diagram or the appearance of first visible light in the high-speed films. During this period both physical and chemical processes occur to certain portions of the fuel. Physical processes include atomisation, impingement on the wall, vaporisation and mixing with air in regions favoured by the swirling movement, while chemical reactions (such as pyrolysis) are complex and not known in detail.

ii) 'Premixed' or rapid combustion phase (bc). The portion of the fuel which was previously mixed with air to within the flammability limits, burns rapidly causing an abrupt pressure rise. This is a key phase in the operation of the HSDI diesel engine since it is associated with noise generation and NO_x formation and differs from other compression ignition concepts in that both the slope and the maximum pressure are

higher.

iii) Diffusion' or mixing-controlled phase (cd). The burning rate of the remaining fuel, which is still injected in medium-to-high loads, is controlled by the rate at which the physical processes proceed. Pre-flame chemical reactions occur at very high rates under the high temperatures generated by burning fuel, so that their effect on the time scale of the process is insignificant.

iv) Late combustion phase (de). Heat release continues at a lower rate well into the expansion stroke generated mainly by the burning of the carbon particles or soot and other incomplete combustion products, such as HC and CO. The degree of success in mixing with the remaining air and eventually burning these products before temperature falls, determines the amount of pollutants emitted in the atmosphere.

It should be noted that the terms 'premixed' and 'diffusion' do not correspond to the exact definitions referred to steady combustors, since the nature of the whole process in HSDIs is clearly diffusive, but they are frequently used in the literature to identify the different phases.

B. Noise and pollutant formation

The common pollutants of all internal combustion engines are either gaseous or small solid/liquid particles of around 0.1μm diameter, better known as particulates, consisting of various substances according to the engine type. Gaseous emissions are oxides of nitrogen (mainly NO and small quantities of NO_2, collectively known as NO_x), carbon monoxide (CO) and organic compounds, which are either unburnt or partially burned hydrocarbons (HC).

The HSDI diesel engine emits very low levels of CO due to the overall lean mixtures it operates. Gaseous HC emissions are also low under medium-to-high load and steady operating conditions, increasing only in extreme cases of over- or under-fuelling. At low load/idle speed very lean mixtures can be formed locally due to overmixing, whereas during acceleration under full throttle, undermixing of fuel-rich mixtures can occur. Low-velocity fuel dribbling due to relatively large sac volumes gives rise to significant gaseous

HC emissions and can be avoided by VCO-type nozzles (Greeves et al, 1977). However, the major problems of the HSDIs operation are combustion-related noise, gaseous NO_x and particulate emissions.

Noise is generated during the 'premixed' phase and is associated with the abrupt pressure rise, steeper gradients yield higher noise levels. The slope in DI diesel engines operation is larger than in IDIs (Lyn, 1962) intensifying the noise problem but can be partly dumped by the appropriate design of the crankcase and engine head. Further improvement can be achieved through modifications of the timing and rate of fuel injection, which are discussed later due to their simultaneous effect on emissions.

NO_x is formed from the oxidation of atmospheric nitrogen and fuel nitrogen-containing compounds. The rate of NO_x formation is maximum when the equivalence ratio of the mixture is close to stoichiometric and burned gas temperatures are at a maximum (Heywood, 1988). For the HSDIs operation this means that the critical period is the 'premixed' phase; NO_x is formed in areas with local air-fuel ratios close to stoichiometric until the time of maximum cylinder pressure. The decreasing temperature due to expansion and mixing of high temperature gas with cooler air results in decomposition of a certain portion while the remaining undergoes a chemical 'freezing' process and appears in the exhaust.

Diesel particulates are defined as any matter collected on a filter paper from the diluted engine exhaust at a temperature below 52°C excluding condensed water vapour (MacDonald et al, 1984). They are usually measured (expressed in milligrams per cubic meter of exhaust gases at standard conditions) in dilution tunnels which simulate the physical and chemical processes occurring in the atmosphere (MacDonald et al, 1980); alternative methods, much faster but inaccurate, are filter-based soiling smoke meters (the best known is the Bosch smoke meter) where the degree of darkening of the filter paper is measured by an optical technique (Alkidas, 1984). Particulates consist of an organic insoluble fraction, which is soot or carbonaceous material plus sulfates and bound water, and of organic soluble fraction, originating from unburnt fuel hydrocarbons and lubricating oil (Cartellieri and Herzog, 1988). Soot is formed mainly during the diffusion phase in areas where there is lack of oxygen, especially on the combustion

chamber surfaces when wall-wetting is severe (Norris-Jones et al, 1984). Soot particles are formed through coagulation, agglomeration and surface growth due to absorption of other gaseous or liquid substances such as HC, sulfates and lube oil. They are subsequently oxidised through contact with air, promoted by swirl, but a certain portion survives until the opening of the outlet valve (Cartellieri and Wachter, 1987).

Noise levels and NO_x/particulate emissions are affected by various engine parameters, i.e. fuel injection system characteristics, gas conditions at the time of injection and combustion chamber geometry (discussed in the next paragraph), the fuel composition and especially its sulphur content, as well as the mechanical engine parameters (such as valve head-seat and cylinder liner-piston ring designs) governing the amount of lube oil inside the combustion chamber.

In diesel engines the timing of fuel injection is an important parameter affecting the trade-off between particulates and NO_x emissions. Advance injection timing generally results in higher NO_x and lower particulates and in HSDIs the best compromise is within the range 5-14°CA BTDC depending on speed and load. The effect of injection pressure has been investigated extensively and a general trend is that higher pressure, and the associated improved fuel atomisation, results in lower particulate emissions for the same NO_x levels especially in medium size DI diesel engines (Kato et al, 1989). However, inside the HSDI bowl-piston, increased spray penetration may reduce or eliminate the benefits from better atomisation especially at medium-to-high loads (Oblander et al, 1989; Ikegami, 1990). Smaller nozzle hole diameters (reduction from 0.20mm to around 0.12mm if possible) combined with larger number of holes (e.g. from 4 to 6) can both decrease penetration and improve atomisation (Wojik, 1989), although they can increase emissions at low-to-medium loads and speeds. Herzog (1989) indicated that the only feasible method to overcome these problems is the shaping of the injection rate, and consequently the injection duration, according to speed and load especially during the ignition delay period when the amount of injected fuel should be limited. Dual-spring injectors resulting in two-stage fuel injection offer some advantages, but only electronically-controlled unit injectors employing fast solenoid valves can fully exploit the variable injection rate concept, combining also variable injection timing

according to pre-determined 'maps'.

The gas conditions in the cylinder include pressure and temperature, associated with the compression ratio, gas motion i.e. swirl distribution and turbulence levels, and the percentage of oxygen which, in some cases, is reduced by returning a certain portion of the exhaust gases back into the inlet port (exhaust gas recirculation, EGR). Higher compression ratios result in lower HC emissions and low combustion noise and in practice compression ratios range from 19 to 23. EGR is used mainly at low load/idle speed conditions to decrease maximum in-cylinder pressure, temperature and heat release during the 'premixed' phase, resulting in lower NO_x emissions. The gas motion is closely related to the combustion chamber geometry, which in modern HSDIs is usually a re-entrant type with the minimum possible TDC clearance gap. Turbulence levels especially in the bowl entrance area affect the mixing process with fuel, although the turbulence generated by the sprays plays the dominant role (Harvey and Gosman, 1982; Balles and Heywood, 1988). The effect of swirl levels on emissions was investigated by a number of authors (e.g. Khan et al, 1972; Spicher et al, 1987; Van Gerpen et al, 1985; Belardini et al, 1989) but the conclusions do not fully agree due to the variety of injection systems/chamber geometries employed and the different trends under varying speed and load. Performance and emission tests performed in a medium size DI engine at medium speed and maximum load showed that the general trend is that increasing swirl up to a point results in lower particulates and higher NO_x (Khan et al, 1973). There is at least one engine manufacturer (Shimada et al, 1986) who employed a variable swirl inlet system to a medium size DI diesel engine in order to achieve the optimum combination of bsfc and emissions over the operating range of speed and load. In a comprehensive experimental investigation on small HSDIs, based on performance and emissions tests, Yoshikawa et al (1989) state that the NO_x levels increase with increasing wall wetting and that, in order to reduce both exhaust smoke and particulates, it is more effective to optimize the nozzle hole configuration (ratio of length to diameter) rather than to adjust the intake swirl levels and chamber geometry. A number of recent experimental investigations, involving combined optical and 'conventional' techniques, and their main findings are included in Table 1.1.

1.3 PRESENT CONTRIBUTION

The above review of the high-speed direct-injection diesel engines has indicated the potential of the concept, its advantages and limitations. The particular characteristics of the combustion process were shown to be directly related to the initial air velocity flowfield, generated by the inlet system, its evolution inside the cylinder which is dictated by the piston movement and the particular geometry of the combustion chamber, and its interaction with the fuel sprays prior to ignition. Further reductions on pollutant emissions and noise are needed while maintaining the fuel economy advantage at a wide range of speed and load and this formidable task can only be achieved by detailed experimental investigations performed by optical and 'conventional' techniques, coupled with multi-dimensional calculations.

The purpose of this thesis is to contribute to the understanding of the swirling flows inside HSDI diesel engines and the mechanisms affecting the combustion process. Optical techniques, supported in some cases by 'classical' methods, were applied in geometries of gradually increasing complexity under both motored and firing operation with the following specific objectives:

-To investigate the development of a simplified axisymmetric swirling flow generated by vanes inside the cylinder and to assess the possibility of simulating the engine flow by steady flow experiments. The movement performed by the swirl centre is examined as a fluid mechanics phenomenon inherent to swirling flows and as a possible cause of turbulence overestimation in ensemble-averaged velocity data.

-To study the effect of inlet manifold shape and of throttling the induction air on the TDC swirl velocity flowfield generated by a production helical port. Throttling was considered as a method of decreasing maximum in-cylinder pressures enabling the use of perspex cylinders and pistons-crowns in modified production diesel engines at realistic compression ratios.

-To study the effect of engine speed and swirl levels on the flow evolution during induction and compression stroke inside a research HSDI diesel engine, based on a production engine. Links between the axisymmetric swirling flow and the complex flow generated by a helical port are

established.

-To assess the characteristics of a unit injector in terms of spray tip penetration and axial droplet velocities and to compare with conventional injection systems.

-To study diesel combustion under different conditions of engine speed, load and swirl levels and to identify its different phases. Data from non-firing studies are analysed to provide links between the pre-combustion and combustion flow.

-To compare the performance of purpose-built single-cylinder optical engines and multi-cylinder production engines of nearly identical geometry.

The optical experimental techniques selected were laser Doppler velocimetry for the air and fuel droplet velocities, beam deflection for the spray penetration and high speed photography for the combustion visualisation. All optical and signal processing equipment were tested in a constant-volume combustion chamber which combined ease of operation with some degree of simulating engine conditions.

1.4 THESIS OUTLINE

The remainder of the thesis is divided into four chapters. Chapter 2 is devoted to the experimental techniques applied in the course of this thesis and to the various methods and materials used to obtain in-cylinder optical access. The principles of the techniques are briefly described followed by the presentation of typical results obtained for evaluation purposes in a constant-volume combustion chamber.

Chapter 3 investigates phenomena associated with swirling flows generated by vanes in two steady-flow rig configurations and in a model engine (section 3.2) and by a helical port in a modified production engine (section 3.3). Both engines operate under motored conditions at unrealistically low speed and compression ratio but provide the advantage of full optical access. In each section a brief description of the instrumentation is given followed by the presentation and analysis of the results. The chapter concludes by summarising the main findings of the two studies with

particular emphasis on their relevance to the HSDIs operation..

Chapter 4 describes a complete investigation of the flow, spray, combustion and performance characteristics in a research HSDI diesel engine, operating at almost identical conditions to production engines. All the particular characteristics of the engine are presented in detail followed by a small section summarising the results drawn from steady flow tests of the engine head. The swirling flow during induction and compression is presented in section 4.2 followed by the discussion of the spray characteristics based on tests performed under atmospheric conditions. The combustion process is then analysed based on photographic evidence, pressure recordings and performance data, followed by a summary of the main conclusions.

The final chapter reviews the main findings of the thesis followed by recommendations on the parameters of high-speed direct-injection diesel engines requiring further attention and suggestions on possible improvements to the experimental techniques.

TABLE 1.1 Recent investigations in Direct Injection engines.

Author(s) and Year	Technique and Flow Configuration	Main Findings
Murakami et al, 1986	LDV / Single-cylinder engine running at 1000rpm with three cylinder heads (SR=2.0-3.0), toroidal piston-bowl, 110mm bore, CR=13, 1.3litres displacement and optical access through windows in the liner and the piston walls.	The mean swirl distributions are complex during induction and gradually become near to solid-body rotation during compression exhibiting axial stratification. Mean swirl velocities go through maxima at around IVC and close to TDC. The evolution of the swirling flow is independent of the swirl levels.
Iijima and Braco, 1987	Cycle-resolved LDV / Ported single-cylinder engine running at 1200rpm with swirl induced by swirl inserts (SR=4.0), four bowl-piston configurations, (circular and square, axisymmetric and off-centre), 82.6mm bore, CR=10.8, 0.67litres displacement and optical access through a large circular window on the top.	Square piston bowls result in 35% less angular momentum at TDC than circular ones. The uneven squish generated in the off-centre piston-bowl geometries distorts the swirl mean profiles at TDC, moving the swirl centre towards the bowl axis. Cycle-resolved turbulence intensity is higher in the square piston-bowls and exhibits local maxima at the bowl rims but everywhere else shows signs of isotropy and homogeneity.
Saxena and Rask, 1987	Two-component LDV-cycle resolved analysis / Modified V8 production engine running at 750-1500rpm with optical access to one cylinder through a 2.5mm diameter circular window, variable swirl ratio with helical port or shroud valve (SR=0.5-3.0), flat piston, bore 96.5mm, CR=8 and displacement 0.7litres.	Ensemble-averaged mean and rms velocities scale well with engine speed in contrast with the cycle-resolved turbulence intensity. Initially different swirl levels persist during compression and at TDC both rms and cycle-resolved turbulence distributions tend towards isotropy and homogeneity

Table 1.1 Continued.

Hall and Bracco, 1987	Cycle resolved LDV under motored and spark-assisted firing conditions / engine similar to Iijima and Braco (1987), running at 600-2400rpm with CR=7.5, flat piston, variable swirl (two cases, SR=0-4) and variable volumetric efficiency (or scavenge ratio).	Under motored conditions mean velocities scale almost linearly with intake velocity, for a fixed speed and engine speed for a fixed scavenge ratio. The presence of swirl results in 25% inhomogeneities in cycle-resolved turbulence intensity with maximum values around the cylinder axis. Under firing conditions mean swirl velocities exhibit maxima ahead of the flame followed by a marked drop and scale almost linearly with engine speed.
Cipolla et al, 1987	LDV / Single-cylinder purpose-built engine running at 1000rpm with production helical port (SR=3, measured by paddle wheel), toroidal piston-bowl, 93mm bore, CR=16, displacement 0.65litres and optical access provided by small quartz windows on the liner and a 50mm diameter on the head.	At IVC swirl ensemble-averaged mean and rms velocity distributions and radial position of the swirl centre vary with the axial distance from the cylinder head. Axial vortical structures persist up to 100°CA BTDC of compression while mean swirl profiles outside the piston-bowl evolve from near solid-body rotation to 'flat top' distribution. Squish velocities at 30°CA BTDC depend strongly on the piston crevice volume. At TDC and inside the piston bowl the toroidal shape results in strong axial stratification of the swirl distributions with ensemble-averaged rms levels of $0.6V_p$ approximately

Table 1.1 Continued

Spicher et al, 1987	Two-dimensional LDV under both motored and firing conditions and flame velocity measurements by novel optical fibre technique / Single cylinder purpose-built engine running at 1100rpm with variable swirl ratio with shroud valve (SR=1.8-4.2), cylindrical piston-bowl, 125mm bore, CR=17 and displacement 1.9litres. Optical access for LDV was provided by a small window on the top while the flame appearance was detected by fibres mounted on the engine head, liner and piston.	During compression the mean swirl centre changes location while at TDC the in-bowl swirl distribution resembles solid-body rotation. Comparison between motored and firing operation indicates that fuel injection, from a single-hole injector, and possibly combustion tend to increase cycle-resolved turbulence and decrease mean velocities. Ignition delay is reduced with increasing swirl and smaller TDC clearance. High soot emissions are associated with fuel injected straight onto the pre-ignited flame.
Fansler and French, 1987	LDV / Single cylinder optical engine running at 600rpm with directed port and variable swirl (SR=4.5-6.6 at IVC), two axisymmetric piston-bowl configurations (cylindrical and re-entrant), bore 98.4mm, CR=10.6, displacement 0.82litres and optical access through quartz windows on the cylinder head and the piston base.	The squish flow is strongly affected by geometry and much less by swirl levels. Inside the bowl the mean flow structure is complex and depends both on geometry and swirl levels. High shear regions formed near the entrance of the piston-bowl around TDC of compression, produce high rms fluctuations which are more intense in the re-entrant bowl (up to $1.5V_P$). After TDC reverse-squish and high-shear inside the bowl entrance occur only in the re-entrant bowl-piston case.

Table 1.1 Continued.

Murakami et al, 1988	LDV measurements used for the development of a simplified numerical model / Engine similar to Murakami et al, 1986, running at 250-1000rpm with four cylinder heads (SR=2.0-3.0), four piston configurations (flat and different toroidal shapes) and variable compression ratio (6.6-13).	During intake two counter-rotating vortices appear and evolve in a more organised motion during compression. The effect of the piston-bowl on the mean velocity field is apparent during early induction and after mid-compression. Reduced compression ratios result in less asymmetric swirling flow pattern while higher engine speeds result in more than linearly increased friction.
Tindal et al, 1989	LDV / Single-cylinder modified production diesel engine running at 1000-3000rpm with helical port (SR=3.0), re-entrant toroidal off-centre piston-bowl, 80mm bore, CR=6.7, displacement 0.42litres and optical access through a fully transparent acrylic cylinder.	Mean swirl velocities do not scale with speed at mid-compression whereas at 330°CA ATDC the variation with speed is almost linear. The radial flow patterns during late compression (330°-350°CA ATDC) vary significantly with engine speed and are sensitive to minor geometric variations.
Belardini et al, 1989	LDV compared with three-dimensional calculations and combined with performance tests / Single cylinder optical engine running at 1500-3000rpm with helical port, three cylindrical and one four-lobe bowl-pistons (with different aspect ratios), 100mm bore, CR=18, displacement 0.8litres.	Ensemble-averaged rms velocities in four-lobe chambers are higher by around 120% than those in cylindrical chambers while mean swirl velocities show opposite trends. Excessive reduction in mean swirl levels results in poor particulate-NO_x trade-off at peak torque conditions, while at part load and low speed moderate decrease in swirl levels results in opposite trends.

Table 1.1 Continued.

Arold et al, 1990	LDV combined with high-speed photography / Single cylinder ported engine running under both motored and firing operation at 900rpm, with and without swirl, cylindrical and square combustion chamber incorporated in the head, bore 82.6mm, CR=14, displacement 0.61litres and optical access through a large top quartz window.	Under motored operation mean swirl velocity distributions at TDC resemble solid-body rotation with swirl ratios of 8 and 9 for square and round chambers respectively. The overall rms fluctuations at TDC are not affected by the presence of swirl except around the cylinder axis where they are higher for the swirling case. Under firing operation high speed photography shows that swirl affects the penetration of the sprays produced by the pump-pipe-nozzle injection system.
Espey et al, 1990	High speed shadowgraphy / engine same as Arold at al, 1990	Swirl has greater effect on the sprays during late rather than early injection and reduces overall penetration by around 17%. Air-fuel mixing air is promoted by swirl resulting in leaner initial combustion and visible flame growing more rapidly. After TDC, the presence of swirl reduces flame penetration towards the squish area.

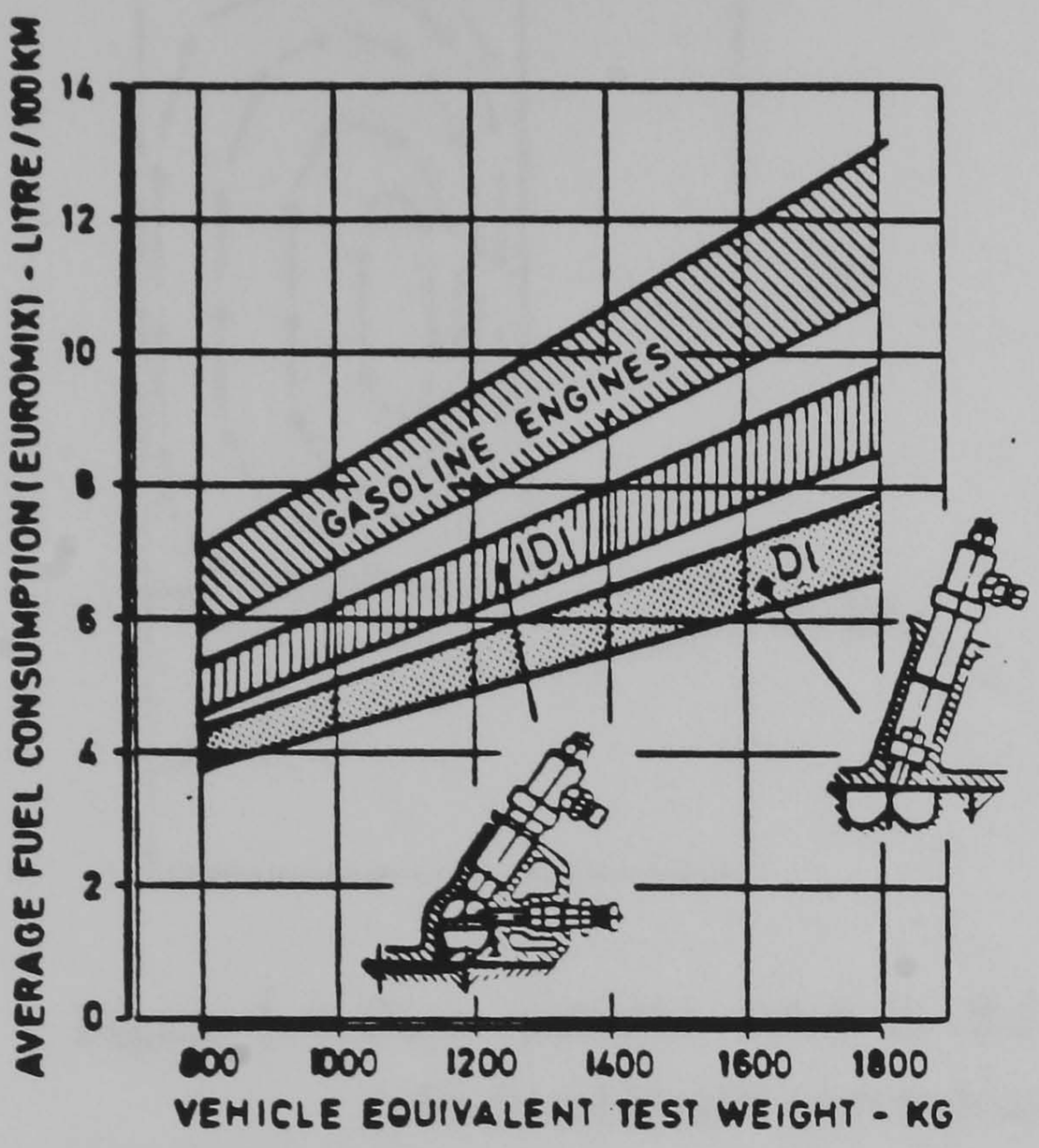


Figure 1.1 Average fuel consumption according to ECE city cycle (90km/h and 120km/h) of light duty vehicles powered by gasoline, IDI and DI diesel engines (Wojik, 1989)

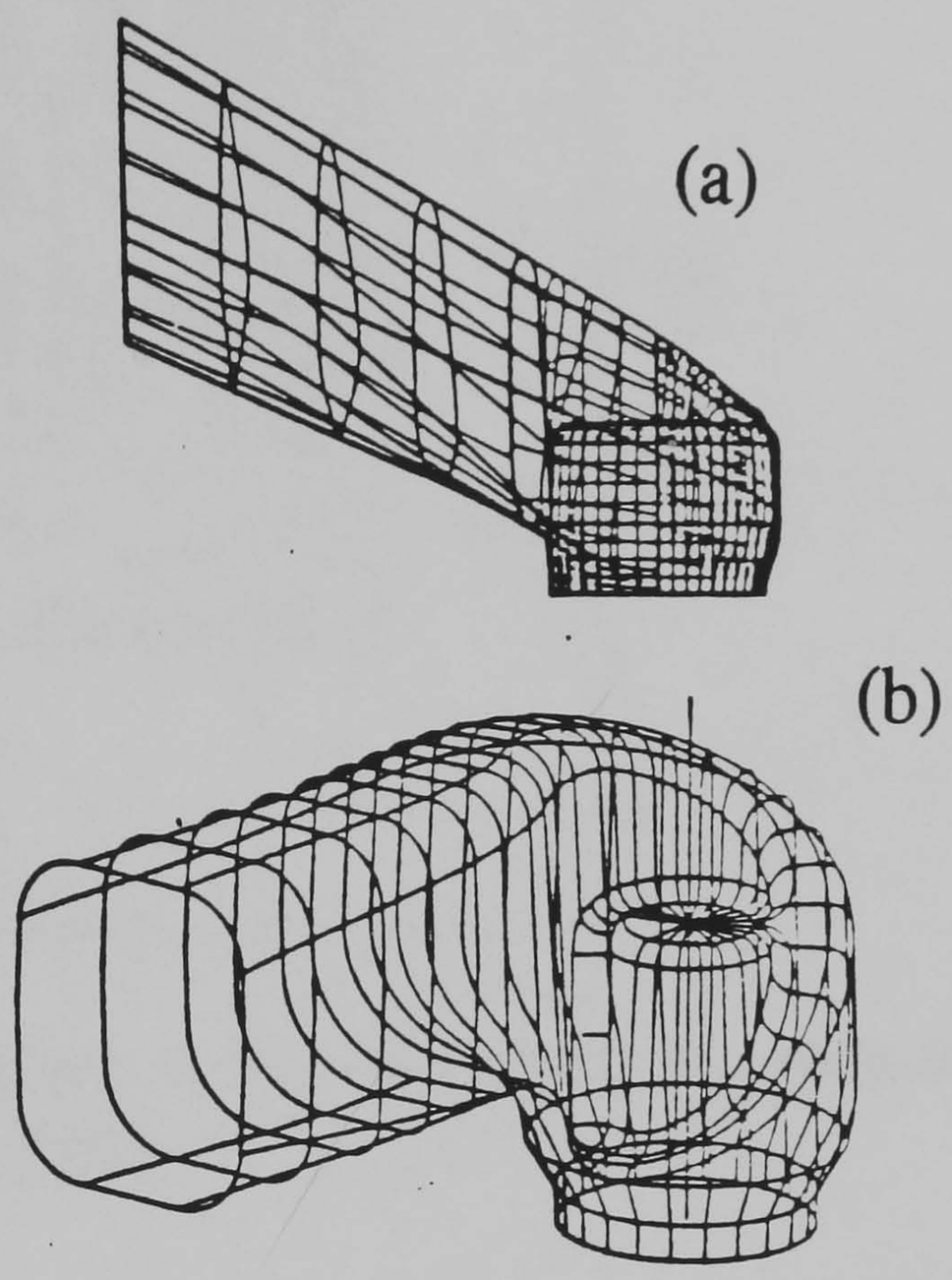


Figure 1.2 Examples of (a) directed and (b) helical ports (Bird, 1985).

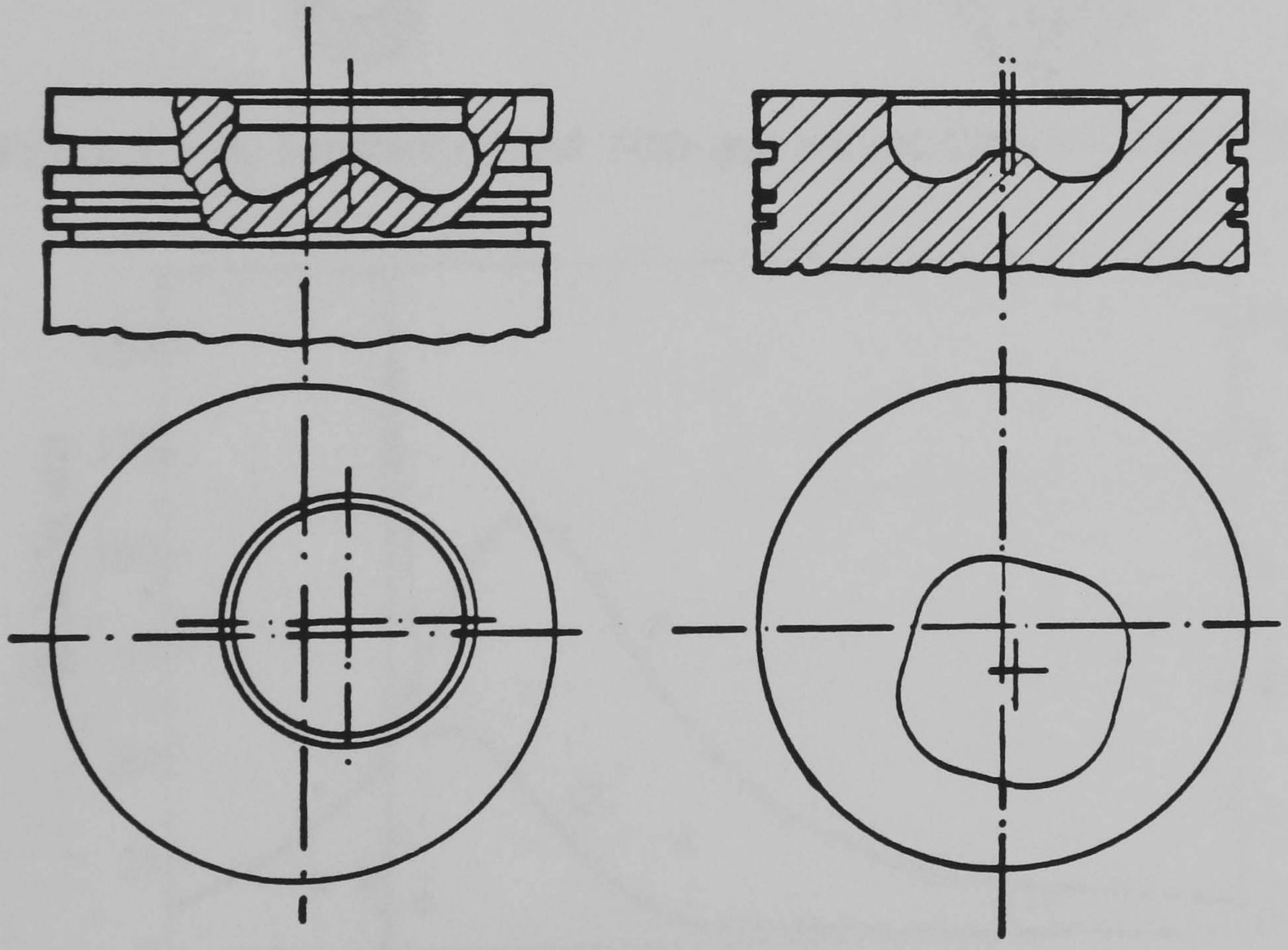


Figure 1.3 Typical piston-bowl geometries used in production HSDI diesel engines (Stephenson and Hood, 1987).

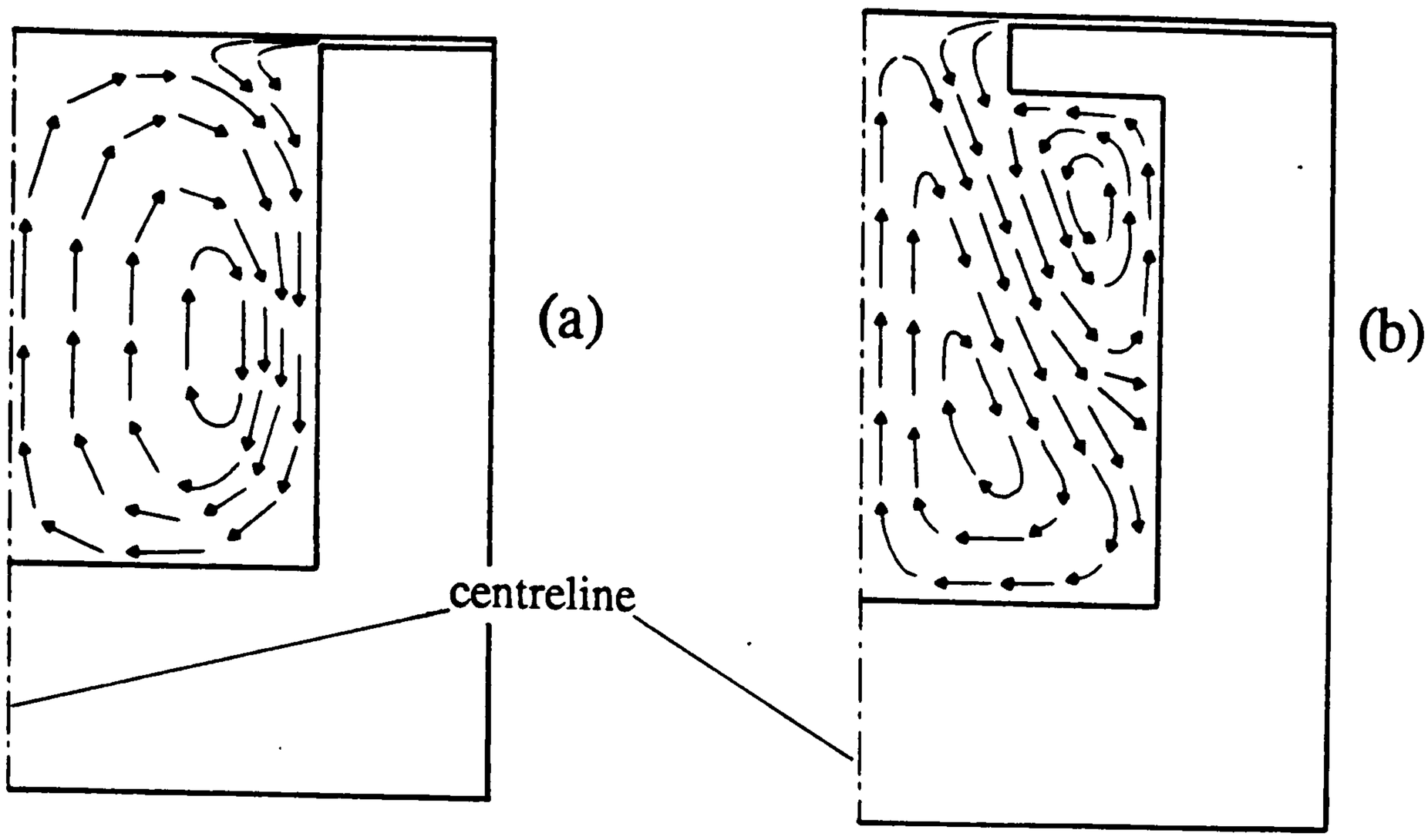


Figure 1.4 Flow patterns setup in the axial plane in (a) simple and (b) re-entrant cylindrical bowls (Arcoumanis et al, 1983).

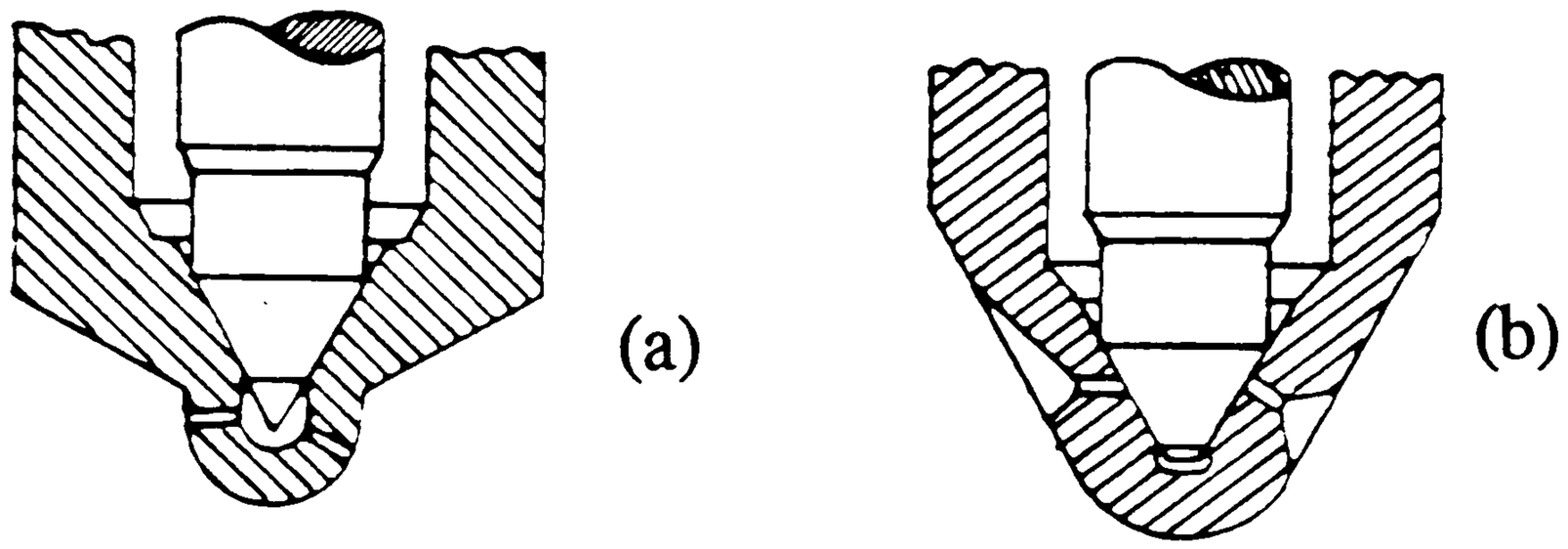


Figure 1.5 (a) Standard (b) and VCO-type nozzles (Greeves et al, 1977).

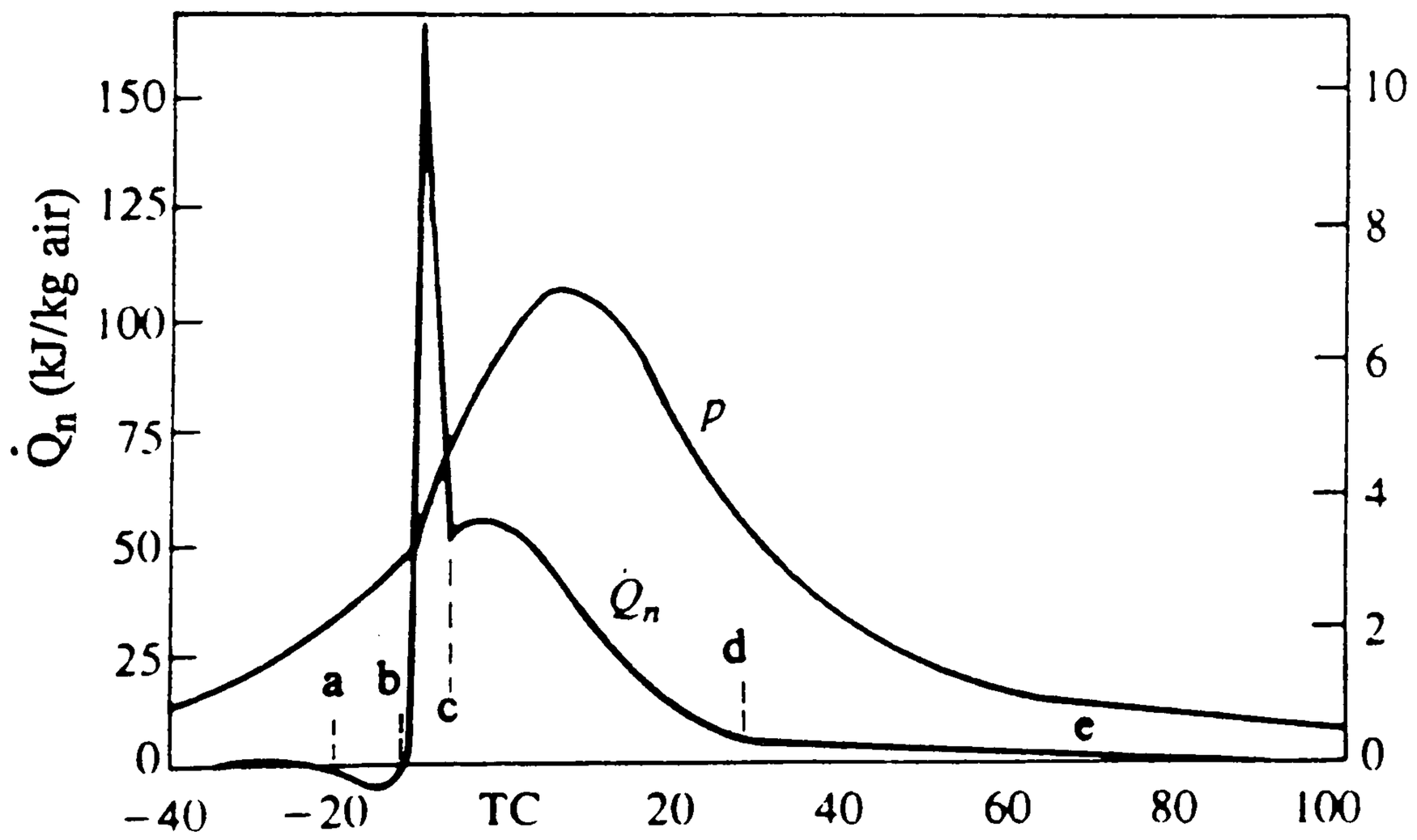


Figure 1.6 Typical pressure and heat release diagram for small HSDI diesel engines (Austen and Lyn, 1961).

CHAPTER 2

OPTICAL INSTRUMENTATION

2.1 INTRODUCTION

Investigation of the flow and combustion in diesel engine cylinders requires a combination of optical and conventional methods and, since the latter have been extensively used in engine research (Amann, 1985), the emphasis in this chapter will be on optical techniques, their requirements for optical access and the corresponding measurement uncertainties.

Three laser-based measuring techniques are described, namely laser Doppler velocimetry, laser beam deflection and high-speed shadowgraphy, and the results are used to evaluate the applicability of the techniques to the internal-combustion engine environment. Of the three techniques LDV proved to be the most useful and is discussed extensively since it is used for most of the results of subsequent chapters. The transparent materials used as windows in conjunction with the above techniques are also described since they play an important role in the application of all three techniques to characterise the in-cylinder flow.

2.2. REQUIREMENTS FOR OPTICAL INSTRUMENTATION IN ENGINES

The most important requirement for the application of optical techniques to reciprocating engines is optical access to the combustion chamber which should be achieved with the minimum possible modification to the engine. Optical access can be obtained through the cylinder liner, the cylinder head and the piston-bowl base. The choice of the transparent material and the method employed depends on the engine type (gasoline or diesel) and whether it is motored or firing, the engine geometry and the experimental technique to be applied i.e. point vs. planar techniques.

Material name	Material type	Tensile strength ($Pa*10^7$)	Elastic modulus ($Pa*10^8$)	Coef. of thermal expansion ($^oC^{-1}*10^{-6}$)	Coef. of thermal conductivity ($W/m*^oC$)	Maximum temperature for safe use (^oC)	Density (Kg/m^3*10^3)
Perspex (Polymethyl-methacrylate)	Plastic	5.5	2.8	7.0	-	70	1.2
Pyrex (SiO_2)	Glass	6.9	600	3.2	1.3	1100	2.2
Quartz (SiO_2)	Glass	4.8	700	0.6	1.4	1100	2.2
Sapphire (AL_2O_3)	Crystal	28-41	3400-3900	8	25	1600	4.0
Cast Iron	Metal	20-41	2000	12	46	1100	7.5

TABLE 2.1. Materials for optical windows in engines.

There are many transparent materials that can be used as windows in optical engines. They can be classified as plastics, glasses and crystals (Bates, 1988) and the properties of typical materials representing each group, together with cast iron as the most common engine cylinder material, are displayed in table 2.1. All of these materials are strong enough to withstand the stresses encountered during motoring operation of all engines. Plastics are inexpensive, easy to machine and polish, but their strength decreases rapidly with temperature and their thermal conductivity is so low that they cannot be adequately cooled and their use in motored engine studies is limited to compression ratios up to 9 which excludes diesel engine geometries. Deformation of a perspex piston-bowl has been observed under continuous motoring operation in a research diesel engine by Arcoumanis et al (1986) and this can be prevented by throttling the induction air thus reducing the maximum in-cylinder pressure; this method was tested successfully during the course of this study and is reported in chapter 3. The properties of quartz (or fused silica) are not seriously affected by the temperatures experienced in motored engines and therefore, despite its poor thermal conductivity, it can be used safely even at compression ratios of 18-22. In firing engines quartz can also be used but with some precautions and for a limited period of time so that the temperature of the window does not exceed 1100^oC (table 2.1). Quartz may also break spontaneously and randomly due to the development of stress cracks, so that a steel guard or cover should always be employed around the engine. Nakanishi et al (1975) and Namazian et al (1980) employed this material in the form of flat windows while Bates (1988) used it in the form of a cylindrical liner. Quartz is more expensive than perspex and

requires special machining, but it is widely available from specialised optical companies, mainly in the form of small flat windows. Well polished and parallel surfaces for laser light transmission can be easily achieved but even minute scratches can make them unusable, due to the stress concentration on these points. Quartz windows were employed in a research DI diesel engine to provide optical access under both motoring and firing operation and the results of this investigation are reported in chapter 4.

According to table 2.1 the best candidate for large windows or cylindrical full liners operating under firing conditions is synthetic sapphire in the form of a single crystal. This material is able to withstand very high temperatures, is strong and very hard and has excellent optical properties. The disadvantages of sapphire are that it is difficult to polish, anisotropic and susceptible to thermal stresses, due to comparatively large coefficients of thermal conductivity and expansion, and has a very high manufacturing cost which prohibits its use in small research projects.

Following this discussion of transparent materials for engine studies, it can be concluded that for low-compression ratio research engines, plastics such as perspex offer an acceptable solution but for diesel engine studies, quartz provides the most viable solution. Wigley (1990) has suggested that transparent liners made of specially treated glass (Borosilicate crown, known as BK7) can be used instead of quartz in firing engines but this remains to be demonstrated.

It is worth noting that careful design of the window shape, mounting and surface finish are important factors for a reliable operation. Complex window shapes with edges are likely to fail due to stress concentration at critical points and direct metal-to-glass contact in the mounting can also result in failure, even under motoring operation.

2.3 EVALUATION OF OPTICAL INSTRUMENTATION

Prior to the measurements in DI diesel engines, optical techniques were used in a constant-volume combustion chamber in order to assess and improve their capabilities. Single-shot experiments can provide useful information on the combustion process occurring near TDC of compression

and are useful in the study of fundamental aspects of flame initiation and propagation of various gaseous fuel-air mixtures at different initial conditions of pressure, temperature and turbulence levels (e.g. Dunn-Rankin et al, 1986; Abdel-Gayed et al, 1987). Thus, the aim was to evaluate the optical diagnostic methods and to develop and test the optical and electronic equipment; a brief discussion of the results will follow so as to assist the evaluation of the optical methods.

Propane and compressed air were introduced through two-way valves into the mixing chamber, see Fig.2.1, where the combustible mixture could be stored at pressures higher than the initial test pressure. A diaphragm-type pressure transducer and a pressure gauge were used to measure accurately the partial pressures of fuel and air in the chamber in order to evaluate the mixture equivalence ratio using Dalton's law. Problems due to residual gases, necessitated the use of an AAL model 523 Hydrocarbon Analyser which, by using a flame ionisation detector to measure hydrocarbon concentration, achieved a better accuracy. The mixture, whose equivalence ratios varied between 0.65 and 1.20, was introduced into the chamber via a high pressure line, which was equipped with a pressure regulator to adjust the initial test pressure.

Optical access into the oval-shaped vessel of Fig.2.2 was provided by two small and two large circular sapphire windows with the temperature of the chamber walls controlled by means of four wire heaters and a K-type thermocouple. The test temperature was set at 400K in order to prevent water condensation on the windows and the chamber was equipped with a spark plug, connected to a commercial ignition system, and two manually operated valves to isolate the vessel and to fill and evacuate. A vacuum pump was connected to the purge line to ensure that no residual gases were left into the chamber after each test.

A piezoelectric pressure transducer (Kistler model 6121) was fitted when required into specially constructed blanks which replaced the windows to monitor the instantaneous chamber pressure. The electric charge generated from the transducer was converted to an electrical signal by a charge amplifier (Kistler model 5007) and was monitored either through an oscilloscope or a recording system incorporating an analog-to-digital

converter (DATALAB DL912 with max. conversion rate of 20MHz) and an Apple IIe microcomputer. The transducer system was calibrated by means of a dead-weight tester over the range of pressures expected in the chamber and the zero-drift was minimised by allowing sufficient warm-up time and by appropriate choice of the integration time-constant in the charge amplifier. The accuracy of the measurements was estimated to be better than 3% of the maximum in-cylinder pressure, taking into account non-linearities of the system and the reading accuracy on the oscilloscope display.

A typical run started with the filling of the chamber with fresh charge at an initial pressure of 6bars. After waiting for about 10s, the quiescent propane-air mixture was ignited with a spark plug which, through generation of an induction pulse, enabled triggering of the A/D converter for the pressure measurement and/or the LDV counter for the velocity measurement, thus allowing accurate synchronisation of the various events. A similar method of triggering the LDV counter was used in the investigation of the spray in the Hydra engine (chapter 4) using the needle lift signal.

2.4 LASER-BEAM DEFLECTION

2.4.1 Principle and implementation

Laser-beam deflection is a non-intrusive technique which detects the presence of refractive index gradients in regions of the flow which are optically-accessible. It was initially developed as a flame-detection technique inside constant-volume chambers (e.g. Dyer and Witze, 1978; Metghalchi and Keck, 1980) and spark-ignition engines (e.g. Richman and Reynolds, 1984). More recently, Arcoumanis et al (1988b) applied it for the measurement of the tip penetration of confined high-density transient jets.

The method relies on the deflection of a laser beam by a change of the refractive index at some point along its path. According to Holder and North (1963) the curvature of a light beam is proportional to the refractive index gradient in the direction normal to the beam. The refractive index may vary across the field because either different media are present at different points along the beam or because the density of the medium changes due to

temperature and/or pressure variations. Since we are often concerned with gases, the refractive index n is related to density ρ by the equation:

$$n-1 = (n_o-1)\frac{\rho}{\rho_o} \qquad (2.1)$$

where ρ_o and n_o are the equivalent values at a reference pressure and temperature for a certain light wavelength. For a beam aligned in the z-direction (Fig.2.3), the deflection angle e_x in the x-direction can be expressed as:

$$\varepsilon_x = \frac{1}{n_o}\int_0^{L_1}\frac{\vartheta n}{\vartheta x}\,dz \qquad (2.2)$$

where L_1 is the length of the beam path in the z-direction within the area undergoing the change of the refractive index.

In the present implementation of the method, two parallel laser beams were used to measure the average flame front speed within the distance defined by the beams. The experimental system employed a 5mW He-Ne laser, a beam splitter to generate two parallel beams and two photodiodes, equipped with amplifiers and power supplies, focused on the laser beams; the distance between the two parallel laser beams was 5mm. A fast transient-recorder (Datalab DL912, maximum conversion frequency 20MHz) interfaced to an Apple microcomputer system was used to record the analog signals of the two photodiodes and a typical output of this system is shown in Fig.2.4. The slope of the intensity variation signal from the single beam was steep enough to determine quite accurately the flame arrival time relative to ignition. The flame front speed could be estimated from the difference in time Δt between the arrival of the flame front at the first and second laser beams, which are spaced at a known distance apart, as indicated in Fig.2.4a. Figure 2.4b shows the output from the two channels when the instantaneous pressure is input to channel 1, to allow the correlation between flame propagation and pressure rise to be determined.

The sensitivity of the beam deflection technique is governed by equation (2.2) and the distance L_2 which represents the lever arm of the optical system. If the sensitivity is too high the signal may respond to

thermal boundary layers on the windows or density gradients within the unburnt gases. In addition for wrinkled flames, where the laser beam passes through multiple flame interfaces, it is not clear whether the angular deflection will increase or decrease.

Ten runs were made with the same stoichiometric propane-air mixture and the flame speed was measured at two different positions along the centreline. In both cases, the scatter of the data was less than ±2% and can be attributed to minor variations of the mixture equivalence ratio and round-off error in the analog-to-digital conversion. All the results presented in the next sub-section were based on 3 to 5 samples.

The above experimental system was used in chapter 4 for the measurement of the tip penetration of diesel sprays. The basic principle remains the same with the beam deflection caused by the liquid spray, in the form of droplets or ligaments, rather than the propagating flame front separating the burned and unburnt gases.

2.4.2 Results and discussion

Figure 2.5.a shows measurements of the flame front speed across the centreline of the chamber for equivalence ratios between 0.65 and 1.20, obtained with the two-beam deflection technique. All graphs exhibit similar trends but, as expected, different values. In accordance with Markstein (1964), two phases of flame propagation can be distinguished with the first confined to the near spark plug region up to x=27mm, where the flame speed remains roughly constant at levels between 1.5-3.5m/s depending on equivalence ratio, and the second phase characterised by flame deceleration up to x=42mm. The small increase close to the end wall, evident in Fig.2.5.a, is due to the particular chamber geometry and the positioning of the exhaust port along the centreline (see Fig.2.2). In order to estimate a representative flame speed for each mixture strength, values within the first relatively constant phase have been averaged and the results are plotted against equivalence ratio in Fig.2.5.b. In agreement with reported data in the literature (e.g. Markstein, 1964), flame speed reaches a maximum at equivalence ratios between 1.0 and 1.1.

The recording of the instantaneous pressure (see channel 1 in Fig.2.4)

was used to identify maximum pressures and elapsed periods between ignition and peak pressure for each mixture strength and the two quantities are plotted in Fig.2.6 as a function of equivalence ratio for an initial pressure of 6bars and temperature of 400K. The peak chamber pressure during combustion reaches a maximum value of 41bars under stoichiometric conditions within the minimum time of 26ms and this is associated with the occurrence of the maximum flame speed.

2.5 HIGH SPEED SHADOWGRAPHY

2.5.1 Principle and implementation.

The shadowgraphy technique employs the same basic principle described in the previous subsection. If the density gradient normal to the light beam is non-uniform, adjacent rays will be deflected by different amounts and will converge or diverge on leaving the test section. Fig.2.7.a shows a typical setup incorporating a laser, although any conventional light source can be used. The initial beam of parallel light (typically 0.8-1.6mm in diameter) is focused by means of lens f_1 which has a small focal length (usually a microscopic objective lens) and a pinhole is placed at the focusing point so that it becomes an ideal 'point' source (Witze and Vilchis, 1980). Parallel light passing through the test section is deflected by an angle ε (ε_x,ε_y) and equation 2.2 is valid for both x- and y-directions. The change in light intensity ΔI for a differential area element dxdy at the image plane, positioned at a distance L_2 away from the test section, can then be shown (Holder and North, 1963) to be:

$$\frac{\Delta I}{I} = -L_2 \left[\frac{\vartheta \varepsilon_x}{\vartheta x} + \frac{\vartheta \varepsilon_y}{\vartheta y}\right] \qquad (2.3)$$

and combining equation (2.2) for x and y:

$$\frac{\Delta I}{I} = -\frac{L_2}{n_o} \int_0^{L_1} \left[\frac{\vartheta^2 n}{\vartheta x^2} + \frac{\vartheta^2 n}{\vartheta y^2}\right] dz \qquad (2.4)$$

where I is the intensity of the incident illumination. The ratio $\Delta I/I$ is a

measure of the contrast or sensitivity of the shadowgraph image. The refractive index depends on the density (equ 2.1) so that it can be concluded that shadowgraphy responds to the second derivative of the local density which varies in space and time for unsteady experiments as in the present case.

The arrangement adopted for the present application, called focused shadowgraphy, is shown in Fig.2.7.b. The only component change was the addition of a third lens f_3 between the test section and the image plane. This was dictated by the need to reduce the size of the image in order to record it on the effective film area of the high-speed camera. An Ar-Ion laser, operating in the green line (λ=514.5nm with maximum power of 0.8W) was used as the light source and the power was adjusted within the range 0.1-0.3W in order to provide optimum light intensity. A Photec IV high-speed camera (manufactured by Hadland Photonics) was used to record flame propagation; this type of camera employs a polygonal prism with variable number of facets (8, 16 or 32 corresponding to full, half and quarter frame mode) and has a nominal maximum filming speed of 10,000 frames/s. In the present configuration it was only available with the 16-facets prism, resulting in a maximum speed of 20,000 frames/s; after considering the total duration of the experiment, the available light and the length of the films used, the operating filming speed was set at 6,000 frames/s. The camera also incorporated a triggering facility, which enabled the spark discharge to be initiated at a time when the film was running at the steady preselected speed, thus avoiding the early accelerating part; the films used were black and white (Kodak Plus-X Negative No 7231). The lenses f_1, f_2, f_3 in Fig.2.7.b had focal distances of 20, 300 and 300mm respectively; in order to minimise image distortion the f_2, f_3 lenses had a large diameter of 120mm so that the expanded beam could pass through a central area of 55mm diameter (about 20% of the total lens area) which had minimum spherical aberration. Despite this, some distortion was observed at the edges of the image, which could be eliminated by means of aberration-free doublet lenses, albeit at a much higher cost.

The nature of the shadowgraphy technique did not allow the use of the front camera lens, normally used for the focusing process, and the system was carefully aligned so that the image size of the test section, measuring

approximately 30x55mm (Fig.2.2), was reduced to fit into a 10x4mm area representing the effective area of a half-frame 16mm film. Safety precautions, such as operating the laser at the minimum possible intensity and using goggles designed for the laser wavelength, are imperative in this experiment, imposing additional difficulties to the focusing procedure through the camera eye-piece. The experience gained in the course of this experiment, especially in matching the available light with the filming speed, was relevant when the same camera was used to record the diesel combustion without the aid of laser light, in the results of chapter 4.

2.5.2 Results and discussion

Figure 2.8 shows a series of frames from a high speed shadowgraphy film at various times from the start of ignition for a stoichiometric propane-air mixture. During the first phase of propagation, which lasts 13.5 ms, the flame speed remains roughly constant. The flame front is initially spherical but, as the flow of fresh charge starts being "channelled" by the side walls, it becomes semiellipsoid (t=5.5ms). From t=8.3ms onwards, the flame front is gradually flattened and at 16.2ms it becomes nearly planar. This evolution of the shape of the flame front coincides with the deceleration of the flame which, as observed in the flame speed results of Fig.2.6.a, is associated with the second phase of flame propagation. At about t=13.5ms some vortices are evident close to the side walls of the combustion chamber, which are probably caused by unburnt gases trapped in the crevices between the large circular sapphire windows and the oval shaped combustion chamber and are of no importance to the flame propagation process.

In order to compare results from the techniques discussed so far, the film of Fig.2.8 was analysed to provide the flame speed as a function of distance from the spark plug and the result is plotted in Fig.2.9 together with the corresponding curve obtained with the two-beam technique. The agreement is reasonable, considering the fact that the high-speed shadowgraphy results are based on a single event whereas the other curve is the mean of a number of events.

2.6 LASER-DOPPLER VELOCIMETRY

This technique was used extensively to investigate the in-cylinder air-flow in diesel engine geometries and the characterisation of the diesel spray under atmospheric conditions. Therefore, the following subsections provide a brief description of the principle and an evaluation of the measurement uncertainties.

2.6.1 Principle

The principle of laser Doppler velocimetry has been extensively described in a number of texts (e.g. Durst et al, 1981), therefore only a brief description is presented here, in order to provide the background for the subsequent description of the optical and electronic instrumentation used in the course of this study.

LDV measures fluid velocities by detecting the Doppler shift of the light scattered from particles following the flow. In the most commonly used method, termed dual-beam or fringe mode, the difference of the Doppler shift from two intersecting beams is used in order to determine the velocity of the scattering particle crossing the intersection volume. This frequency difference is independent of the photodetector's position so that the collection optics axis can be positioned at any angle (side-scatter, forward or back-scatter), utilising large light collection apertures. The technique does not require calibration because the frequency difference is directly proportional to the velocity component of the particle which lies on the plane of the beams and is normal to the bisector of the intersection angle; the proportionality factor is a function of laser wavelength and intersection angle. The velocity direction is resolved by imposing a known frequency difference between the two laser beams, which is added or subtracted from the Doppler frequency. The scattering particles are deliberately introduced in the flow as seeding particles and their size and density characteristics are selected so that they accurately follow the velocity fluctuations. The most common seeding medium for motored engine tests is silicone oil atomised by means of purpose-made blast-type atomisers or commercial microfog lubricators; typical diameter of silicone oil droplets is 1-3μm.

LDV is particularly suitable for engine flows since it does not disturb

the flow, has a high spatial resolution and fast response, is independent of fluid properties and can be applied to combusting flows. Disadvantages include the requirements for optical access and seeding of the flow and the intermittent nature of the output signal which may have a poor signal-to-noise ratio.

The components of a typical LDV system can be described briefly under three basic groups: the laser, the transmitting and receiving optics incorporating the optical frequency shifter and the photomultiplier (PM), and the electronic equipment used for processing the PM signal. During the course of this study various configurations were used depending on the engine requirements and detailed description of the various systems will be given at the relevant section of the thesis.

2.5.2 Measurement uncertainties

LDV measures the instantaneous velocity of the seeding particles and assigns this velocity to the fluid by assuming that they accurately follow the flow fluctuations. Particles in the size range 0.5-5μm (e.g. silicone oil droplets generated by blast-type atomisers) follow flow fluctuations of about 10KHz (Melling and Whitelaw, 1975) and since most of the turbulence energy in engine flows is contained in frequencies below 5KHz (Dent and Salama, 1975), it can be concluded that this seeding method does not introduce errors in the turbulence measurements.

The finite dimensions of the measuring volume may give rise to a broadened and sometimes skewed velocity probability distribution when measuring along a steep velocity gradient. The resulting velocity gradient broadening in the mean and rms velocity measurements is a function of the velocity distribution and the probe volume length (Melling and Whitelaw, 1975). According to Arcoumanis (1983) the estimated uncertainties on the mean and rms values are on average 2% and 5% respectively, and in cases of large non-linear velocity gradients can reach maximum values of 5 and 15%. This error was minimised by selecting the smallest possible dimension of the control volume and, whenever possible, collecting the scattered light at an angle, thus reducing the "effective" probe volume length.

Two common sources of anxieties in LDV measurements are 'fringe

bias' and 'velocity bias'. The former stems from the fact that the frequency-counter requires a finite number of Doppler cycles (usually 8 as in this study) which may not be present for all velocity samples and this error source can be almost eliminated by increasing the frequency shift and the number of fringes in the probe volume. 'Velocity bias' may be present when averaging over a finite number of samples to deduce mean and rms values, since a larger number of high rather than low velocity particles cross the probe volume during the measurement time. Although theoretically shown to introduce significant uncertainties in regions of high turbulence levels (McLaughlin and Tiederman, 1973), results from experimental investigations do not agree on its magnitude and even its existence for turbulence levels below 15%. Several correction methods have been proposed, such as residence-time weighting (George, 1975), time-averaging (Dimotakis, 1976) and the 'slow sampling' procedure (Durao et al, 1980). Vafidis (1985) made a comparison between the two latter methods and concluded that the maximum uncertainties occurring in regions of high turbulence are about 2% and 5% in the mean and rms respectively.

Sources of uncertainty associated with the data processing methods in engine flows (chapter 1) are 'crankangle broadening' and the statistical uncertainty associated with the finite sample size. The former is equivalent to the velocity gradient broadening but in the time domain. Following the recommendations of Arcoumanis (1983) the length of the crankangle window during the course of this study did not exceed 3°CA which renders the contribution of this error negligible. The uncertainties associated with the finite sample size have been theoretically investigated by Yanta (1973), who showed that the error in the mean value is a function of the sample size and local flow conditions, whereas the error in the rms is only dependent on the sample size. A typical sample size in this study was 1000 data points and this resulted to uncertainties in the mean value of 4% and 1%, for turbulence intensities of 50% and 10% respectively, and in the rms of 5% for a 95% confidence level.

The uncertainty in the positioning of the probe volume is related to the precision of the traversing mechanism and the length of the probe volume and, for this study, was estimated to be ±0.3mm. In unsteady flow measurements, another error source is the timing circuit which assigns a crankangle value to each datum; the high resolution of the shaft encoders

used in this study resulted in a small uncertainty of $\pm 0.36^{0}$CA.

Following this discussion, the overall average uncertainty in the measured mean velocities was estimated to be 5%, reaching a maximum value of 10% in high turbulence areas with steep non-linear gradients. The equivalent uncertainty in the rms was 10% in average with a maximum value of 20%.

2.5.2 Implementation

A dual-beam LDV system was employed in the forward-scatter mode (Fig.2.10) with an Ar-Ion laser (Spectra Physics model 164) operating in the green line (514.5nm) with a power output of 0.4-0.8W. The beam was focused by a planoconvex lens (f_1) of 100mm focal length and 20mm diameter onto a rotating diffraction grating (G) (Technisch Physische Dienst, type H) where it was diffracted into zero-order and pairs of higher order beams. The rotation of the diffraction grating provided a frequency shift between the diffracted beams proportional to the rotational speed of the grating and the diffraction order of the beam (Oldengram et al, 1976). In the present application the two first order beams containing about 60% of the overall laser power were used, leading to a maximum shift of 7MHz. These beams were subsequently collimated by another planoconvex lens (f_2) of 300mm focal length and 95mm diameter and focused by an identical imaging lens (f_3) to form the intersection (measurement) volume. An integrated optical unit (Dantec 55X34) was used to collect light and incorporated two achromatic lenses of 300mm (f_4) and 100mm (f_5) focal lengths, an adjustable pinhole of 0.1mm and a photomultiplier tube (RCA model 4526); the f_4 lens was used to collimate the scattered light from the probe volume, which was subsequently focused on the pinhole by lens f_5. The signal generated by the PM was fed to a 1ns resolution frequency-counter (TSI model 1990C), which was operating in the single measurement per burst mode (minimum number of zero crossings 8) in order to evaluate frequency values of the Doppler bursts. The same frequency-counter was used extensively in the course of this study due to its wide input frequency range (1KHz-150MHz), selectable input filters and both frequency- and amplitude-validation circuits. The digital information generated by the frequency-counter was transferred to an IBM PC-AT compatible microcomputer via a Zech-Electronics interface card for storage

and processing.

The flow was seeded with zirconium dioxide particles (ZiO_2) which were deposited onto the intake passage of the combustion chamber near the valve prior to each test and had a nominal diameter before agglomeration of around 1μm. The two most common seeding particles in combustion studies, aluminium oxide (Al_2O_3) and titanium dioxide (TiO_2) (Witze and Baritaud, 1985) were also considered here; Al_2O_3 particles provide low data rates and tend to agglomerate easily while TiO_2 has better light scattering efficiency which, unfortunately, is greatly reduced after combustion due to its low melting temperature. ZiO_2 (or ZrF_4 reacting at low temperatures to produce ZiO_2) performs overall better but can cause wear problems due to its abrasive nature which makes its use difficult for engine applications.

2.5.3 Results and discussion

Figures 2.11.a-c show instantaneous axial velocity profiles obtained with laser velocimetry at different positions in the chamber, as indicated in the upper right hand corner of each figure. All graphs exhibit similar trends with the axial velocity rising suddenly from zero to a maximum value which is a function of the equivalence ratio; comparison with the corresponding flame speed deduced from the two beam technique (Fig.2.5.a) shows good agreement. The negative values,which were present in some cases very early in the velocity trace, are possibly due to the insufficient time allowed for the mixture to become quiescent. The sudden rise of the velocity trace is a direct consequence of the flame front approaching the measurement location. The signal immediately afterwards disappears indicating the passage of the flame from the control volume and the velocity values decrease and become negative. The momentary absence or sudden data rate reduction of the LDV signal is attributed to large refractive index gradients in the reaction zone which deflect the beams; the unsteady refractive index gradients are caused by the presence of different species (intermediate or end-products of combustion) and abrupt changes of pressure and temperature. Another potential problem is the possibility of pseudo-velocities, attributed to the

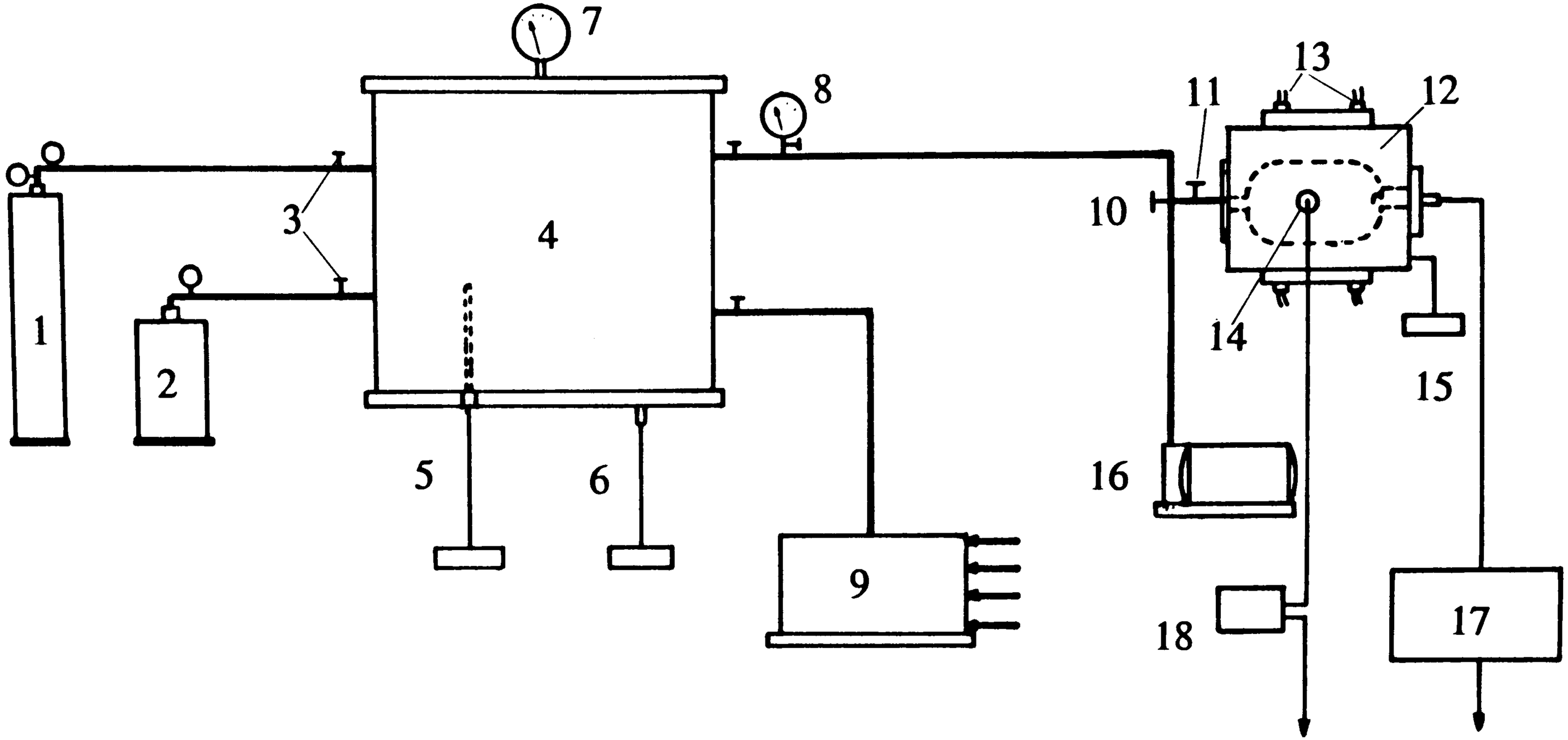
change of the beam intersection angle, but that seems unlikely according to Hashimoto et al (1983), who argue that pseudo-velocities can appear only in highly turbulent flames.

At the centre of the combustion chamber (Fig.2.11.a), the results for a stoichiometric and a lean propane-air mixture of 0.65 equivalence ratio show that in each case the maximum positive and negative velocities have approximately the same absolute value, due probably to the fact that the reaction zone is expanding equally towards the two end walls which are equally spaced relative to the position of the control volume. However at a point nearer to the spark plug (Fig.2.11.b), the negative part of the velocity trace observed at the centre of the chamber is not present as a result of the positioning of the ignition point very close to the wall. In Fig.2.11.c the control volume was positioned near the side wall where it was found that the data rate was much improved and the signal was sustained longer. Comparison between Figs.2.11.a and 2.11.b shows that the velocity near the wall reaches its maximum value about 1ms later than at the central point (same plane) due to the curvature of the flame front observed in the shadowgraph pictures. The shape of the velocity trace is very similar to that observed by Dunn-Runkin and Sawyer (1986) for a constant volume combustion chamber of slightly different geometry and at atmospheric initial pressure and temperature.

2.6 CONCLUDING REMARKS

The application of the above laser techniques to the spark-ignited flame propagation in a constant-volume combustion chamber under well controlled initial conditions allowed evaluation of the suitability and accuracy of the techniques to characterise the flow and combustion in direct-injection diesel engines, which represent the focus of this investigation. Laser velocimetry was used to quantify the induction and compression stroke in idealised and production engine geometries under motored conditions, as well as the droplet spray velocities, the two-beam deflection technique characterised spray tip propagation and velocity, while high speed photography allowed the temporal and spatial development of the compression-ignition combustion to be monitored with high resolution.

Overall, the measurement uncertainties of the above laser-based techniques are such that allow the application to motored and firing engines in the knowledge that they do not influence the validity of the conclusions drawn.



1 Compressed air
2 Propane
3 Two-way valve
4 Mixing chamber
5 Resistance thermometer
6 Diaphragm pressure transducer
7 Pressure gauge
8 Pressure regulator
9 FID Analyser
10 Three-way valve
11 Two-way high pressure valve
12 Combustion chamber
13 Heater
14 Kistler pressure transducer
15 K-type thermocouple
16 Vacuum pump
17 Ignition system
18 Charge amplifier

Figure 2.1 Schematic of experimental rig.

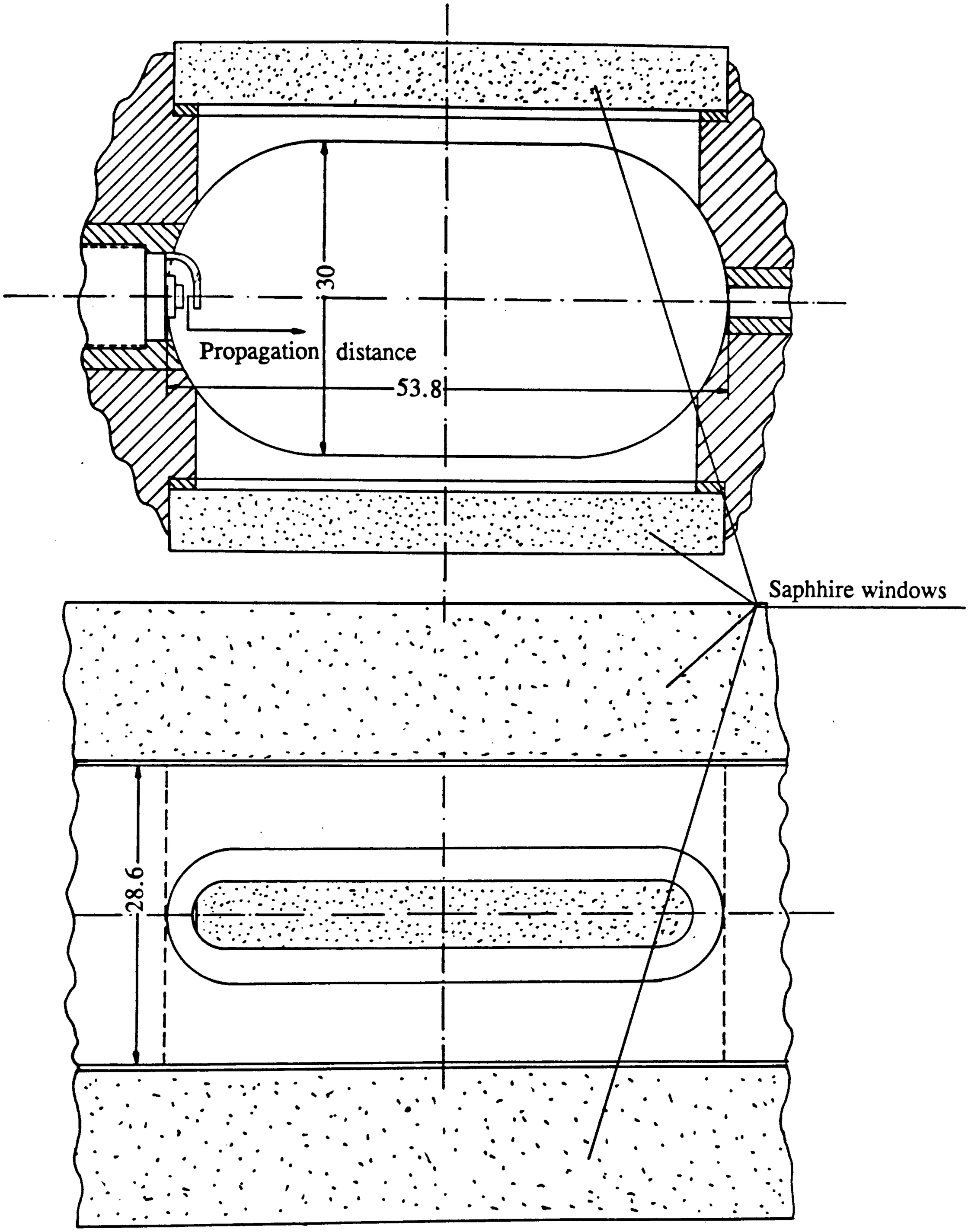


Figure 2.2 Constant volume chamber.

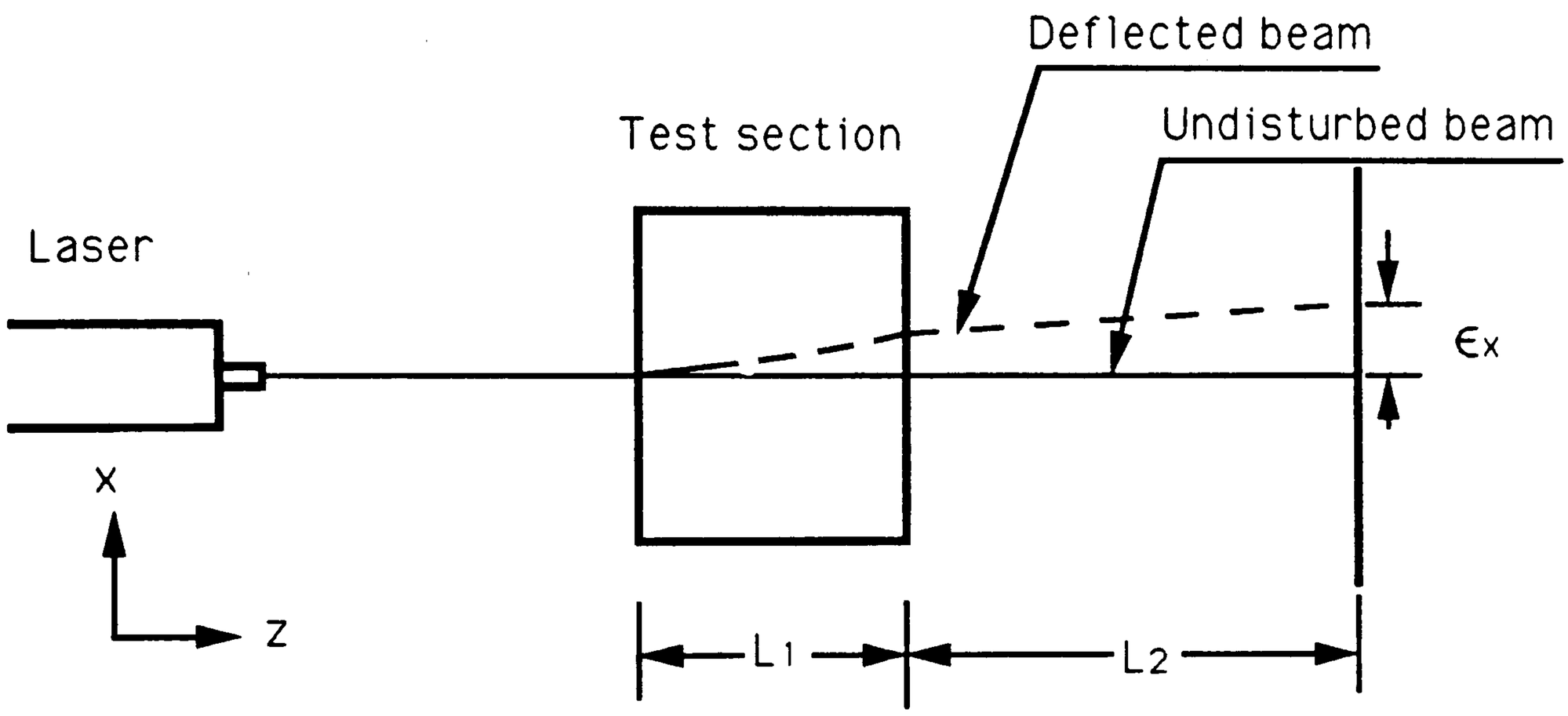
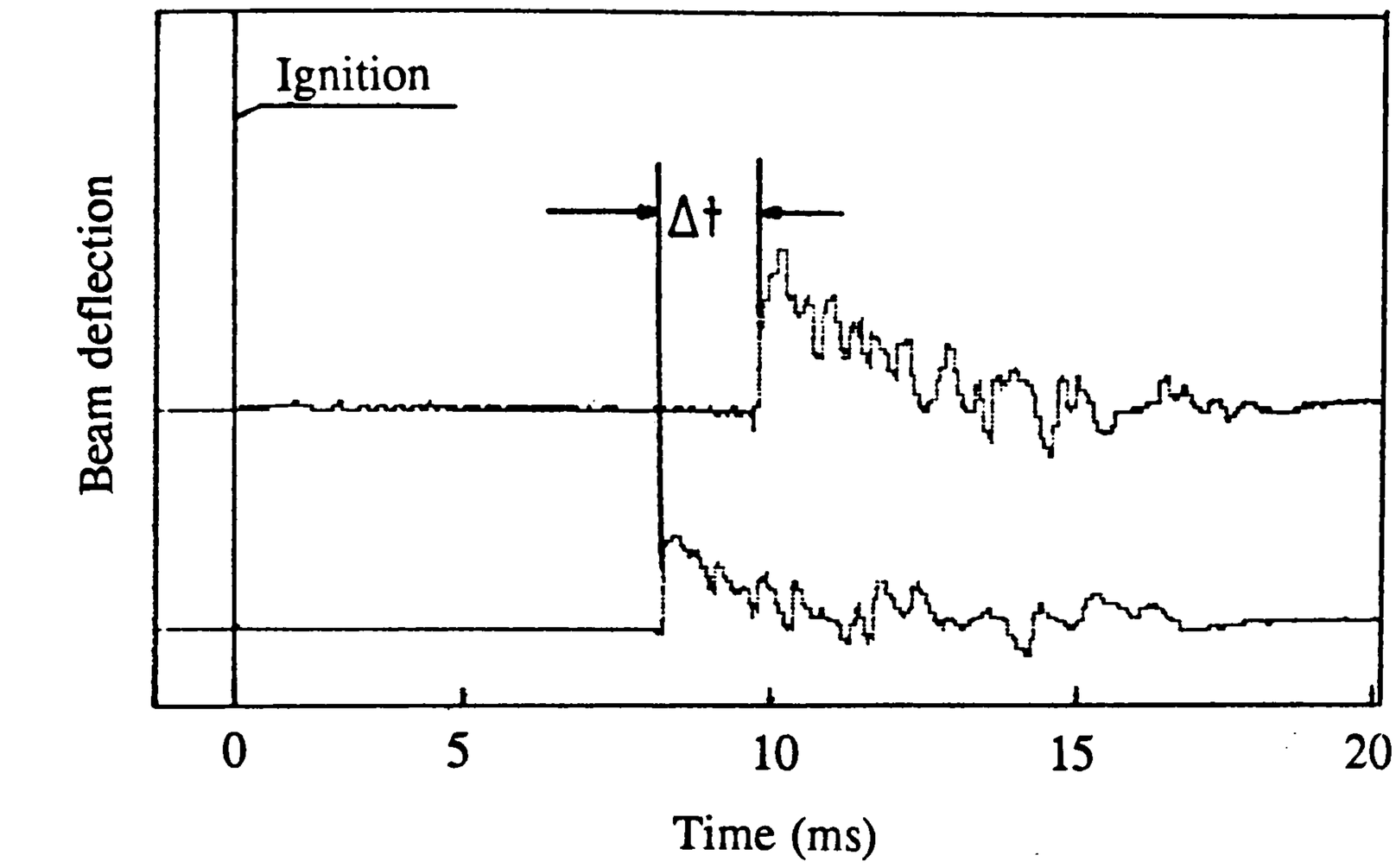
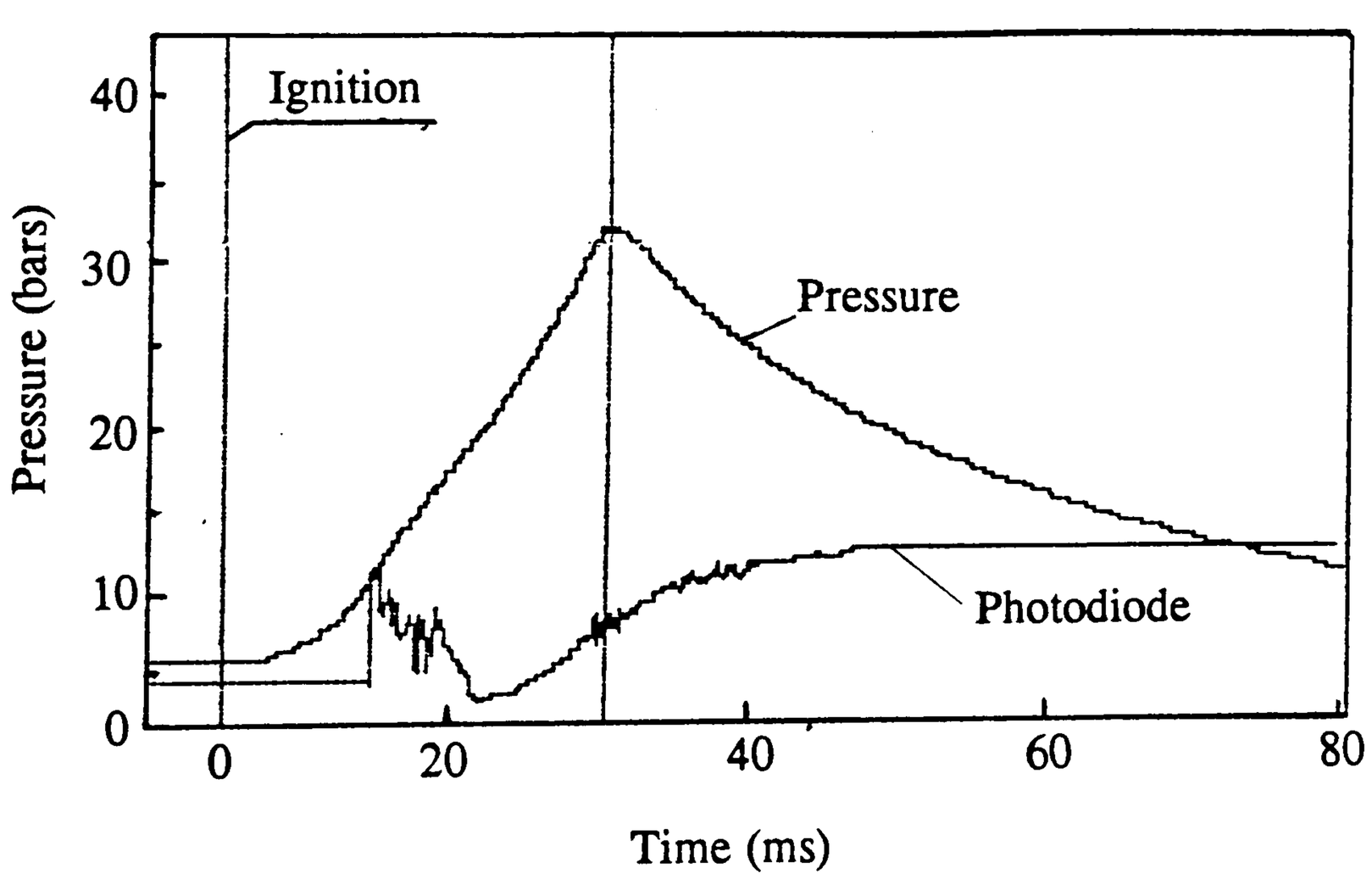


Figure 2.3 Laser beam deflection principle.



(a)



(b)

Figure 2.4 Typical signals from (a) two photodiodes (b) pressure transducer and photodiode.

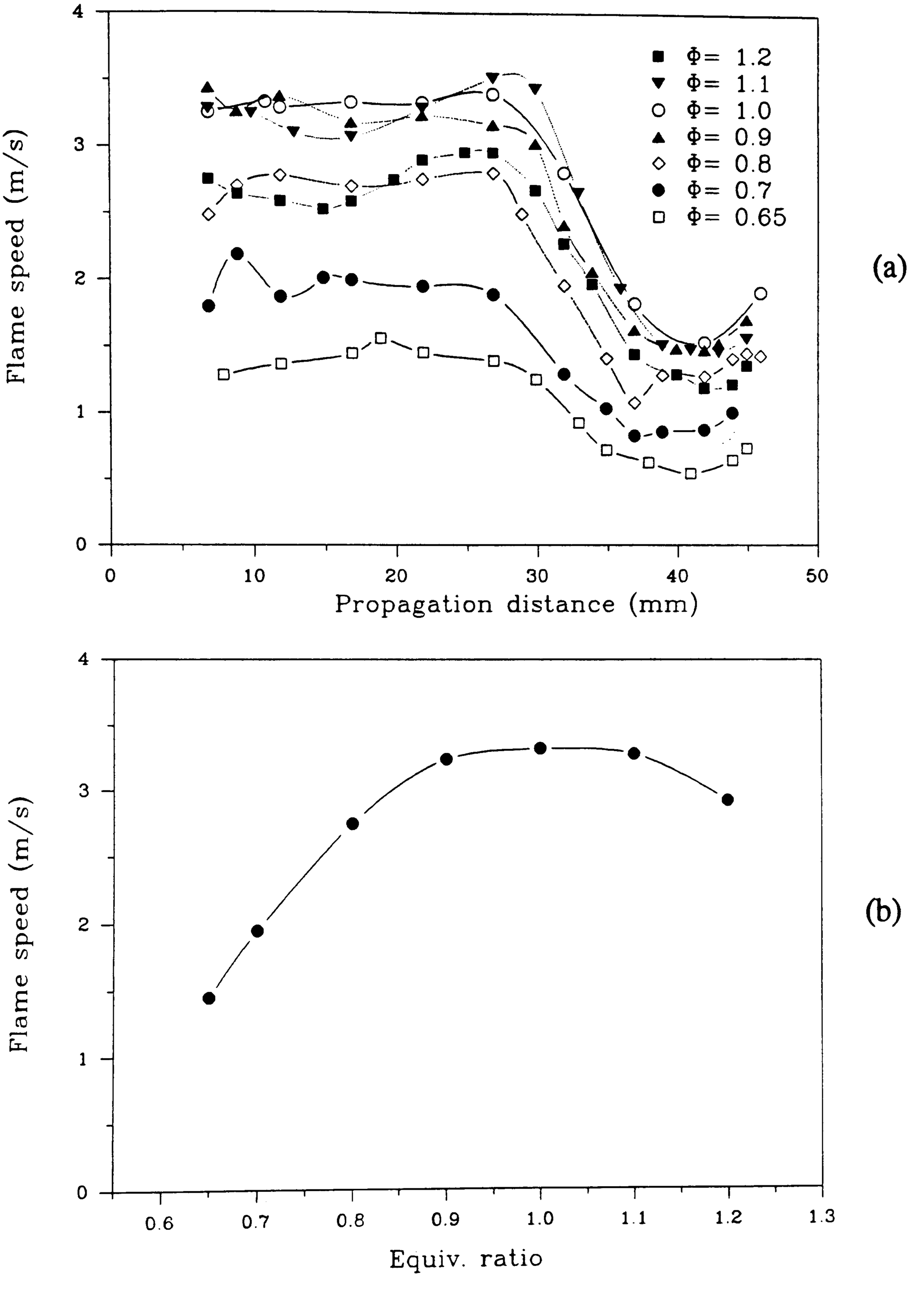


Figure 2.5 Variation of flame speed with propagating distance (a) and flame speed with equivalence ratio (b).

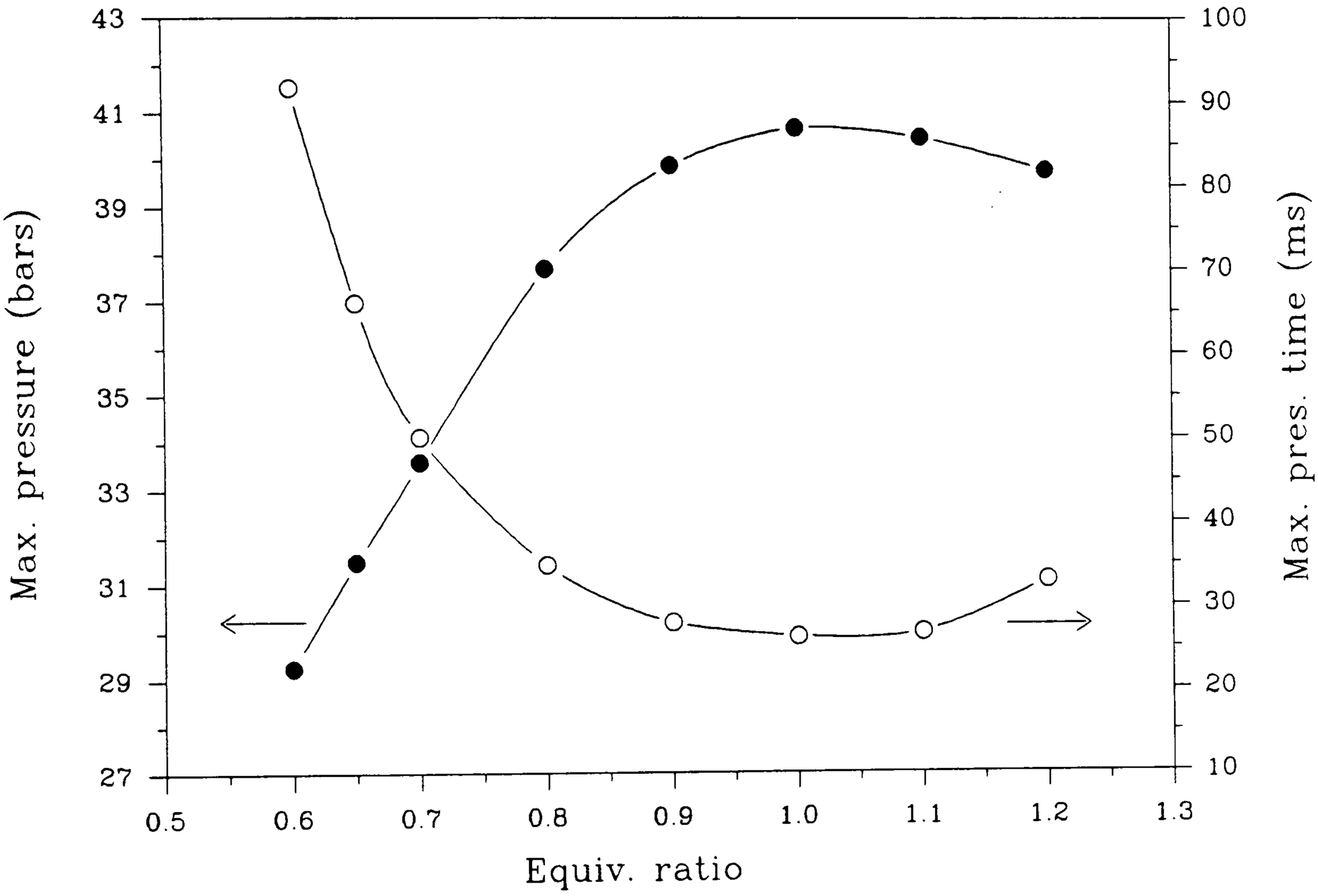


Figure 2.6 Variation of maximum chamber pressure and time at which maximum pressure occurs with equivalence ratio.

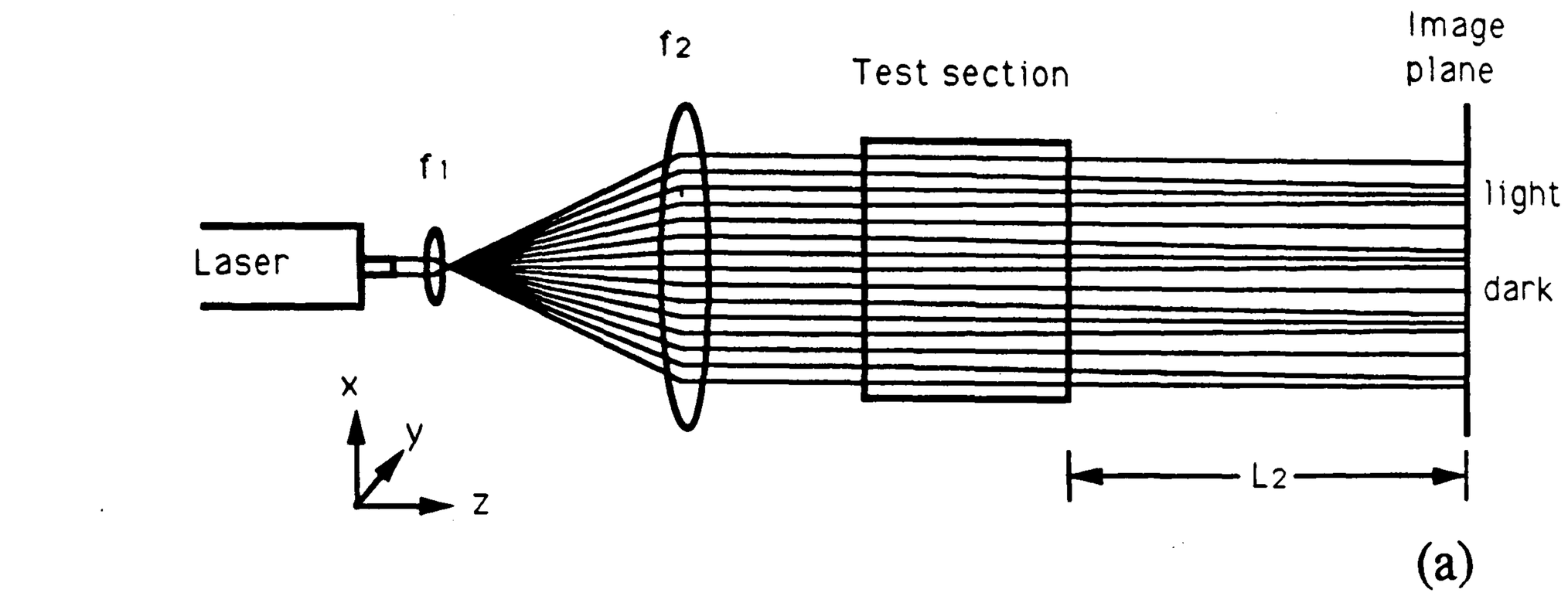


Figure 2.7 (a)Principle of laser shadowgraphy and (b) Schematic of focused laser shadowgraphy system.



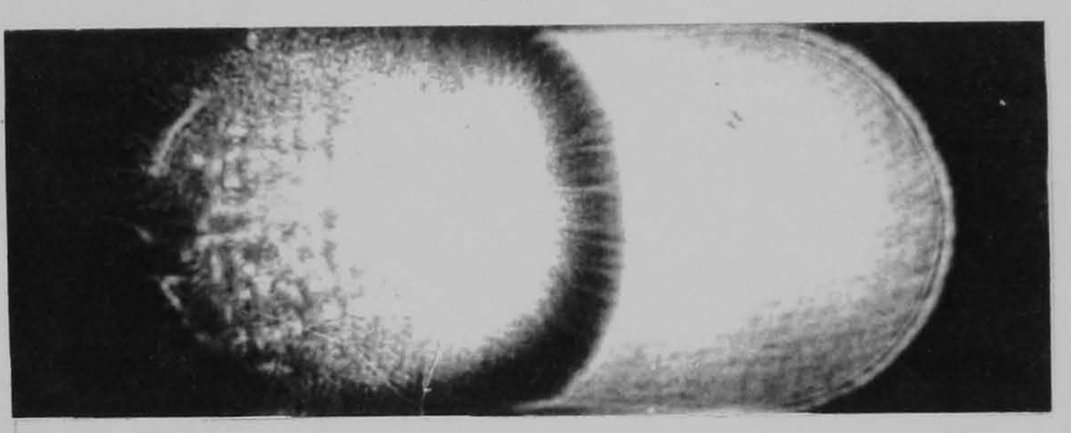
0ms



8.3ms



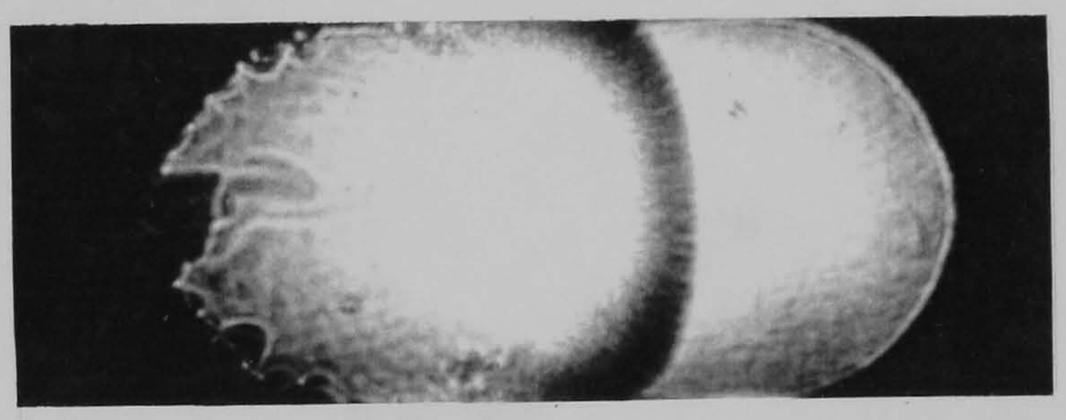
1.3ms



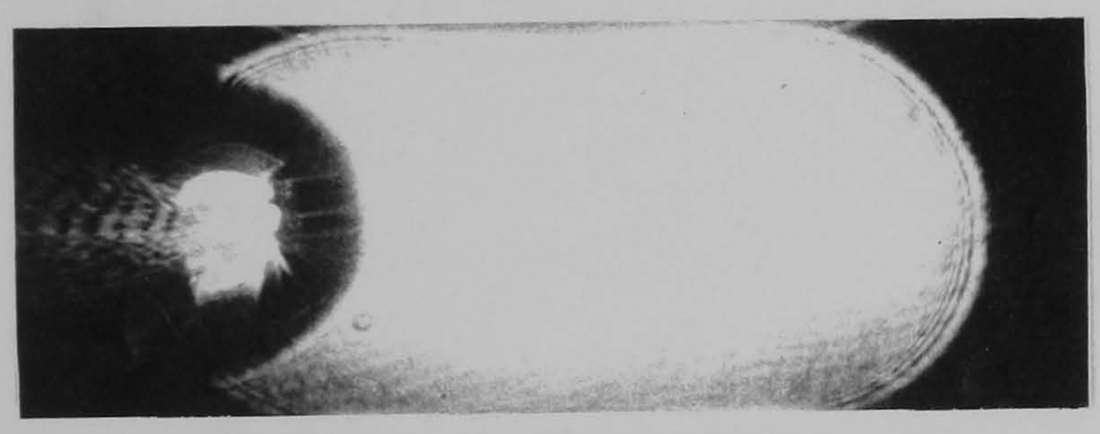
10.8ms



2.8ms



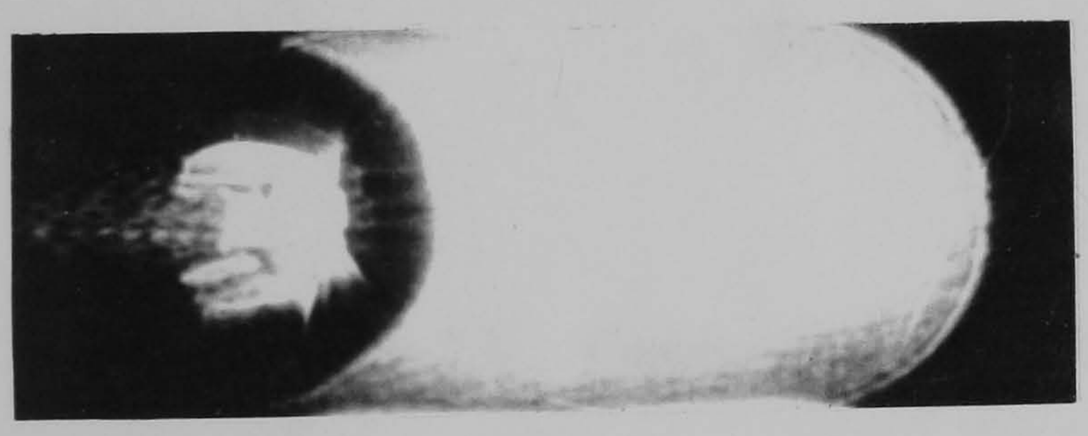
13.5ms



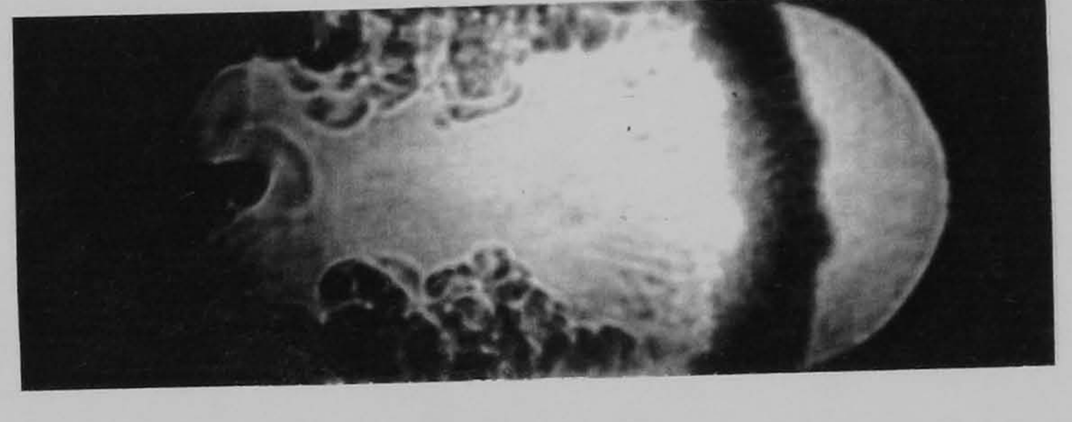
4.0ms



16.2ms



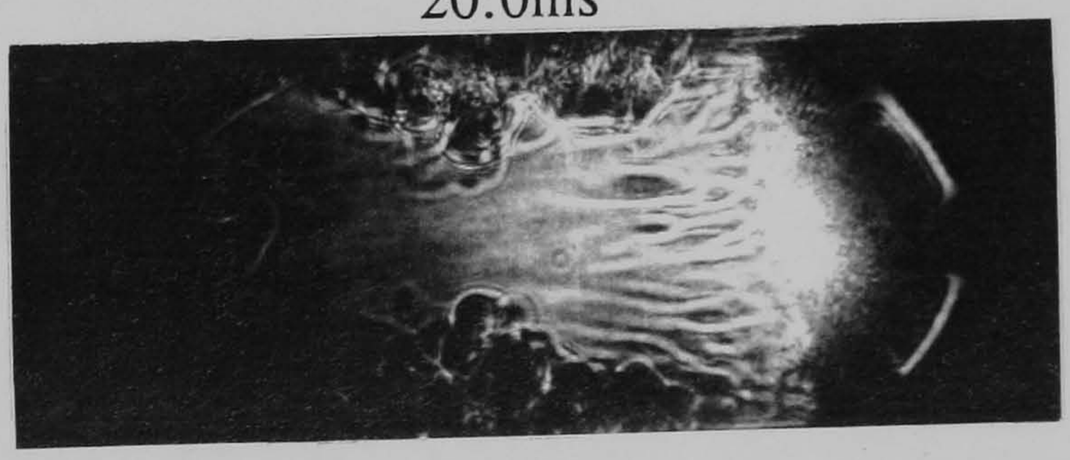
5.5ms



20.0ms



6.7ms



24.3ms

Figure 2.8 Photographs of propagating flame obtained by high-speed laser shadowgraphy.

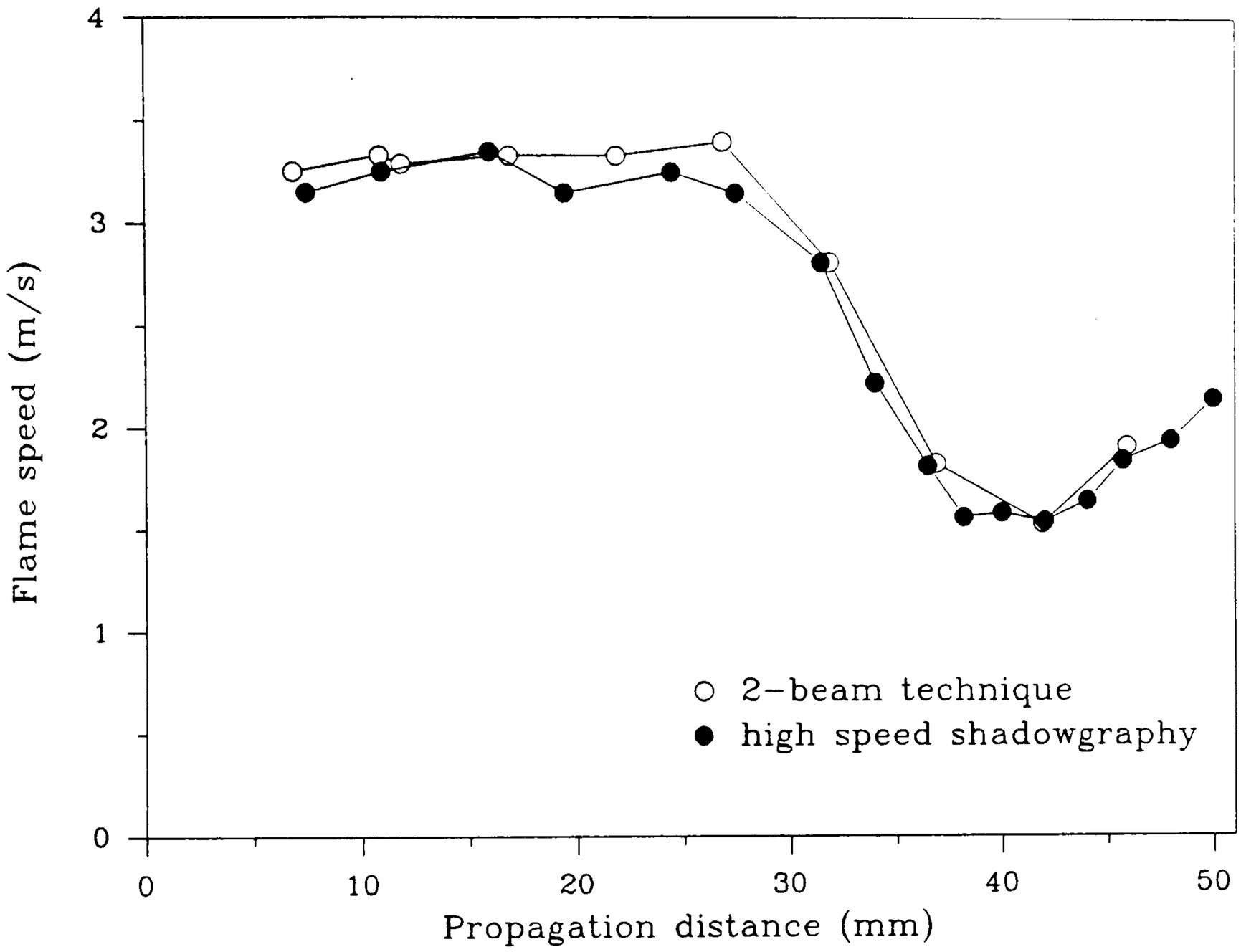


Figure 2.9 Comparison of data obtained with two laser techniques.

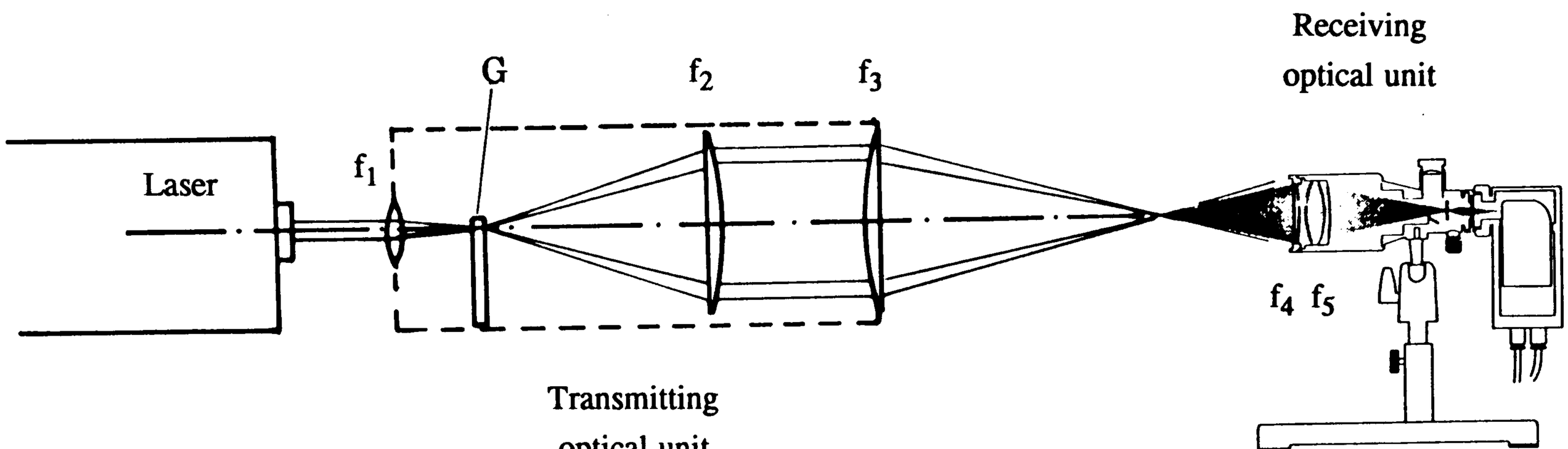
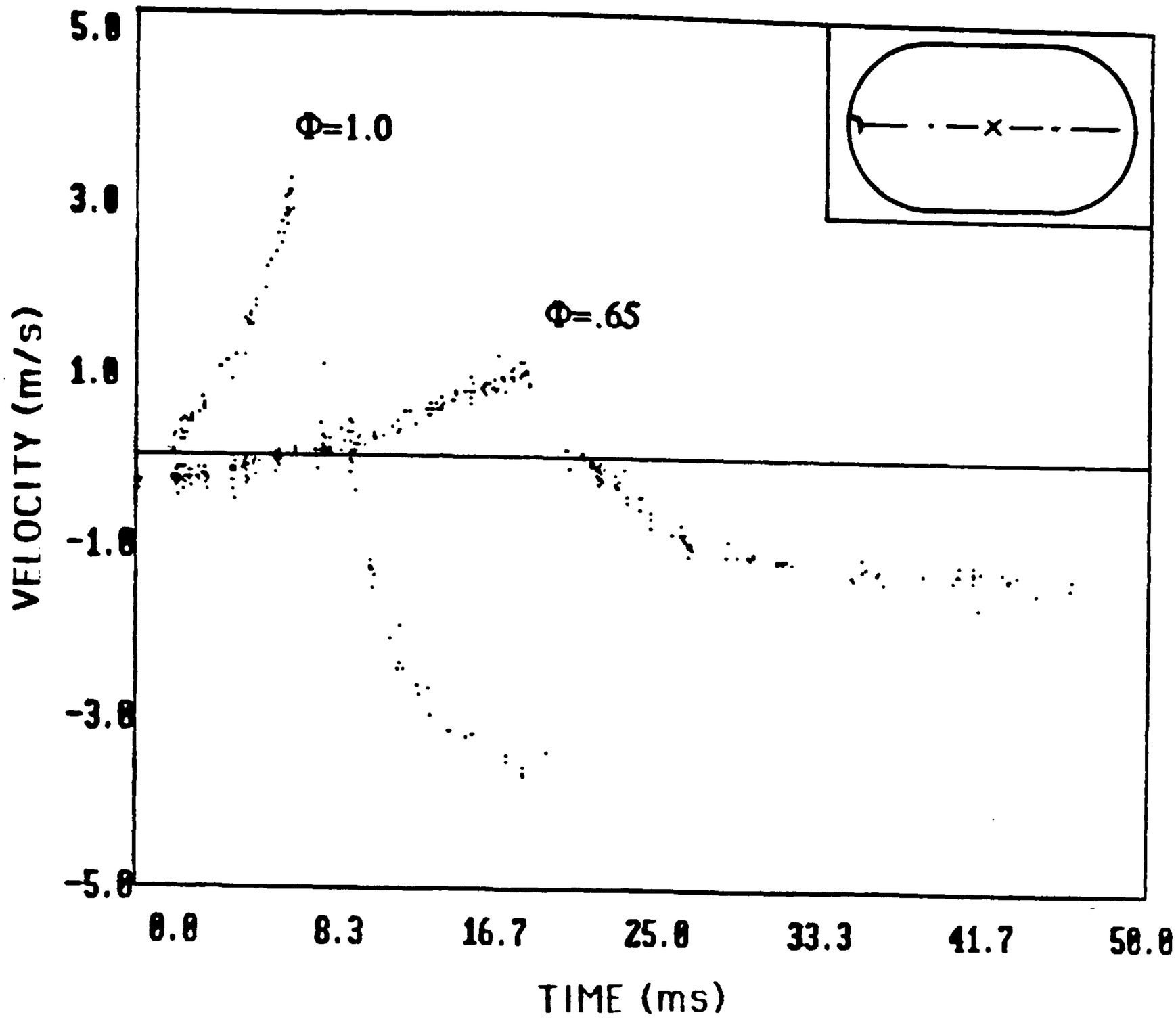
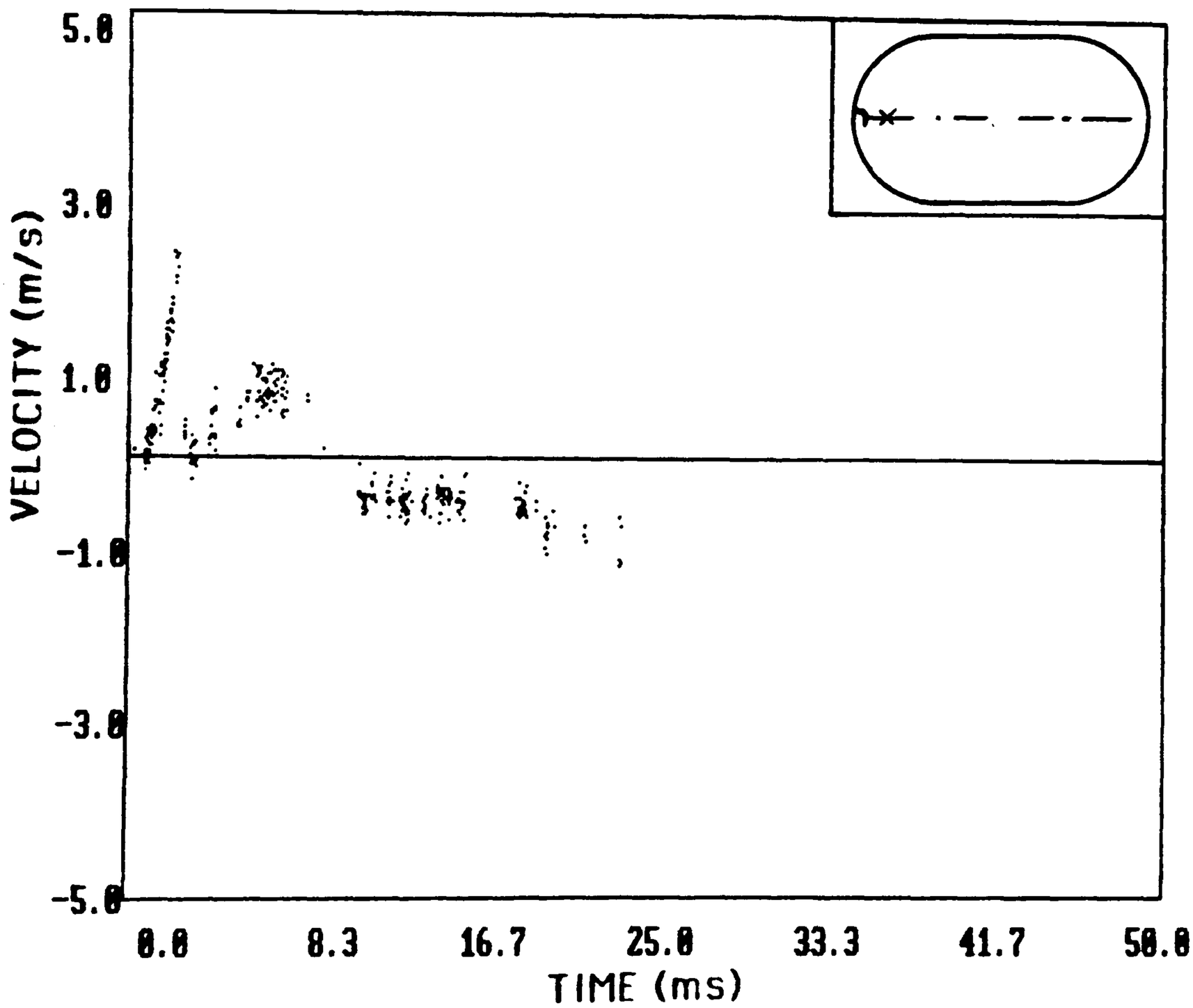


Figure 2.10 General arrangement of an LDV system

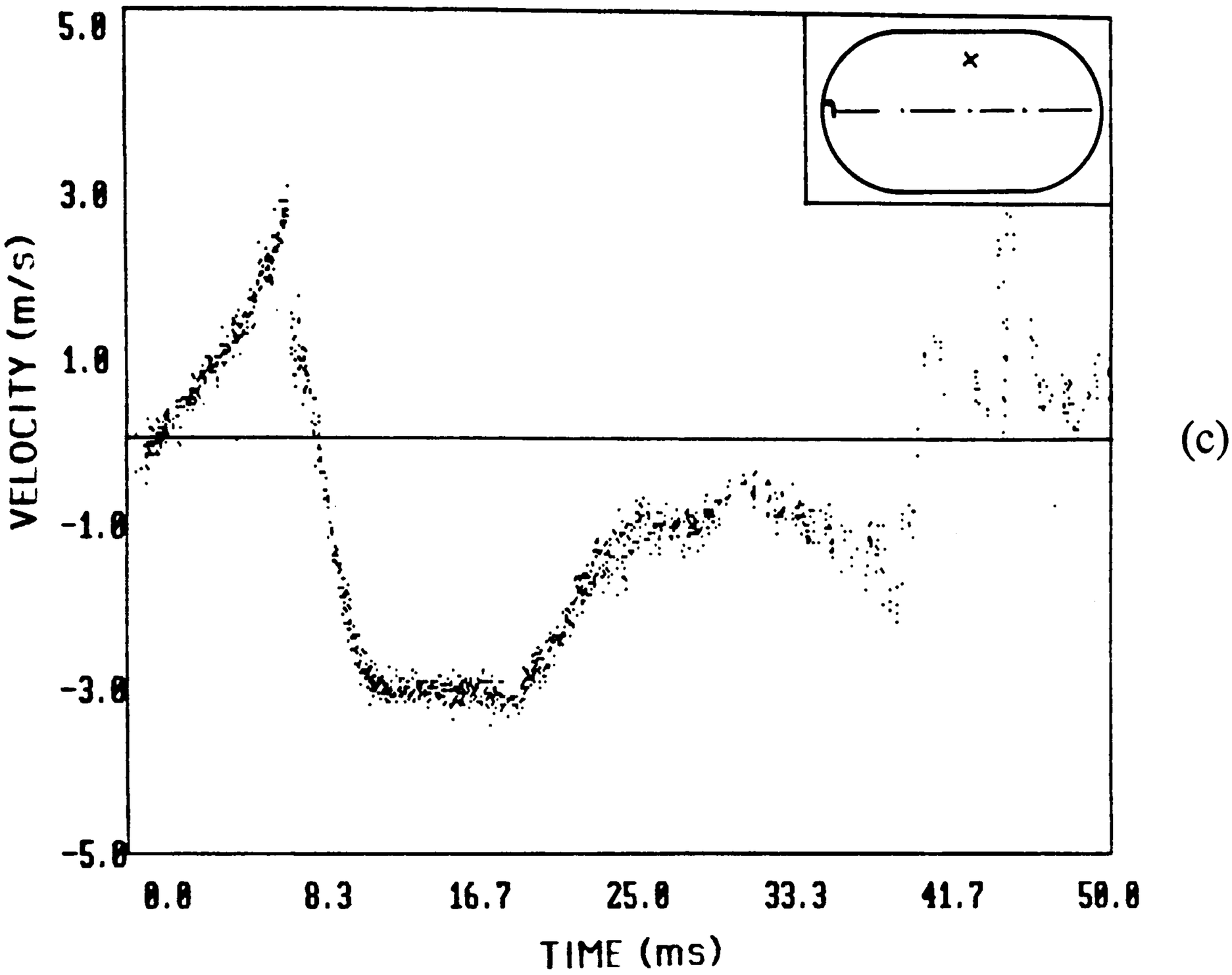


(a)



(b)

Figure 2.11 Velocity traces as a function of time from the start of ignition for three locations in the combustion chamber (a) center of chamber (b) near the spark plug (c) near the wall.



(c)

Figure 2.11 Continued

CHAPTER 3

SWIRLING FLOWS IN IDEALISED DIESEL ENGINES

3.1 INTRODUCTION

This chapter investigates the development of swirling flows generated by vanes and a helical port inside cylinders typical for HSDI diesel engines. The investigation was performed in a steady-flow rig and in motored engines operating at compression ratios and speeds which are relatively low compared with production engines. The use of these engines is justified by the requirements of full optical access into the cylinder volume, low cost and flexibility in altering major components such as cylinder liner, cylinder head and piston crown for parametric studies. Laser Doppler velocimetry was used in all cases to measure the mean and rms values of the tangential and axial velocity components which were time-averaged in the case of the steady-flow rig and ensemble-averaged in the case of the periodic engine flows.

Section 3.2 describes an investigation of an idealised swirling flow generated by an axisymmetric inlet port geometry with vanes under steady and unsteady conditions. The objective is to analyse the initiation and development of the swirling flow pattern inside the cylinder and to assess the ability of the steady-flow rig to simulate the flow in the model engine of identical cylinder head geometry. Particular emphasis is put upon the movement performed by the swirl centre in space and time, usually termed swirl centre precession. Inherent in any rotating flow, this phenomenon has been observed in both steady (e.g. Chanaud, 1964; Syred and Beer, 1972) and reciprocating engine flows (e.g. Vafidis, 1984). In this study it is investigated in more detail due to its possible contribution to cyclic flow variations. The experiments of section 3.3 were performed in a modified diesel engine in an order of increasing complexity towards production diesel engine geometries. The objective is to examine the effect of various inlet manifold configurations and of induction air throttling on the swirl velocity flowfield at TDC of compression. The latter was used as a method to reduce peak in-cylinder pressure, thus allowing the use of piston bowls and cylinder liners made of

transparent cast acrylic material (perspex), at compression ratios similar to production engines. It should be noted that at normal diesel pressures and temperatures perspex can not only deform but also become opaque, thus prohibiting measurements of the flow inside the piston-bowl or engine cylinder.

3.2 SWIRLING FLOWS IN AXISYMMETRIC PORT GEOMETRIES

3.2.1 Flow configuration

This investigation was carried out in three stages, consisting of steady flow through an axisymmetric cylinder head with and without a porous plate, simulating a stationary 'piston', and unsteady flow in a simplified model engine equipped with the same cylinder head.

The axisymmetric single-valve/port cylinder head, shown in Fig.3.1, consisted of a duraluminium contraction with an area ratio of 7.5 leading to a short cylindrical section which ended at a 60° valve seat (with respect to the cylinder head). A valve with a matching valve head and rounded edges was inserted into a valve stem, which was supported by means of two thin spiders along the axis of the head. Swirl was introduced by means of vanes which had an angle of 60° with respect to the cylinder axis and were located close to the narrow end of the contraction upstream of the valve. This method of generating swirl offers advantages because of the flexibility it provides in controlling the strength of swirl through variation of the vane angle, thus resulting in swirl levels comparable to those generated by helical or directed ports in production engines. The single-valve geometry creates an initial axisymmetric or near-axisymmetric flow pattern which does not resemble the induction flow pattern generated by the off-centre inlet valve of a typical production cylinder head but allows better understanding of the origin and sustaining mechanism of swirl centre precession.

A. Steady flow/open-ended cylinder

The axisymmetric cylinder head was mounted on a suction-type steady flow rig (Fig.3.2), which was capable of generating air mass flowrates up to

50 kg/h. The steady flow rig was driven by a multi-stage centrifugal exhauster and incorporated a transparent cylinder, a plenum chamber, tubes and an orifice meter for measuring the mass flow rate. The cylinder was made of cast acrylic plastic (perspex) and had a bore of 74mm, length of 300mm and wall thickness of 3mm. The valve lift was adjusted within 0.01mm by means of a micrometer mechanism connected to the narrow end of the stationary valve. The cylinder head could be mounted on the cylinder in four different orientations through rotation around its axis, to allow investigation of the sensitivity of the swirling flow pattern to possible asymmetries of the swirl vanes. As it will be discussed later in this section, this proved to be quite critical.

B. Steady flow/stationary porous piston

The open-ended cylinder of the previous steady flow arrangement was confined by a porous plate made of sintered brass, which was kept in place by means of a duraluminium ring incorporating a rubber O-ring to minimise air leakages through the annular crevice between the porous plate and the cylinder wall (Fig.3.1.b). This flow configuration allowed steady flow of air through the cylinder head/dummy piston arrangement, albeit at reduced flow rates due to the much increased pressure drop through the system, and at the same time simulated the engine geometry in terms of the downstream solid boundary.

C. Model engine

The cylinder head used in the steady flow rig was then mounted on a model engine, which consisted of a horizontally orientated crank mechanism driven via a gear mechanism by an electric motor at a constant speed of 200rpm (±1%). The single valve was operated by a double lobe camshaft, acting as both inlet and exhaust in a conventional four-stroke mode and having a maximum lift of 9mm. The transparent acrylic plastic cylinder had a bore of 75.4mm, slightly larger from the steady flow rig and increased wall thickness of 13mm to be able to sustain the higher air-pressure during the compression stroke. The flat-top piston, fabricated from duraluminium, incorporated three graphite-reinforced and one PTFE compression ring to ensure good sealing and to minimise friction, and had a stroke of 94mm,

which, combined with a TDC clearance of 38mm, resulted in a compression ratio of 3.5. The engine was also equipped with an optical shaft encoder mounted on the half-speed camshaft in order to provide the necessary crankangle information to the microcomputer. All the characteristics of the model engine are summarised in Table 3.1

Cylinder bore, mm		75.4
Stroke, mm		94.0
Piston diameter, mm		74.8
Connecting rod length, mm		363.6
Engine speed, rpm		200
Clearance height at TDC, mm		38
Compression ratio		3.5
Intake/exhaust valve:	diameter, mm	34
	seat angle, ^{o}	60
	max. lift, mm	9.0
Intake valve:	opens, IVO,^{o}BTDC	10
	closes, IVC,^{o}ATDC	210
Exhaust valve:	opens, EVO, ^{o}BBDC	30
	closes, EVC, ^{o}ATDC	10

Table 3.1 Characteristics of the model engine

3.2.2 Measurement systems

Measurements of mass flowrate - The mass flow rate of the steady flow arrangement (Fig.3.2) was regulated by a gate valve and measured by means of an orifice meter according to the procedure described in B.S.1042 (1981). The pressure upstream of the orifice plate was monitored with a single limb mercury manometer and the pressure drop across the orifice was measured by a Betz micromanometer with an accuracy of 0.1mmWg. The settling chamber of 0.6m^3 was large enough to eliminate any fluctuations of the flow rate, which were monitored by measuring the stagnation pressure inside the chamber by another Betz micromanometer. The accuracy of the mass flow rate measurements was estimated to be around 2%.

Velocity measurements - The velocity measurements were obtained with a dual-beam laser Doppler velocimeter operating in the forward scatter mode. The optics consisted of a He-Ne 5mW laser, a transmitting optical unit identical to the one described in sub-section 2.5.2, a planoconvex lens of 100mm as collection optics and a photomultiplier tube (EMI type 9817B). The PM output signal was high-pass filtered at 1-2 MHz by an active filter (Krohn-Hite, model 3200) and fed to a purpose-built 4ns resolution frequency counter (maximum input frequency 20MHz) which was interfaced to an Apple IIe microcomputer operating in two ways. In the first mode the internal microcomputer clock was used in order to measure the elapsed time between measurements so that it provided a velocity-vs-time (or crankangle) trace over consecutive cycles. In the other mode velocity data were averaged to provide mean and rms values of the measured velocity component, being either time-averaged as in the case of the steady flow or ensemble-averaged as in the case of the unsteady flow in the model engine. The latter was achieved by a gating circuit which processed the optical encoder signal and produced a TTL compatible electronic pulse which was high only during a preselected crankangle window; this pulse was fed to the counter which accepted velocity data for processing only when the pulse was high, i.e. within the crankangle window, which was set at 3° for this study.

In order to perform frequency analysis in the steady flow tests, a frequency tracker (Cambridge Consultants, model LDV Mk2) was used to provide a continuous analog signal output of the measured velocity component, which was then fed to a spectrum analyser (Spectral Dynamics Corp., model SD340) operating on the fast Fourier transform principle. A plotter interfaced to the spectrum analyser was used to draw the power spectral densities (PSDs) for further study. The average sampling rate of the velocity signal was estimated to be around 3KHz, which, according to Nyquist theorem, corresponded to a value of 1.5KHz for the upper limit of the PSDs' frequency range. According to Press et al (1986) in a Fourier transform, frequencies higher than the Nyquist limit cannot be resolved and, if they do exist, introduce errors to the spectrum due to aliasing effects; this was prevented by low-pass filtering the tracker output at 3KHz.

Seeding in all cases was provided by one or two blast-type atomisers which produced silicone oil droplets of 1-2μm mean diameter introduced at

the upstream end of the cylindrical port. The swirl velocities were corrected for refraction effects of the laser beams, intersecting the cylinder's curved optical boundaries at different angles, according to the procedure described by Vafidis (1985). The uncertainty in the ensemble-averaged axial and swirl velocity components was estimated to be less than 5% and 10% for the mean and rms values respectively (sub-section 2.5.2); the accuracy of the in-cycle instantaneous measurements was expected to be better since they were free of the error sources associated with the ensemble-averaging procedure.

3.2.3 Results

The velocity results are presented in terms of diametral profiles at certain axial locations from the cylinder head or centre-line profiles of the ensemble-averaged mean (open symbols) and rms(closed symbols) axial and swirl velocities. The instantaneous velocities are plotted against either time (in ms), as in the case of the steady flow tests, or crankangle (in ^{o}CA) as in the case of the model engine. In all cases, however, velocity magnitudes are normalised by the mean piston speed of the model engine (V_P=0.628m/s at N=200rpm), given by:

$$V_P = 2\,S\,N \qquad (3.1)$$

Following this argument and in order to directly compare the steady with the unsteady case, nearly all of the steady flow tests were obtained at a constant air mass flowrate of 11.8Kg/h corresponding to the 200rpm of the model engine, according to:

$$\dot{m} = V_P\,(\pi\,D^2/4)\,\rho \qquad (3.2)$$

Since, however, there is some evidence (e.g. El Tahry, 1982; Vafidis, 1985) that the swirling flow generally scales with engine speed, the present results are expected to be valid over the speed range of a production engine. The dependence of swirl velocities on engine speed will be further examined in Chapter 4.

The presentation of the results follows the order of geometrical complexity, starting with the steady flow tests without the stationary dummy piston and concluding with the in-cylinder measurements in the model

engine.

A. Steady flow/open-ended cylinder

The ensemble-averaged mean and rms values of the tangential velocity component are presented along three diameters at axial distances of 0.5, 1.0 and 2.0 bore (D) from the cylinder head and for three valve lifts of 2, 4 and 8mm covering the range of the operating engine. Since it was observed that profiles at a given axial plane and different valve lifts exhibit similar trends, these are presented and discussed in groups according to their axial distance from the cylinder head.(Figs.3.3-3.5, a-c).

Near the cylinder head (z=0.5D), as Figs.3.3.a, b, and c show, the mean swirl velocity profiles reflect the geometry and orientation of the swirl vanes with a non-linear distribution near the cylinder axis and maximum velocities of 6.5-8.0V_p at radial distances of 25-30mm. The balance between the swirl-induced radial pressure gradient and the centrifugal forces, scaling with the square of the mean tangential component, determine the exact shape of the swirl distributions (Vafidis, 1984). The swirl centre almost coincides with the geometrical centre and the effect of the wall on the swirl velocities at the larger radii is limited, as expected, due to the proximity of the measurement plane to the cylinder head and the short time available for flow development. The effect of the valve lift on the mean profiles is restricted to a slight variation of the distribution in the central area. All three rms profiles of the velocity fluctuations exhibit similar trends with a flat area near the centre with levels of 1.7, 1.0 and 0.7V_P corresponding to 2, 4 and 8mm valve lift, which increase towards the wall to maxima of about 3.0, 2.5 and 2.0V_P, respectively.

Further downstream at z=1.0D, as Figs.3.4.a, b and c show, the mean swirl distributions around the cylinder axis become linear, indicating the formation of a forced-vortex core. Approaching the wall, the trend towards solid body rotation breaks down due to friction by the solid boundaries and diffusion, which not only prevent the swirl velocity maxima from occurring next to the wall but also smooth out the mean velocity variations at larger radii. For each valve lift, the overall turbulence levels have decayed relative to those at z=0.5D, especially near the walls, with the differences for the

three valve lifts reduced within the range 0.7-2.0V_P; the distributions around the centre remain uniform as those closer to the cylinder head.

At z=2.0D, according to Figs.3.5.a, b and c, the mean swirl flow has developed even further to a central forced vortex-core but of reduced size compared to that at z=1.0D, and to an extended nearly uniform annular region with magnitudes of 5-6V_P for all valve lifts. Turbulence has decayed even further to levels of about 0.8V_P for 2mm valve lift and 0.5V_P for the other two cases, but this time a peak is present around the cylinder axis with corresponding rms velocities 80% higher on average compared to those in the rest of the cylinder. Since only a small part of the observed increase in the rms level can be attributed to velocity gradient broadening (according to sub-section 2.5.2), a possible cause of this local maximum is movement of the swirl centre around a mean location, so-called swirl centre precession, at a low frequency or range of frequencies, characteristic of this region (Claypole et al, 1986). The increase in the rms levels is accompanied by an eccentricity of the swirl centre from the geometrical axis, which is examined further in Fig.3.6, where mean and rms swirl velocities measured along the cylinder axis are plotted as a function of distance from the cylinder head. Due to the close similarity in the observed trend for valve lifts of 2, 4 and 8mm, this profile and most of the following results are presented only for the case of the medium valve lift. Two sets of data are presented in Fig.3.6 for different orientations of the cylinder head with respect to the cylinder and, subsequently, measurement axis; both show that the eccentricity of the swirl centre starts at an axial distance of about 0.8D and is associated with a gradual increase of the rms velocities. Moreover, the direction of the initial eccentricity depends on the orientation of the cylinder head which indicates that a minor asymmetry of the swirl vanes, attributed to manufacturing tolerances, can trigger a small disturbance to the swirling flow pattern which is amplified further downstream from the cylinder head. The path of the mean swirl centre is a helix which initiates at an instability point and spirals downstream of the cylinder head. Similar helical motions of the swirl centre were observed in steady flows through production engine helical ports (Uzkan et al, 1983; Coghe et al, 1985), or when the working fluid is simulated by a mixture of oils to allow application of the refractive index-matching technique (Nadarajah et al, 1991).

The velocity flowfield is examined further in terms of the diametral profiles of the axial component at the three axial locations of 0.5, 1.0 and 2.0D downstream of the cylinder head, the same as those for the tangential component, together with the centreline distribution of the axial mean and rms velocities. The aim is to investigate the effect of the swirl vanes on the development of the axial flow and to identify possible mechanisms for the helical motion of the swirl centre.

Near the cylinder head (z=0.5D, Fig.3.7.a), the mean axial flow distribution is dominated by the annular jet issuing from the valve gap and developing close to the cylinder walls with maximum levels of $8.5V_P$; in the annular area within r≅7 to 27mm the axial flow is reversed towards the cylinder head, whereas in the central area (up to r=±7mm), contrary to what is expected for a non-swirling pipe-flow in the wake of a bluff body, the direction of the axial flow is towards the open end of the cylinder. Further downstream (z=1.0D, Fig.3.7.a) the reverse flow area expands towards the centre and forms a nearly uniform distribution around the cylinder axis; the profile of the same component along the cylinder axis (Fig.3.7.b) reveals the existence of a stagnation point at about z=0.8D. The mean velocities have decreased overall compared to those at z=0.5D with maximum values of approximately $2V_P$ in both directions. This trend is more pronounced at z=2.0D (Fig.3.8.a), where the mean profile appears smoother with minor magnitude differences. The turbulence intensity profiles of the axial component follow closely the development of the corresponding profiles for the swirl component in terms of both shape and magnitude, as the comparison of Figs.3.3.b, 3.4.b, 3.5.b with Fig.3.7.a reveals.

A similar flow pattern was also observed in isothermal studies of swirl combustors (e.g. Escudier and Keller, 1985; Hagiwara and Bortz, 1984). The presence of swirl results in the setting up of radial and axial pressure gradients which, in turn, influence the flowfield; in the case of strong swirl, the adverse axial pressure gradient is sufficiently large to result in reverse flow along the axis (Beer and Chigier, 1974). Furthermore a comparison between the centreline profiles of the two velocity components (Figs.3.6 and 3.7.b) reveals that the initiation of the eccentricity of the swirl centre coincides with the upstream side of the recirculation zone on the cylinder axis. This implies that the helical precessing motion of the swirl centre,

termed as precessing vortex core (Claypole et al, 1986) initiates as an instability at a free stagnation point and is associated with the reverse flow region (Chanaud, 1964). Since previous investigators have emphasized that this motion is periodic with one or more characteristic frequencies, it was decided to examine in more detail the instantaneous velocity traces.

Figure 3.8 shows three temporal profiles of the swirl velocity component at the centre of the cylinder and at an axial distance of 2.0D from the cylinder head, obtained respectively at valve lifts of 2, 4 and 8mm. In all cases a sinusoidal motion can be easily identified and its frequency was estimated to be within the range 14-20Hz. More accurate determination of the frequency values cannot be made because at all these profiles, obtained over relatively small (150-190ms) windows, the random velocity fluctuations are superimposed on the periodic signal and obscure the result. In order to estimate more accurately the dominant frequency (or frequencies), all measurements were repeated using a frequency tracker whose analog signal was spectrum analysed. Some excerpts from this investigation, obtained for the swirl velocity component and medium valve lift (4mm) are shown in Fig.3.9. At z=0.5D and at any radial location (only r=0mm is shown here) the spectra exhibit no dominant frequencies in the range under investigation (0-100Hz) in agreement with the swirl profile at the corresponding axial location which did not show any increase in the tangential velocity fluctuations around the cylinder axis. At z=1.0D a small frequency peak is barely identifiable, becoming gradually higher further downstream at z=1.5-2.5D along the cylinder axis. Away from the axis of symmetry the presence of a characteristic frequency cannot be confirmed at z=1.0D and r=5mm, whereas it can be identified at z=1.5D and r=5mm (but not at r=10mm); further downstream (z=2.0-2.5D) its presence extends in the radial direction, appearing even at r=30mm (only z=2.5D is shown in Fig.3.9). In all cases the distinct peak happens at a constant frequency of 16Hz (±0.5) which seems to be associated with a unique scalar quantity of the flow under investigation; according to Chanaud (1964) this quantity is the air mass flowrate and/or the angular velocity of the steady flow. The existence of a characteristic frequency is probably the result of the precessing motion of the swirl centre around its mean location at each measurement plane; the precessing vortex core is confined around the axis to a distance of about 1.0D from the cylinder head, developing downstream and expanding towards the cylinder wall. A

parametric investigation of this phenomenon as a function of the air flow rate is presented in the next sub-section, together with results from the second steady-flow experiment.

B. Steady flow/stationary porous piston.

The steady flow configuration of the previous experiment was modified so that results could include the effect of a stationary solid boundary simulating the piston in an engine; a flat porous circular plate was placed at an axial distance of z=3.0D and most of the previous measurements were repeated. This study was also prompted by the known sensitivity of the swirl distribution to the downstream boundary conditions (Escudier and Keller, 1985). This configuration bridges the geometric gap between the open-ended cylinder discussed previously and the confined cylindrical geometry of the model engine.

Figure 3.10 presents the tangential velocity profiles obtained at the same axial locations with the previous case (Figs.3.3.b, 3.4.b, 3.5.b) and at a valve lift of 4mm. Comparison between the corresponding mean and rms swirl profiles indicates differences in both magnitude and trend. Close to the cylinder head (z=0.5D) the mean distribution is similar to that obtained at the furthest downstream location (z=2.0D) in the absence of the porous plate, but with increased levels by around 50% (compare Figs.3.5.b and 3.10.a). The two mean profiles at the intermediate distance of z=1.0D obtained with and without the solid boundary have the same shape with only small differences of about 5% in magnitude (Figs.3.4.b, 3.10.b); additionally there is a similarity in the spatial distribution, especially at the outer radii, between the mean swirl profile far downstream (z=2.0D), as modified by the presence of the porous plate, and the profile nearest to the cylinder head for the open-ended cylinder. These observations indicate that a roughly opposite trend in the mean swirl velocities exists, with swirl developing from the piston towards the cylinder head; it seems, therefore, that the porous piston although allowing air to pass through it, acts as a reflecting mechanism for the swirling flow patterns. The rms levels measured with the porous plate are in all cases higher than the corresponding ones in the open-ended cylinder. Most noteworthy is the presence of local rms maxima along the cylinder axis for all measurement levels; rms levels at r=0mm are more than double the

magnitudes measured at r=20mm. According to the arguments of the previous subsection, these are indications that the periodic motion of the swirl centre initiates very close to the cylinder head, which is also confirmed by the centreline profiles of the swirl component obtained at two different orientations of the intake port (Fig.3.11). Both mean traces show that the helical motion starts just behind the valve with eccentricities of the swirl centre determined by minor manufacturing asymmetries of the swirl vanes. It is also worth noting that the rms levels decrease with increasing axial distance, following opposite trend to those observed without the dummy piston (compare Figs.3.6 and 3.11). Overall, it can be said that the tangential velocity flowfield is determined by the interaction of the downstream convected and the upstream reflected by the dummy piston swirling flow patterns.

The axial flowfield in the presence of the stationary porous piston has been also investigated and compared with the open-ended cylinder by measuring the mean and rms velocity profiles at the same axial locations. As Fig.3.12.a shows, the mean axial profile near the cylinder head (z=0.5D) is very similar to that of Fig.3.7.a, in terms of both the magnitude and shape. This is not, however, the case further downstream; at both z=1.0D and 2.0D the mean levels are reduced and, most important, there are no signs of reverse flow near the cylinder axis but only at radial distances of 10-15mm. This is more clearly shown in the centreline profile of the axial component (Fig.3.12.b) where no change of sign takes place. It seems that the presence of the porous plate transforms the recirculation zone present in the case of the open-ended cylinder into an annular recirculation region extending radially over a distance which decreases downstream of the cylinder head. This phenomenon is probably associated with the reverse development of the precessing periodic motion, as mentioned previously. In the absence of the free stagnation point, observed previously in the case of the open-ended cylinder, the helical motion originates just behind the valve, due probably to the interaction of the annular swirling valve jet with the wake formed behind the valve.

Confirmation of the periodic motion of the swirl centre identified in the swirl profiles of Fig.3.10 has been provided by the spectrum analysis of the swirl velocity signal at a number of locations along the centreline (Fig.3.13).

The same characteristic frequency (16Hz) observed with the open-ended cylinder has been identified at the same air mass flowrate (11.8 kg/h) with the porous piston. The frequency maxima are not as sharp as in the previous case, indicating that a narrow range of frequencies around this value may be present rather than a single value. Most noteworthy is that the intensity of the peak exhibits a consistent trend increasing from the piston towards the cylinder head; this implies that the imposition of a downstream boundary gives rise to axially reversed phenomena, not only in terms of mean and rms swirl profiles but also of swirl centre precession.

A parametric study has been performed in the steady flow rig to identify the dependence of the characteristic frequency of swirl centre precession on mass flowrate. The air flowrate was varied between 10-41 Kg/h (corresponding to engine speeds of 180-700rpm) for the open-ended cylinder and 10-25 Kg/h for the confined cylinder, due to the higher pressure drop imposed by the porous plate; the velocity signal on the centreline was analysed in order to obtain the PSDs and thus deduce the dominant frequencies. As Fig.3.14 shows, a linear dependence was found to exist between the frequency of swirl precession and the air mass flowrate. Batchelor (1967) claims that in solid-body rotating flows, an initial displacement which leads to a non-zero expansion in the plane normal to the axis of symmetry, is accompanied by Coriolis forces opposing this movement. This can give rise to oscillations whose natural frequencies are proportional to the angular velocity. In the present experiment almost all the mean swirl profiles have a solid-body distribution around the cylinder axis, occupying a cylinder of about 10mm radius. Since it is well established that swirl strength or angular velocity scales with mass flowrate, it can be argued that the frequency of the precessing motion scales with air mass flowrate through the fact that for a given flow geometry the later determines the angular velocity of the rotating fluid. It is also interesting to note that when the distribution was far from solid-body rotation (z=0.5D in the open-ended cylinder), swirl precession could not be detected.

This analysis is expected to have some implications on the reciprocating engine flowfield. During the induction stroke, the air mass flowrate varies over a wide range depending both on engine speed as a mean value (as defined at the beginning of this section) and on crankangle as an

instantaneous value, which implies that a wide range of characteristic frequencies may be present. After the closure of the inlet valve (IVC), during the compression stroke, the air trapped inside the cylinder rotates at a certain angular velocity, therefore swirl centre precession is expected to happen at a narrower range of frequencies, similar to those found in the steady flow tests at equivalent angular velocities. Further discussion of this phenomenon, supported by results obtained from the model engine, is presented in the next sub-section.

C. Model engine.

Following the procedure of the steady flow investigation, swirl and axial ensemble-averaged velocity profiles were measured at the middle (90° ATDC) and at the end of induction stroke (180° ATDC) at two axial locations (z=0.25D and 0.5D) inside the corresponding displaced volume of the model engine. At the above mentioned crankangles, the piston was situated 1.2D and 1.75D downstream of the cylinder head, respectively. The engine, in all cases, was motored at 200rpm which, according to equation (3.2), corresponds to the mass flow rate (11.8Kg/h) of the steady flow tests.

As Figs.3.15.a-d show, the mean swirl distributions at both crankangles exhibit similar characteristics to the mean swirl profiles of Fig.3.10 obtained with the dummy piston. This justifies the use of the stationary piston as an intermediate step between the open-ended steady flow rig and the model engine. At mid-induction swirl velocities have maximum values of 8-9V_p, similar to those obtained with the dummy piston close to the cylinder head (Fig.3.10.a). Later at BDC, maximum swirl velocities have increased to 9.5-11V_p and occur closer to the cylinder axis; this observation resembles the trend found in the mean swirl profiles with the dummy piston further downstream the cylinder head. In both cases the time allowed for flow development is the governing factor: in the steady flow case the flow develops as a function of the distance from the cylinder head and in the unsteady case of the model engine it also develops with crankangle.

In order to characterise the swirl intensity of the in-cylinder flow, the two mean swirl profiles at 180°CA (Fig.3.15.c,d) were processed by the method described in Appendix A. Equivalent swirl ratio values (SR_e) were

found to be 7.6 and 7.7 for the profiles at z=0.25D and 0.50D, respectively; these values are more than double the swirl ratios (SR=2.2-3.5) encountered in real direct-injection diesel engine geometries employing helical ports. It follows that the 60° swirl vanes generated unrealistically high levels of swirl but their use is justified by the fact that, under the present conditions, the observed phenomena were intensified and, therefore, more easily identified and analysed.

The ensemble-averaged rms fluctuations at mid-induction vary within the range 1.5-3.5V_P but, later at BDC, they are reduced to 1-2.5V_P; these values are comparable to those obtained at z=0.5 and 1.0D with the dummy piston and share the same general trend of swirl decaying as a function of distance from the cylinder head and, additionally, crankangle. Local maxima in the ensemble-averaged rms profiles can be identified around the swirl axis, of either high (Fig.3.15.d) or lower intensity (Figs.3.15.a,b); this observation as discussed in the previous sub-sections is associated with swirl centre precession.

The axial velocity flowfield in the engine cylinder is presented in Figs.3.16.a-d. At mid-induction, where the valve lift is at its maximum value (9mm), mean axial velocities vary from -3V_P to +7V_P close to the cylinder head (z=0.25D), whereas further downstream (z=0.5D) they are reduced to the range -2.5 to +4.5V_P. Comparison with the axial profiles of Fig.3.12.a, obtained with steady flow through the cylinder head in the presence of the porous plate, shows similar trends in the mean velocity distributions with high positive velocities near the cylinder wall and smaller but, again, positive velocities near the cylinder axis; an annular area with reverse mean axial velocities is present at radial distances of 5-20mm. At BDC (Fig.3.16.b), when the inlet valve begins to close, the mean axial distributions are transformed to an extended area of positive velocities (up to r=25mm) and low negative velocities close to the cylinder wall. The axial rms fluctuations at mid-induction vary within the range 2-3.5V_P, decaying to 1.5-2V_P at the end of the induction stroke.

The ensemble-averaged mean and rms axial velocities obtained along the cylinder axis at mid-induction and BDC (Figs.3.16.c,d) complete the description of the axial flowfield. No reverse mean flow is observed around

the cylinder axis during the induction stroke; as discussed in the previous steady-flow configurations, if an instability develops, a helical motion of the swirl centre can be sustained, with or without the reverse flow around the axis. It is also interesting to note that the two axial profiles of Fig.3.16.a exhibit a certain degree of eccentricity from the geometric axis which, according to Kito (1984), is related to the eccentricity of the swirl centre at the same axial locations.

In order to analyse further the movement performed by the swirl centre in the unsteady flow case of the model engine and assess its significance during the compression stroke, instantaneous traces of the swirl velocity component have been obtained over a number of engine cycles close to the cylinder head (z=0.25D) on the cylinder axis (Fig.3.17). A nearly periodic motion with variable amplitude and frequencies around 20-30Hz can be identified in all traces. During the induction stroke, the superposition of high turbulence makes difficult the identification of characteristic frequencies, whereas during the compression stroke the periodic motion can be more easily recognised. Closer comparison between these arbitrarily selected traces reveals that, although they are generally in-phase, cycle-to-cycle variations do exist and are attributed to minor phase variations; this phenomenon is a direct result of the swirl centre precession observed in the steady flows, and it seems to be the cause of the increased velocity fluctuations around the swirl axis present in the ensemble-averaged swirl profiles of Fig.3.15.

The fact that the instantaneous traces remain generally in-phase is reflected on the tangential mean velocity trace at the same point (Fig.3.18), which was obtained by ensemble-averaging a statistically-adequate number of velocity data, such as those presented in Fig.3.18. The variable-period periodic motion of the mean swirl profile is evident on the axis of symmetry, indicating the presence of a helical motion equivalent to the one found in the steady flow rig. Furthermore, it seems that during the compression stroke the piston 'compresses' the helix and that the mean trace of Fig.3.18 on the centreline is the transformation of the spatial helical structure, created during late-induction and early compression, by the sinusoidally-moving piston. This explanation is supported by another experimental investigation in a production engine (Haghgooie and Kent, 1987), where it is argued that

the variation of the swirl centre with crankangle during compression is mainly the result of layers with different swirl centres crossing the measurement plane. A numerical investigation (Johns, 1985) in a production engine geometry with an off-centre bowl-in-piston, showed that during compression the swirl structure is undergoing gyroscopic precession rather than simply 'dragged' towards the bowl centre.

Figure 3.18 can also be used to deduce characteristic frequencies which are attributed to the variation of the mean swirl velocity with crankangle. Local maxima can be identified and the period of the motion can be estimated by converting crankangle degrees into absolute time (ms). Frequency values lie within the range 10-27Hz for the whole cycle and, most significantly, 13-27Hz for the compression stroke, which compares reasonably well with the value of 16Hz measured in the steady flow case. Since the engine rotates at 200rpm (3.3Hz), it follows that the swirl centre precesses at frequencies 4-8 times the rotational frequency of the crankshaft (rpm). This agrees well with the equivalent factors (6-8 times) estimated in Haghgooie and Kent (1987), for an engine speed variation between 200-1000rpm.

3.2.4 Conclusions

Investigation of the swirling flow in two steady flow configurations and in a low speed idealised motored engine revealed the following:

(1) In the steady flow cases the axisymmetric swirling flow patterns exhibit signs of axial stratification developing from the cylinder head towards the open end of the cylinder and showing opposite trends when a porous plate is placed at an axial distance of 3.0D from the head. The use of a porous plate in steady-flow studies is proposed as a research tool to simulate the moving piston of the engine flow.

(2) The swirl centre performs a helical periodic motion with a characteristic frequency which scales with the mass flow rate. The area within which the vortex core precesses, depends on the axial distance and the presence of the porous plate

(3) The ensemble-averaged swirl centre position in the model engine exhibits a helical motion both in time (or crankangle) and in space. The

characteristic frequency of this mean motion is 4-8 times the frequency corresponding to the engine speed.

(4) Small phase variations exist between different cycles and are responsible for the increase of the ensemble-averaged fluctuations around the cylinder axis; a fictitious turbulence is measured, but, since the phenomenon is confined locally, the degree of overall volume-averaged turbulence overestimation is small. High-pass filtering employed in cycle-resolved analysis (see section 1.2.2) can eliminate the contribution of this motion to the measured velocity fluctuations around the cylinder axis but it could result in underestimation of turbulence magnitudes by removing all energy content below the frequency cut-off.

3.3 SWIRLING FLOW IN A MOTORED DIESEL ENGINE

The investigation of swirling flows is extended in this section to a typical diesel engine geometry. Swirl was generated by means of a helical port, which is common to nearly all modern DI diesel engines; a flat piston crown was initially used in order to assess the influence of the inlet manifold alone on the TDC tangential flowfield in the absence of squish effects. This investigation was prompted by differences experienced in the performance of diesel engines equipped with and without an inlet manifold. Due to constraints imposed by the transparent acrylic material of the cylinder liner used in this research engine, speed and compression ratio were kept low relative to production engines. The unrealistic for diesel engines compression ratio (CR=8) was not considered a major disadvantage since the aim of this study was to disclose trends rather than quantitative results. Higher geometric compression ratios (up to 19) were employed only when they were combined with throttling of the induction air at various levels to allow operation of the engine at reduced maximum cylinder pressure. The effect of throttling on the TDC tangential flowfield was investigated for both flat and bowl-in-piston geometries and the objective was to develop a method of comparing diesel engine geometries at realistic geometric compression ratios, using transparent liner and piston made of acrylic plastic. It should be noted that throttling was only considered as a research tool and not as an operating

variable, since in diesel engines load is controlled by the fuelling system rather than a throttle as in petrol engines.

3.3.1 Flow configuration

The research engine employed in this investigation consisted of parts from two production engines. The cylinder head was from a modern four-cylinder DI diesel engine (Ford York 2.5L) which was cut so that one fourth could be mounted on the block of a single-cylinder diesel stationary engine (Petter PJ1). The liner of the base engine was extended by 70mm with a transparent perspex cylinder of 93.7mm internal diameter, identical to that of the Ford engine, and 13mm wall thickness in order to withstand high air pressures (Fig.3.19). Similarly, the original piston of the Petter engine was extended by incorporating either a flat cylindrical piece made from aluminium and of variable length, or an aluminium piston-bowl with flat perspex windows. The geometry of these flat inserts determined the TDC volume and, thus, the geometric compression ratio of the engine. The geometry of the piston-bowl was based on a production Ford piston, by keeping the same bumping clearance and squish area but reducing the compression ratio to 8.5 through an increase of the bowl depth for the same bowl base (Fig.3.19). This was necessitated by the need to use perspex cylinder wall and piston bowl windows to obtain optical access inside the bowl and by the relatively low tensile strength and deformation temperature of perspex (see Table 2.1). All the characteristics of the research diesel engine are summarised in Table 3.2.

Rather than using the overhead camshaft of the Ford engine, the intake and exhaust valves were operated through pushrods and rockers by the original camshaft of the Petter engine. The lubrication system remained unaltered and the engine was motored by a 3KW thyristor-controlled DC motor through a toothed belt with a gear ratio of 2:1. The engine-motor assembly was rigidly fixed on a 800Kg concrete block and was mounted on the ground through a vibration damping pad. The modified engine could be motored at speeds up to 1000rpm, limited by the rated speed of the DC motor and the torque requirements of the engine. The system was operating with negligible vibrations and a satisfactory rate of oil contamination of the transparent cylinder.

Cylinder bore, mm		93.7
Stroke, mm		110
Piston diameter, mm		92.5
Connecting rod length, mm		231.9
Compression ratio		8-19
Engine speed, rpm		450
Intake valve:	diameter, mm	42
	seat angle, (^{0})	30
	opens, IVO,^{0}BTDC	4.5
	closes, IVC,^{0}ATDC	215.5
Exhaust valve:	diameter, mm	36.5
	opens, EVO, ^{0}BBDC	35.5
	closes, EVC, ^{0}ATDC	4.5

Table 3.2 Characteristics of the research diesel engine

Previous experience with the same engine (Arcoumanis et al, 1986) showed that a fully transparent perspex bowl cannot withstand geometric compression ratios higher than 8.5. In order to reduce the peak cylinder pressure of the air corresponding to higher compression ratios, the induction air was throttled to manifold pressures as low as 0.3bars. Reduction of the manifold pressure has allowed operation of the engine at geometric compression ratios up to 19 without piston-bowl distortion. This method can allow LDV measurements in identical to production piston-bowl geometries through transparent cylinder liners; in particular, it allows measurements to be obtained very near to the bowl entry plane where information of squish and swirl-squish interaction is essential.

A schematic of the experimental rig is shown in Fig.3.20. Throttling of the induction air was achieved by means of a valve, located upstream of a cylindrical chamber which was connected to the inlet port acting as an 'idealised manifold' (Fig.3.21); the degree of throttling was characterised by the differential pressure between the manifold and the atmosphere, termed as inlet manifold vacuum (ΔP). The idealised manifold was sufficiently large compared to the cylinder volume to suppress pressure fluctuations present upstream of the port and, at the same time, minimise the effect of the throttling valve on the velocity distribution in the inlet port. Two alternative manifold configurations were also examined: a production 4-cylinder

manifold used in the Ford York 2.5L but with the three branches blocked (Fig.3.22) and the same Ford manifold with 30° swirl vanes incorporated in its downstream side just upstream of the inlet port. All measurements were obtained with the engine running at a constant speed of 450rpm rather than at its maximum permissible speed of 1000rpm to facilitate measurements inside the bowl at TDC of compression and permit longer measurement periods with less frequent cleaning of the transparent cylinder and piston bowl.

3.3.2 Measurement systems

Pressure measurements - The in-cylinder pressure was measured by means of a piezoelectric transducer mounted on the cylinder head in the position of the fuel injector; the signal processing system was identical to that described in section 2.3. A single limb mercury manometer was used to measure the inlet manifold vacuum downstream of the throttling valve.

Velocity measurements - A dual beam LDV system operating in the near forward-scatter light mode was used and comprised an Ar-Ion laser operating at 514.5mm with 0.2-1.2W power together with similar optics and signal processing equipment to those of previous experiments (sub-section 3.2.2). Silicone oil, atomised by means of a microfog lubricator, was used as seeding material and was recirculated in a closed circuit through a settling chamber (Fig.3.20). The measurement position and the magnitude of the swirl velocity component were corrected for refraction effects of the laser beams through the cylindrical wall according to the procedure described by Vafidis (1985).

3.3.3 Results

The effect of the inlet manifold on the port-generated swirling flow pattern at TDC of compression has been investigated with the diesel engine equipped with the flat piston at a compression ratio of 8. All three inlet configurations, described in section 3.3.1, were used. The results for the three cases are summarised in Table 3.3(a) in terms of the measured specific angular momentum AM (per unit mass), which provides information about

the average swirl at the measurement plane; these values were estimated from the measured velocity profiles according to the procedure described in Appendix A. Turbulence at TDC was characterised by the volume ensemble-averaged rms of the velocity fluctuations along the measurement plane which are normalised by the mean piston speed (V_P=1.65m/s at 450rpm).

Table 3.3 Summary of in-cylinder swirl and turbulence characteristics

Inlet geometry	Specific Angular Momentum (m^2/s)	Volume-average rms velocity (V_P)
Idealised manifold	0.125	0.38
Ford manifold	0.127	0.38
Ford manifold + vanes	0.108	0.36

(a) Effect of manifold

Piston geometry	Geometrical Compression ratio	Manifold vacuum (mmHg)	Manifold pressure (bars)	Max. cyl. pressure (bars)	Spec.Angul. momentum (m^2/s)	spec. AM loss (%)	Vol. aver. rms vel. (V_P)
Flat Piston	8	0	1.02	11.4	0.125	0	0.33
		100	0.88	9.0	0.104	17	0.32
		300	0.61	5.9	0.094	25	0.30
Flat piston	12	200	0.74	10.7	0.088	0	0.29
		400	0.48	6.4	0.079	10	0.29
Flat piston	19	350	0.53	10.6	0.074	-	0.28
Bowl-piston	8.5	0	1.02	10.3	0.067	0	0.85
		400	0.48	4.0	0.059	12	0.85

(b) Effect of air throttling

Figure 3.23 shows the swirl velocity distributions superimposed for direct comparison. From the calculated values in Table 3.3(a) and the corresponding velocity profiles it becomes clear that the shape of the manifold has a very small effect on both the angular momentum and the volume-averaged turbulence intensity. The incorporation of swirl vanes upstream of the inlet port, however, resulted in a more uniform solid body distribution with lower mean velocities especially towards the cylinder wall and a smaller overall angular momentum (reduced by 17%). It is interesting to note that the

more organised swirl motion obtained with the Ford manifold/swirl vanes configuration gave rise to slightly lower in-cylinder turbulence levels.

The effect of throttling on the TDC flowfield has been investigated at compression ratios of 8, 12 and 19 with the flat piston and 8.5 with the idealised re-entrant piston-bowl over a range of inlet manifold pressures; the idealised cylindrical manifold was used in all cases. The flowfield was characterised in terms of the maximum cylinder pressure and the swirl mean and rms velocity distributions at the mid-plane between the cylinder head and the flat piston at TDC of compression. Figure 3.24 shows the variation of maximum in-cylinder pressure with inlet manifold vacuum for three compression ratios in the case of the flat piston; the mean and rms swirl velocity distributions over the cylinder diameter (or bowl diameter) are shown in Figs.3.25-3.28. In all cases, the mean (open symbols) and rms (closed symbols) velocities were normalised by the mean piston speed (V_P). The mean swirl distributions were processed according to the procedure described in Appendix A to provide the specific angular momentum and allow direct comparison with the unthrottled case in terms of angular momentum losses and Table 3.3(b) summarises all the test results.

At all three compression ratios, the decrease of peak pressure with increasing vacuum (or decreasing absolute pressure) is linear over most of the pressure range, except for the first 100mmHg where the reduction of peak pressure is higher (Fig.3.24). The maximum in-cylinder pressure is directly proportional to the amount of air trapped inside the cylinder volume during the induction stroke, so it can be concluded that the present method of throttling, employing a valve upstream of a cylindrical chamber connected to the inlet port, resulted in a relatively high reduction in the mass flow rate during the first stages and a less so thereafter.

Figure 3.25.a shows the mean and rms swirl distributions for the fully-open throttle case at a compression ratio of 8 and provides the reference condition for the two partially-closed cases of Figs.3.25.b and c. The mean profile of Fig.3.25.a is nearly concentric with the cylinder axis and exhibits trends of solid body rotation with maximum swirl velocities of $3.1V_p$. When the manifold absolute pressure is reduced to 0.88 bars, corresponding to a vacuum of 100mmHg, the swirl distribution remains very similar in shape to

that of the unthrottled case but the maximum swirl velocity is reduced by around 16% to $2.6V_p$. Integration of the swirl profile along the radius resulted in similar specific angular momentum losses relative to the unthrottled case of 17% (Table 3.3.b) which implies close similarity of the swirl distributions. Further reduction of the manifold pressure to 0.61bars resulted in a proportionally smaller reduction of the peak swirl velocities ($2.4V_p$) with an associated specific angular momentum loss of 25%. This implies that the degree of throttling and the associated reduction in the air-mass trapped inside the cylinder volume, is not proportional to the corresponding reduction in the angular momentum per unit mass. This trend can be partly explained by the non-linear effect of throttling on mass flow rate discussed in the previous paragraph. Another reason is that swirl levels at TDC are depending on air velocities during the induction stroke, which do not scale with the mass flow rate but with the volume flow rate; the latter is reduced by a lower percentage due to the simultaneous reduction of the air density in the manifold.

A similar trend in the magnitude of the mean velocity with the degree of throttling or volumetric efficiency has been observed in a gasoline engine (Lancaster, 1976). As volumetric efficiency was decreased, the mean axial velocity decreased almost proportionally during induction and less so during the compression stroke. In the present case, we expected and obtained a smaller reduction in the magnitude of the swirl velocity for similar throttling levels, since it is well known (e.g. Arcoumanis et al, 1986) that swirl relative to the axial flow has a much stronger memory of the induction boundary conditions.

In agreement with the results of Lancaster (1976), the effect of throttling on the ensemble-averaged rms velocities is smaller than its effect on the mean flow with maximum differences between the throttled (Fig.3.25.c) and unthrottled (Fig.3.25.a) cases of the order of 10%. This is probably due to the fact that any differences in the turbulence levels associated with the velocity gradients of the intake jet are expected to decay to similar levels at the end of the compression stroke in disk-type engine geometries.

Figure 3.26 shows the mean and rms distributions at the intermediate

compression ratio of 12 for the two partially throttled cases. Measurements with wide open throttle were not possible since the corresponding pressure at that compression ratio was higher than the maximum permissible pressure for perspex at the given temperature. The trend of solid body rotation is evident in both mean swirl distributions, with differences in the specific angular momentum between the two cases of 10% (Table 3.3.b). A comparison between the corresponding angular momentum values for different compression ratios indicates that for similar vacuum differences (200mmHg) in the partially-throttled cases, the losses in specific angular momentum at TDC were nearly identical; for compression ratio of 12, the specific angular momentum reduced by 10.2%, (from 0.088 to 0.079m^2/s) compared to 9.6% with compression ratio of 8 (from 0.104 to 0.094m^2/s). When the geometric compression ratio was further increased to 19 (Fig.3.27), to simulate the conditions present in diesel engines, a vacuum of 350mmHg corresponding to 0.53 bars manifold pressure was required to allow operation of the engine with the perspex cylinder; the magnitude of the required pressure drop was determined on the basis of the peak cylinder pressure. From the above it becomes clear that a loss of around 28% in the specific angular momentum should be expected relative to the unthrottled case for operation at geometric compression ratios of 19.

Figure 3.28 shows the mean and rms swirl velocities obtained in an idealised re-entrant piston bowl at a compression ratio of 8.5 with and without throttling. Comparison between the mean velocity distributions indicates that the angular momentum loss between the two cases (Table 3.2.b) is only 12%, despite the larger depression of the manifold pressure relative to that with the flat piston at a compression ratio of 8. This is probably due to residual mass trapped inside the piston-bowl and rotating at higher speeds than the fresh charge entering the engine cylinder. Since the mass of exhaust gas remaining as residual in the cylinder tends to be constant independent of the induction pressure (Obert, 1973), the percentage of residual mass diluting the fresh charge tends to increase as the vacuum manifold pressure decreases.

Since throttling has a quantifiable effect on the mean swirl velocity of TDC of compression and a relatively small effect on turbulence intensity, it offers a cost-effective method for reducing the peak pressure in the cylinder,

thus allowing the use of cylinder liner and piston-bowls made from acrylic plastic. By using perspex piston-bowls of identical geometry to those used in production engines and motoring the research engine at realistic engine speeds and compression ratios, the optical access to the engine cylinder near TDC can be maximised and the pre-combustion flowfield adequately mapped.

3.3.4. Conclusions

Investigation of the swirling flowfield by means of laser Doppler velocimetry in a research diesel engine operating under motoring conditions for various induction system geometries revealed the following:

(1) The effect of inlet manifold geometry on the TDC swirl velocity flowfield in the presence of a helical port is negligible; only when swirl vanes were incorporated into the inlet manifold, a measurable difference on the swirl velocity flowfield was observed.

(2) An acceptable simulation of the flow in diesel production engines can be achieved by reducing the peak pressure in the cylinder through throttling and using a cylinder wall and piston-bowl made from perspex. This allows maximum optical access near TDC of compression for measurements of all three velocity components in identical piston bowls to those of production engines and at realistic compression ratios.

(3) Throttling of induction air causes a reduction in the magnitude of the mean swirl velocities at TDC which is less than proportional to the degree of throttling; for the case of disk-type geometries and compression ratio of 8, specific angular momentum losses amounted to 25% when the absolute inlet manifold pressure was reduced to 0.6bars. A smaller effect on the mean swirl flowfield was found inside piston-bowls due to residual flow effects.

(4) The effect of throttling on the TDC turbulence levels is small (~10%) over a wide range of manifold vacuum pressures and for compression ratios from 8 to 19.

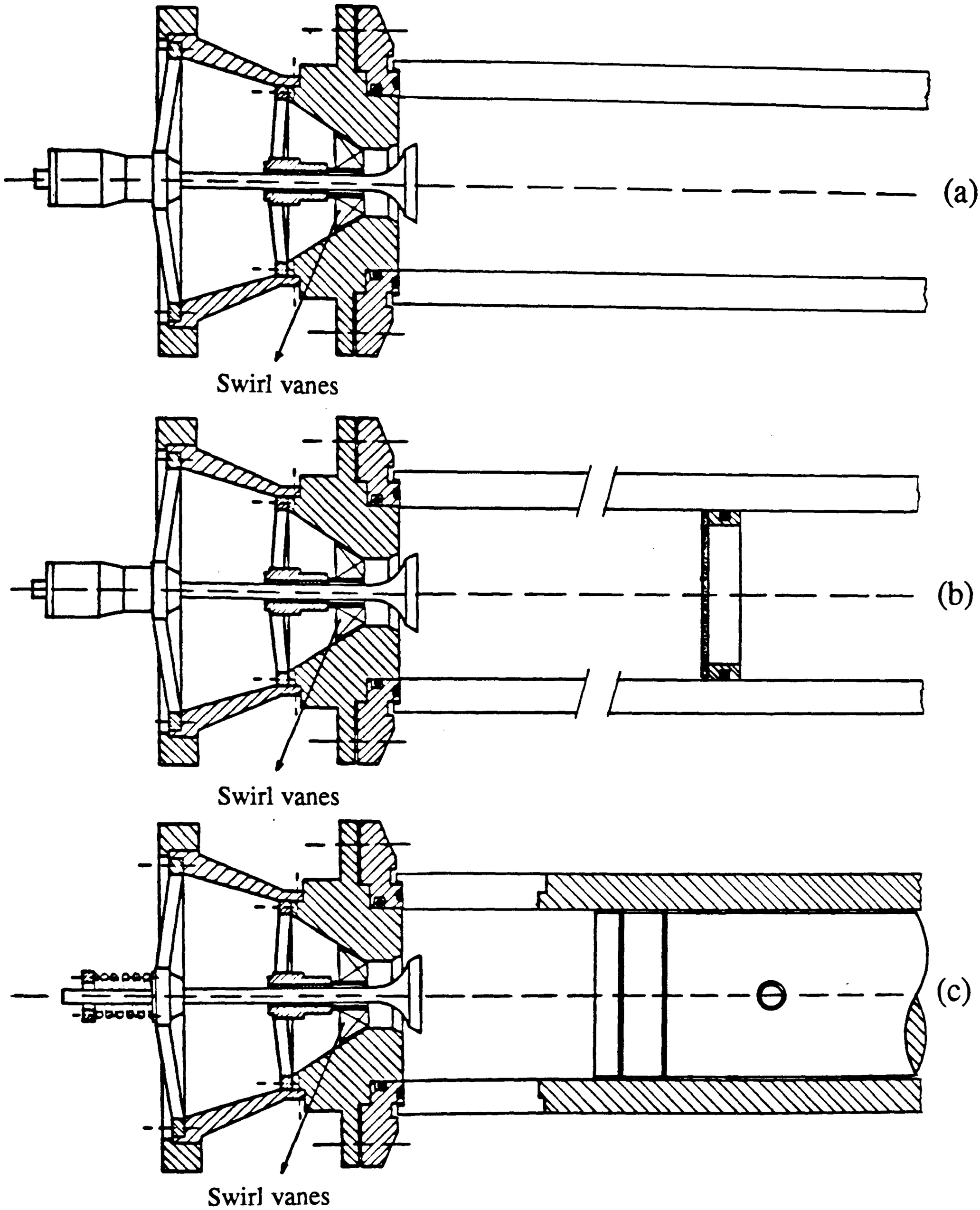


Figure 3.1 Flow configurations (a) steady flow/open ended cylinder (b)steady flow/stationary porous piston (c) model engine.

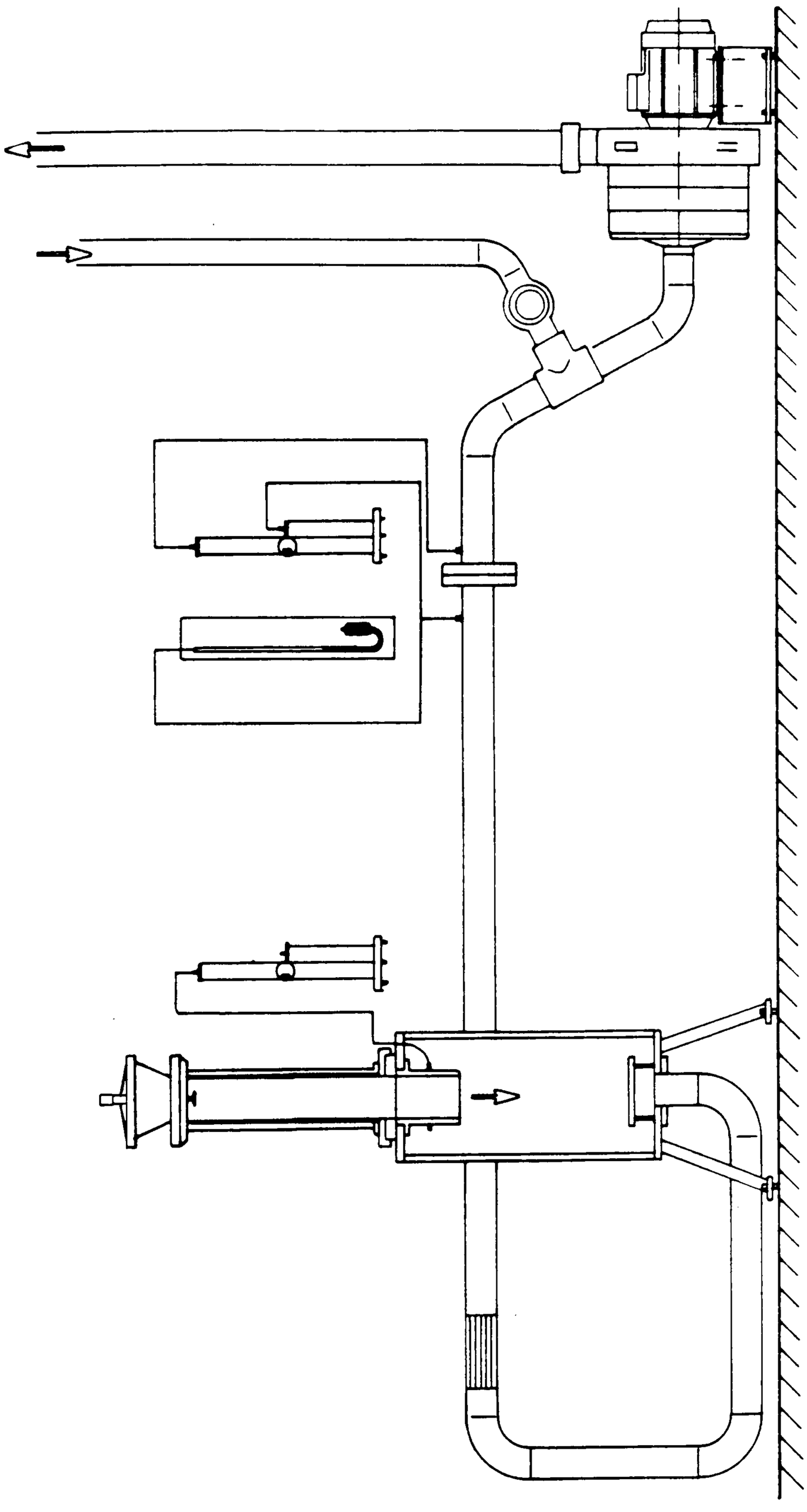


Figure 3.2 Steady flow rig

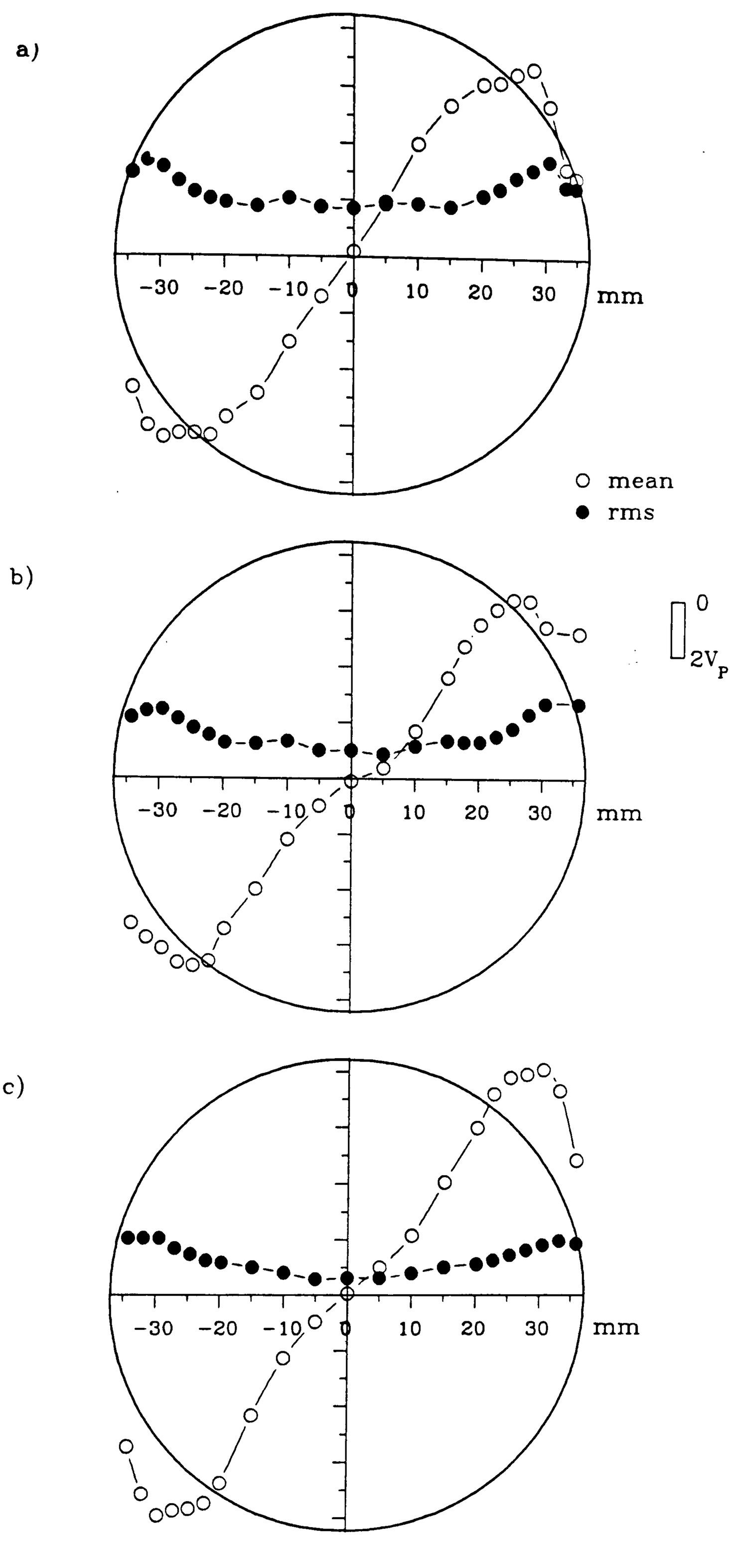
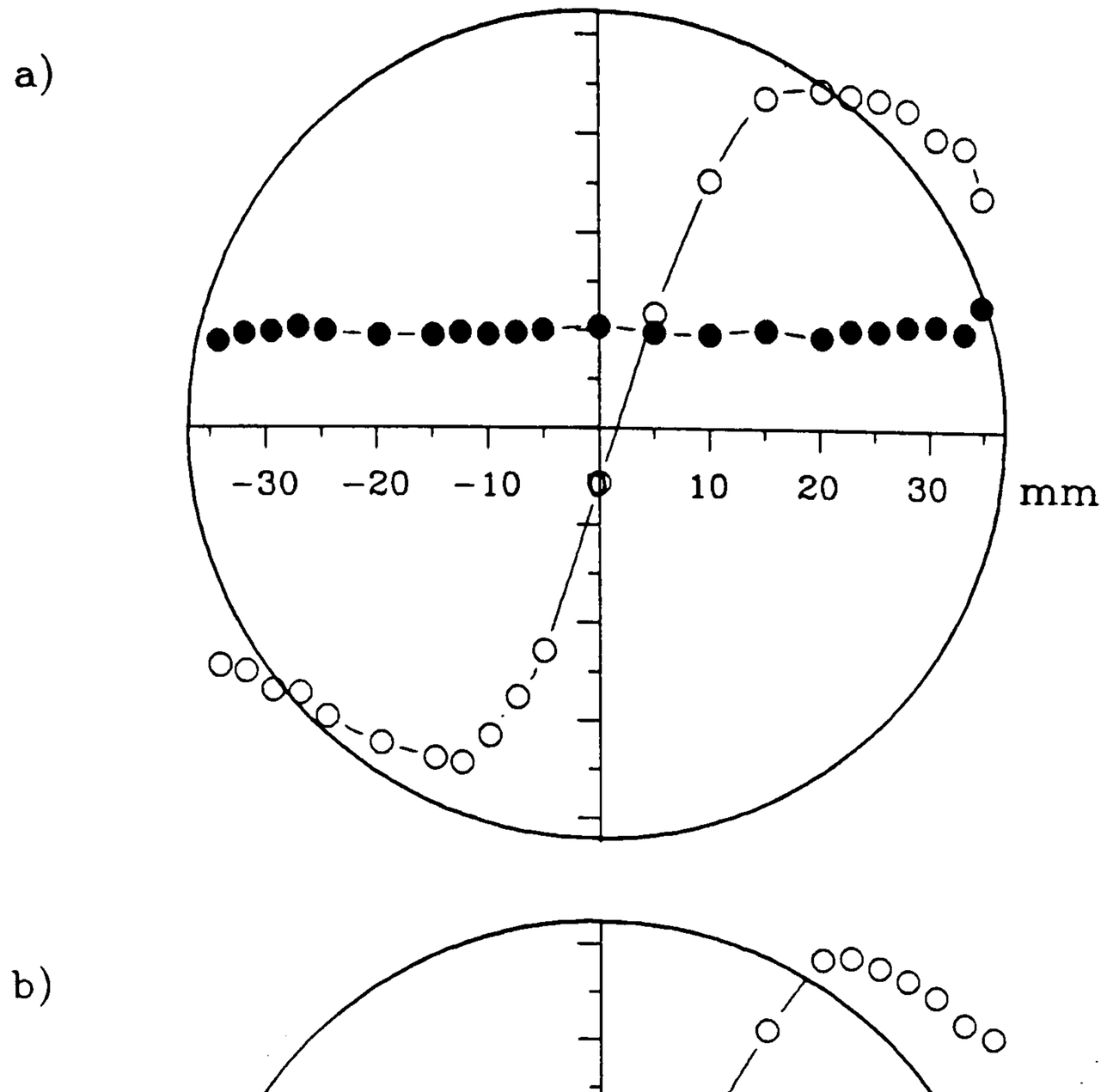
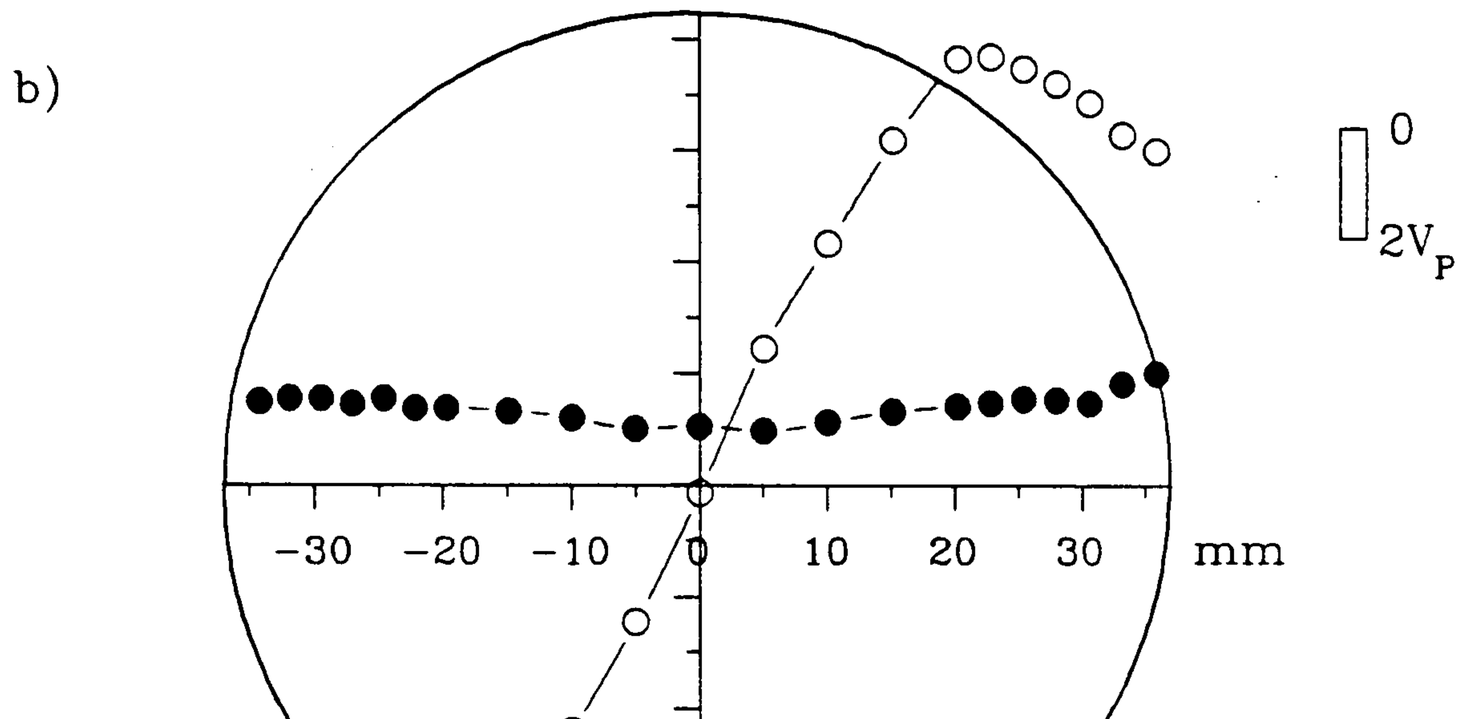


Figure 3.3 Ensemble-averaged swirl velocity profiles, steady flow rig/open-ended cylinder at z=0.5D for valve lifts of (a) 2mm (b) 4mm (c) 8mm.





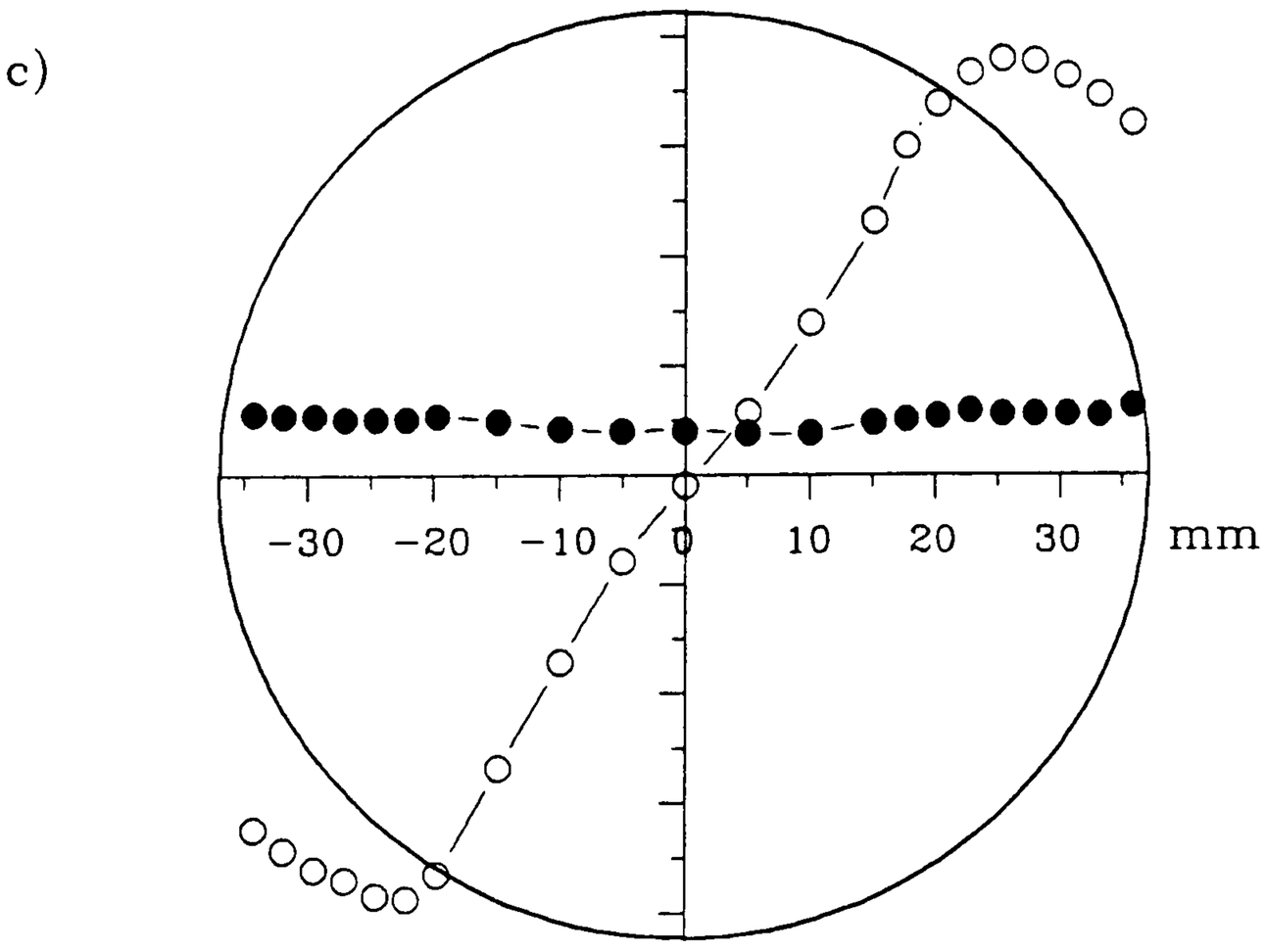


Figure 3.4 Ensemble-averaged swirl velocity profiles, steady flow rig/open-ended cylinder at z=1.0D for valve lifts of (a) 2mm (b) 4mm (c) 8mm.

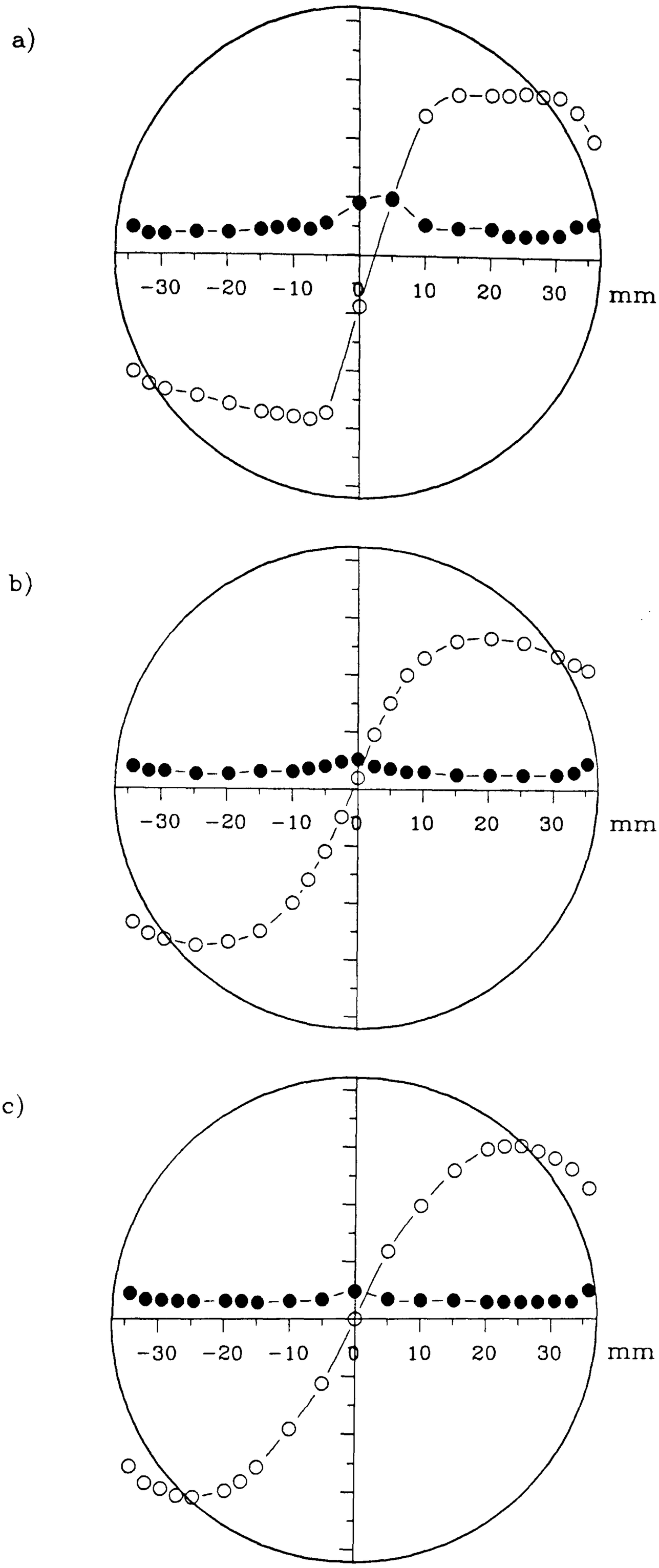


Figure 3.5 Ensemble-averaged swirl velocity profiles, steady flow rig/open-ended cylinder at z=2.0D for valve lifts of (a) 2mm (b) 4mm (c) 8mm.

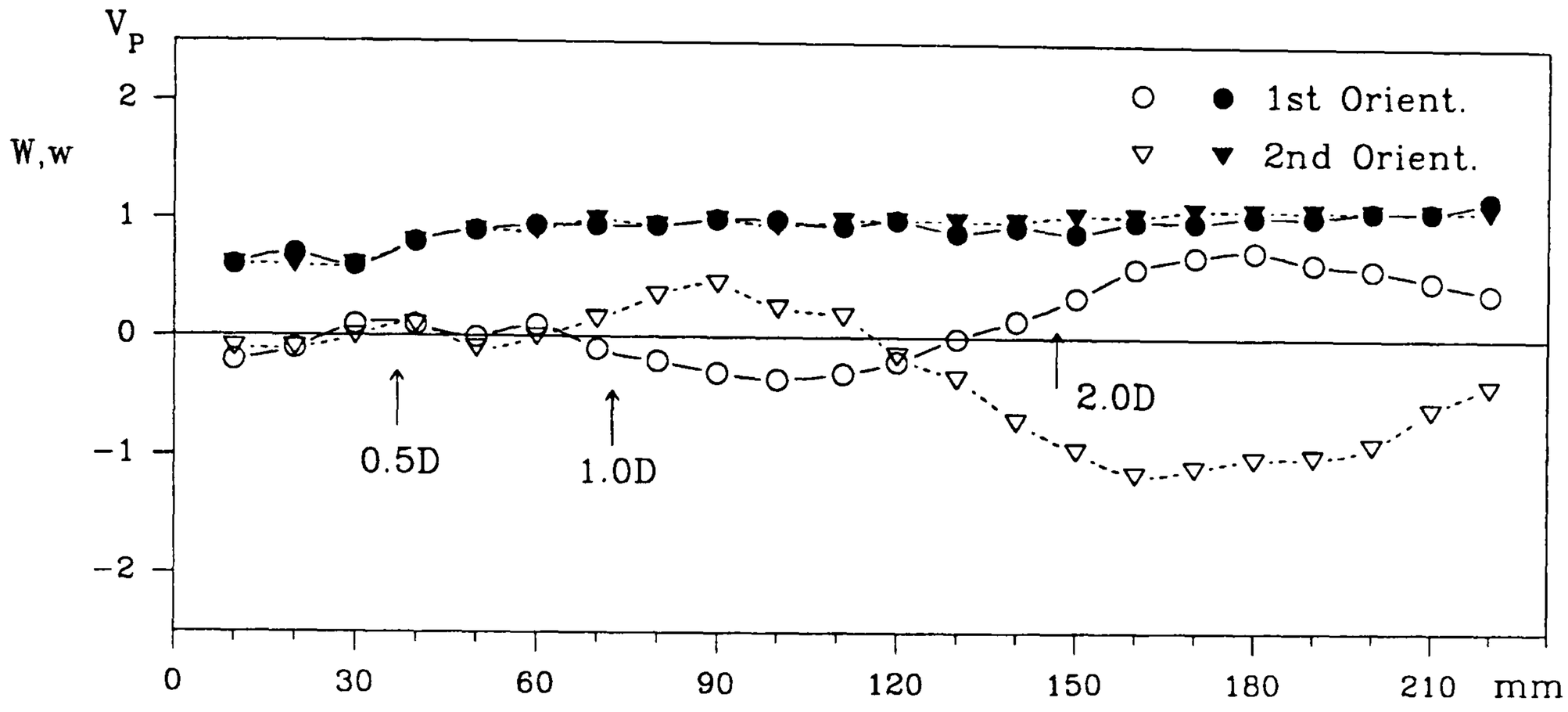


Figure 3.6 Centreline swirl velocity distribution for valve lift of 4mm steady-flow rig/open-ended cylinder (two orientations).

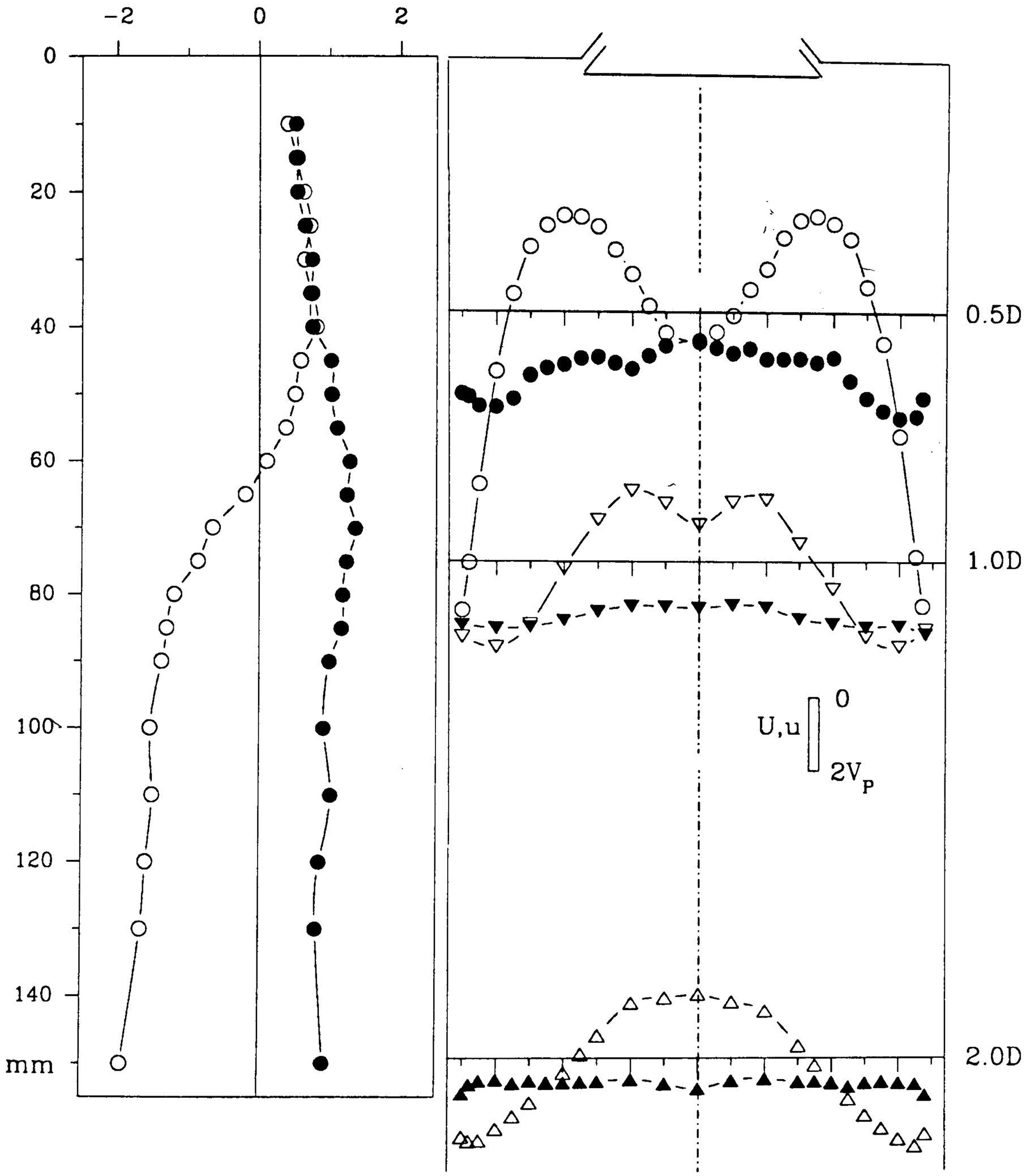


Figure 3.7 (a) Ensemble-averaged axial velocity profiles, steady flow/open ended cylinder at z=0.5D, 1.0D & 2.0D (b) Centreline axial velocity distribution.

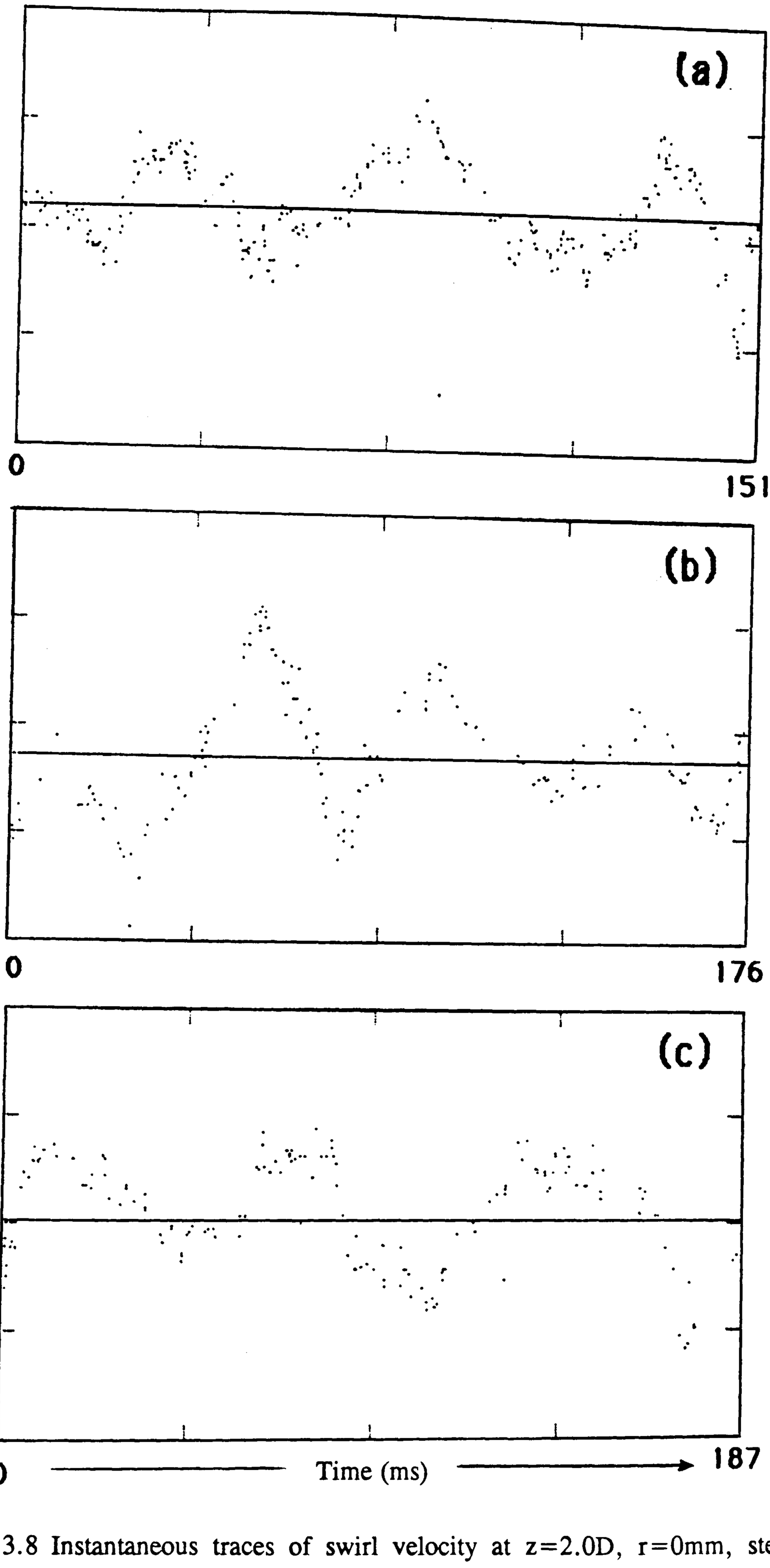
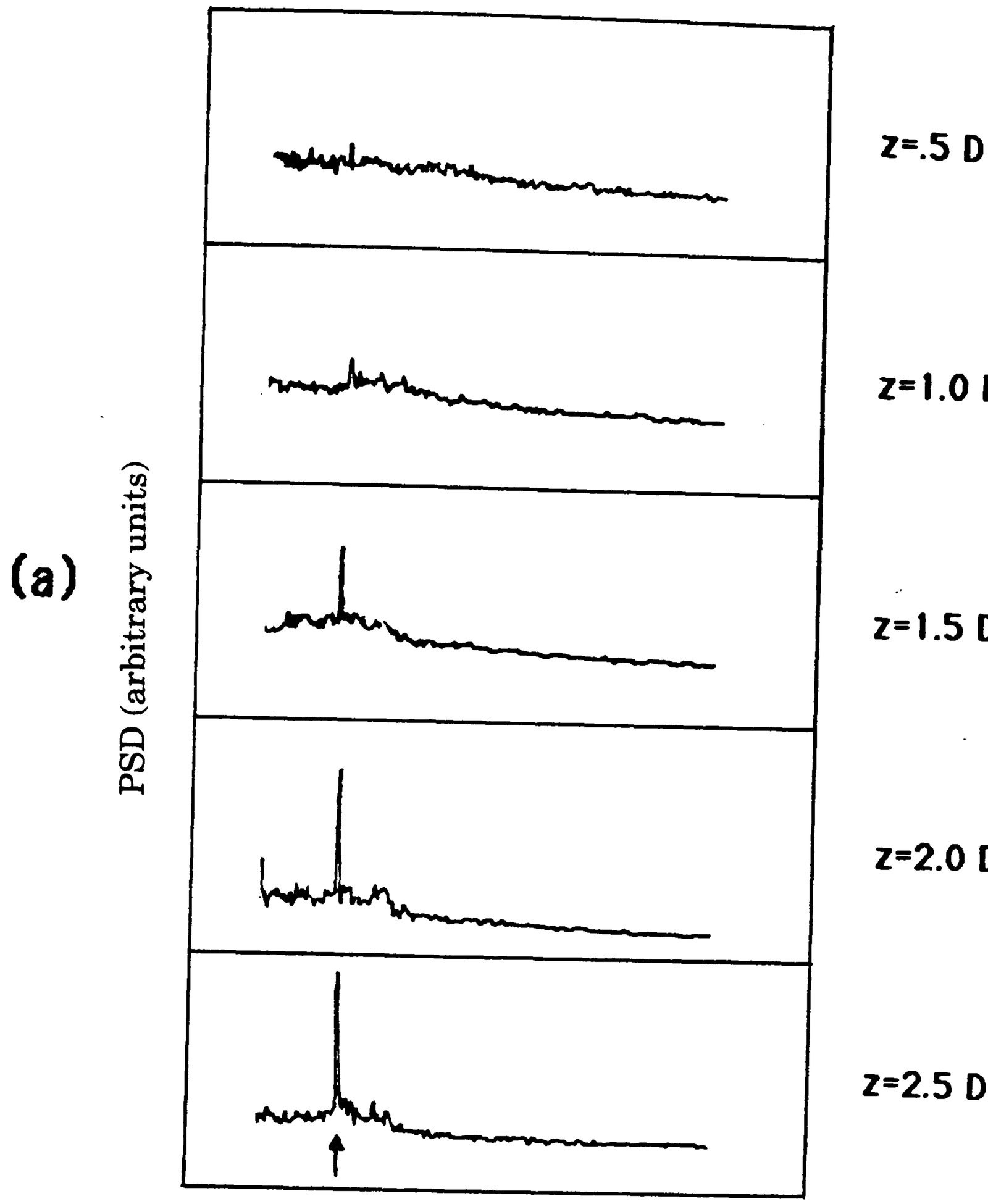


Figure 3.8 Instantaneous traces of swirl velocity at z=2.0D, r=0mm, steady flow rig/open ended cylinder at valve lifts of (a) 2mm (b) 4mm (c) 8mm.



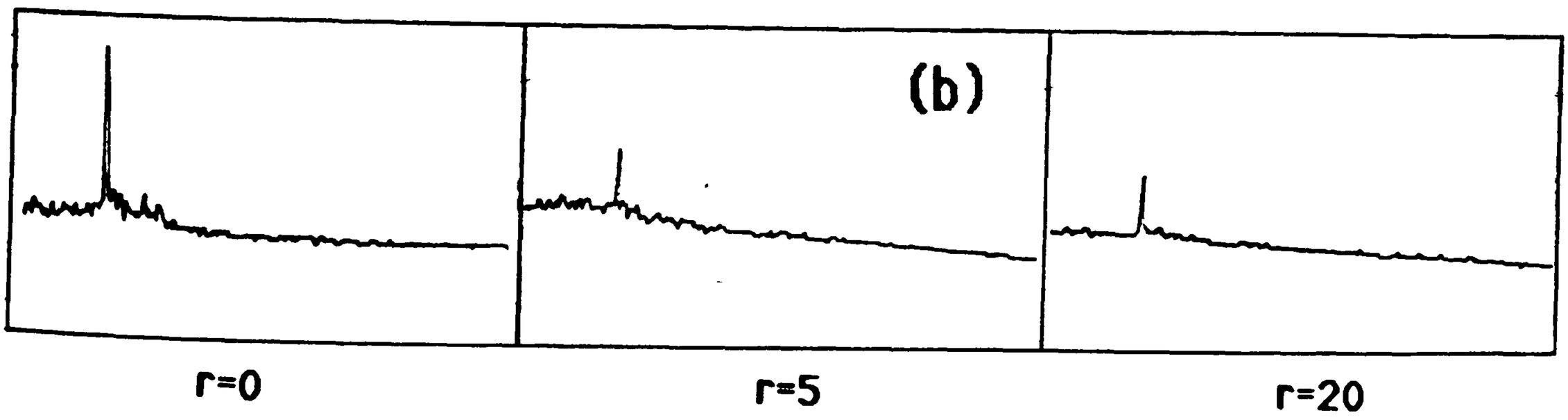


Figure 3.9 Frequency spectra of the instantaneous swirl velocity at various locations, (a) r=0 (b) z=2.5D, steady-flow rig/open ended cylinder.

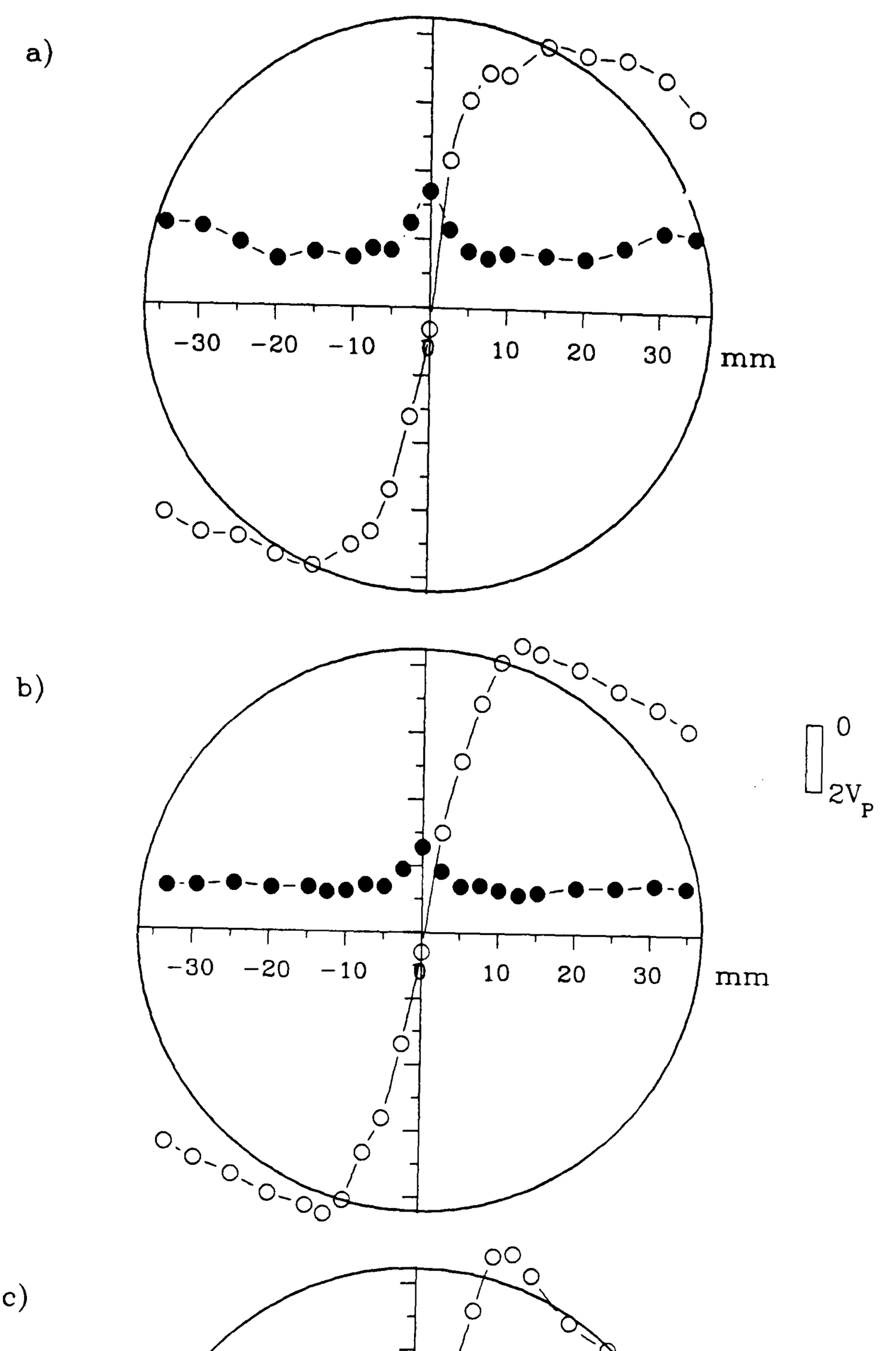


Figure 3.10 Ensemble-averaged swirl velocity profiles, steady flow rig/stationary porous piston at (a) z=0.5D (b) z=1.0D and (c) z=2.0D for valve lift of 4mm.

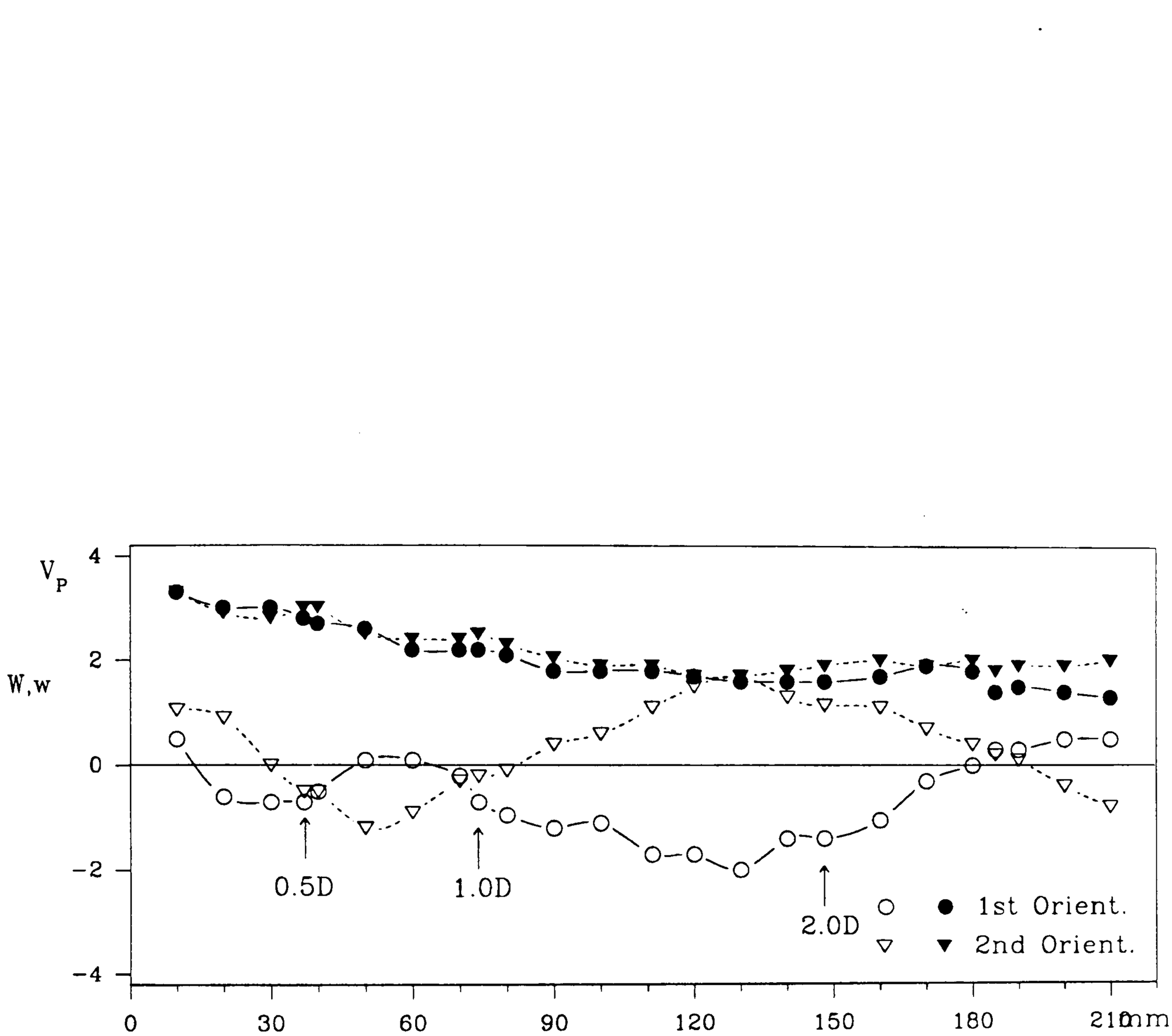


Figure 3.11 Centreline swirl velocity distribution for valve lift of 4mm steady-flow rig/stationary porous piston (two orientations).

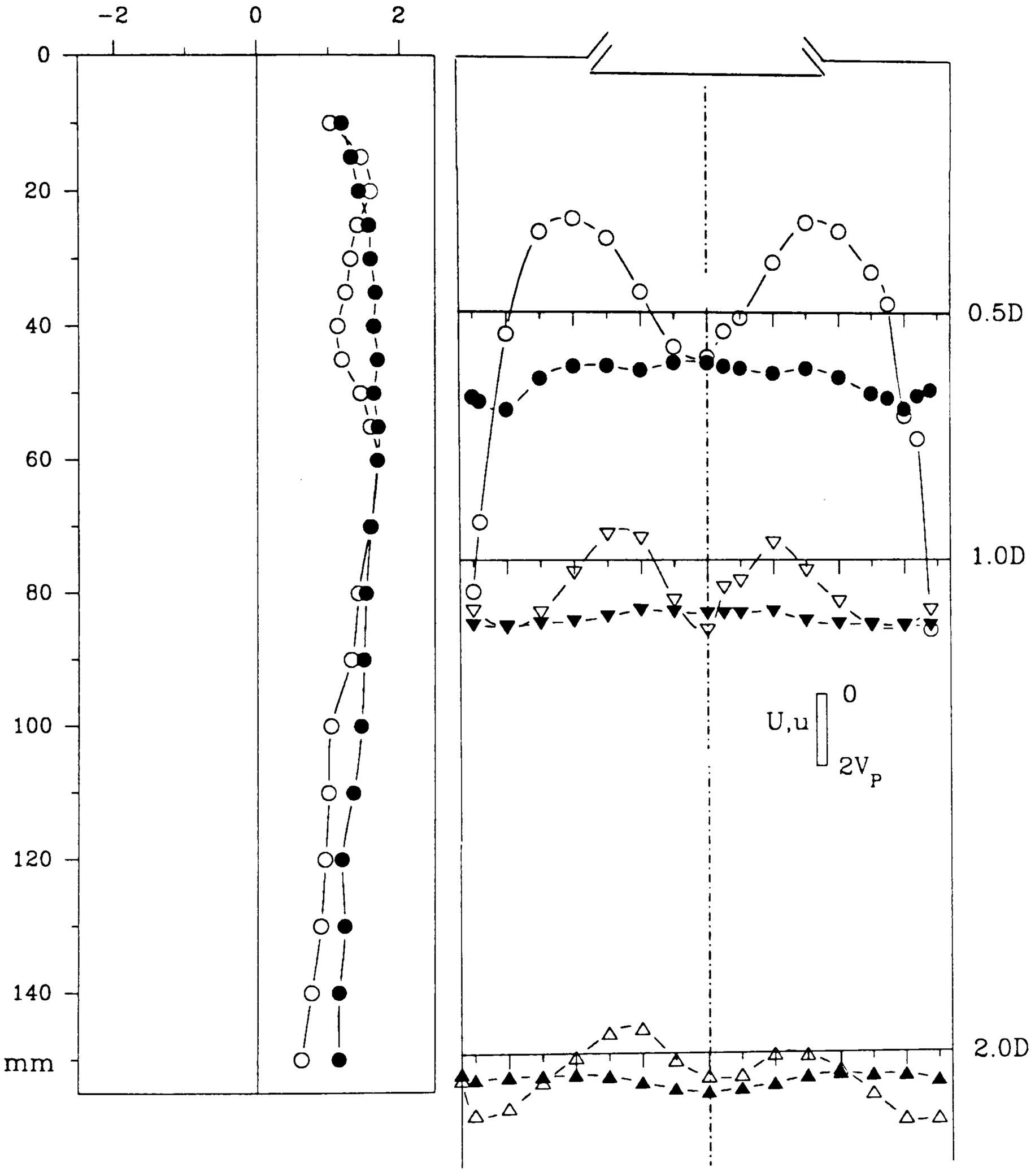


Figure 3.12 .(a) Ensemble-averaged axial velocity profiles, steady flow/stationary porous piston at z=0.5D, 1.0D & 2.0D (b) Centreline axial velocity distribution.

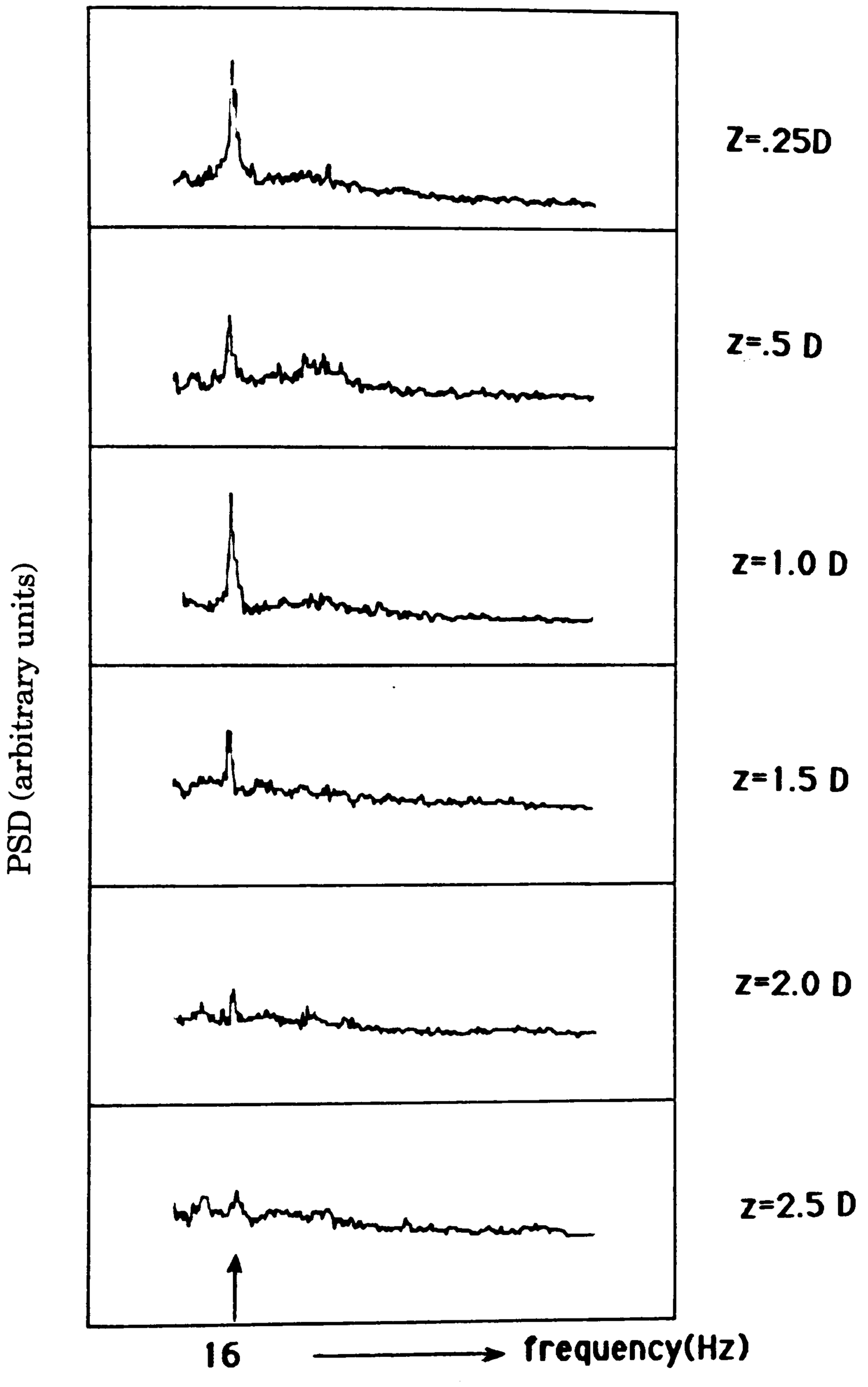


Figure 3.13 Frequency spectra of the instantaneous swirl velocity at various locations, r=0, steady-flow rig/stationary porous piston.

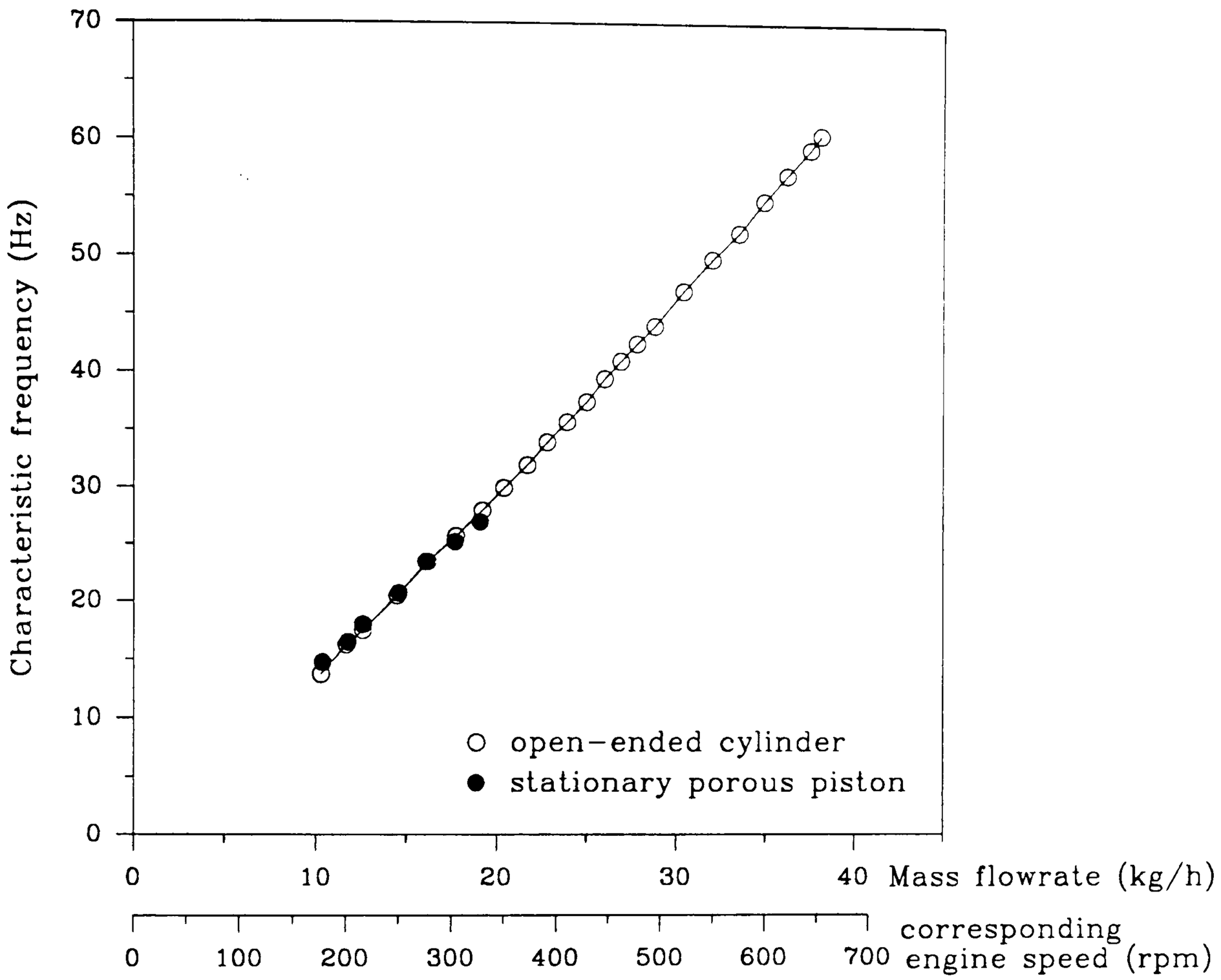


Figure 3.14 Variation of characteristic frequency of swirl centre precession versus air mass flowrate, steady flow.

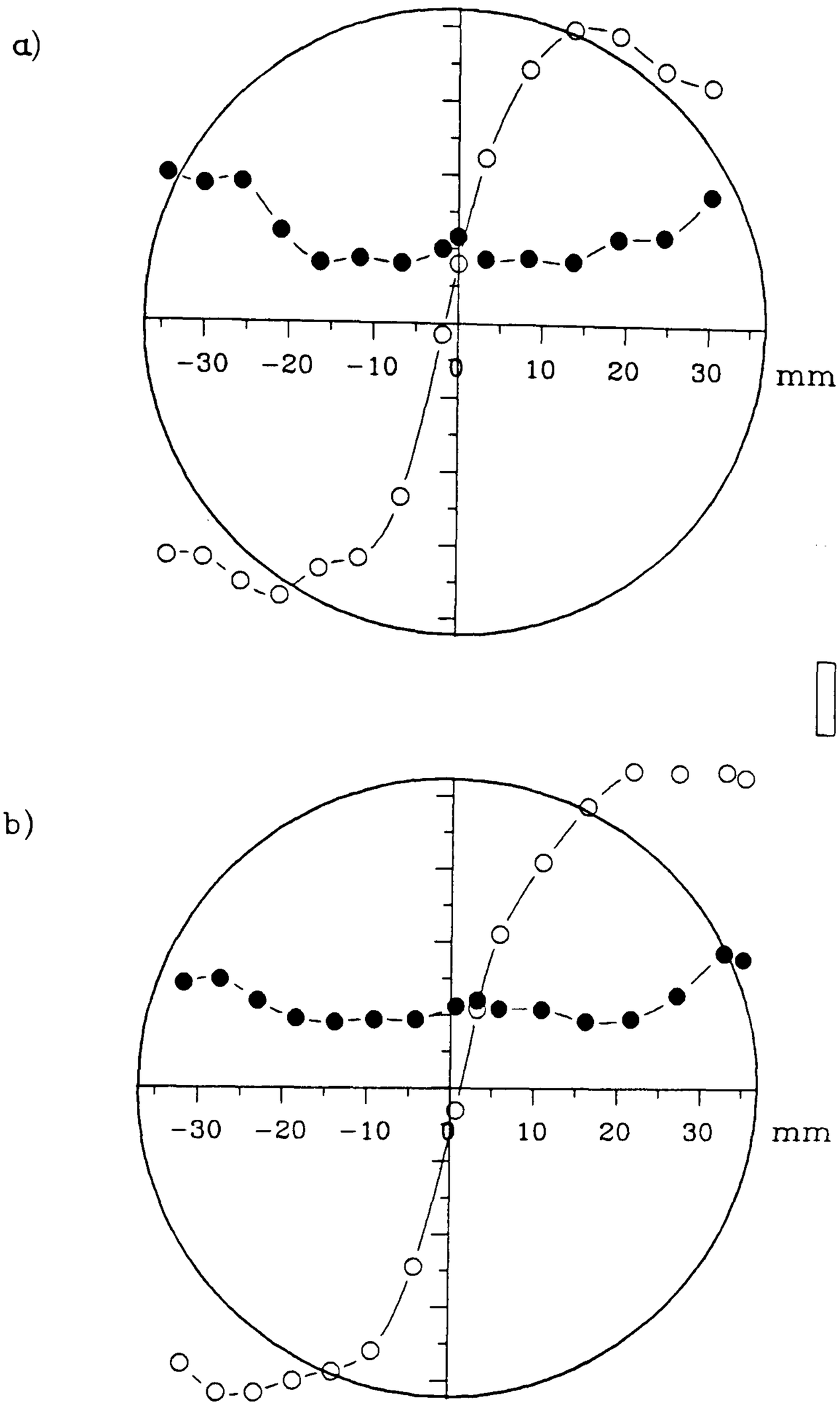


Figure 3.15 Ensemble-averaged swirl velocity profiles, model engine at (a) $\theta=90^{o}$, $z=0.25D$ (b) $\theta=90^{o}$, $z=0.5D$ (c) $\theta=180^{o}$, $z=0.25D$ (d) $\theta=180^{o}$, $z=0.5D$.

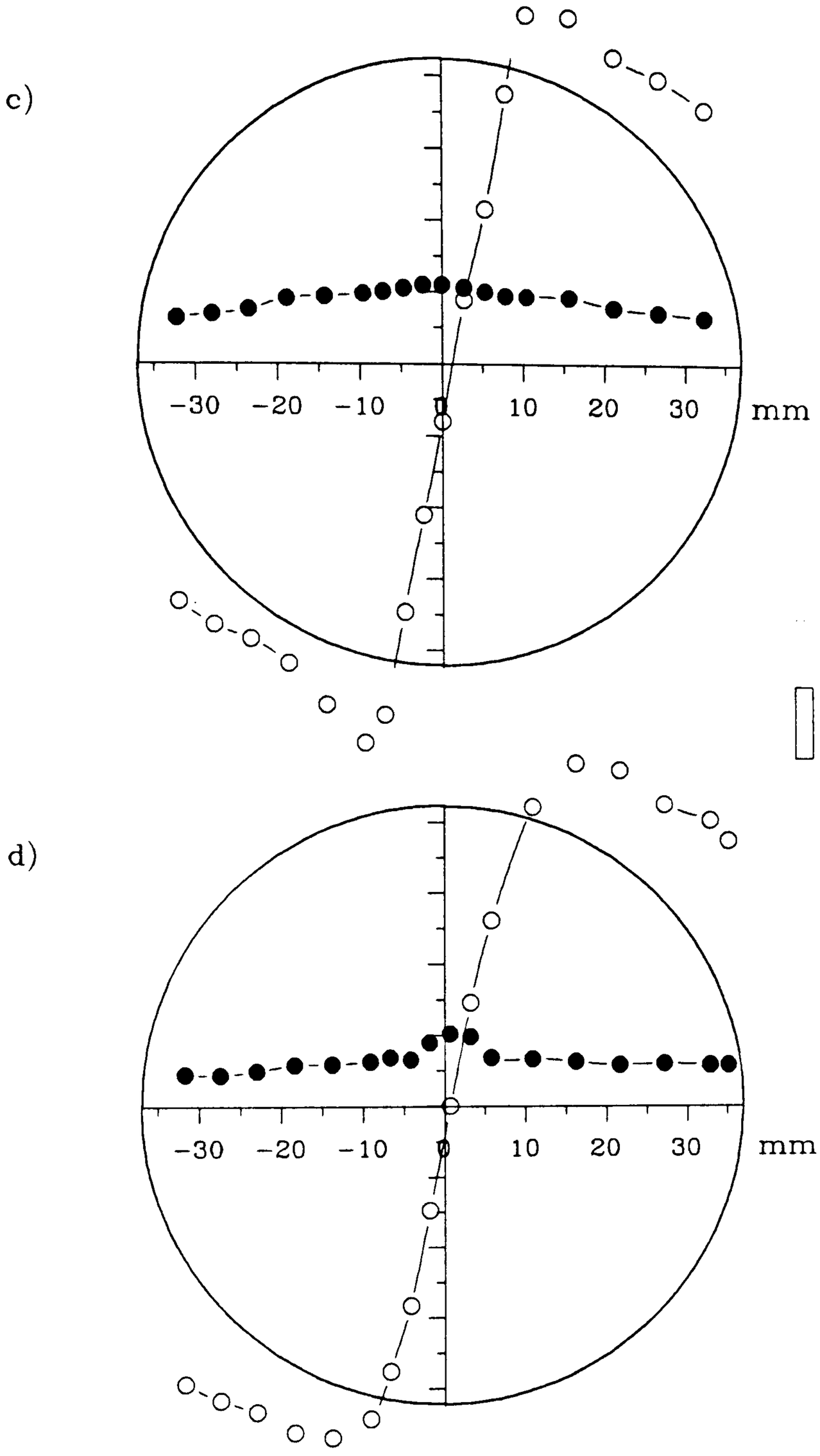


Figure 3.15 Continued

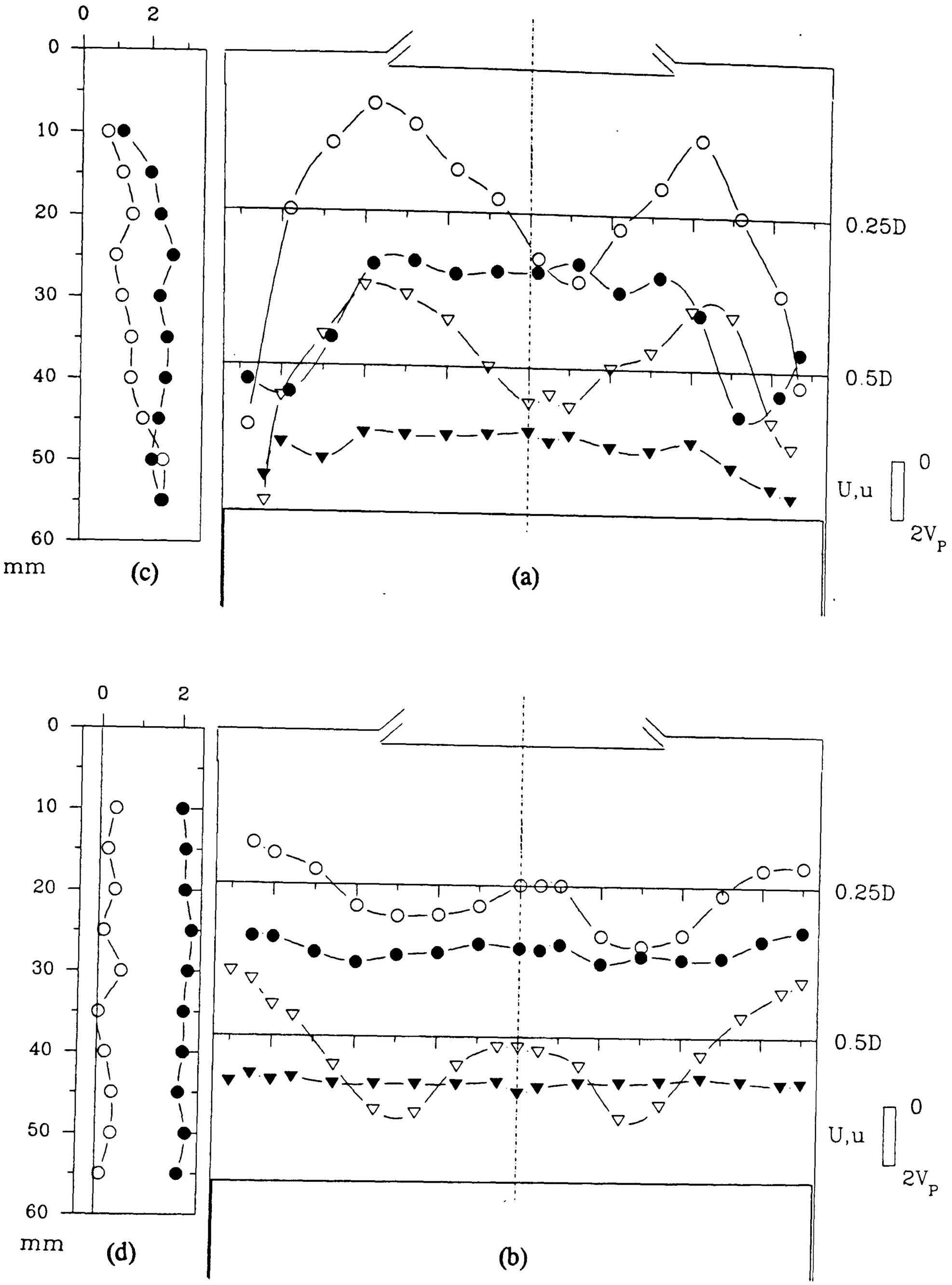


Figure 3.16 Ensemble-averaged axial velocity profiles, model engine at (a) $\theta=90^{o}$, $z=0.25D$ and $z=0.5D$ (b) $\theta=180^{o}$, $z=0.25D$ and $z=0.5D$, and centreline distributions at (c) $\theta=90^{o}$ and (d) $\theta=180^{o}$.

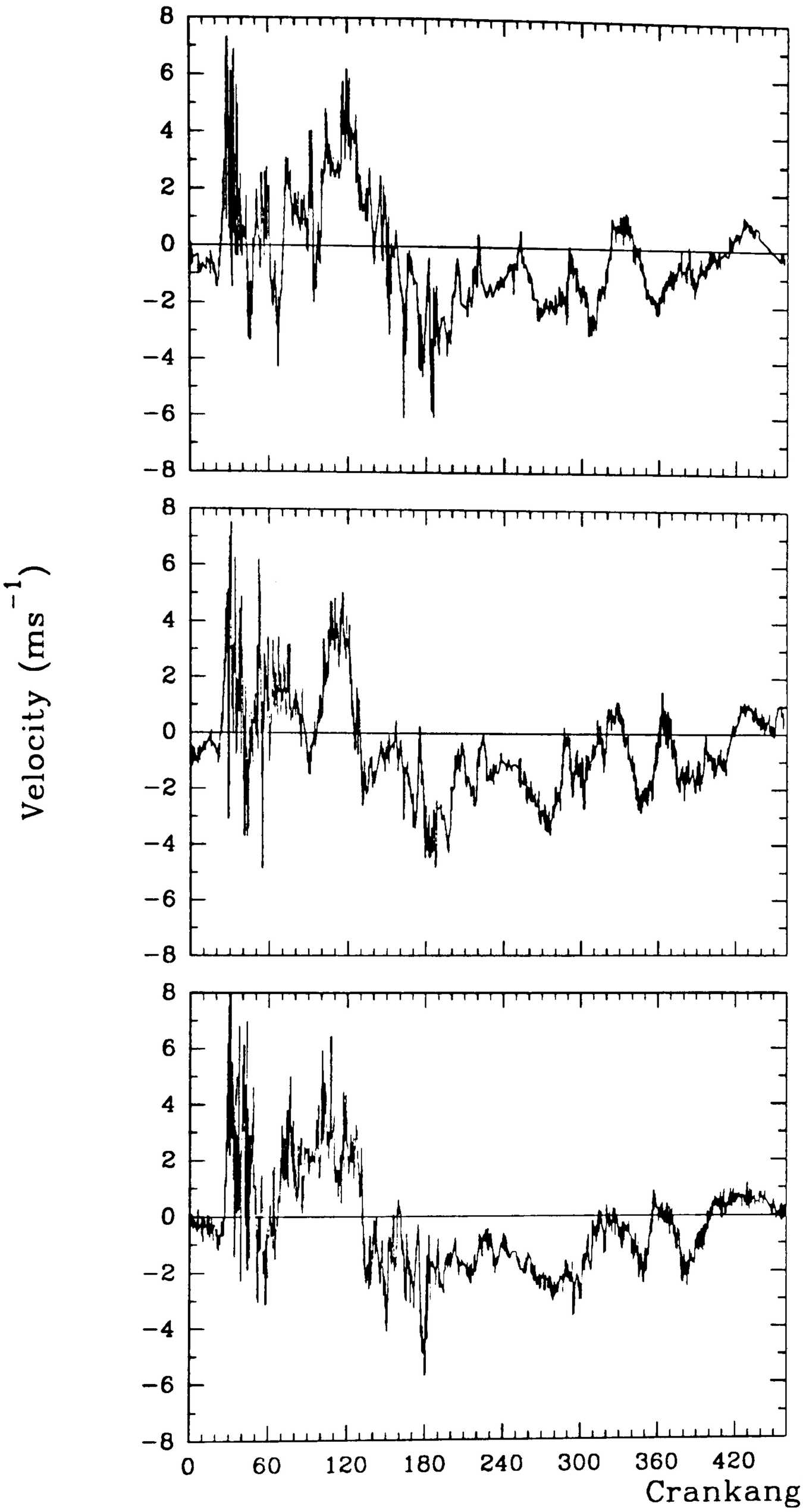


Figure 3.17 Instantaneous traces of swirl velocity at z=0.25D, r=0mm, model engine.

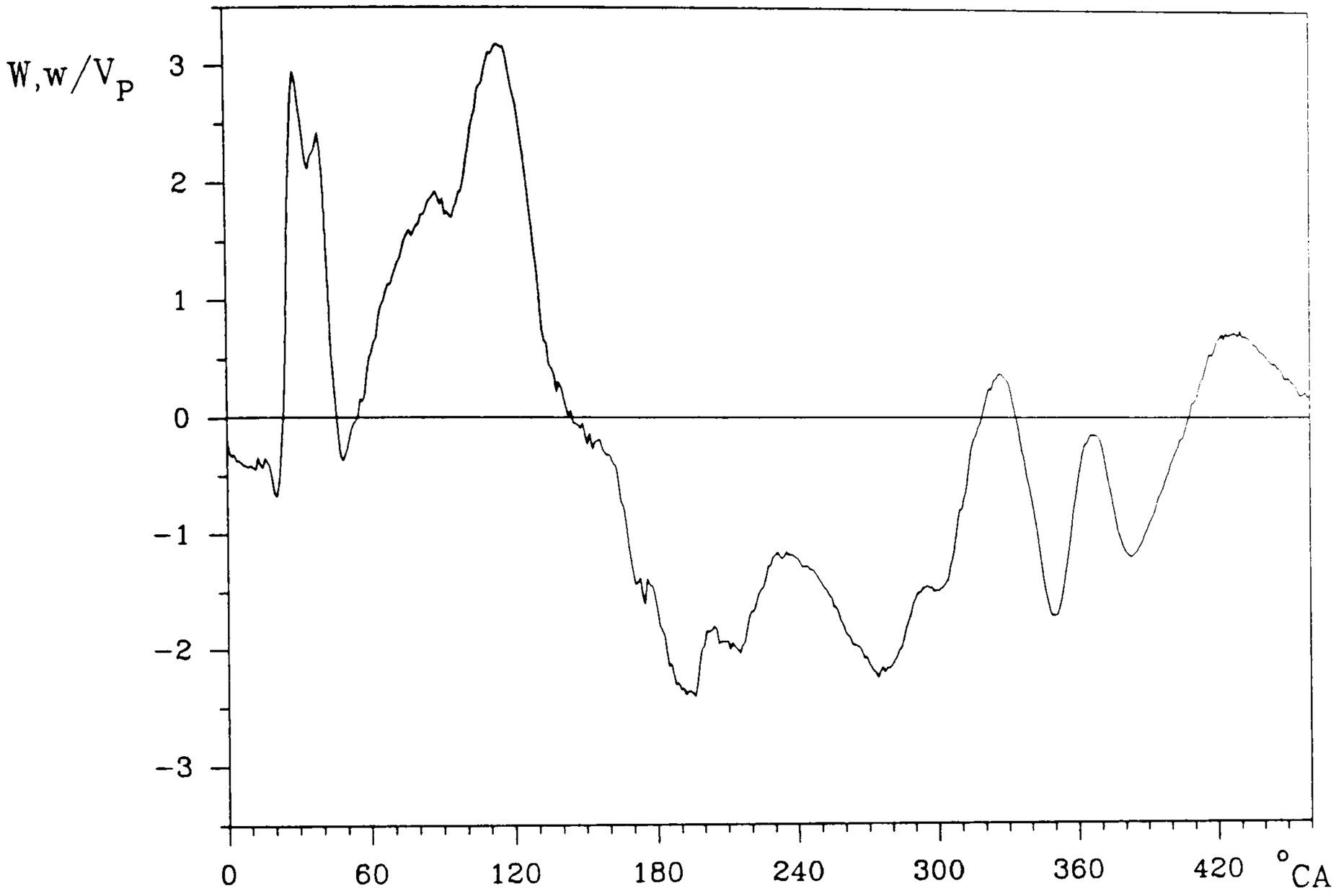
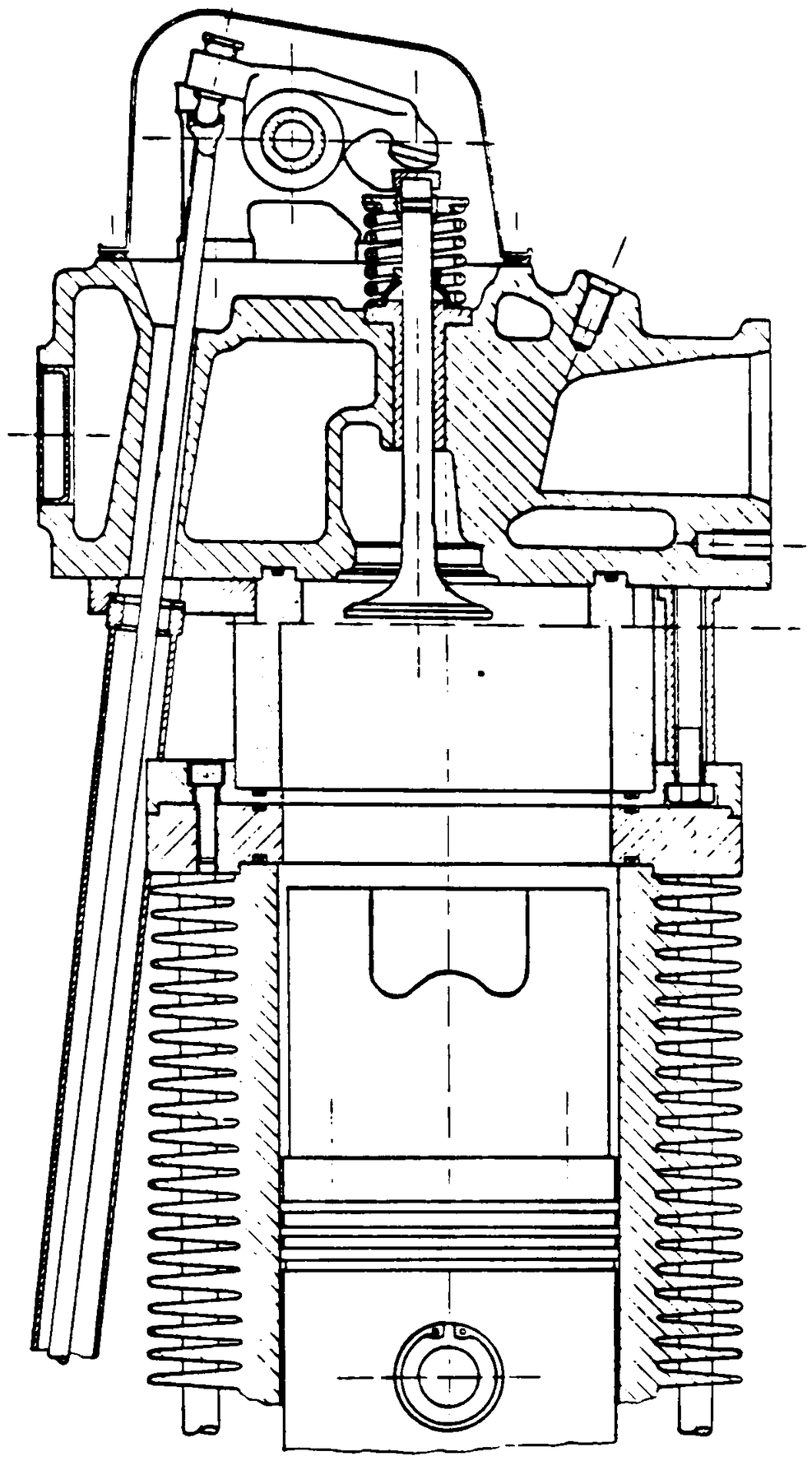


Figure 3.18 Temporal variation of ensemble-averaged mean swirl velocity at z=0.25D, r=0.



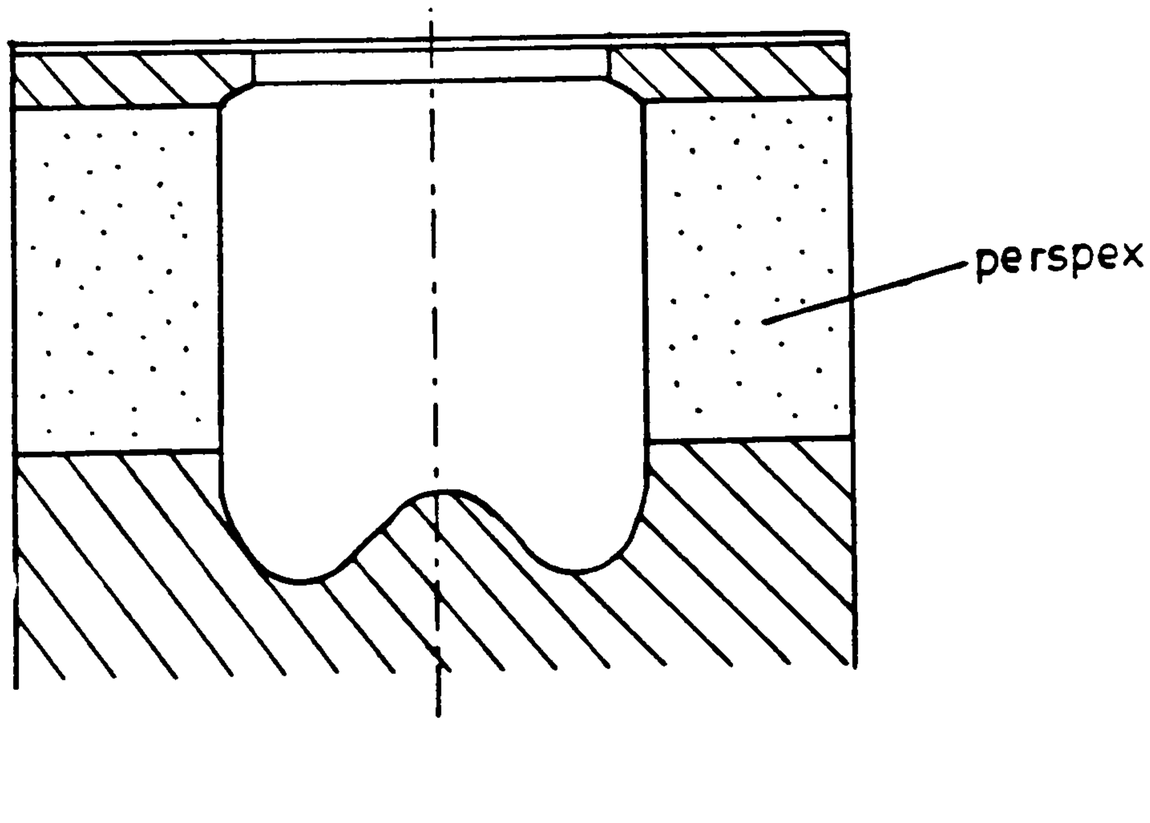


Figure 3.19 Research Diesel engine with detail of the re-entrant extended piston bowl.

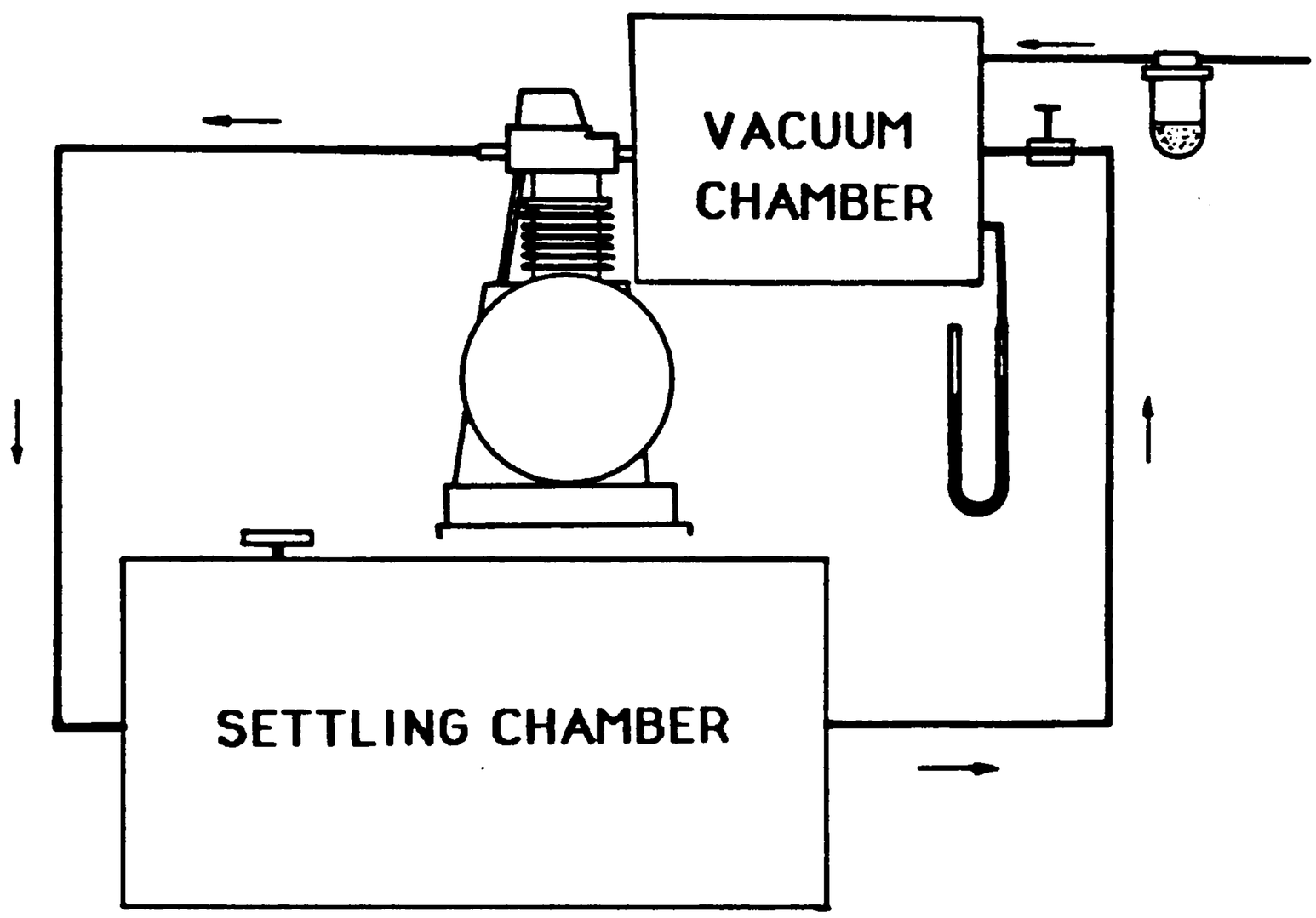


Figure 3.20 Overall view of the experimental rig.

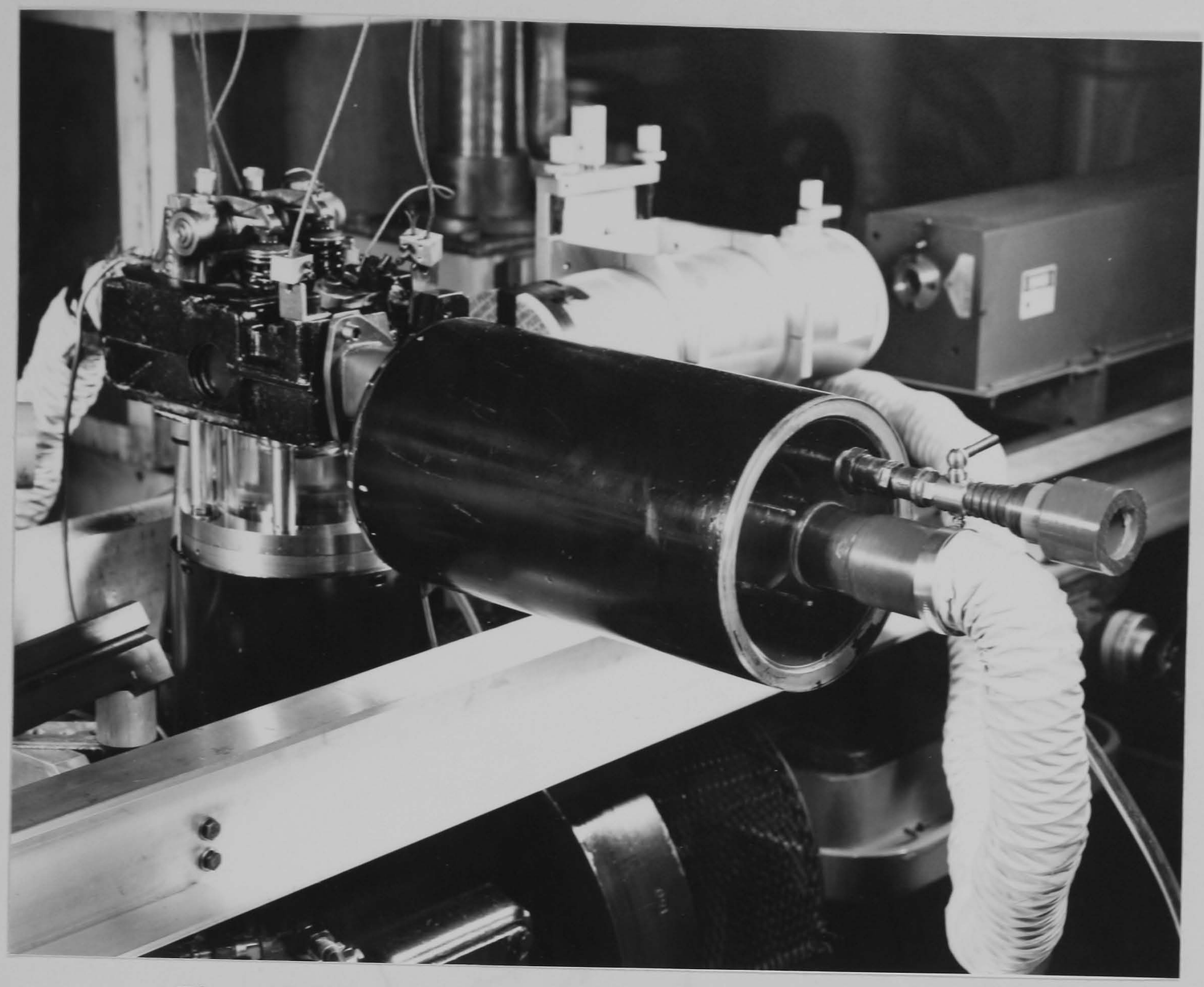


Figure 3.21 Photograph of the idealised manifold.

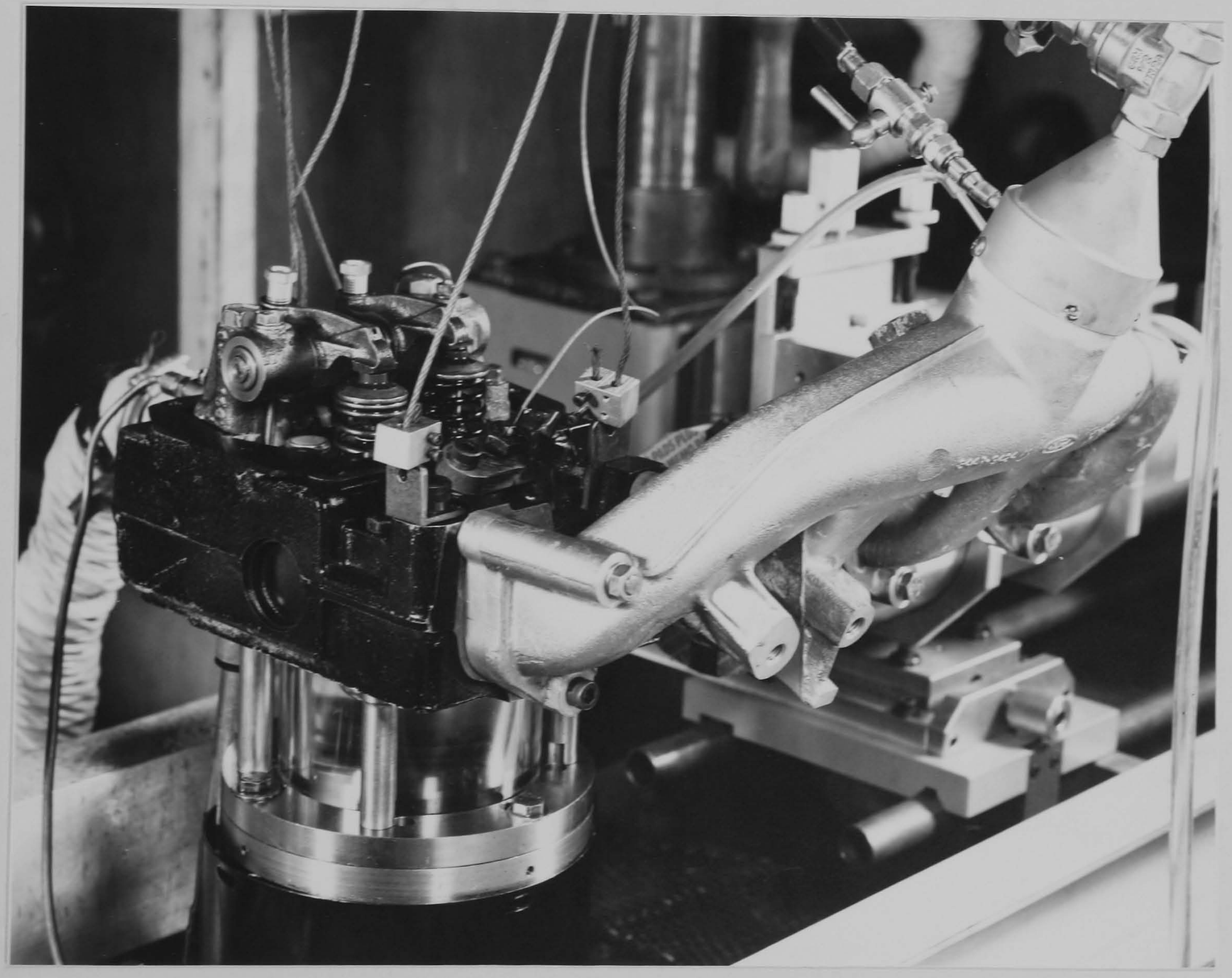


Figure 3.22 Photograph of the Ford manifold.

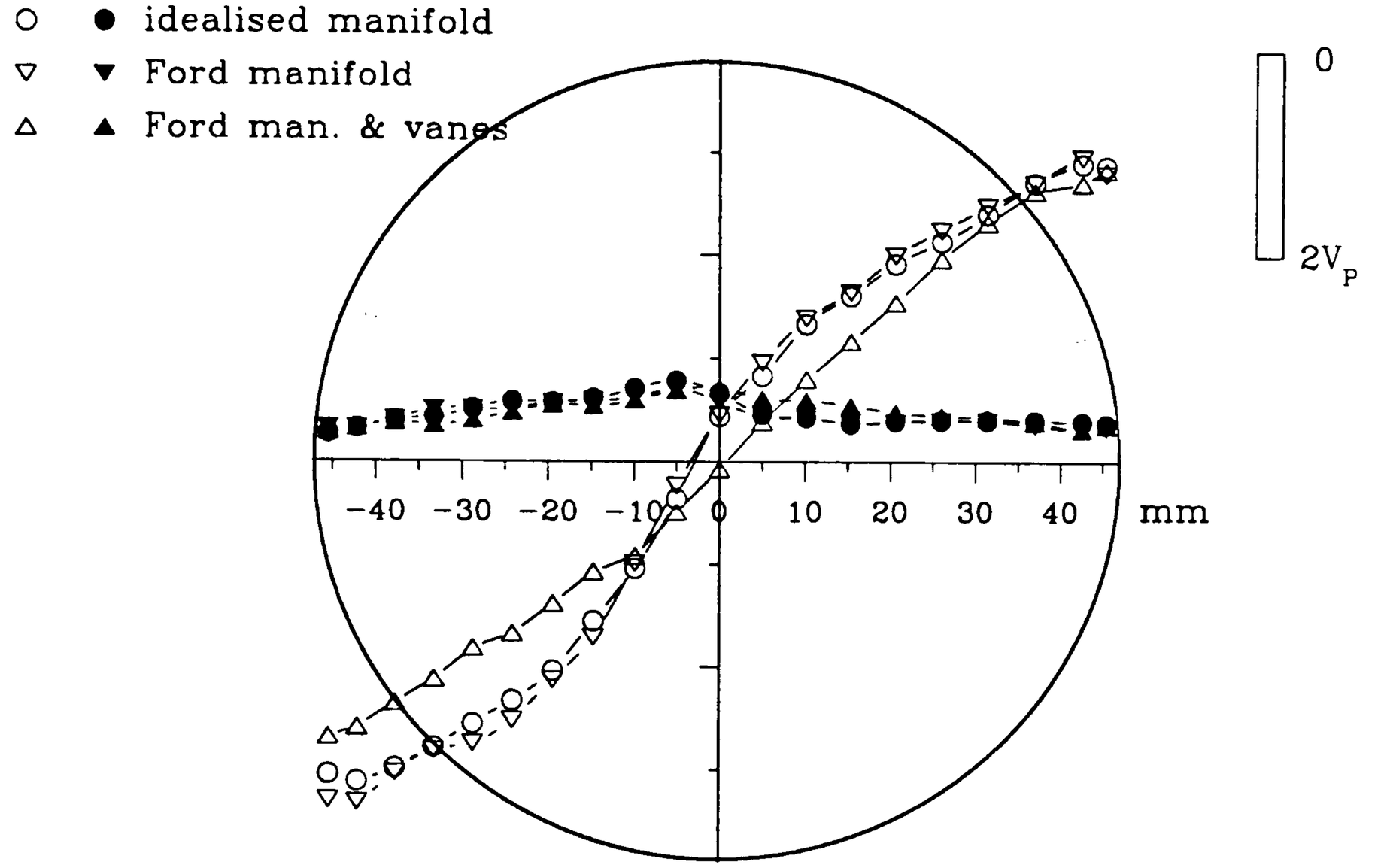


Figure 3.23 Ensemble-averaged swirl velocity profiles along the mid-plane (z=8mm), at TDC, compression ratio of 8, flat piston, with three inlet manifold configurations.

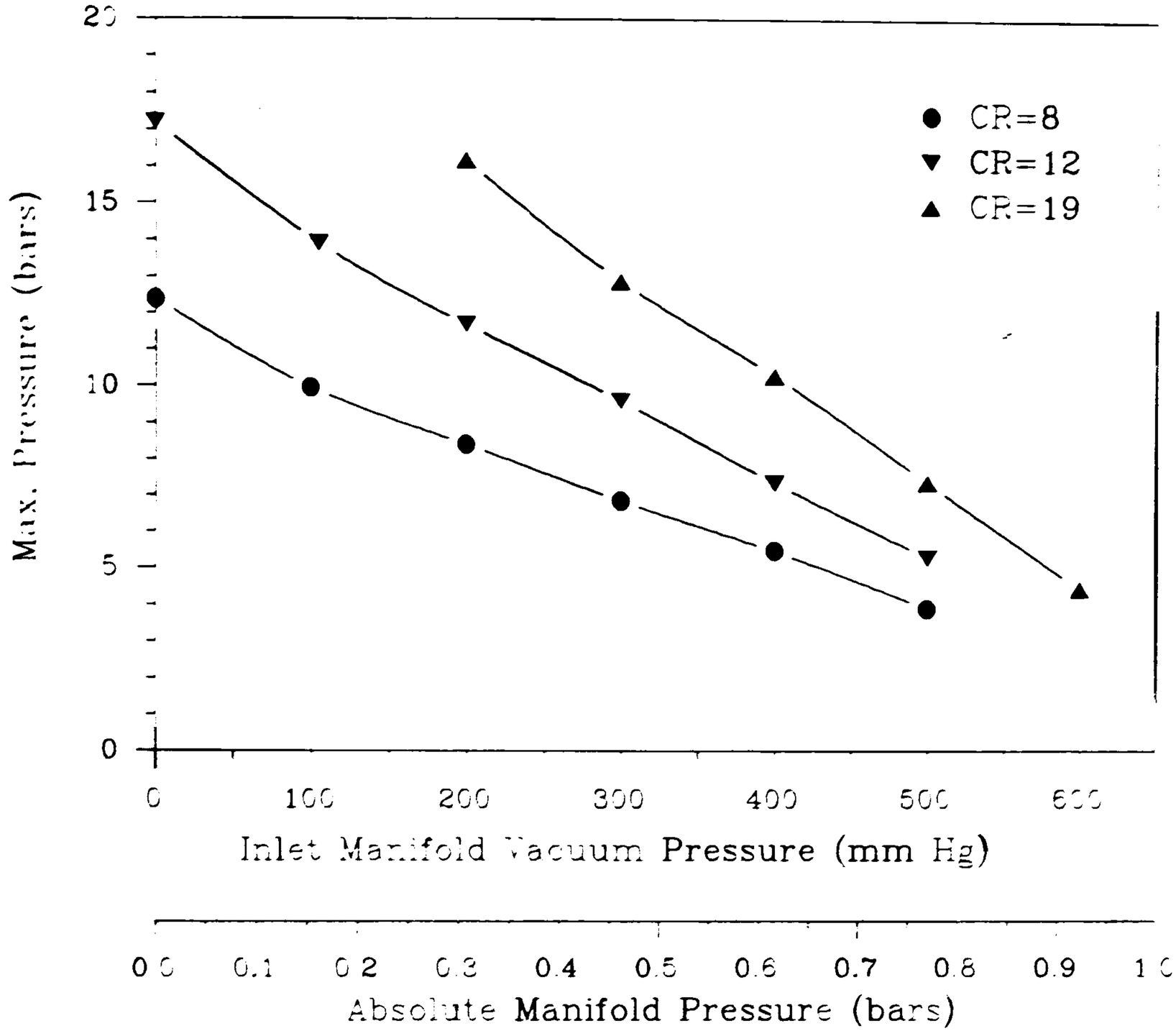


Figure 3.24 Variation of peak cylinder pressure at TDC as a function of degree of throttling

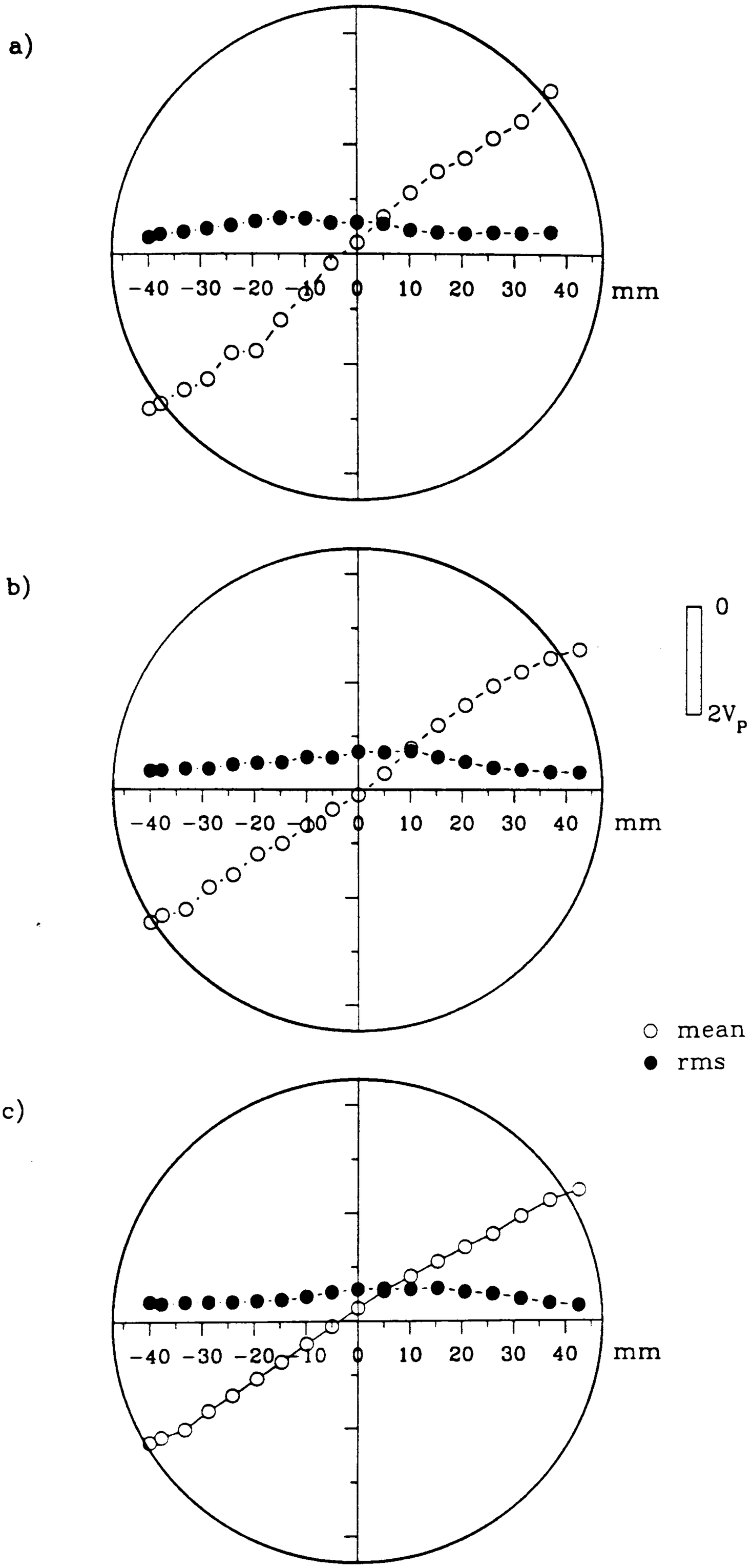


Figure 3.25 Ensemble-averaged swirl velocity profiles along the mid-plane (z=8mm), at TDC, compression ratio of 8, flat piston (a) unthrottled intake (b) partially throttled $\Delta P = 100$mmHg (c) partially throttled $\Delta P = 300$mmHg.

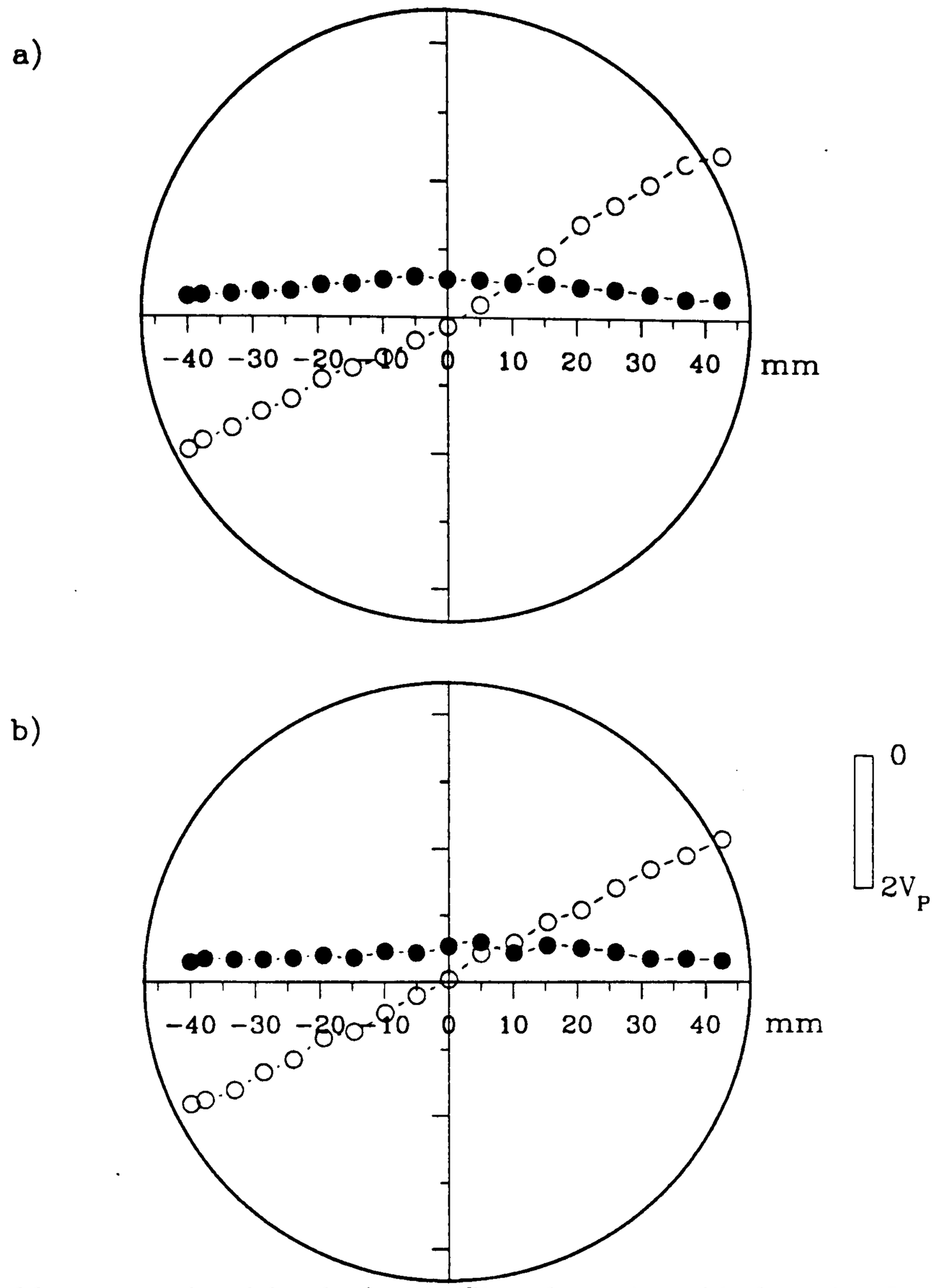


Figure 3.26 Ensemble-averaged swirl velocity profiles along the mid-plane (z=5mm), at TDC, compression ratio of 12, flat piston (a) partially throttled intake ΔP=200mmHg (b) partially throttled ΔP=400mmHg.

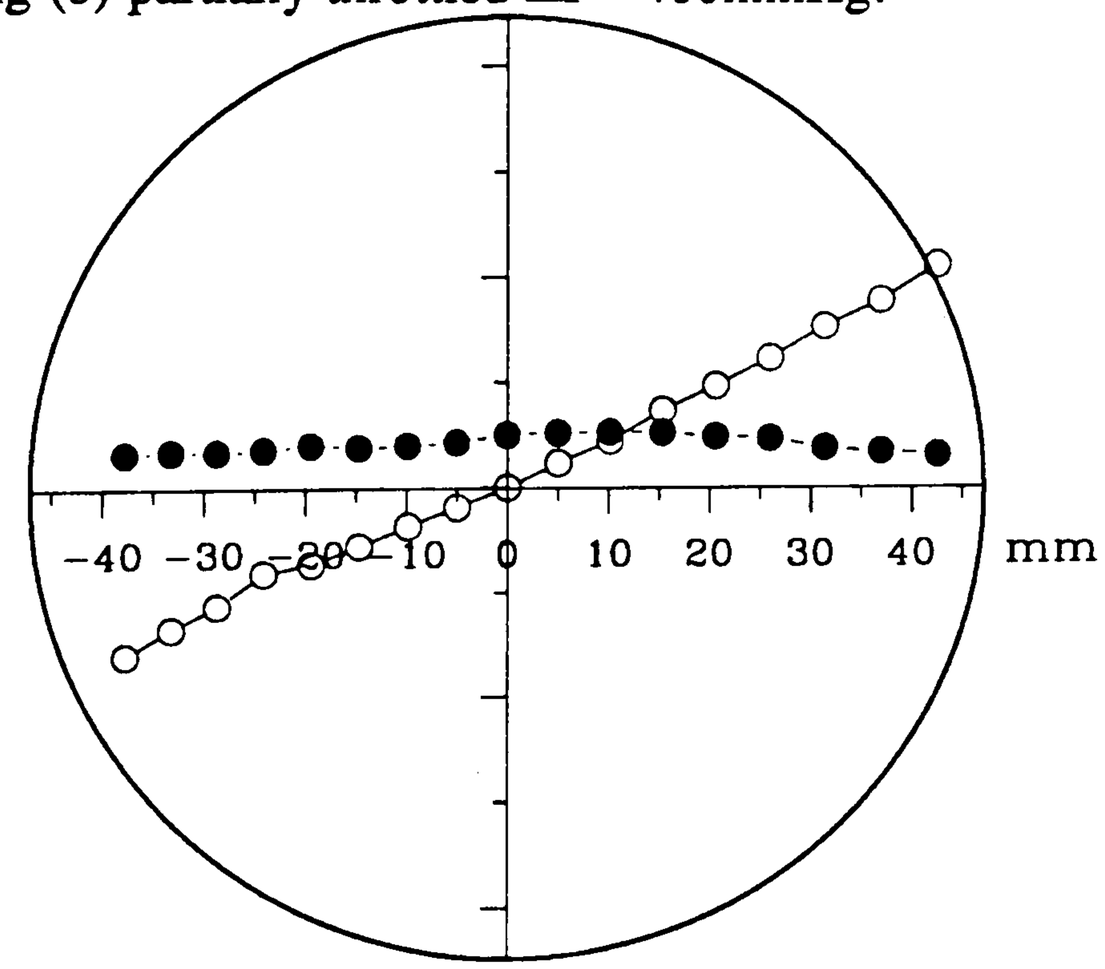


Figure 3.27 Ensemble-averaged swirl velocity profiles along the mid-plane (z=3mm), at TDC, compression ratio of 19, flat piston, partially throttled intake ΔP=350mmHg.

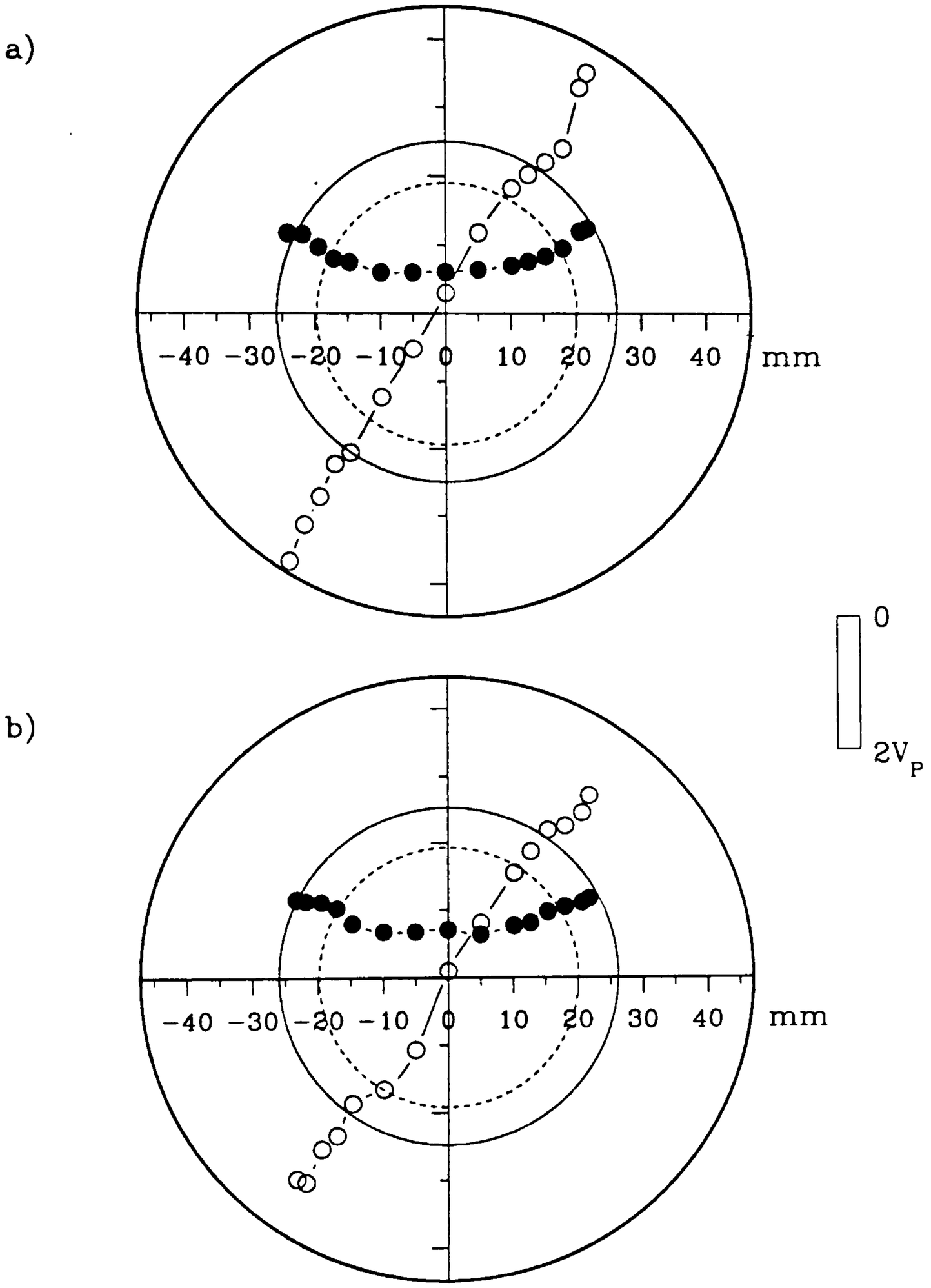


Figure 3.28 Ensemble-averaged swirl velocity profiles at TDC, z=10mm, in the re-entrant piston-bowl at compression ratio of 8.5, unthrottled and partially throttled intake ΔP=400mmHg

CHAPTER 4

FLOW AND COMBUSTION IN A HIGH-SPEED DI DIESEL ENGINE

4.1 INTRODUCTION

This chapter describes the investigation of the flow, spray and combustion in a Hydra DI diesel engine by means of the complementary experimental techniques described in Chapter 2. The main objectives are to establish links between the pre-combustion and combustion flow and, at the same time, between single-cylinder optical research engines and multi-cylinder production engines of similar combustion geometry and to provide data for validating multi-dimensional computer codes.

The Hydra research engine was designed to have geometrical characteristics identical to that of the production 4-cylinder HSDI diesel engine (Ford York 2.5L), mentioned in section 3.3, combined with the ability to vary the swirl levels by means of a mechanism placed inside the inlet port. Contrary to the other research engines employed in this study, the modifications necessary to obtain optical access under both motoring and firing operation did not affect the main operating variables of the engine, i.e. compression ratio and range of engine speed. The fuel injection system was electronically controlled to allow variability of the injection timing characteristics.

The motored studies focused on the effect of engine speed and swirl level on the in-cylinder flow during the induction and mainly compression stroke by means of laser Doppler velocimetry. This same method complemented by laser beam deflection were used to characterise the injection system under non-firing conditions, while the initiation and evolution of the compression-ignition combustion were studied by means of high speed photography combined with standard experimental techniques.

The particular features of the research engine are described in section 4.2 which is followed by a brief presentation of the steady flow tests performed to characterise the induction system. Section 4.4 presents the

results from the motored studies while the performance of the injection system is assessed in section 4.5. The next two sections are concerned with the firing tests, followed by a summary of the main findings in section 4.8.

4.2 HYDRA TEST-BED FACILITY

The single cylinder research engine is a Hydra (serial No.45) manufactured by Ricardo as a versatile and flexible tool for internal combustion engine research. The code name 'Hydra' derives from the large number of alternative cylinder heads, which can be fitted on the same base assembly (French, 1983). The standard Hydra engine is an evolution of the original Ricardo E6 research engine whereas the Imperial College Hydra is based on the Ford York 2.5L DI diesel and incorporates additional features such as a variable swirl port and a Lucas unit fuel injector. In the next four sections the characteristics of the standard Hydra test-bed facility are briefly presented, together with a detailed description of the No 45 Hydra engine.

4.2.1 Base frame assembly

The Hydra engine is mounted on a 450Kg cast iron block, which is attached by four rubber mountings to a rigid welded base frame. The weight of the block was selected to reduce the vertical vibrations to levels insignificant for LDV measurements. The whole system was also designed to minimise the transmission of engine excited vibrations to the floor. The remaining part of the frame is occupied by the cooling module and the dynamometer assembly (Fig.4.1).

The cooling module, which is bolted on the frame behind the engine, is an assembly consisting of three separate circuits: the lubricating oil, the coolant and the water circuit. The main parts of this module are:

a. Oil and coolant circulating pumps.
b. Coolant assembly with integral oil filter and heat exchangers for oil and coolant.
c. Pressurised header tank for the coolant.
d. Oil and coolant temperature control sensors and associated valves.

The lubrication and cooling circuits are shown in Fig.4.2. The

temperature of both the coolant and the oil is maintained within the desirable limits (up to 95°C) by water heat exchangers, electrical heaters and associated automatic devices. The coolant system, which is basically a conventional automotive pressurised circuit, uses a mixture of de-minerilised water and commercial anti-freeze inhibitor as working fluid. The lubricating oil (viscosity grade 15W/40 or 10W/30) is contained in the engine sump, where it can be warmed rapidly to the working temperature by means of two electrical heaters. The oil pressure of the system is limited to 4 bars by a relief valve which delivers the excess oil back to the sump. The main lubricating points are the crankshaft, big end, valve camshaft and unit injector camshaft bearings.

The dynamometer is an electrical DC machine (type shunt wound with a separate excitation unit manufactured by McClure), rated at 30KW (400volts/65amps). Its bearing housings are supported in 'A' shaped frames mounted on supporting feet which stand on the base frame behind the cooling module. It is operated through a thyristor convertor unit (KTK model 6P4Q30) so that it can act as a dc motor to drive the engine during starting and motoring operations, or as a dc generator when loading the engine. Torque, either positive or negative, is measured by means of a 20Kg load cell, connected to the motor shell through a 407.8mm torque arm and a load limiting device, to avoid damaging the cell. During loading, the DC power from the dynamometer is converted to 3 phase AC by the convertor unit and fed back to the mains supply. A tachogenerator mounted on the dynamometer shaft provides a speed signal to the closed-loop speed control system, so that the speed selected at the control console is maintained by automatic adjustments to the motoring or loading torque.

4.2.2 Control console

The control console is a free standing 19" rack cubicle, incorporating a small desk top and housing the following components:

a. ACU (automatic control unit)
b. Torque-speed-ignition display
c. Remote control unit
d. Power supply unit

In the present set-up, some of the functions of the console are de-energised, due to the special fuel injection system with which the engine is supplied. The ACU is a safety system designed to protect the equipment and/or the operator by monitoring continuously the oil pressure and temperature, coolant level and temperature, speed and dynamometer system fault. In the event of any of the above conditions being unsatisfactory, the system shuts down automatically, indicating the cause of the failure. Torque and speed are shown in both analog and digital display. The remote control unit provides the means to operate the dynamometer and the cooling module.

4.2.3 Standard Hydra engine

An overall view of the Hydra No45 in baseline version can be seen in Fig.4.3.a. The engine retains from its predecessor the separate crankcase and cylinder block feature. The crankcase is made of heavy cast iron with removable side panels for ease of maintenance. The crankshaft is machined from nitriding steel bar, hardened and ground and incorporates two integral balance weights which give first order rotational balance. The absence of counterweights, turning at double the crankshaft speed make the engine susceptible to vibrations caused by second order inertia forces; the cast iron block, mentioned in section 4.2.1 was added to remove this problem. The crankshaft bearings are of the lead bronze plated type. The main bearings are bushes and the big-end has two half shells. The flywheel is of the forged steel disc type, incorporating a drive spigot. The connecting rod is made of forged steel with a straight split big end cap located by fitted bolts with bi-hexagonal nuts. The overhead camshaft, which is housed in an aluminium alloy box, is driven from the crankshaft by a two point toothed belt drive with an adjustable jockey tensioner. The camshaft operates two vertical valves, through inverted bucket type tappets with pallets between the valve and tappet to set the tappet clearance. The valves are housed in a cast iron, crossflow type cylinder head.

For the engine-dynamometer connection, a 'Gelenk' flexible coupling is employed; it uses rubber in torsion and enables the system to operate over the entire speed range without resonances, which can cause torsional vibrations. Unfortunately,it is also sensitive to angular deflections, so that zero setting of the torque readout device is difficult.

Finally, the exhaust port of the engine is connected to the laboratory ventilation system by means of a 600mm long stainless steel flexible pipe, two Bowman silencers connected in series and associated tubing.

4.2.4 Special Hydra engine

The engine has been designed in two basic versions: the standard baseline and the optical. The latter accepts interchangeable parts, according to the kind of optical access required by the measurement system.

The standard version is the closest of the two to the production 4-cylinder Ford York 2.5L HSDI engine. It has identical bore and stroke and incorporates the standard Ford piston and a cylinder head with the same positioning of the valves and the injector nozzle. Essentially, the Hydra and the Ford York engines share the same combustion chamber geometry. The cylinder is a cast iron barrel with centrifugally cast iron wet liner. The Hydra incorporates in addition a variable swirl inlet port and a CAV Lucas electronic fuel injection system based on a unit injector.

The variable swirl inlet port, as the name implies, is capable of achieving different levels of swirl by simply rotating a lever which operates the inlet manifold in and out of the inlet port (see Fig.4.5). The inlet manifold is a straight 300mm long tube inserted half way into the appropriately machined inlet port. It has been cut out at one end so that it covers partially (depending on the setting of the tube) the area close to the valve stem, thus changing the angular momentum of the air flow entering the engine cylinder. At the other end of the inlet manifold, a conventional automotive air-filter is mounted to clean the induction air. It should be noted that there is an inherent shortcoming to the design of the variable swirl port; an increase of induction swirl is associated with a reduction of volumetric efficiency due to the decrease of the inlet port cross-sectional area.

The CAV/Lucas fuel injection system consists of the unit injector (model EUI50), the low pressure fuel circuit and the electronically-controlled engine management unit. The main difference from conventional direct-injection diesel systems, with either an in-line or distributor type injection pump, is that high pressure (500-1000 bars) is generated individually at each unit to eliminate the need for high pressure fuel delivery lines. The

advantages over a conventional system are the higher injection pressure which potentially allows for better atomisation and more versatile and accurate control of both fuelling level and injection timing. On the other hand, it is complicated, more expensive and it is uncertain whether it will be used in production passenger cars. As a research tool, the unit injector allows fast and precise tuning of the engine at various speeds and loads. It is fixed in the cylinder head by means of two 8mm diameter studs and nuts and is driven by a separate camshaft, as shown in Fig.4.3. The camshaft is housed in an aluminium alloy box and is driven via a second toothed belt from the engine crankshaft. A cross-section of the unit injector can be seen in Fig.4.4. It comprises the main body or barrel, an 8mm diameter plunger, a 4-hole nozzle (4 x 0.2mm) and the 'colenoid' valve. The latter is a fast solenoid having a patented construction to provide an almost instantaneous response to signals generated by the electronic unit. High fuel pressure is building up by the inward movement of the plunger and,if the 'colenoid' is closed upon energisation by the electronics, the fuel flows to the nozzle and the associated engine cylinder. When the 'colenoid' is open, the fuel which is displaced by the plunger flows to the drain port. Fuel feed and return fuel lines are connected to the fuel circuit through suitable drilled holes in the cylinder head and are sealed by two O-rings supplied with the injector assembly. The electrical connections consist of two heavy duty wires (10amps rating) fitted with Lucar blade connectors.

The fuel circuit of the Hydra engine, shown in Fig.4.5 (Penwarden and Clarke, 1987) comprises the feed pump, fuel filter, fuel tank and associated valves, hoses and pressure gauges. The feed pump supplies fuel to the head at a pressure of 3-4bars in order to ensure efficient operation of the unit injector. The by-pass valve is used to aid the setting of feed and return line pressures and also to provide extra recirculation through the fuel cooler, if excessive fuel temperatures are encountered and fuel vaporization occurs.

The engine management system comprises the Electronic Control Unit (ECU), two sensors and the control box. The two sensors, corresponding to the crankshaft and valve camshafts, transmit information about the positioning and speed of the engine, while the control box sets the fuelling and timing demand. Based on this information the ECU generates the injection pulses which govern the release of energy from the inductive drive unit to the

'colenoid' valve. More details about the operation and the performance of the unit injector can be found in section 4.5.1.

The optical version of the Hydra (see Fig.4.3.b) employees a special elongated hollow double-piston assembly matched to a barrel extension to allow optical access to the combustion chamber through the piston. On top of the lower cylinder, an intermediate barrel extension is fitted via four 14mm bolts and has large diametrically-opposed openings. The standard Ford York piston has been replaced by an elongated hollow double piston assembly with the same openings as the barrel extension. The bottom piston is a modified York type equipped with a double lipseal in order to prevent oil leakage from the engine crankcase; it does not compress and its function is to guide the piston assembly inside the barrel assembly. The upper piston operates in dry conditions using two carbon rings, supplied as two semi-circular pairs, and a standard compression ring for gas sealing. The top cylinder, bolted to the top of the intermediate extension, is either a steel liner with four openings for the quartz window assemblies, or a fully transparent sapphire liner incorporating a steel guard with wide openings. The 20mm thick quartz windows are inserted in steel housings and sealed by means of Klingerit gaskets at either end and special grade RTV material. When optical access through the liner in not needed the windows can be replaced by blanks made of steel. The optical access to the cylinder through the bottom is achieved by a 30mm thick quartz window fitted to the upper piston; the quartz window can be replaced, if not needed, by an aluminium alloy blank incorporating fins for cooling purposes. A rectangular mirror, positioned at 45° to provide optical access through the piston window, or a specially constructed triple air-jet for prolonged firing tests, can be secured to the lower part of the barrel extension.

The engine is equipped with an optical shaft encoder (Hewlett Packard series HEDS-6000) in order to synchronise the engine rotation with the measurement systems. The encoder is mounted on the camshaft and provides 2000 pulses per engine cycle thus resulting in an angular resolution of 0.36°CA. The pulse train is fed to a purpose-built electronic control unit which can provide a variable duration pulse corresponding to a pre-selected crankangle window.

The specifications of the Hydra engine in baseline and optical form are summarised in Table 4.1.

Cylinder bore, (mm)			93.67
Stroke, (mm)			90.54
Swept volume, (litres)			0.624
Connecting rod length, (mm)			154
Compression ratio			16.75
Inlet swirl ratio, (R_s, see Appendix A)			1.6-3.0
Toroidal piston bowl (baseline version:)		diameter, (mm)	46.4
		depth, (mm)	16.8
Cylindrical piston bowl (optical version)		diameter, (mm)	46.4
		depth, (mm)	12.4
Inlet valve:	diameter, (mm)		42
	maximum lift, (mm)		10.7
	opens, IVO ^{o}BTDC		13
	closes, IVC ^{o}ABDC		39
Exhaust valve:	diameter, (mm)		37
	maximum lift, (mm)		11.3
	opens, EVO ^{o}BBDC		51
	closes, EVC ^{o}BTDC		13
Injection system:	Fuel feed pressure (bars)		4
	Plunger diameter, (mm)		8
	4-hole nozzle,	diameter (mm)	0.2
		cone angle (^{o})	150
		opening pressure (bars)	250

Table 4.1 Operating and geometric characteristics of Hydra engine

4.3 STEADY-FLOW TESTS

This section presents briefly the results from the steady-flow tests performed with the cylinder head of the Hydra engine by other researchers. The Hydra cylinder head was characterised in terms of discharge coefficient

and Ricardo swirl ratio (see Appendix A) at different positions of the variable swirl mechanism, in order to assess the range of swirl levels generated inside the cylinder and to compare them with the corresponding swirl strength of the production Ford York helical port (Penwarden, 1987). The three components of velocity were also measured at the inlet valve curtain area at four locations around the valve circumference and for valve lifts of 5 and 10mm; the results were reported by Arcoumanis et al (1988a) and subsequently analysed by Arcoumanis and Tanabe (1989) to allow comparison with the valve flow characteristics of the Ford York cylinder head.

4.3.1 Results and discussion

The variable swirl mechanism described in section 4.2.3 has two ranges of swirl strength; transition from the lower to the higher level is achieved by replacing two spacers supporting the assembly on the cylinder head.

Figure 4.6.a (Penwarden, 1987) shows the variation of the discharge coefficient of the inlet system of the Hydra engine at constant valve lift and constant pressure drop across the port as a function of the setting of the variable swirl mechanism; the two overlapping ranges are displayed. Fig.4.6.b presents values of the Ricardo swirl ratio (R_s), based on impulse swirl meter tests (see Appendix A) for the same settings, as well as the corresponding swirl ratio of the Ford York production engine which is shown as a straight line. These figures show that the higher swirl levels, generated by the variable swirl mechanism, are associated with higher losses inside the port, as indicated by the lower discharge coefficients, due to its particular design.

Figure 4.6.b also indicates that, between the two ranges of swirl, the higher level (noted as "single groove spacers range") is closer to that of the Ford York and this is why most of the present measurements were obtained at this swirl range.

The velocity distributions around the valve curtain area have showed that at low swirl settings of the variable swirl mechanism, the Hydra inlet port and the Ford York port exhibit the same general behaviour. The pre-

valve swirl generated by the helical shape of both ports decreases with increasing valve lift whereas the post-valve swirl due to the directional effect of the port has the opposite trend. At the medium and high swirl settings, however, the variable swirl port behaves in the opposite manner which is more typical of directed ports. It should be noted that at all swirl settings the pre-valve swirl contributes about 60-70% of the total swirl capacity of the inlet port, which is similar to the corresponding value for the Ford York cylinder head.

These observations lead to the conclusion that the Hydra variable swirl port is capable of producing overall swirl levels similar to equivalent production engines but behaves as a helical port only at low swirl setting while at medium-to-high settings its flow characteristics are typical of a hybrid directional/helical port.

4.4 MOTORED TESTS

The air flow inside the cylinder of the Hydra engine was investigated by means of laser Doppler velocimetry as a function of engine speed and swirl level. All the swirl settings mentioned in this section correspond to the high swirl range ('single groove spacers' of Fig.4.6)

4.4.1 Experimental system

Hydra engine - The optical Hydra engine was used in the course of these experiments and incorporated the extended hollow piston assembly with the aluminium alloy blank on the upper piston and the steel liner, which provided optical access through the four rectangular quartz windows. Fig.4.7 indicates the relative positions of the inlet port, valves, piston bowl and windows. Although the position of the unit injector tip is shown in the figure, the injector was not mounted on the cylinder head during the motored tests. For safety reasons the fully transparent sapphire liner was not used and all measurements were obtained with two of the quartz windows installed, the other two replaced by steel blanks.

A number of technical problems were encountered during the commissioning of the engine and most were associated with the elongated

piston assembly. Various materials for the upper piston rings were tested at Ricardo to achieve proper sealing under dry lubrication conditions. The gas sealing problem was finally resolved by a combination of two carbon rings with a conventional compression ring. The lower piston was initially constructed from a solid aluminium alloy piece based on the design of the standard Ford York piston and it was reinforced at the critical points in order to withstand the stresses imposed by the additional moving mass of the upper piston. Unfortunately, the lower piston ceased three times during the tests, despite alterations made by Ricardo and this led to the decision to use a modified standard Ford piston. However, subsequent calculations showed that this design was not able to function safely at the rated speed of the engine (4000rpm) and a lower limit of 3000rpm was adopted for all the tests.

Prior to the velocity measurements, the vibrations caused by the unbalanced second order inertia forces (section 4.2.3) were investigated within the operating speed range in order to see whether they could influence the velocity results. The displacement of a laser beam reflected on a small mirror supported on the cylinder head was monitored on a screen and confirmed that the amplitude of the engine vibrations was not more than 0.5mm throughout the speed range.

Laser Doppler velocimetry system - The velocity data were obtained with a dual-beam laser velocimeter, comprising a 5W Ar-Ion laser, a Dantec 55X transmitting optical unit and a Dantec 55X34 receiving optical unit. The laser was operating in the 514.5nm green line and with maximum power of 1.4W. The light transmitting unit consisted of a beam splitter, an acousto-optic modulator (Brag-cell) which could shift the frequency of one of the two beams by 40 MHz relative to the other, and a planoconvex imaging lens. The receiving unit, described in section 2.6.3, was placed either in the direct forward-scatter position or at 10-20 degrees off-axis in order to minimise the effective size of the control volume. The latter, however, was not always feasible due to the restricted optical access provided by the quartz windows in the cylinder liner.

Two methods of seeding the flow with particles suitable for laser velocimetry were tested; the first involved atomisation of silicone oil and the second atomisation of a dilute suspension of titanium dioxide (TiO_2) particles

in methanol. Sediment formation was prevented by stirring the suspension with a magnetic stirrer. Despite the reservations expressed by Arcoumanis et al (1986) and Cipolla et al (1987), silicone oil survived the high pressure and temperature of the Hydra engine and resulted in high data rates. Silicone oil droplets were introduced into the intake port via a tube located downstream of the intake filter. Unfortunately, the quartz windows were fouled by silicone oil after approximately 6-7 minutes of engine operation, which resulted in deterioration of the LDV signal quality. It was, therefore, considered necessary to stop the engine at regular intervals and clean the windows; this did not seriously disturb the measurement programme since it was possible to collect two to four data sets between runs and the cleaning of the windows could be completed within 15 minutes.

The signal from the photomultiplier was passed through a Dantec frequency downmixer, which reduced the effective frequency shift within the range of 0-9 MHz, and then input to a frequency counter (TSI model 1990c) operating in the single measurement per burst mode. The minimum number of zero crossings for the Doppler signal was set at 8 and the maximum error for validating a measurement with the 5/8 comparison at 2%. The counter was connected to an IBM/AT compatible microcomputer through a Dostek interface card. The frequency and crankangle information was transferred to the microcomputer memory at high speed using direct memory access (DMA) and stored to disk for subsequent analysis using software described by Enotiadis et al (1990). Measurements were taken with resolution of 0.3°CA over large (150°-300°) windows, as opposed to the 2°-5° windows reported in section 3.3.2, and, therefore, velocity information was available simultaneously for a number of small crankangle windows, thereby reducing substantially the measurement time. The instantaneous data were then ensemble averaged over 2° windows to provide information about the variation of ensemble-averaged mean and rms velocity with crankangle as well as joint probability density functions of crankangle and velocity. The probability density functions were used to allow identification of spurious data and, after filtering, the ensemble-averaged mean and rms velocities were calculated. Finally, spatial velocity distributions at a given crankangle were estimated by selecting the velocity values at this crankangle from the temporal traces measured at the different locations along a given diameter.

4.4.2 Results.

Measurements of the swirl and axial velocity components were obtained along the diameter shown in Fig.4.7.a and b at spatial intervals of 5mm. The crankangle periods examined were 180°-326° ATDC for the swirl velocities, and 38°-322° ATDC for the axial velocities. The end of the measurement period was determined by the crankangle at which the piston arrived at the plane of measurements; in the case of the axial component the piston crossed one of the two intersecting beams about 4°CA earlier due to the measurement plane being vertical to the moving piston. Measurements were obtained at engine speeds of 1000, 2000 and 3000 rpm which correspond to most of the speed range of the production Ford engine and, for the swirl component, at three settings of the variable swirl mechanism corresponding to different swirl levels: high swirl (setting 1), medium swirl (setting 6) and low swirl (setting 13). Considering all possible combinations for the two variables of engine speed and swirl, nine data sets were obtained at each point. It is worth mentioning that in order to avoid any uncertainties in the position of the control volume, all measurements for a certain location were completed before moving to the next location. For the measurement of the axial velocity it was not considered necessary to vary the swirl strength since the axial flow patterns are less sensitive to induction swirl; therefore all axial velocity data were obtained at medium swirl level. The results are presented in the form of temporal or spatial profiles of the ensemble-averaged mean and rms velocities, normalised by the corresponding mean piston speed. Open symbols denote mean velocities while closed symbols represent the rms of the turbulent fluctuations. In order to assist the interpretation of the results an outline of the cylinder and piston boundaries is provided in all spatial velocity profiles.

A. Swirl velocities

Typical temporal profiles of the mean and rms values of the swirl velocity component obtained at two different locations are shown in Fig.4.8. Both traces were recorded with the engine running at 2000rpm and the variable swirl mechanism set at position 1. At r=35mm (see Fig.4.8.a), relatively close to the wall, both mean and rms swirl levels change little

during the compression stroke, remaining between 4.2 and 5.5V_p for the mean values and decaying slowly from 0.9 to 0.6V_p for the rms values. However, closer to the centre (r=15mm), as shown in Fig.4.8.b, the mean swirl velocity rapidly achieves maximum at approximately 200° and then remains fairly constant at around 2.5V_p. Additional information about the spatial swirl distribution and its variation with crankangle can be deduced from the mean velocity traces of Fig.4.9, obtained at different radial locations, where positive values represent clockwise movement. All the data presented in this graph were obtained at the medium engine speed of 2000rpm and medium swirl strength. The mean swirl velocity traces show that between 180° and 250°CA, the mean tangential flowfield around the cylinder axis (r=-20 to 20mm) is continuously transformed and local maxima can be identified around IVC (218°CA), which shows that the induction flow determines the tangential flowfield.

The evolution of swirl is examined further with respect to engine speed and swirl strength in Fig.4.10.a, where data were obtained at the same location and swirl strength but at different engine speeds. The figure shows that swirl does not scale with speed until 270° in terms of both maximum value and crankangle location at which the velocity peaks. The reduction in normalised peak velocity values as engine speed increases, is probably associated with the more-than-linear increase of friction at the cylinder boundaries, due to the higher swirl velocity magnitudes (in m/s). The delayed occurrence of maximum swirl can be attributed to the reduced time available to the flow for development at higher engine speeds, as demonstrated in Fig.4.10.b, where the three peaks almost coincide when swirl velocities are plotted against absolute time. During the second half of the compression stroke, i.e. after 270°CA swirl shows trends of better scaling with engine speed so that at 326°CA the normalised velocity values corresponding to the three engine speeds vary within the range 3.2-3.7V_p. Figure 4.11 shows the temporal evolution of the mean swirl velocity obtained at r=20mm for different settings of the swirl mechanism and an engine speed of 2000rpm. A similar behaviour to that obtained with the different engine speeds can be seen in Fig.4.11; the peaks are shifted to later crankangles as swirl strength decreases which is explained by the different patterns of the tangential flowfield generated by the variable swirl port (see discussion later on Fig.4.17).

The temporal distribution of the normalised rms of the swirl velocity fluctuations and its variation with respect to engine speed and swirl strength are examined in Figs.4.12 and 4.13. These values are based on data obtained at the same point (r=20mm) as Figs.4.10.a and 4.11 under all combinations of engine speed and swirl strength. At BDC the rms for the nine different cases range from 1.4 to 2.0V_P and subsequently decay to 1±0.2V_P at IVC; the poor scaling of the rms values is attributed to the unsettled flow during the initial stages of the compression stroke, which was previously observed in the mean profiles. Later in the compression stroke (270°CA) rms levels are similar for all swirl settings and scale with engine speed; at 300°CA they are nearly identical with values between 0.6-0.7V_P.

Five crankangles, from BDC of induction to TDC of compression, were selected to represent the temporal development of the spatial swirl profiles for the different combinations of engine speed and swirl strength. Three of them (180°, 200°, 218°CA) concern the last phase of the induction stroke prior to IVC, which determines the initial conditions of the compression stroke. At the first crankangle and for all three settings of the swirl mechanism (Figs.4.19, 4.20, 4.21), the swirl distribution is dominated by a clockwise vortex at the side of the cylinder towards the outlet valve with peak swirl velocities of 3-4V_P. However, the swirl distribution at the side of the cylinder towards the inlet valve is influenced by engine speed and, in most cases, an anti-clockwise vortex is present. This is probably due to the position of the inlet valve and the associated flow pattern which persists at high engine speeds, and to the relatively short time available for flow development (compare for example Fig.4.14.c with Figs.4.15.a, b). It should be noted, however, that the anti-clockwise vortex is present at the low swirl strength (setting 13) even at low engine speeds (compare Fig.4.14.a with Fig.4.16.a). This can only be related to the geometry and operation of the variable swirl mechanism which was described briefly in section 4.2.4 and will be explained below in more detail.

In common with most helical ports, two main jets emerge during early induction from the valve gap generating vortices of different rotational direction in the engine cylinder (Fig.4.17); viewed from above, the stronger vortex (shown by the bold arrow) has a clockwise direction and initially occupies an annular volume close to the cylinder wall. The weaker jet (shown

by the thin arrow) issues from the other side of the valve and spirals downwards in the opposite direction occupying the volume between the cylinder axis and the inlet valve axis. The two vortices interact until the anti-clockwise motion dies out during the initial stages of the compression stroke. The position of the tube inside the variable swirl port controls the relative strength of the two jets. At low swirl strength (setting 13) the tube is positioned upstream from the valve so that it does not obstruct the flow of the two jets issuing from both sides of the valve. The two rotational movements interact for longer period and, therefore, generate lower angular momentum. At high swirl strength (setting 1) due to the tube moving inwards and blocking part of the flow area, the anti-clockwise jet is very much reduced in strength and the main vortex dominates the in-cylinder flow giving rise to high angular momentum and induction swirl levels.

The swirl velocity profiles later in the compression stroke (200°CA) are presented in Figs.4.18-4.20 and provide further evidence of the evolution and destruction of the small anti-clockwise vortex. At the medium and high swirl levels the velocity distributions are distorted only at the higher engine speeds (Figs.4.18.c and 4.19.c), whereas at low swirl levels the effect of the slowly decaying anti-clockwise vortex is identifiable at all engine speeds (Figs.4.20.a, b, c).

At the crankangle of IVC (218°CA), swirl velocity profiles begin to scale well with engine speed at all swirl port settings, in terms of both the peak values of the mean swirl velocity and the rms values (Figs.4.21-4.23). Maximum swirl levels of approximately 5.5, 5 and $3.8V_p$, corresponding to high, medium and low swirl respectively, are present at a radius of about 35mm from the swirl centre and are independent of engine speed. The rms values of the swirl velocities are relatively uniform in space away from the cylinder axis with levels of about 0.8 to $1V_p$ and increase to approximately $1.5V_p$ near the centre of rotation due probably to the precessing swirl centre. The distribution of the mean swirl velocity exhibits a clear dependence on engine speed, which is more pronounced in the case of high swirl levels (Figs.4.21.a-c). At 1000rpm, the distribution resembles solid body rotation with uniform levels over a region extending for about 15 mm near the wall. At 2000rpm, the flat regions are more extended and the slope in the vicinity of the swirl centre steepens and at the highest engine speed of 3000rpm, the

same tendency is even more evident, with the central area of the steep velocity gradient extending over only a 20mm radius. The dependence of the mean swirl distribution on engine speed is associated with the time available to the flow in the cylinder to develop as a function of engine speed from the initial distribution reflecting the port/valve geometry towards solid body rotation. Additional evidence is provided by the corresponding profiles at mid-compression (270°CA, Figs.4.24-4.26), where all swirl profiles look similar and scale well with engine speed due to the adequate time available for flow development.

At 320°CA (Figs.4.27-4.29) there is a change in the swirl distribution towards the initial pattern of a steep velocity gradient in the near axis region at all engine speeds and swirl levels, followed by eccentricity of the swirl centre towards the direction of the inlet valve. It can be argued that this trend in the swirl distribution is a consequence of the cylindrical piston-bowl which at 320°CA is only 5mm below the measurement plane. The swirling flow is gradually centred around the axis of the eccentric bowl and spins up towards the bowl entry plane.

In order to investigate the decay of swirl during the compression stroke, irrespective of the swirl distribution and swirl centre position, the magnitudes of the angular momentum and the corresponding equivalent swirl ratios were calculated in steps of 10°CA, following the procedure described in Appendix A. It should be noted that the estimated swirl ratios are based only on swirl velocities measured along a plane located 9mm from the cylinder head and stratification effects such as those observed in a modified Ford York engine (Arcoumanis et al, 1987a) are necessarily neglected. Figure 4.30 shows the evolution of the estimated swirl ratio during the compression stroke for the nine different test cases. As an overall conclusion it can be argued that initial differences in swirl levels, caused by the variable swirl inlet port during induction, persist during the compression stroke, altering the pre-combustion flowfield and potentially affecting the combustion process. At low swirl levels (Fig.4.30.c), the temporal variation of the swirl ratio scales well with engine speed during most of the compression stroke, whereas at medium and high swirl levels (Figs.4.30.a, b) the profiles coincide only at mid-compression (240°-250°CA) and around 320°CA. Swirl ratios at IVC and 320°CA were averaged over all engine speeds and included

together with the Ricardo swirl ratios (deduced from Fig.4.6) in Table 4.2. Comparison between the steady flow and motored engine results at IVC show that the former underestimates the swirl strength by about 20%. However, in relative terms the two methods give similar results; the difference is 7-10% between high and medium swirl setting and 29-30% between high and low swirl settings. The decay of swirl level between IVC and 320°CA is about 12% for medium and high swirl, but only 7% for the low swirl case, which implies that higher initial swirl is associated with higher losses due to increased friction with the cylinder wall, head and piston surfaces.

Swirl ratio	Swirl setting (position)			% variation	
	High (1)	Medium (6)	Low (13)	High-to-medium	High-to-low
R_s (Ricardo)	2.98	2.77	2.08	7	30
SR (220° CA)	3.83	3.43	2.72	10	29
SR (320°CA)	3.40	3.04	2.53	11	26
% SR decay 220° to 320°	11	11	7	-	-

Table 4.2 Swirl ratio values

Since there are no measurements inside the piston-bowl near TDC of compression, an attempt was made to estimate the TDC swirl ratio based on first principles and compare with results in the literature. Assuming solid-body rotation inside and outside the bowl, negligible TDC clearance and conservation of angular momentum, the swirl ratio at TDC is given by

$$SR_{TDC} = \left(\frac{B}{D}\right)^2 SR_{IVC} \qquad (4.1)$$

where B is the bore and D the bowl diameter. Due to frictional losses equation (4.1) becomes

$$SR_{TDC} = a\left(\frac{B}{D}\right)^2 SR_{IVC} \qquad (4.2)$$

where $0.5 < a < 0.7$ according to multidimensional flow predictions (Gosman, 1986). Different investigations have shown that (i) a=0.59 for an engine with

B/D=1.9 and TDC measurements obtained with LDV (Monaghan an Pettifer, 1981), (ii) a=0.55 for a toroidal piston-bowl with B/D=1.8 (Cipolla et al, 1987) and (iii) a=0.68 for a toroidal piston-bowl with B/D=1.53 and based on LDV measurements at different speeds and swirl ratios (Murakami et al, 1986). Following the above results, a factor of a=0.60 was used to estimate the TDC swirl ratios in the Hydra engine which has a B/D=2.02 and resulted in swirl ratios of 7.8, 7.2 and 5.8 for high, medium and low swirl, respectively. These ratios correspond to maximum swirl velocities at r=20mm inside the bowl of 16.3m/s ($5.4V_p$) at high swirl, 15.1m/s ($5.0V_p$) for medium swirl and 12m/s ($4.0V_p$) for low swirl. These values will be compared later with the combustion photography results (section 4.6) to examine their validity as an approximate method of determining swirl velocities inside piston bowls.

The movement of the swirl centre was investigated in detail in Chapter 3 and is also examined here, in order to identify possible implications for real diesel engine geometries. Spatial mean velocity distributions for the nine different cases were generated at each crankangle window and the zero swirl velocity points were determined by linear interpolation between the data points close to the cylinder axis in order to provide a representation of the variation of the swirl centre with crankangle during compression. Figures 4.31-4.33 show the variation of the zero swirl location, i.e. the eccentricity of the swirl centre, for low, medium and high swirl levels, respectively. It should be noted that these locations represent the projection of the centre onto the diameter along which measurements were performed rather than the successive positions of the actual centre of the swirling motion. The swirl centre moves from one side of the cylinder to the other until about 280°CA and then approaches the piston-bowl axis which indicates that the upwards motion of the piston can be felt at fluid layers about 30mm ahead. Since a periodicity has been identified in most graphs, the characteristic frequencies were estimated from the crankangle intervals separating two successive peaks and plotted against engine speed in Fig.4.34 for all three swirl settings. The results show that the frequency of swirl centre precession is higher than the rotational frequency of the crankshaft and increases almost linearly with engine speed; the proportionality factor lies between 5 and 6, which compares well with the 4-8 range found in the model engine (see section 3.2.3) and the 6-8 range observed by Haghgooie and Kent (1987). However, the ensemble-averaged rms of the swirl velocity fluctuations exhibit nearly uniform

distributions, except early in the compression stroke (Figs.4.14 to 4.23) when the increase around the cylinder axis is lower than that observed in the model engine. This can be explained by the different methods of generating swirl in the two research engines; the single-valve head incorporating the 60° swirl vanes generates an axisymmetric swirling flow with an equivalent swirl ratio of about 7 (see section 3.2.3), whereas the Hydra helical port produces at all swirl settings a complex asymmetric flow during induction with less than half values of swirl ratio.

B. Axial velocities

The temporal profiles of the axial velocity component measured at r=15mm are shown in Figs.4.35.a, b, c for the three engine speeds. At low and medium engine speeds, the mean and rms velocities scale reasonably well with engine speed. The mean velocity traces go through a maximum of 7-8V_P at about 70°CA, a minimum of around zero at 130°CA and a second peak of 2.5-4V_P at 170°CA; during the compression stroke they never exceed the mean piston speed. At 3000rpm the distribution of the mean axial profile changes significantly, showing a double maximum of 4-5 V_P early in the induction stroke, and a third peak at the beginning of the compression stroke. All three peaks are associated with the incoming jet through the annular valve passage which affects the flow at the measurement location differently during the induction stroke according to the instantaneous valve lift. The different pattern at 3000rpm is possibly due to tuning effects in the inlet manifold (Margary et al, 1990), which affects considerably the instantaneous mass flow rate through the valve, thus generating different flow patterns early in the induction stroke. Axial velocity fluctuations scale well with engine speed, varying from initially 3-4V_P (60°-90°CA) to around 0.8V_P towards the end of compression stroke (320°CA).

The spatial distributions of the axial velocity component for the medium swirl setting were examined at six crankangles during the induction and compression stroke and found to vary with engine speed. At 70°CA and low-to-medium speed (Figs.4.36.a, b) the in-cylinder flow is dominated by the asymmetric annular jet which enters the cylinder through the off-centre inlet valve and generates negative velocities at the exhaust valve side, indicative of the formation of a side vortex; at 3000rpm (Fig.4.36.c), the distribution is

different in that axial velocities in the exhaust valve side are positive. The rms of the velocity fluctuations varies between 2 and $5V_p$ at all engine speeds. Later in the induction stroke (150°CA, Fig.4.37), the axial velocity distributions become symmetrical; at medium-to-high engine speeds there are negative velocities close to the cylinder axis and near the cylinder wall, indicative of a main toroidal vortex and a pair of weaker corner vortices. At BDC (Fig.4.38), while the inlet valve is still open, the mean axial velocities range from -1 to $4V_p$, and rms values have decayed to $1\text{-}3V_p$, especially for the low speed case. At IVC (Fig.4.39), the axial velocities are between -2 and $+1V_p$ and remain small during the compression stroke, according to the profiles at 270°CA (Fig.4.40) and 320°CA (Fig.4.41). It is interesting to note that at IVC the spatial distributions at 1000 and 2000rpm (Figs.4.39.a,b) indicate back-flow towards the inlet valve which is not present at 3000rpm (Fig.4.39.c). Similar trends were observed in other motored studies (Arcoumanis et al, 1987c) and attributed to the low inertia of the fluid at low engine speeds. According to Heywood (1988) the inlet valve is always closed some 40°-60° after BDC (39° in the Hydra engine) to take advantage of the ram effect, whereby at higher engine speeds the inertia of the gas in the intake system increases the pressure in the port and the charging process continues after the piston passes the BDC; consequently the mass of air induced into the cylinder and, hence, volumetric efficiency increases. The reverse flow at lower engine speeds is the inevitable consequence of the late IVC, selected in order to take advantage of the ram effect at higher engine speeds.

During the compression stroke the rms of the axial velocity fluctuations remain less than $0.8V_p$ for almost any spatial location and at all engine speeds and are comparable to the corresponding levels of the swirl component; similar rms levels were measured at the same crankangle in the modified Ford York engine employing a flat piston and lower compression ratio (Arcoumanis et al, 1987a).

4.5 SPRAY CHARACTERISTICS OF FUEL INJECTOR

Prior to the combustion tests, the transient spray from the unit injector was characterised in terms of the instantaneous line pressure and needle lift,

tip penetration and axial droplet velocities under atmospheric conditions. Although quantitative differences are expected between the engine environment and atmospheric tests, results from this investigation can be used to facilitate the interpretation of the results under firing conditions.

4.5.1 Experimental system

Injection system - For the purpose of this study the aluminium alloy box which included the unit injector, the separate camshaft and the associated lubrication and driving belt equipment, was mounted on the cylinder head. To allow fuel injection into the atmosphere the cylinder liner was replaced by four spacers of equal height and the inlet and exhaust valves were removed from the cylinder head to permit the positioning of a nozzle adaptor, capable of covering all but one of its holes, thus allowing characterisation of one of the four sprays without blocking the exit of the other three. The nozzle incorporates a needle covering the upstream side of the holes into the nozzle body (VCO-type) and has four 0.20mm diameter holes, producing a spray with a cone angle of 150°. Since the sprays did not interact in the near nozzle area, only one spray was characterised while the others were collected downstream by an exhaust system equipped with a cyclone to separate liquid droplets from the air stream. Preliminary tests showed that this method of collection and discharge of the remaining three sprays had no effect on the penetration of the fourth spray under investigation. The fuel used was Shell gas oil SH with density of 0.844 kg/l and viscosity of 3.5cSt at 40°C. It should be noted that the unconventional arrangement of the engine for the engine tests imposed a safe speed limit of 2000rpm.

Measurement systems - Laser beam deflection, described in detail in Chapter 2 (section 2.3.2), was used to measure the spray tip penetration. Changes in the intensity of the light falling onto the photodiodes were associated with refractive index variations caused by small droplets existing in the spray tip and allowed measurement of the tip penetration at various distances from the nozzle exit. The delay between the signals from the two photodiodes corresponded to the time of flight of the spray tip between the two laser beams set 5mm apart, thus allowing the evaluation of the mean spray tip velocity within this distance. Difficulties were encountered in

aligning the system axis to the spray centreline due to the non-adjustable inclined position of the injector which was housed rigidly in the cylinder head.

LDV was used to measure the axial component of droplet velocities at various positions from the nozzle tip. The optical and electronic equipment was identical to that used for the motored in-cylinder flow tests although some modifications were made to accommodate the very transient and high spray velocities; the half-angle of the intersecting beams was reduced to 3.2°, resulting in a 4.60 velocity to frequency conversion factor. In order to reduce the effective size of the control volume and, thus, increase the spatial resolution and reduce velocity gradient broadening, the receiving optical unit was positioned 15° to 20° off-axis. Droplet velocity data were collected over 2-3ms windows and the time information from the start of the injection was set for each velocity value by means of a 2.5MHz clock and a pulse counter incorporated in the Dostek interface card. An oscilloscope, triggered by a needle lift sensor, provided two TTL pulses; a narrow pulse indicating the start of each injection cycle by resetting the counter and a delayed pulse with variable width (2-3ms) which defined the window during which data were allowed to be transferred to the microcomputer for processing. Droplet velocity data were ensemble-averaged over 50μs windows, while the minimum number of samples per window was set at 2000.

A sensor was attached to the back end of the nozzle and provided a signal proportional to the needle movement based on the Hall effect (Bosch, 1986). The unit injector was also instrumented with a fuel-line high pressure transducer (max. pressure 2000bars), connected to a Lucas bridge amplifier; the transducer was fixed to the unit injector body very close to the nozzle exit in order to minimise any errors associated with compressibility effects.

4.5.2 Results

The characterisation of the diesel fuel injector was divided into two phases. First, the initial conditions of the spray were determined it terms of the amount of injected volume, the instantaneous injection pressure and needle lift signal; these data were used to estimate the nozzle average discharge coefficient during the injection period. The second phase involved

measurements of the spray tip velocity and time-resolved axial droplet velocities. Tests were made at low (1000rpm) and medium (2000rpm) engine speed, while the settings of the electronic injection system in terms of load were decided based on the results of the first phase combined with the expected engine air consumption at the corresponding speeds; this procedure was necessary in order to ensure that the resulting air-to-fuel ratios were typical of DI diesel engines.

A. Initial conditions.

Two control switches operating independently, monitor the injection pulse which energises the 'colenoid' valve (see section 4.2.4); the fuelling control determines the duration of the pulse, i.e. the injected volume while the timing control determines the start of injection. The injected volume was measured by weighting the fuel collected over a large number of injections for various settings of the fuelling control at speeds of 1000 and 2000rpm; these data were used to draw the lines in Fig.4.42, which represent the injected volume per cycle as a function of injection duration. In order to determine the working range of the injection system for the Hydra engine, an average value of 0.88 was assumed for the volumetric efficiency of the inlet port (derived from preliminary performance tests at Ricardo) and two horizontal lines were drawn corresponding to typical minimum (20) and maximum (50) air-to-fuel ratios. Four test cases were selected representing low-to-medium and high load at 1000 and 2000rpm and are shown in Fig.4.42 and table 4.3 as cases A-D.

Case No	Engine speed (rpm)	Fuelling (mm^3/inj)	Average exit droplet velocity V_m (m/s)
A	1000	22.8	134
B	1000	37.6	162
C	2000	23.2	185
D	2000	36.2	192

Table 4.3 Unit injector tests

Figure 4.43 shows the temporal variations of the instantaneous injection pressure and needle lift for all four cases under investigation. The

injection pressure rises during the whole injection period especially at 2000rpm and falls sharply just before the needle lift starts decreasing. This trend is in contrast to conventional pump-pipe-nozzle systems, where the injection pressure at higher loads reduces gradually during the second half of the injection period or even immediately after the initial peak at lower loads (Arcoumanis et al, 1990). The multiple oscillations of the pressure signal in the central part of the injection period can be attributed to the response of the fuel behaving as a compressible fluid under the very high pressures existing inside the unit injector. From the injected volume and injection duration, as determined from the needle lift signal, the mean droplet exit velocities were calculated and found to vary between 134 m/s for case A and 192 m/s for case D (Table 4.3).

B. Spray tip velocities

Spray tip velocities for the four cases are plotted as a function of distance from the nozzle exit in Fig.4.44. In agreement with results obtained with multi-hole pump-pipe-nozzle systems (Arcoumanis et al, 1990), the tip velocities are strongly dependent on the injection frequency (engine speed) and are nearly independent of the injected fuel volume (engine load). At 1000rpm (Fig.4.44.a) the tip velocity initially rises reaching a maximum of approximately 150m/s at 15mm from the nozzle exit and then decreases gradually. However, at 2000rpm (Fig.4.44.b) and after the initial maximum of 160m/s at 15-20mm from the nozzle, the tip velocity drops slightly before increasing again and reaching a second maximum of nearly 200m/s further downstream. These values agree well with the calculated mean droplet exit velocities shown in Table 4.3 and confirm that higher injection pressures associated with higher injection frequencies give rise to higher spray tip penetration. The trends in the velocity-distance traces are directly associated with the pressure variations of Fig.4.44, particularly during the first 0.3-0.4ms of the injection period, i.e. the time that it takes for the spray tip to travel 50mm at average speeds of 130-160 m/s. In all four cases, the spray tip velocity traces are similar during the first 0.1ms due to the same value of the nozzle opening pressure, which is determined by the nozzle spring characteristics. Later, the sharp increase in the line pressure observed at 2000rpm, as opposed to the weak increase at 1000rpm, results in different

flow regimes inside the nozzle, which may involve cavitation and successive detachment and reattachment of the flow from and to the nozzle walls; this is probably the reason for the observed second maximum in the tip velocity curve at 2000rpm.

The spray tip velocity-vs-distance graphs of Fig.4.44 were used to derive the variations of spray tip penetration distance as a function of time from the start of the injection and equivalent crankangle. Figure 4.45 shows the results for cases A and C only since cases B and C are very similar. As expected the slope of the penetration curve at 2000rpm is steeper than that at 1000rpm due to the higher tip velocities associated with the higher injection pressure. To relate the penetration distance S_p of the spray under atmospheric conditions to those in the Hydra engine at the time of fuel injection, the following correlation was used (Dent, 1971).

$$S_P = 3.07 \left[\left(\frac{\Delta P}{\rho_g} \right)^{0.5} t\, d \right]^{0.5} \left(\frac{294}{T_g} \right)^{0.25} \qquad \text{(SI Units)} \quad (4.3)$$

where $\Delta P = P_{inj} - P_g$ is the differential pressure, t is the time elapsed from the start of injection, d is the nozzle orifice diameter and ρ_g, T_g are the gas density and temperature, respectively. The results are plotted in Fig.4.45 as dotted lines. The spray tip penetration distances (filled squares) deduced from the high speed photographs (section 4.6) at different times from the start of the injection agree well with the corrected penetration data at the engine pressure and temperature during the short in-flight time of the spray prior to its impingement on the piston-bowl wall.

C. Axial droplet velocities

The axial component of the spray droplet velocities was measured by LDV on the centreline of the spray at distances from the nozzle of 10, 20 and 30 mm for cases A-D and the results are shown in Figs.4.46-4.49; the start of the measurement period in all cases coincides with the needle rise.

Figure 4.46.a shows that the ensemble-averaged mean droplet velocities at 1000rpm, low load and close to the nozzle (z=10mm) reach a maximum of about 220m/s some 0.2-0.3ms after the arrival of the spray tip at the measurement point followed by a small decrease and immediate recovery

to the same level (Fig.4.46.a). During the next 0.6ms, which corresponds to the rest of the injection period, droplet velocities remain fairly constant until they decays sharply indicating the passage of the spray tail which moves at much lower speeds due to the low injection pressure at the end of the injection period. At 20mm from the nozzle, the velocity trace exhibits a higher initial value of about 150m/s, a maximum of 235m/s and pronounced oscillations during the main injection period (Fig.4.46.b). Further downstream at 30mm (Fig.4.46.c) the maximum velocities are smaller and the trend towards multiple oscillations becomes more evident. It should be noted that the data rate is reduced when the main fuel cloud passes through the measurement volume due to the obscuration of the laser beams by the dense core of the spray.

Comparison between spray tip velocities (Fig.4.44.a) and ensemble-averaged droplet velocities at the first measurement windows (Fig.4.46.a,b,c) confirms that the small group of droplets forming the spray tip moves with velocities in the range 100-150 m/s. However, the much higher droplet velocities observed at all measurement locations immediately after the spray tip passes the control volume reveal that there is a continuous succession of the droplets which form the spray tip; the leading droplets are decelerated by drag and are overtaken by faster moving droplets (Arcoumanis et al, 1990; Koo and Martin, 1990). This process occurs throughout the injection period with decreasing strength due to the fact that the later leading droplets experience less drag from the surrounding air. Another interesting observation is that the rate at which the velocity decreases at the tail of the fuel cloud is reduced as the axial distance from the nozzle increases, confirming the results of Koo and Martin (1990); this implies that the fuel cloud grows in length far from the nozzle. The rms levels remain fairly constant within the range 30-40m/s during the main injection period and reduce to about 5-10m/s when the last droplets pass through the measurement volume. However, it should be noted that the rms levels may be overestimated due to the wide size range of the droplets and the likely existence of a correlation exists between droplet velocity and size (Hardalupas et al, 1989).

Figure 4.47 shows the mean and rms droplet velocities at 1000rpm but at the higher load of 9.4mm^3 per hole. As the load increases, the duration of

the spray increases but the ensemble-averaged mean and rms velocities remain nearly at the same level. The mean velocity oscillations, which were observed at lower load, are also present especially at the distance of 30mm from the nozzle exit (Fig.4.47.c). It is interesting to note that these oscillations match very well the pressure oscillations of Fig.4.44.b, which implies that the mean droplet velocities are directly related to the pressure variations inside the injector body.

At the higher speed of 2000rpm and at both loads (Fig.4.48 case C, Fig.4.49 case D) the spray droplet velocities are higher than those at 1000rpm as a result of the higher injection pressures, reaching maximum values of about 260m/s. The temporal variations at all locations exhibit similar trends with the previous cases and the initial values at early injection are in good agreement with the spray tip velocities of Fig.4.45.b. It is worth mentioning that the velocity data near the nozzle do not always represent droplet velocities since non-spherical droplets or ligaments may exist in the process of atomisation, particularly in the near-nozzle region, i.e. within 100 nozzle diameters according to Yule and Aval (1989), which corresponds to 20mm in the present case. These unconnected structures, however, are able to give good quality LDV signals as long as the obscuration of the beams is not severe.

4.6 COMBUSTION PHOTOGRAPHY

In order to obtain time-resolved information about the combustion process inside the cylinder of the Hydra engine, high speed photography was employed. The light which is emitted during combustion was found to be adequate for direct recording on the film, thus eliminating the need for applying other methods such as shadowgraphy (described in Chapter 2) or Schlieren photography. Optical access was provided by the flat quartz window incorporated in the piston bowl base (see section 4.2.4 for more details). Sequences of selected frames are presented and the fuel impingement on the walls together with combustion initiation and development have been investigated, as a function of engine speed, swirl strength and load; the swirl ratio values estimated in section 4.4.2 and the spray tip velocities calculated in section 4.5.2 are used for the interpretation

of the high speed films.

4.6.1 Application to the Hydra engine

The high speed camera described in section 2.5.1 was used to visualise combustion in the Hydra engine. The speed was fixed at 6000 frames/s resulting in an effective filming speed of 12000 frames/s, as the camera is equipped with a half-frame 16-sided rotating prism; the aperture of the 45mm Mamiya objective lens was fully open (set to f/2.8) and the films were 16mm Ektachrome 7250 with sensitivity ASA 400 (DIN 27°). The camera, when loaded with 30m film rolls has about 250ms usable run at this speed, which was enough to capture at least two consecutive combustion events even at the lowest engine speed (at 1000rpm the cycle duration is 120ms).

The basic components of the photographic set-up included a mirror placed under the upper piston and providing optical access to the combustion chamber through the quartz window and an assembly of two small mirrors which were used to enable the camera to record simultaneously the flywheel timing marks. Two Thorn 120V 250W spot lights were employed, one on the fuel sprays, the other on the timing marks. The in-cylinder view obtained through the quartz window is shown in Fig.4.50 together with the orientation of the fuel sprays and the direction of swirl.

Preliminary tests in the Hydra optical engine, involving motoring and short firing operation (i.e. for periods up to 5s) with the quartz piston, revealed two problems: (i) oil mist escaping from the crankshaft case through the lower piston rings fouled the 45° mirror and, (ii), the upper piston crown shifted slightly clockwise with respect to the piston extension. The former was partly resolved by reducing the oil quantity to the minimum possible level and the latter by shortening further the duration of the firing tests. In order to obtain a high-speed film, the engine was motored at the required speed, the electronic fuel injection system was activated and the camera was switched on immediately afterwards. The quartz window could remain adequately clean for about 10-20 firing strokes depending on the load. After each run the unit injector assembly and the engine head had to be removed to enable window cleaning; this proved to be a long and tedious procedure and suggests that a different way of getting access to the window for cleaning is

needed, e.g. removing the window from the bottom through the hollow intermediate barrel of the piston assembly.

One severe problem inherent to most photographic studies of diesel combustion is the relatively long ignition delay period associated with the lower than normal working temperature of the metal surfaces inside the combustion chamber. Following the recommendations of Fisher (1983), the coolant temperature was maintained at 94°C and inlet air was heated to about 40°C; to compensate for the reduction in air density, the fuelling level was adjusted accordingly. Despite these measures, the estimated ignition delay periods were longer by up to 40% than equivalent production engines since both the piston temperature and the residual gas composition over the few firing cycles were unrepresentative of common practice.

4.6.2 Analysis of films

High speed photography provided the spray penetration data used in Fig.4.45 for comparison with the corrected results for engine conditions obtained by the beam deflection technique (section 4.5.2). The conditions examined are identical to those of the flow and spray investigations and are summarised in Table 4.4; the medium swirl setting was not considered here due to its small difference from the high swirl setting (10% at IVC in terms of angular momentum according to Table 4.2). Cases $A_{1,2}$-$D_{1,2}$ correspond to cases A-D of Table 4.3 with the addition of the swirl setting as a working variable. The start of injection (SOI) was set to obtain start of combustion (SOC) at about 1-2°CA BTDC, which was identified by the change in slope of the instantaneous pressure curve as monitored on an oscilloscope and associated with the crankshaft position via a shaft encoder. To ensure that the SOI settings were justified, prolonged performance tests were carried out with the quartz windows replaced by steels blanks and showed that maximum torque was achieved.

Combustion sequences for the seven cases are shown in Figs.4.51-4.57. Figure 4.57 presents case A_1 in more detail than the others and is discussed here as representative of a typical sequence. The initial stage of fuel injection can be seen at 9.5°CA BTDC where the spray tips appear halfway between the nozzle and the bowl periphery in agreement with the start of injection at

Case No	Engine speed (rpm)	Swirl setting	Swirl ratio at 320°CA	SOI °CA BTDC	Injection period (ms)	Injection period (°CA)	Fuelling (mm³/inj)	AFR	SPR °CA BTDC	Ignition delay (ms)	Ignition delay (°CA)
A_1	1000	Low	2.53	11	1.35	8.1	22.8	34	0.5	1.75	10.5
B_1	1000	Low	2.53	11	1.90	11.4	37.6	20	1.0	1.66	10.0
C_1	2000	Low	2.53	13	1.00	12.0	23.2	33	1.0	1.00	12.0
D_1	2000	Low	2.53	14	1.40	16.8	36.2	21	1.0	1.08	13.0
A_2	1000	High	3.40	11	1.35	8.1	22.8	34	0.5	1.75	10.5
B_2	1000	High	3.40	11	1.90	11.4	37.6	20	0.5	1.75	10.5
C_2	2000	High	3.40	13	1.00	12.0	23.2	33	1.5	0.96	11.5
D_2	2000	High	3.40	14	1.40	16.8	36.2	21	1.5	1.04	12.5

Case & Figure No	SOC °CA BTDC	End of visible light °CA ATDC	Ignition delay ms	Ignition delay °CA	Swirl ratio ATDC
A_1, 4.57	2.0	70	1.50	9.0	3.2
B_1, 4.58	1.0	80	1.66	10.0	3.1
C_1, 4.59	0.5	80	1.04	12.5	--
D_1, 4.60	0.5	85	1.12	13.5	--
A_2, 4.61	2.0	72	1.50	9.0	5.6
B_2, 4.62	1.5	90	1.58	9.5	4.0
C_2, 4.63	1.0	85	1.00	12.0	4.7
D_2	1.5	--	1.04	12.5	--

Table 4.4 Summary of photographic tests in optical Hydra engine.

11°CA BTDC as also indicated by the needle lift transducer output (Table 4.5). At the next four frames (9°-7.5°CA BTDC) all four sprays propagate and impinge on the wall but no visual sign of combustion can be identified. All sprays appear to have a narrow spreading angle and to be unaffected by the air swirl in the piston bowl. This implies that the momentum of the sprays is much higher than that of the compressed swirling air. For an in-bowl swirl velocity at r=20mm of 16.2m/s, estimated in section 4.4.2, and a spray tip velocity of 52m/s (section 4.5.2) at 1000rpm, the momentum ratio between the spray and swirling air is about 150.

The first signs of combustion appear at 2°CA BTDC, which coincide with the end of fuel injection, in the downwind side of each spray as a result of the swirl motion and close to the bowl periphery. However, the ignition sites do not appear simultaneously for all four sprays, which implies that the sprays are not uniform in space and time. It is interesting to note that despite the visual identification of flames, the in-cylinder pressure trace is unaffected until 0.5°CA BTDC (Table 4.4) The location of the ignition sites suggests that combustion starts when small droplets at the spray edge, which were previously mixed with the entrained air and carried clockwise by the air swirl, generate local air-to-fuel ratios favourable for combustion. These flames spread quickly towards the bowl periphery, where clouds of evaporated fuel with low momentum due to the spray impingement on the wall, are convected by swirl. Flame propagation towards the injector follows extremely rapidly along the paths of the fuel sprays while the colour of the flames is predominantly yellow-white due to the soot formed by the rich mixture. At 2°CA ATDC the bowl is filled with flames which persist during the initial stages of the expansion stroke. Four distinct brown areas are present corresponding to each spray. At 15°CA ATDC the colour of the flames is still mainly white, although the temperature decrease affects some areas turning them to orange. The cooling of the soot particles continues well down the expansion stroke and at 40-50°CA ATDC they appear dull-red, whereas the last visible sign recorded on the film is at about 70°CA ATDC.

The exact crank angles at which these events take place and some particular combustion features vary for the different engine operating conditions. The ignition delay was calculated in terms of both the start of pressure rise (SPR) and the first appearance of visible light and both values are given in Table 4.4 with a maximum uncertainty of ±0.5°CA. The effect of

engine load, engine speed and swirl strength are examined separately and are summarised in Table 4.4 based on particular frames taken from the corresponding films.

A. Effect of engine load

Figure 4.52 shows the combustion development for case B_1 which is similar to A_1 but for the higher load of 37.6mm^3 per injection. The injection period and the combustion phase overlap by about 3º-4ºCA, which has also been observed in case D_1 (Fig.4.54); this seems to have an important influence on combustion development. At the lower load (Figs.4.51 and 4.55) almost all the fuel burns after the spray impinges on the wall, whereas at high load and towards the end of the injection period (around TDC), a portion of the fuel ignites before hitting the wall and burns with the characteristic colour of rich mixtures. Photographic records taken by endoscopic high speed photography in a similar type of engine using conventional fuel injection equipment (Werlberger and Cartellieri, 1987; Karimi, 1989) have shown that at high loads a substantial proportion of the fuel hits the wall before ignition at these loads. With the unit injector system and its higher injection pressures, it seems that an even higher proportion of the injected quantity impinges on the wall; this could give rise to longer combustion duration and higher soot emissions. The combustion duration, as indicated by the last visible light, is longer at higher loads and the difference between the two loads examined in terms of crankangle is 10-15º.

B. Effect of engine speed

The initiation of combustion at 1000rpm takes place simultaneously at several points about half-way across the bowl and close to the bowl periphery, whereas at 2000rpm the ignition sites are all close to the bowl wall. This is attributed to the increased penetration rate at the highest engine speed, observed also in the spray tip measurements (see section 4.5) in agreement with Fisher (1983). The effect of engine speed on ignition delay period is to increase it in terms of crankangle but not linearly, which effectively means a reduction in absolute time (see Table 4.4); this trend was found to be independent of both load and swirl.

C. Effect of swirl

From Figs.4.51 and 4.55, where the spray trajectories are clearly visible, it can be concluded that there is no effect of the swirl level on the penetration of the sprays before their impingement on the wall; as already discussed, this is attributed to the high spray momentum relative to that of the swirling air. The ignition delay period also does not seem to exhibit clear trends (Table 4.4) independent of load and speed. Extensive studies by Takahashi et al (1987), Spicher et al (1987) and Cartellieri and Herzog (1988) have shown contradictory results, probably due to the fact that swirl can act as both a positive and a negative mechanism on the ignition delay period (Karimi, 1989). High swirl levels can assist fuel evaporation and its rapid mixing with air, but at the same time can increase the heat transfer through the piston wall and disturb prepared fuel nuclei by making them too lean to ignite. This explains why different trends in the present study are present at high and low load. However, comparison between cases A_1 and A_2 shows that higher swirl levels can lead to faster burning. At 1°CA ATDC and high swirl (Fig.4.55) the piston bowl is almost entirely filled with white flames, whereas at the corresponding frame for low swirl (Fig.4.51) there are brown colour fuel-rich areas covering about half the bowl volume. This is due to the variable effect of swirl on the low-momentum clouds of evaporated fuel following their impingement on the wall; higher swirl carries more evaporated fuel and improves mixing with the fresh air. In small DI diesel engines, where even at low loads the sprays impinge on the piston walls, the role of swirl after the start of ignition becomes more crucial.

An estimate of the swirl velocities inside the piston bowl was made during the initial stages of combustion (5°-15°CA ATDC) by following the movement of a certain feature on successive individual frames, whenever that was possible. This assessment is difficult and the errors involved could be as high as ±10%. Assuming solid body rotation, swirl ratio values were calculated and are included in Table 4.4. The validity of these velocity estimates is relative since they are based on the swirling mass near the bowl base, which may not be representative of the whole mixture swirl ratio if flow stratification is present within the piston bowl. Based on the LDV results discussed in section 4.4.2 it can be deduced that initial differences of the swirl levels generated by the variable swirl mechanism persist even after TDC and

scale to some extent with engine speed. The swirl ratios after impingement are also affected by engine load due to the variable duration of the injection period during which the sprays interact with the swirling air.

4.7 PERFORMANCE TESTS

The performance of the optical Hydra engine was compared to its baseline version in terms of frictional losses, bmep and torque/power output, while data from the Ford York 2.5L production engine were used as reference. The baseline engine was tested at Ricardo and similar tests were performed in the course of this study with the optical engine employing the piston equipped with an aluminium blank, a triple air-jet to cool the piston and four steel blanks in the place of the quartz windows (see section 4.2.4 for more details).

The present study uses the definitions of engine mean effective pressure employed by Lancaster et al (1975), which are summarised below:

(i) tmep and $tmep_m$: thermodynamic mean effective pressure, based on the work generated or done at the face of the piston for the complete cycle and divided by the cylinder displacement. It is equal to the sum of the indicated and the pumping work and has a positive value for a firing engine and negative for a motored engine

(ii) bmep: brake mean effective pressure estimated from the torque absorbed by the dynamometer during firing tests.

(iii) mmep: motoring mean effective pressure estimated from the torque supplied by the dynamometer during motored tests.

(iv) fmep and $fmep_m$: friction mean effective pressure including the losses due to piston ring and bearing friction and the work to drive the valve train and accessories.

The following equations apply:

(i) mmep = fmep - tmep for the motored engine

(ii) bmep = tmep - fmep for the firing engine

4.7.1 Experimental system

In the course of these studies torque was measured by means of a load

cell which was calibrated prior to the tests and in-cylinder pressure was recorded by a piezoelectric transducer using the system described in section 2.3; the air consumption was measured by an orifice plate positioned upstream of a surge tank, which was connected to the engine inlet and was large enough (about 200 times the cylinder volume) to ensure steady flow through the plate. The exhaust emissions of the engine in terms of particulates and NO_x were measured by means of a Variable Split Particulate sampler (Cussons model P1815) and a chemiluminescent NO_x analyser (Signal series 7000). The exhaust flow from the engine was divided into two streams so that only part of the total flow could pass through a tunnel incorporated in the sampler; a certain quantity of the diluted exhaust gases was sampled via a probe, located on the tunnel centre line, and then passed through a membrane filter. The filter was weighted before and after the test by means of a scale with an accuracy of 0.1mg, while the dilution ratio was estimated by measuring the concentration of NO_x in the raw and diluted exhaust gases.

4.7.2 Results

The baseline engine tests were performed at 1200, 2400, 4000rpm, and the optical engine tests at 1000, 1200, 2400, 3000rpm. Preliminary engine tests at Ricardo with the baseline version showed that the swirl level generated by the variable swirl port did not affect the exhaust smoke at full load (Penwarden, 1987) and, therefore all the data reported by Ricardo were obtained at a medium swirl strength (corresponding to R_s=2.2, Fig.4.6.b); this swirl setting was selected as the best compromise between swirl ratio and volumetric efficiency. The injection timing was optimised at each engine speed and load to give minimum brake specific fuel consumption.

Prior to the firing tests, both engine versions were motored over their equivalent speed range in order to determine their frictional losses; results are plotted in Fig.4.58, together with the motoring losses for the Ford York 4-cylinder engine. Both versions of the Hydra engine exhibit higher mmep due to the inherently higher frictional losses of single cylinder engines; the mmep of the optical version is consistently higher than that of the baseline engine by about 0.5bars due to the higher frictional losses associated with the extended piston and liner. The volumetric efficiency of the optical engine was

Motored tests

Engine speed (rpm)	Maximum pressure(bars)	Polytropic exponent	MMEP (bars)	TMEM (bars)	FMEPm (bars)
1030	34.5	1.25	2.76	1.80	0.96
1200	35.8	1.29	2.79	1.74	1.05
1800	39.1	1.30	3.02	1.64	1.38
2000	40.8	1.31	3.15	1.74	1.41
2400	42.3	1.33	3.41	1.79	1.62
3000	43.5	1.33	4.03	1.96	2.07

Firing tests

Engine speed 1200 rpm					
Swirl setting	AFR	Max. pressure (bars)	BMEP (bars)	TMEP (bars)	FMEP (bars)
high	47	57.1	0.82	2.84	2.02
high	35	58.9	1.95	4.43	2.48
high	27	60.3	2.91	5.75	2.84
high	20	59.5	3.38	6.38	3.00
low	47	56.8	1.06	3.11	2.05
low	35	57.6	1.83	4.26	2.43
low	27	59.0	2.93	5.66	2.73
low	20	58.8	3.50	6.52	3.03

Engine speed 2000 rpm					
Swirl setting	AFR	Max. pressure (bars)	BMEP (bars)	TMEP (bars)	FMEP (bars)
high	46	63.8	0.82	2.25	1.68
high	34	67.0	1.90	3.77	1.87
high	26	68.4	3.02	4.88	1.86
high	19	68.3	3.79	5.71	1.92
low	46	62.4	1.03	2.72	1.69
low	34	65.6	1.99	3.80	1.81
low	26	67.0	3.15	5.14	2.00
low	19	67.0	3.86	5.87	2.01

Engine speed 3000 rpm					
Swirl setting	AFR	Max. pressure (bars)	BMEP (bars)	TMEP (bars)	FMEP (bars)
high	34	72.0	1.51	3.67	2.16
high	23	71.5	2.88	5.10	2.22
high	17	72.0	3.52	5.88	2.35
low	34	69.0	1.67	3.80	2.13
low	23	70.4	3.10	5.37	2.27
low	17	71.8	3.61	6.03	2.42

Table 4.5 Summary of performance tests in optical Hydra engine.

also measured and found to be identical to the baseline engine at the same swirl setting, due to the fact that the same air filter-inlet manifold-port assembly was used; the variation of volumetric efficiency with engine speed is presented in Fig.4.59.

The performance of the two engine versions is presented in Fig.4.60 in terms of bmep plotted against air-to-fuel ratio (AFR) at three engine speeds. These curves were combined with the fuelling levels derived from Fig.4.42 to produce the simulated torque and power curves shown in Figs.4.61.a, b at the lower air-to-fuel ratio (i.e. higher load) of 20; the torque and power curves of the 4-cylinder Ford York engine (Bird, 1985), are also included in Fig.4.61 for comparison.

In-cylinder pressure measurements were obtained under both motoring and firing operation in the optical Hydra at various settings of engine speed, load and induction swirl. These instantaneous traces were processed to provide the maximum in-cylinder pressure and the thermodynamic mean effective pressure for each test case. The results, combined with the dynamometer measurements, are presented in Table 4.5 as values averaged over at least five individual cycles in order to reduce the effect of cycle-to-cycle variation.

The exhaust emissions of the optical engine in terms of particulates and NO_x were measured at the same settings of speed and load used for the characterisation of the fuel injector (cases A-D, Table 4.3). The particulate emissions at medium to high load for both engine speeds (1000, 2000rpm) were within the range 500-1000 mg/m^3 which according to Alkidas (1984) correspond to Bosch smoke numbers of 6-7. These values are higher by about 2 units from the corresponding values for the baseline version (Penwarden, 1987) and justification for this is given in the next section. The NO_x levels emitted by the optical engine varied between 200 and 600ppm, which are comparable to those of the baseline version due to the similar compression ratios.

4.7.3 Discussion

The baseline Hydra engine will now be compared with the Ford York production engine, followed by a more detailed discussion on the two versions

of the Hydra engine.

Figures 4.61.a, b show that the power and torque of the 4-cylinder Ford engine are 4-5 times higher than the corresponding values of the baseline engine throughout the speed range. On a smoke level basis, the baseline Hydra engine compares well with the Ford multi-cylinder at high AFR but poorly at low AFR especially at high engine speeds (Penwarden, 1987). It was expected that the unit injector fitted to the Hydra would enhance the combustion performance, due to the improved atomisation associated with the higher injection pressures. This, however, proved not to be the case and a possible explanation is the non-detailed matching of the injector nozzle with the particular combustion chamber geometry. It seems that the overpenetration of the four sprays, observed in the high speed photography (section 4.6.2) and supported by the atmospheric fuel injection results (section 4.5.2), dominated the combustion process causing increased smoke levels. Another contributing factor at high load and medium-to-high speeds is the reduced volumetric efficiency (7% lower than the Ford multi-cylinder engine according to Penwarden, 1987).

An initial check on the correct operation of the optical Hydra engine was to examine the motoring pressures. Table 4.5 indicates that peak in-cylinder pressure was a function of engine speed, ranging from 34.5bars at about 1000rpm to 43.5bars at 3000rpm; this is due to the fact that air leakages through the special compression rings (section 4.2.4), as well as heat losses through the cylinder walls decrease as the duration of the compression stroke shortens with increasing engine speed. The polytropic exponent values were evaluated based on the real geometric compression ratio (i.e.V_{IVC}/V_{TDC}) and found to vary within the range 1.25-1.33, which is considered to be reasonable (Lancaster et al, 1975) for research or even production engines.

Figure 4.60 shows that at engine speeds of 1200 and 2400rpm, where data are available for both engines, the performance of the optical engine is consistently inferior to that of the baseline. The reduction, in terms of bmep is negligible at low load and medium engine speed (Fig.4.60.c) but increases to around 1bar at medium load and low speed(Fig.4.60.a), and reaches more than 2bars at high loads (Fig.4.60.a and c). The deterioration in brake performance is partly attributed to the increased frictional losses of the

double piston assembly used in the optical engine, as illustrated in Fig.4.58. Furthermore, the cylindrical shape of the piston-bowl in the optical version is different from the toroidal shape with the central tip of the Ford York engine which has proven to offer superior performance. Sampling-probe techniques have shown that in DI diesel engines the highest particulate concentration is found in the core region of each spray close to the nozzle tip, where local average equivalence ratios are very rich (Heywood, 1988). The presence of the central tip in the bowl base physically constrains this area and enhances the mixing process of the rich core giving rise to leaner equivalence ratios towards the bowl periphery. On the contrary, the flat bottom of the optical engine piston-bowl is not able to enhance this vital mixing process, resulting in relatively large quantities of hydrocarbons left unburnt. This explains the excessive particulate emissions mentioned in the previous section and, along with the increased frictional losses, contributes to the poor brake performance of the optical engine; the relative importance of these two factors is examined further using the results from the in-cylinder pressure recordings.

Table 4.5 shows that the friction mean effective pressure during the motored tests of the optical engine increases monotonically with speed, varying within 0.96-2.07bars According to Lancaster et al (1975), the corresponding values during firing operation should be similar, which is not the case for the present engine. Fmep is 1-2bars higher than $fmep_m$ at 1200rpm and 0.3-0.6bars higher at other engine speeds; however, it is only a weak function of load and cannot explain the severe reduction in the brake performance (Fig.4.60) at medium to high loads. Additional losses are probably due to the irregular double piston movement which, at low engine speeds, wobbles excessively under the forces caused by the combusting gases.

Following this investigation it can be concluded that the increased frictional losses are the main cause of the inferior brake performance of the optical engine at low loads (especially at low speeds), whereas the poor combustion efficiency of the cylindrical piston-bowl/unit injector combination prevails at medium and especially high load, resulting in drastically reduced brake performance.

The effect of swirl on the combustion performance of the optical engine was also examined based on Figs.4.60.a, b, c and Table 4.6. The results show

that only minor differences exist between the brake or the thermodynamic values with no clear trends within the range of the swirl levels examined. It should be noted however, that there is a clear trend in the maximum in-cylinder pressures recorded during these tests; higher swirl is consistently associated with higher pressures, which implies faster burning. This is in agreement with the findings of the combustion photography investigation (section 4.6.2) and other studies (Khan et al, 1972; Taylor, 1985). The fact that this trend was not observed in the brake performance is related to the excessive momentum of the sprays relative to the swirling air mass at all swirl settings (section 4.6.2).

4.8 CONCLUSIONS

A detailed study was performed on the flow, spray, combustion and performance of a Ricardo single-cylinder DI diesel based on the Ford York 2.5L production engine and equipped with a variable swirl inlet port, an electronic unit injector and windows to allow the use of optical techniques under motored and firing conditions.

The steady-flow tests performed with the Hydra cylinder head showed that:

(1) The variable swirl port generated swirl ratios between 1.6 and 3 which are comparable to the 2.6 swirl ratio of the Ford production engine, but reduced the breathing capacity at medium and high swirl settings.

(2) The velocity distributions around the valve curtain area were typical of helical ports at low swirl setting of the Hydra port, whereas at medium and high swirl setting they exhibited characteristics of a hybrid helical-directed port.

Measurements of the swirl and axial velocity components obtained by laser Doppler velocimetry close to the cylinder head during the induction and compression stroke at three swirl settings and engine speeds between 1000 and 3000 rpm showed that:

(3) The variable swirl mechanism influences the in-cylinder flowfield during the induction and compression stroke by controlling the relative strength of the two counteracting vortices, which is typical of helical

ports.

(4) The swirl spatial distributions reflected closely the port characteristics at BDC of induction but during the compression stroke the dominant factor that shaped the swirl profiles was the time available for flow development which is inversely proportional to engine speed.

(5) Higher initial swirl gave rise to higher losses during compression.

(6) The swirl centre oscillated periodically during the compression stroke with a characteristic frequency scaling with engine speed; it was close to the cylinder axis at early compression and moved progressively towards the eccentric bowl axis.

(7) The axial flow patterns were dominated during the induction stroke by the incoming jet through the annular valve passage and did not scale with engine speed. Between BDC and IVC at low-medium engine speeds a back flow towards the inlet valve was identified. During the compression stroke, the axial mean velocities were reduced to less than $2V_p$, while maintaining different spatial distributions at different engine speeds. By 320°CA the rms of both the axial and swirl velocity fluctuations have decayed to less than $0.8V_p$.

The unit injector was characterised under atmospheric conditions by means of laser Doppler velocimetry and laser beam deflection in terms of spray-tip penetration and axial droplet velocities and the results showed that:

(8) Spray-tip velocities along the centreline varied within the range 100-200m/s as a function of the distance from the nozzle tip and depended on engine speed rather than engine load. These values were reduced under engine operating conditions by a factor of 2.5 relative to the atmospheric tests.

(9) Ensemble-averaged droplet velocities measured by LDV close to the spray tip were in good agreement with spray-tip measurements, while droplets or ligaments existing inside the main fuel cloud were found to move with even higher velocities in the range 200-260m/s. Some oscillations of the temporal mean profiles were observed and attributed to the fuel line pressure variations inside the injector body.

(10) At higher engine speeds, injection-line pressures were higher and gave rise to higher droplet velocities.

High speed photographs of the combustion process under different conditions of engine speed, swirl ratio and load showed that:

(11) The penetration of the injected fuel from the unit injector remained unaffected by swirl strength, whose influence became important after impingement on the wall.

(12) At low-to-medium load ignition started after the end of fuel injection and at different sites midway along the bowl radius, whereas at high loads injection and combustion overlapped and ignition started near the piston walls.

(13) At constant load, ignition delay was found to increase but less than linearly with engine speed.

(14) Combustion duration, as determined by the last visible light, became shorter with increasing swirl strength despite the fact that the effect of swirl on ignition delay was not consistent with changes in load and speed.

Overall performance and emissions tests showed that the optical Hydra engine gave 40% lower torque output and higher particulate emissions than the baseline engine tested at Ricardo under similar operating conditions due to higher frictional losses caused by the extended piston and liner and the non-optimised combination of induction swirl level, injection system and piston-bowl geometry.

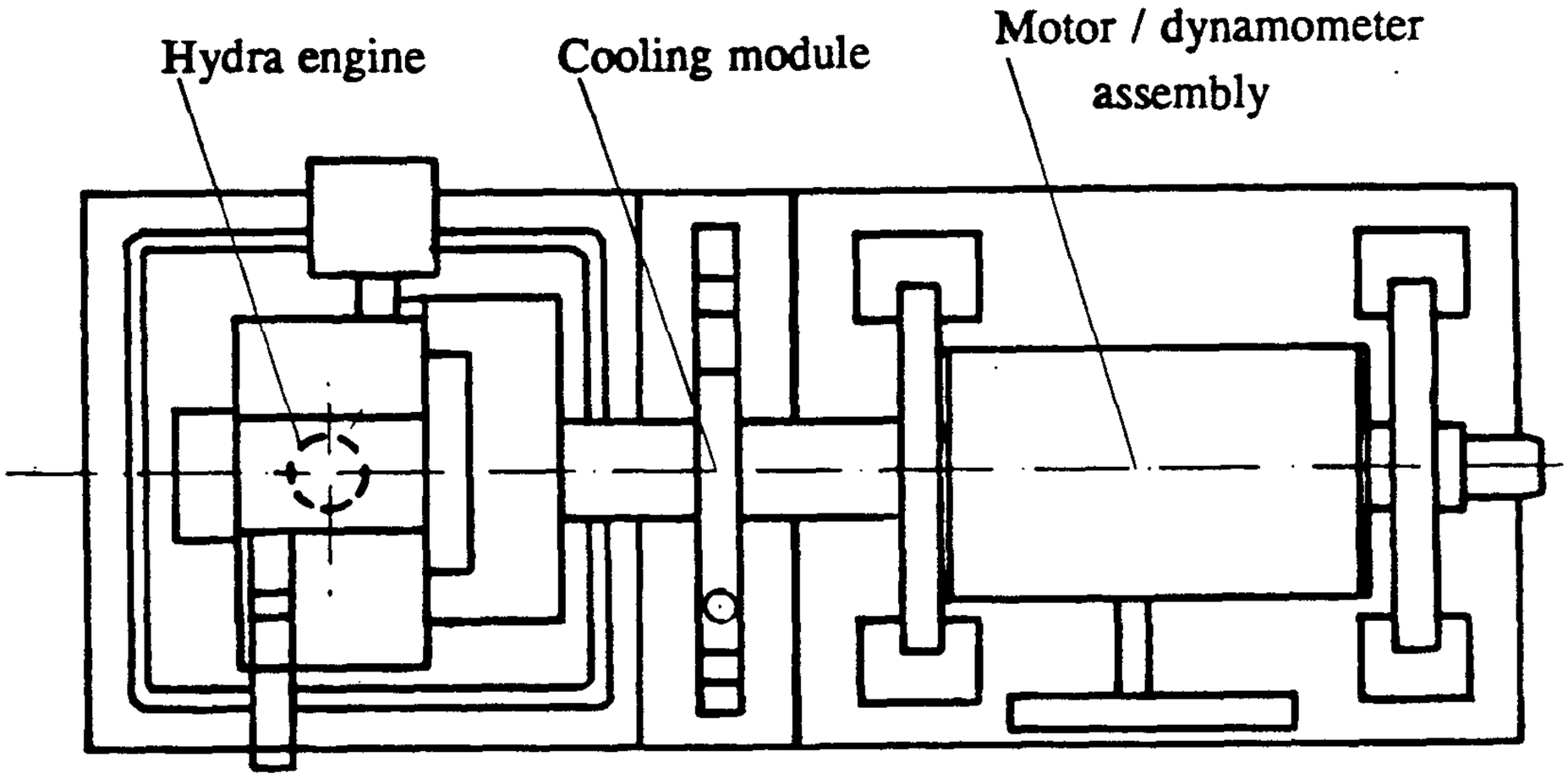


Figure 4.1 Top view of the Hydra engine rig.

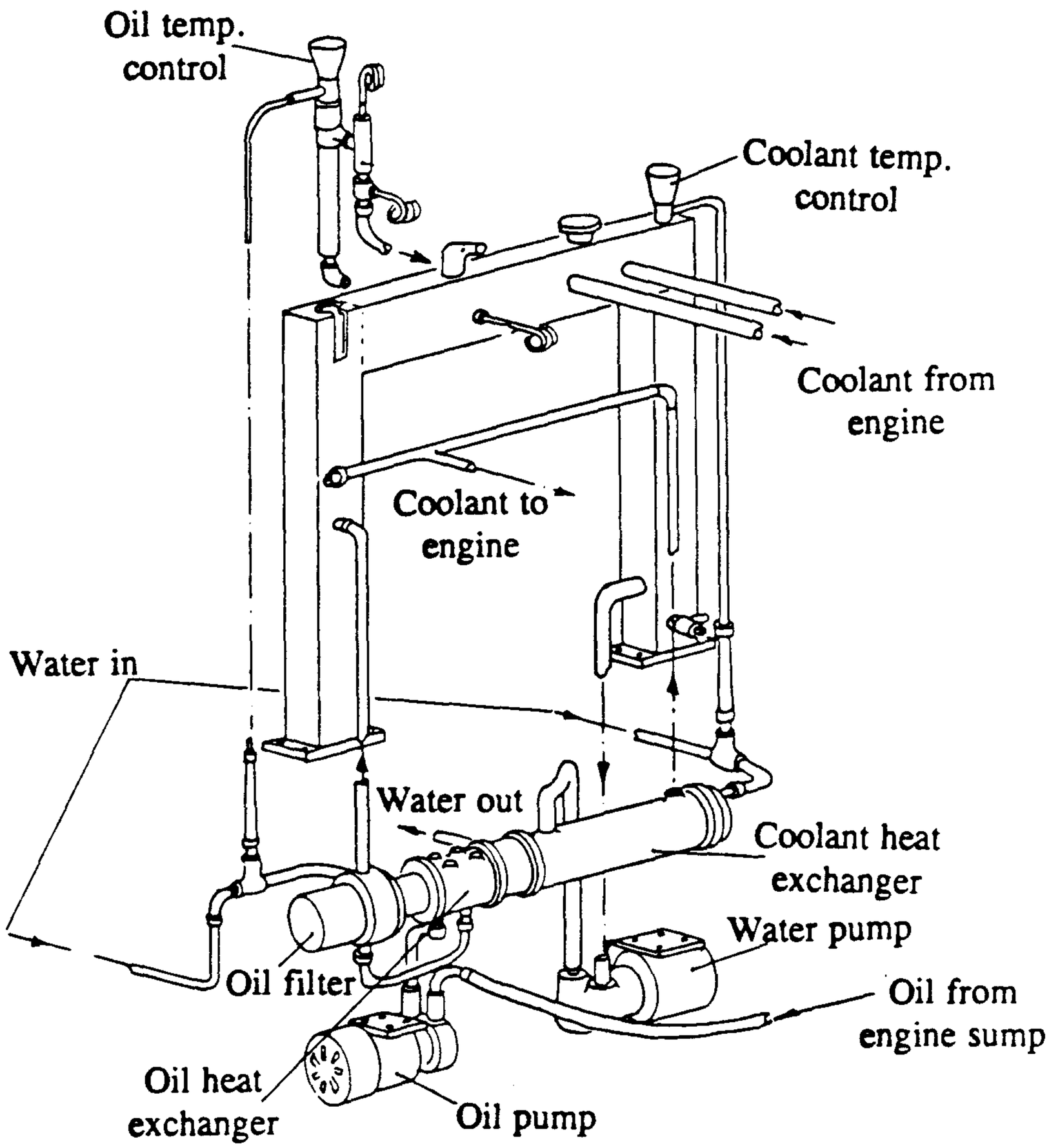


Figure 4.2 Cooling module.

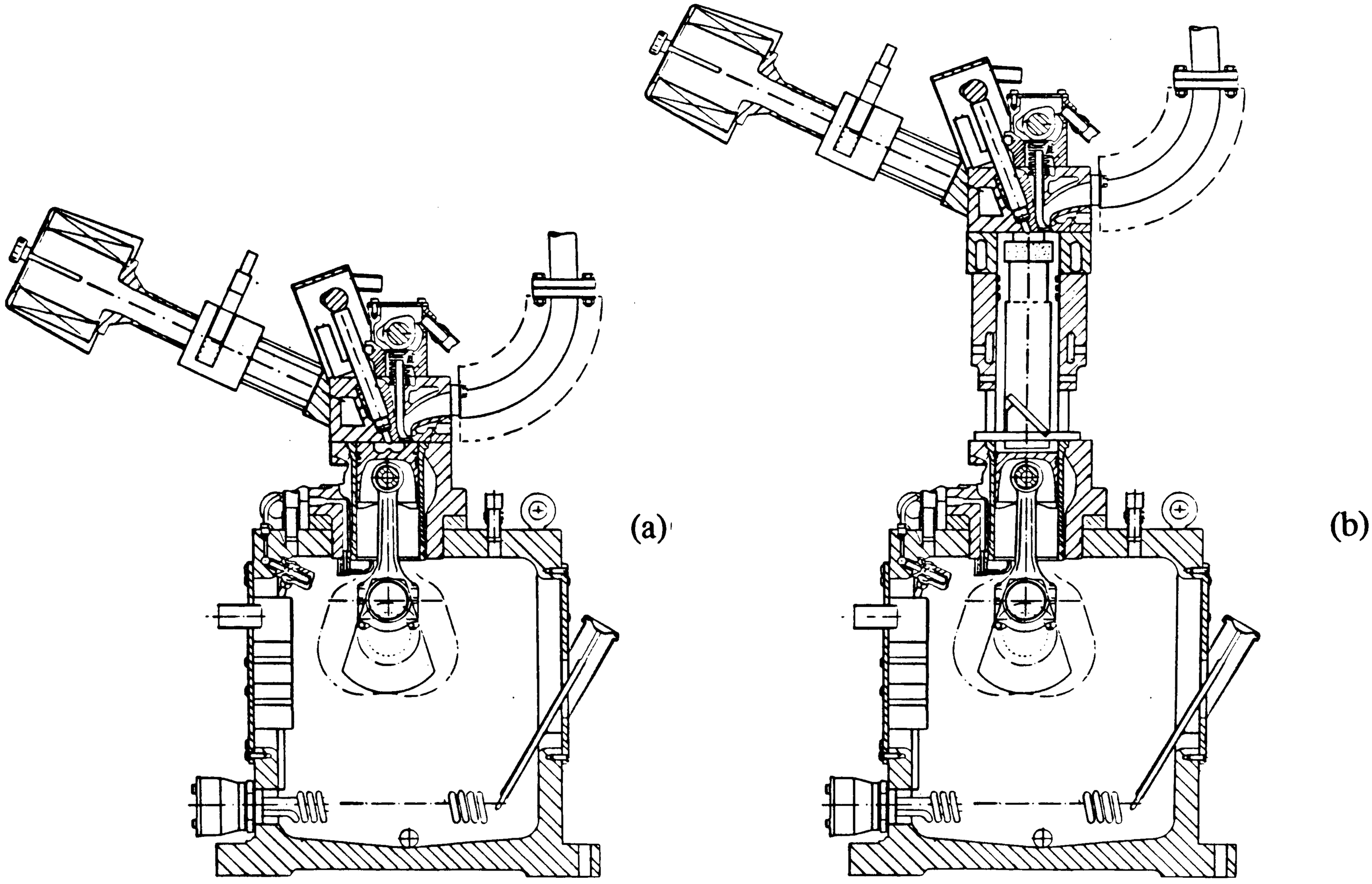


Figure 4. 3 Overall view of the Hydra engine. (a) baseline version (b) optical version

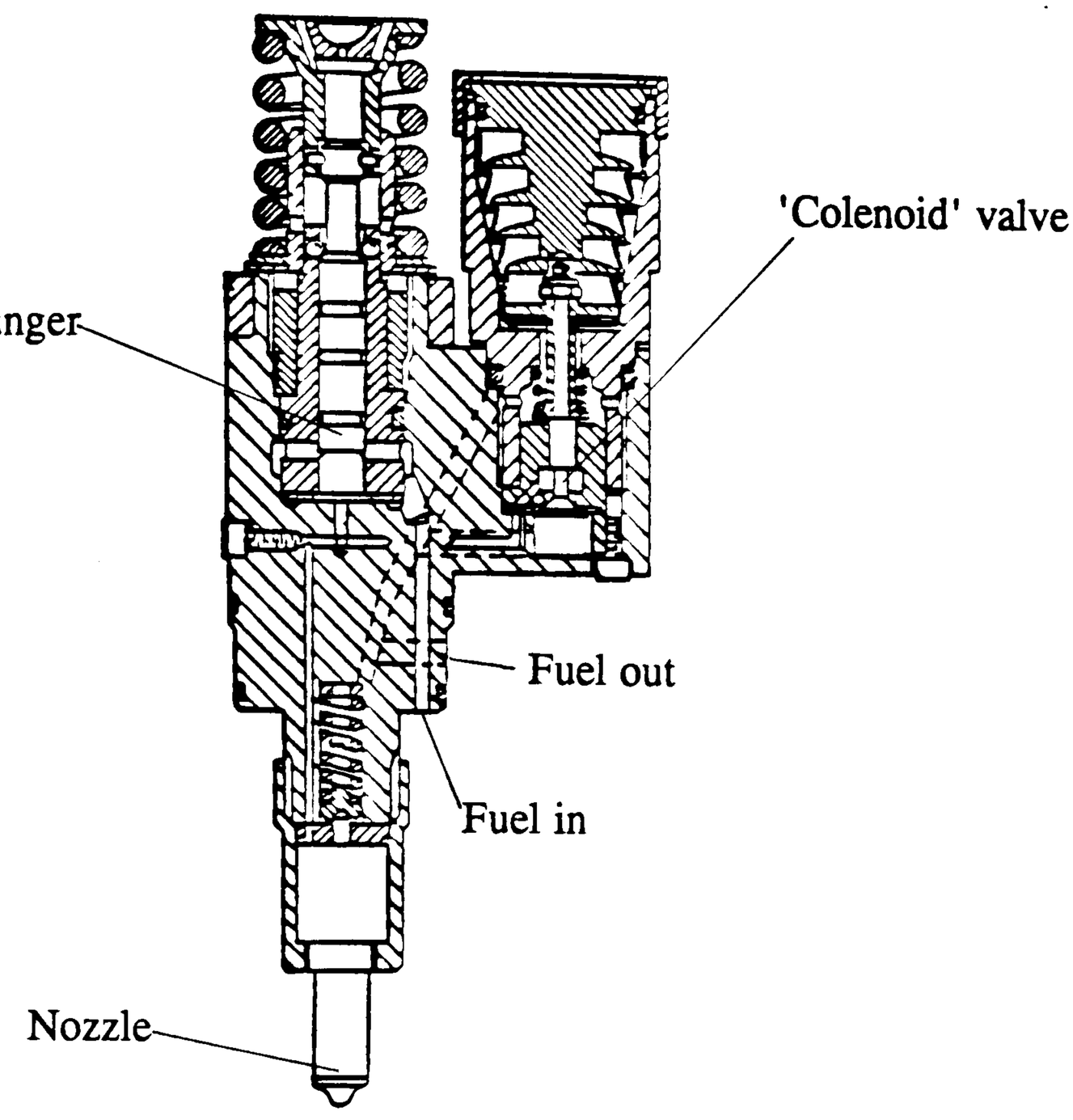


Figure 4.4 Cross-section of the unit injector.

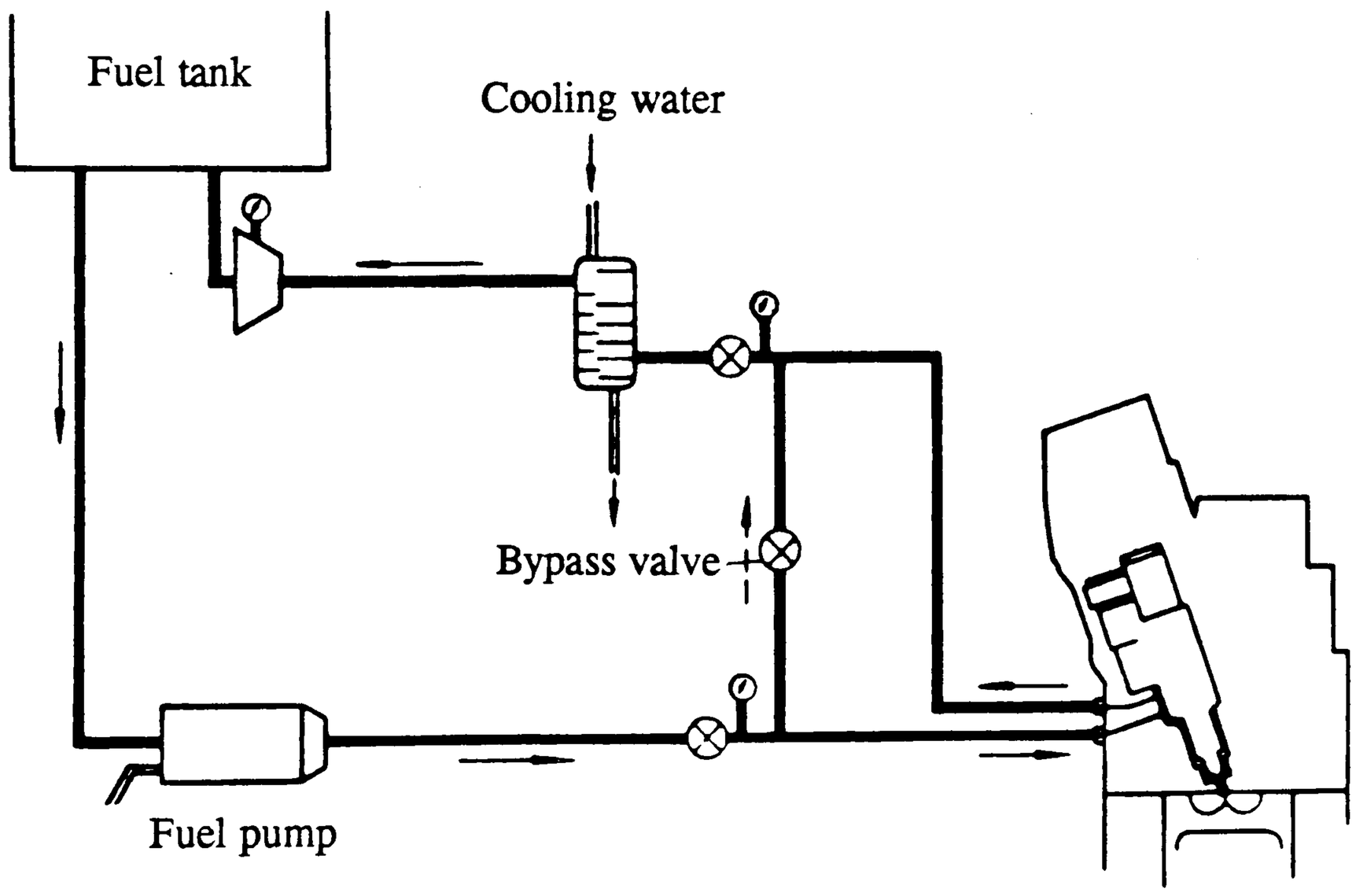


Figure 4.5 Layout of the fuel circuit.

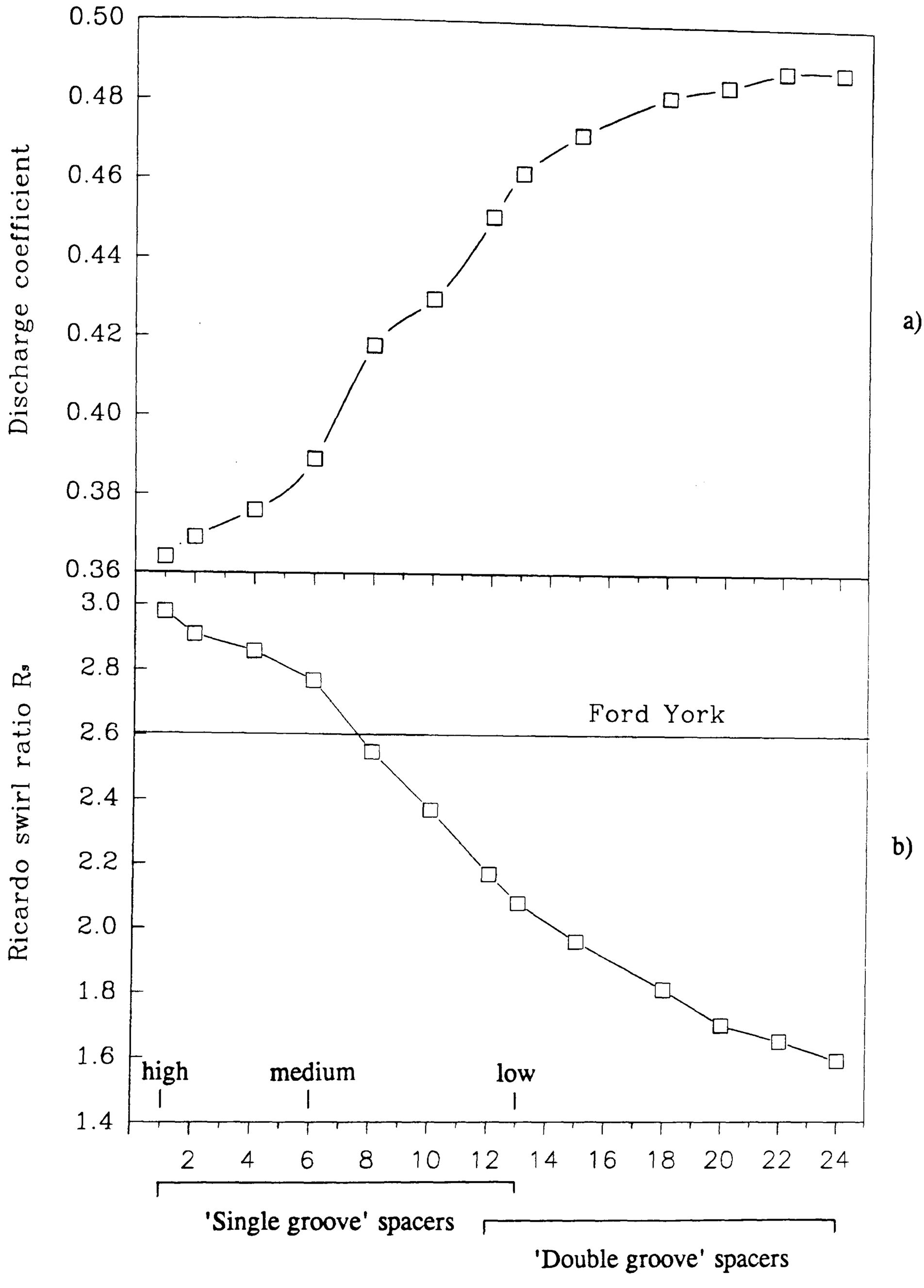


Figure 4.6 Variation of (a) discharge coefficient and (b) Ricardo swirl ratio with setting No of the variable swirl mechanism.

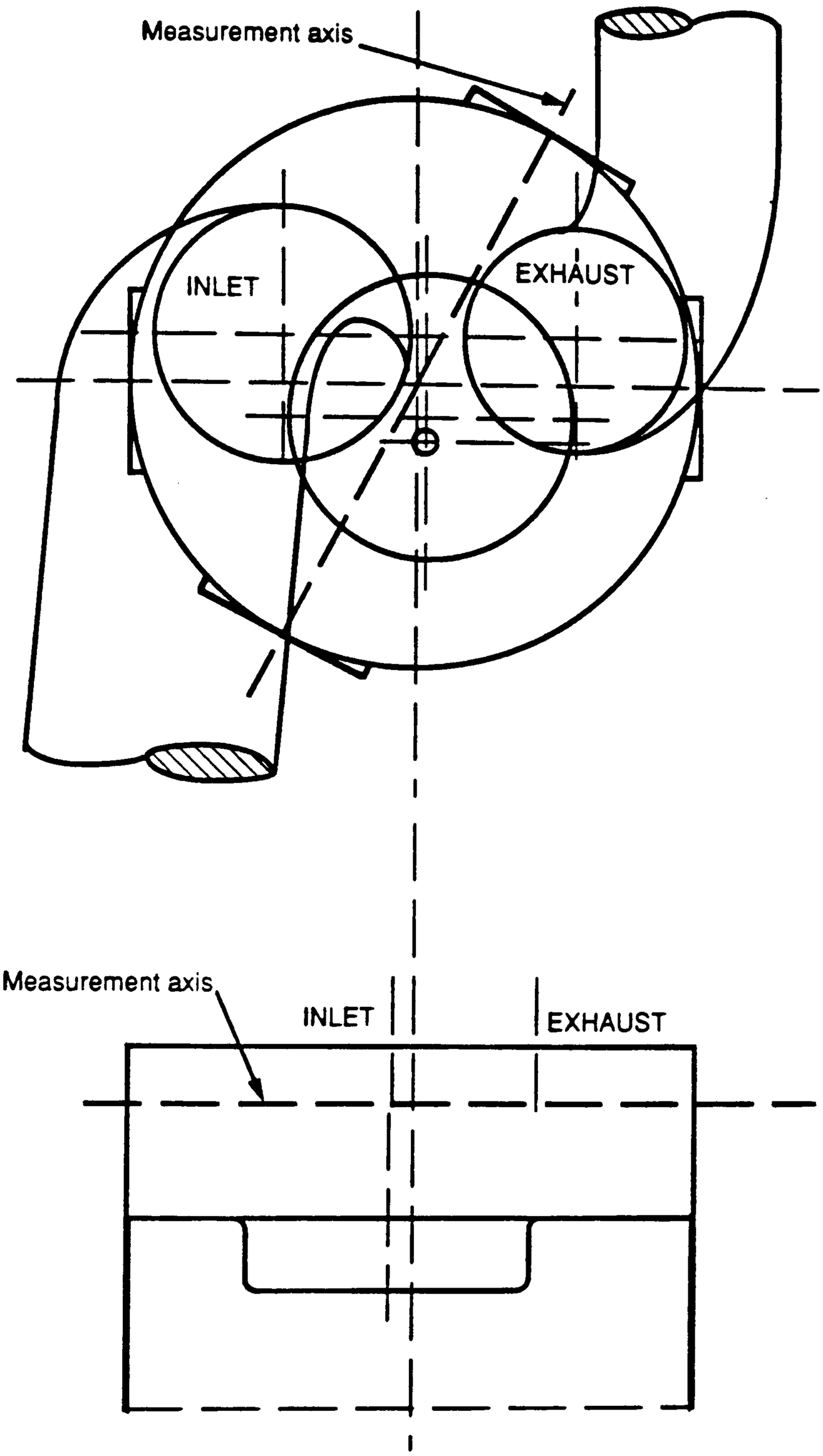


Figure 4.7 Top (a) and front (b) view of the optical engine cylinder showing measurements axis.

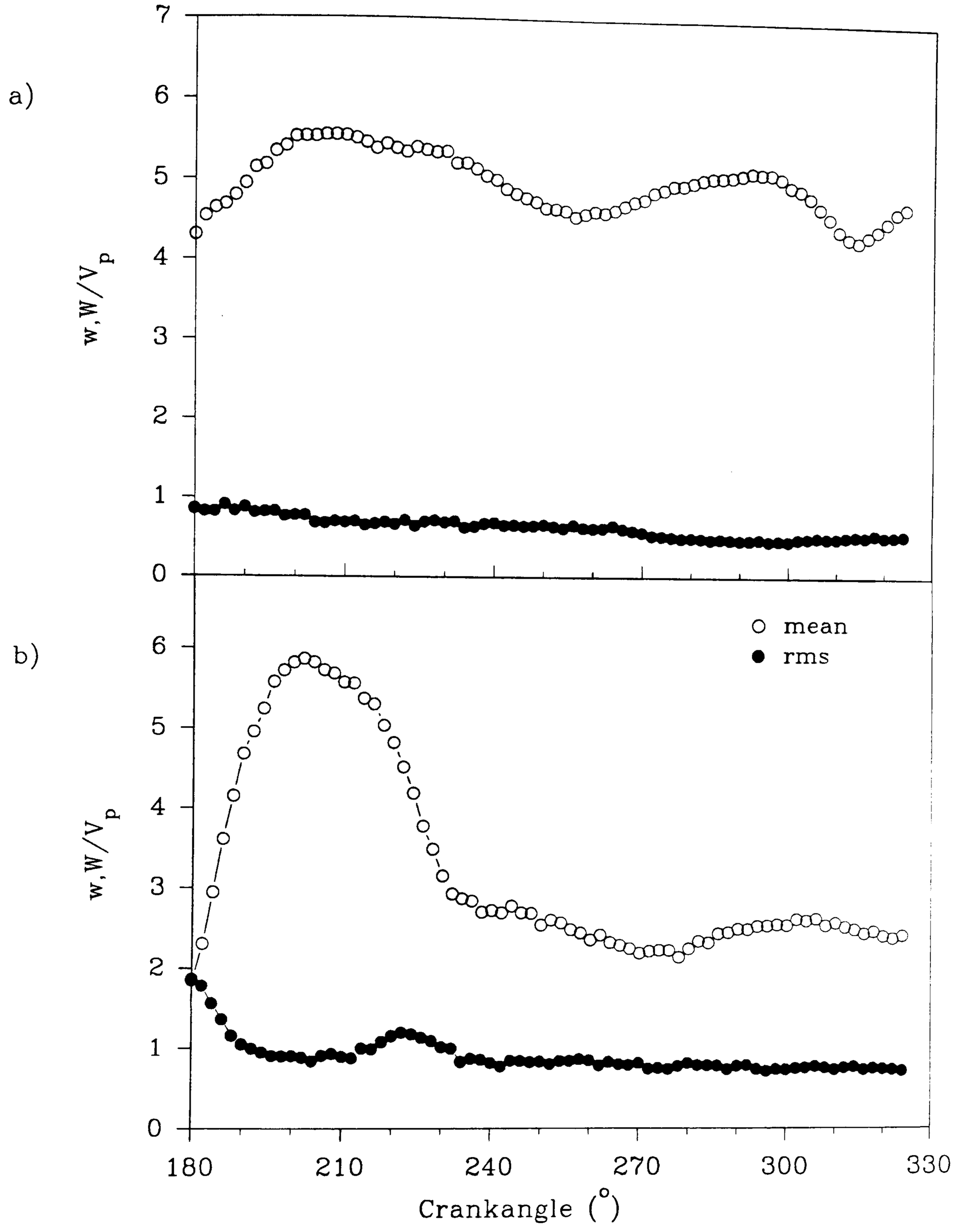


Figure 4.8 Temporal profile of swirl mean and rms velocities at (a) r=35mm and (b) r=15mm (high swirl, 2000rpm).

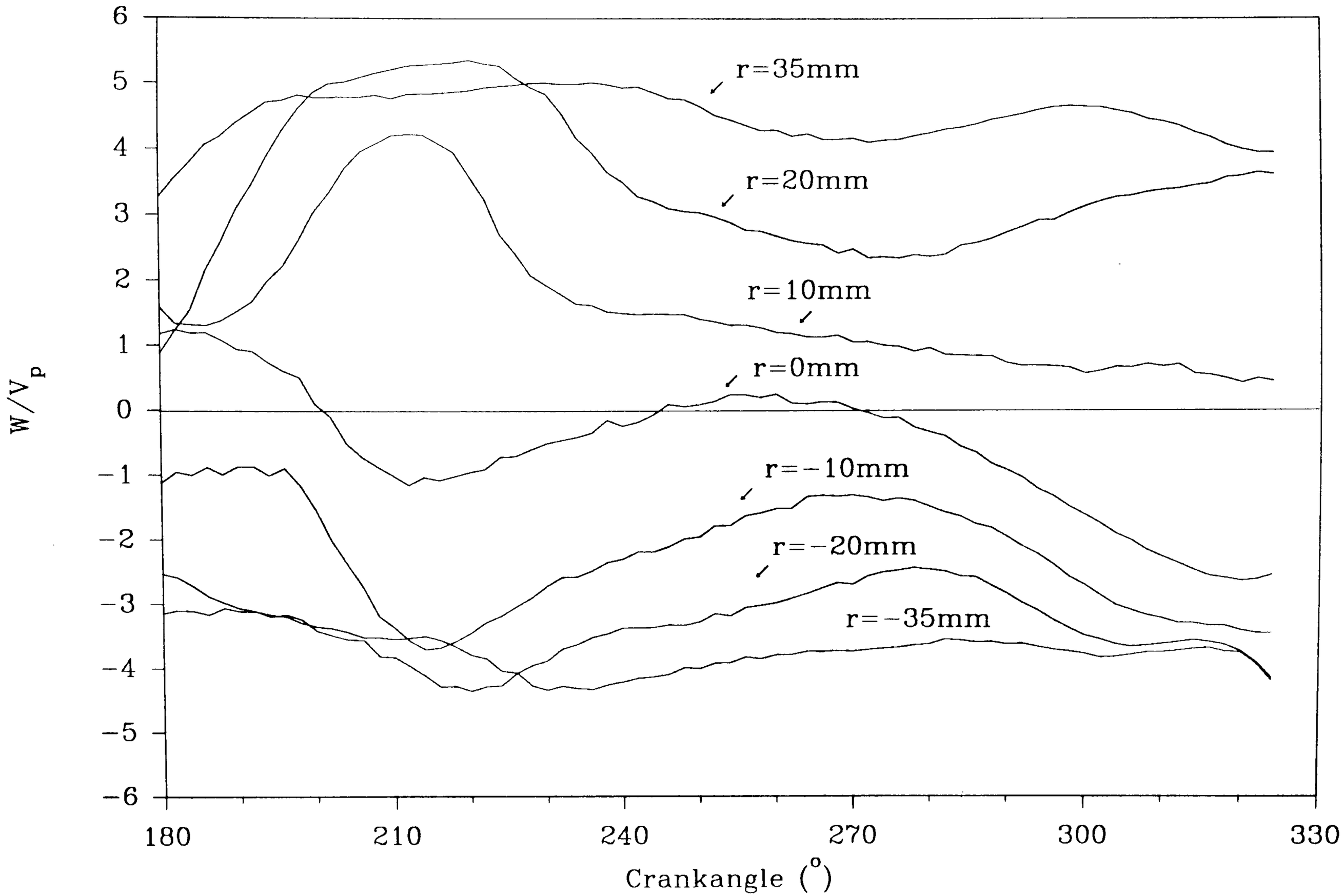
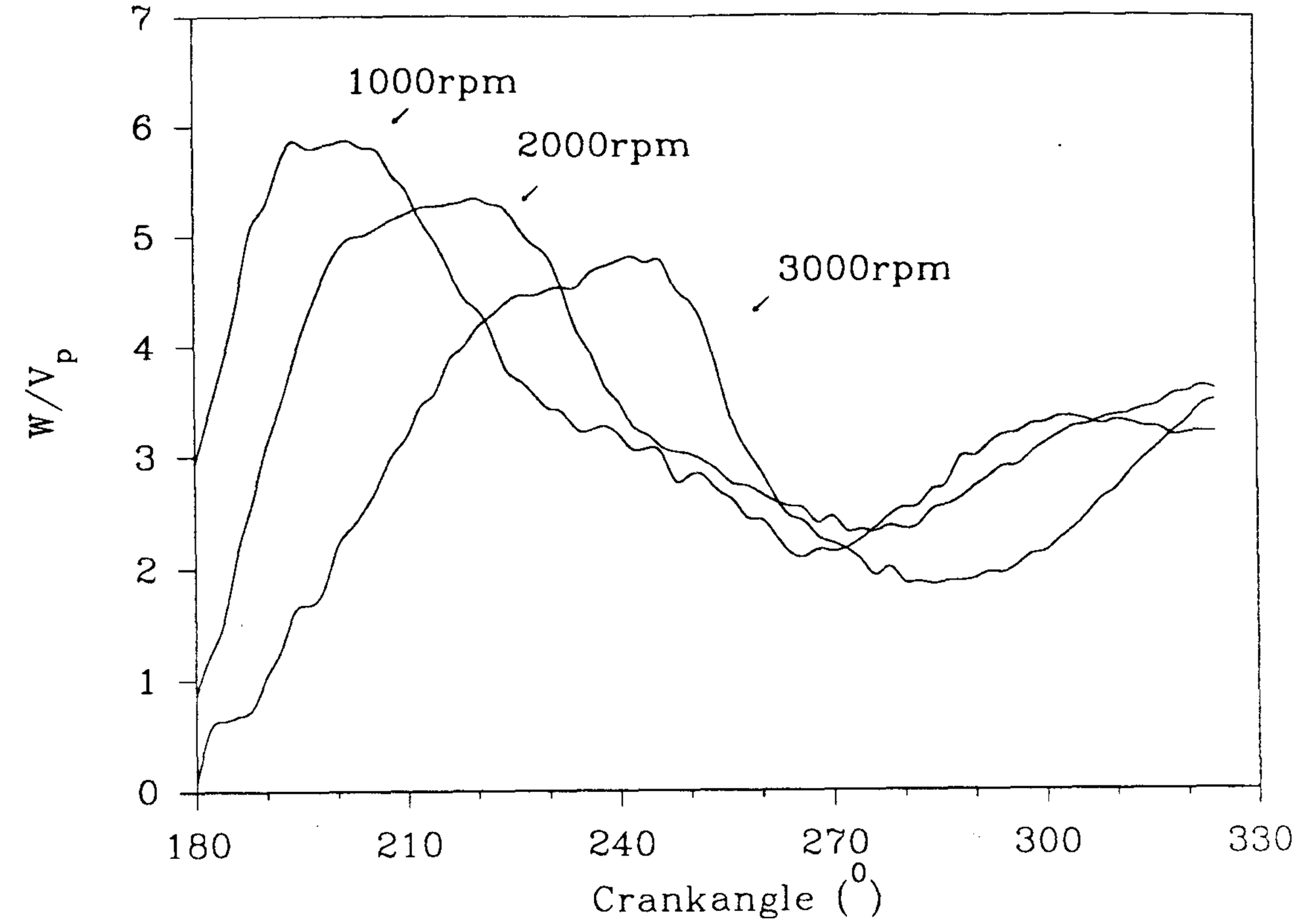


Figure 4.9 Temporal profiles of swirl mean velocities at different radial locations (medium swirl, 2000rpm)



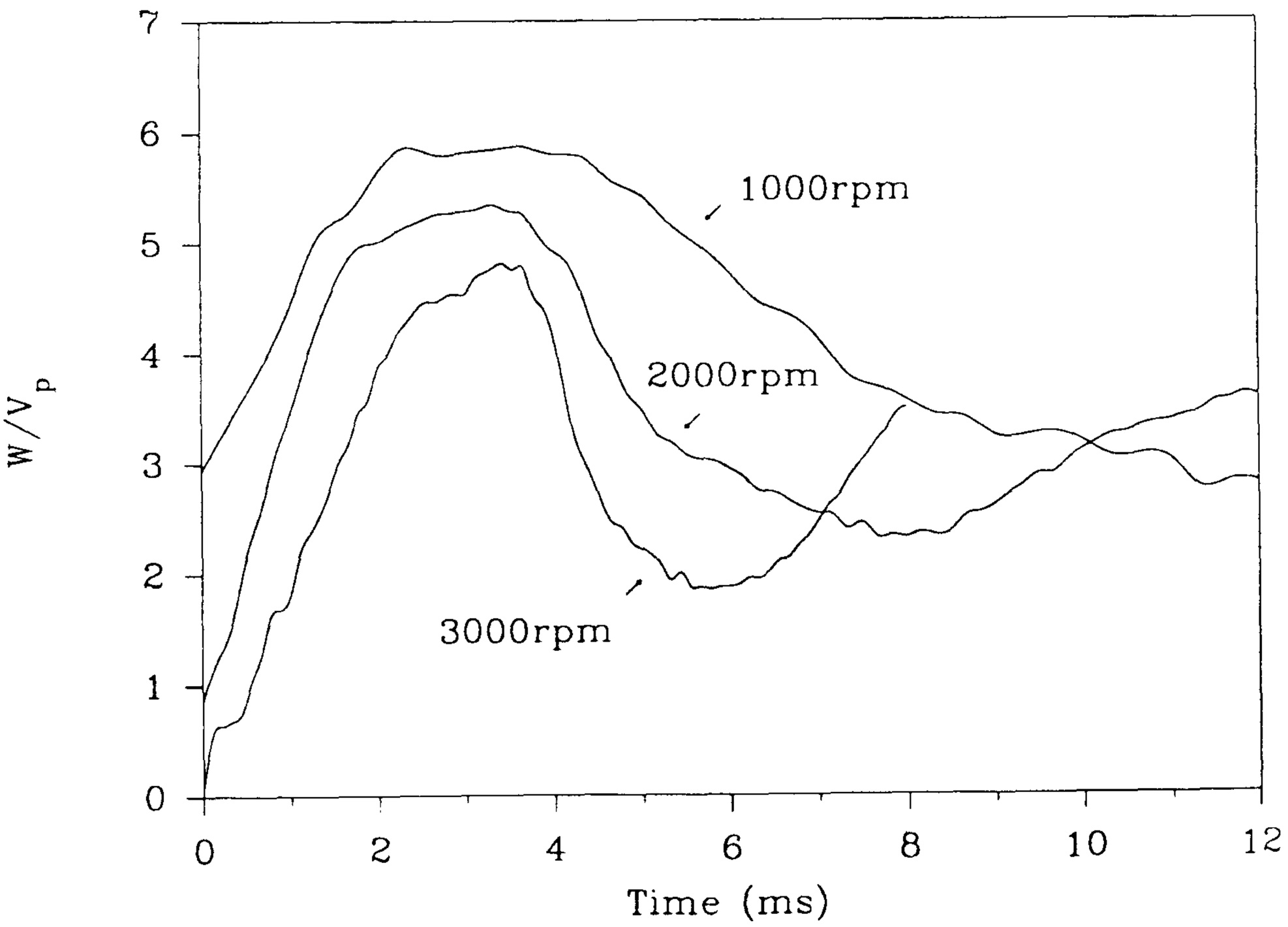


Figure 4.10 Swirl mean velocities at different engine speeds as a function of (a) crankangle and (b) time (r=20mm, medium swirl).

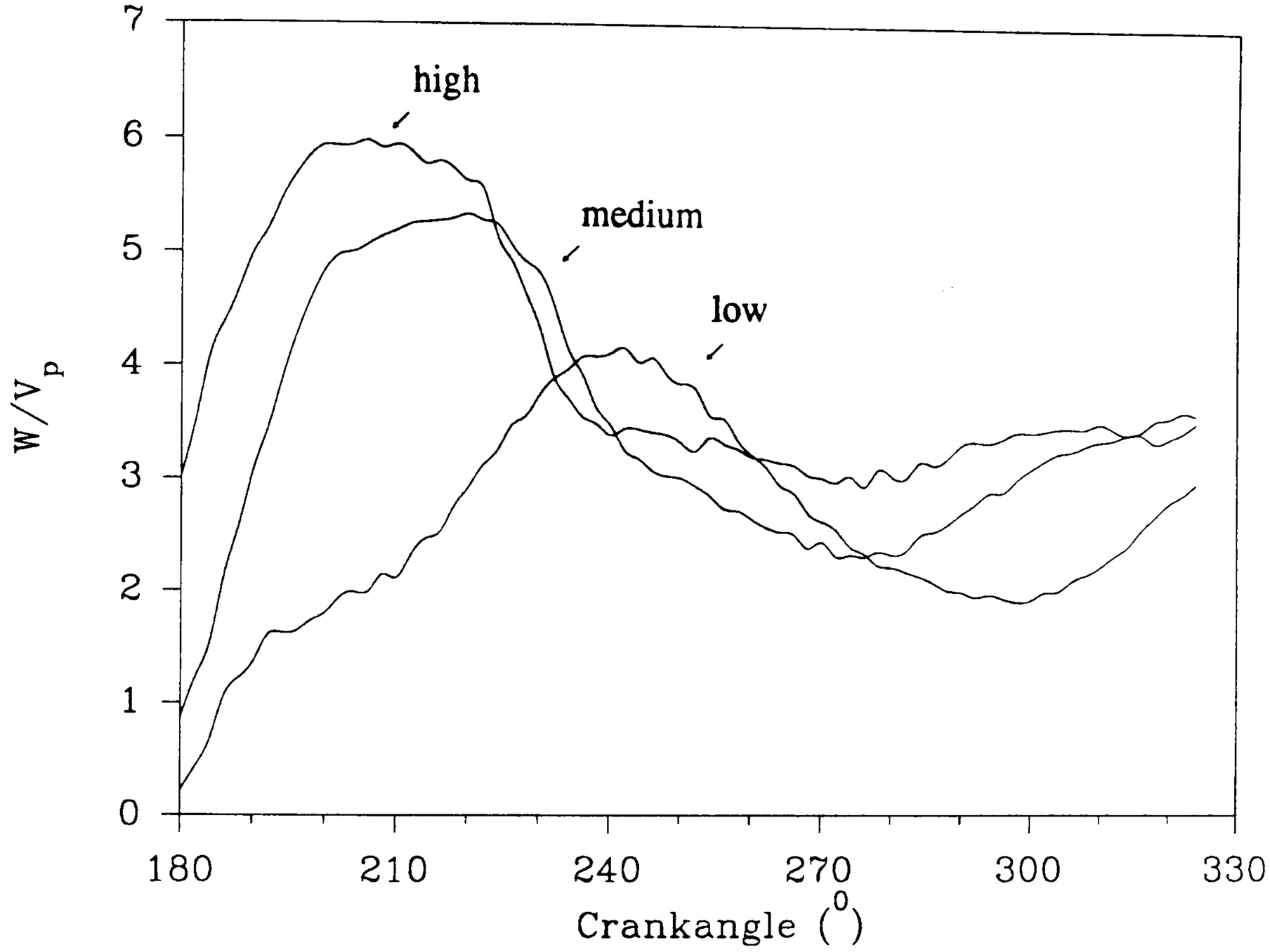


Figure 4.11 Temporal profiles of swirl mean velocities at different swirl levels (r=20mm, 2000rpm).

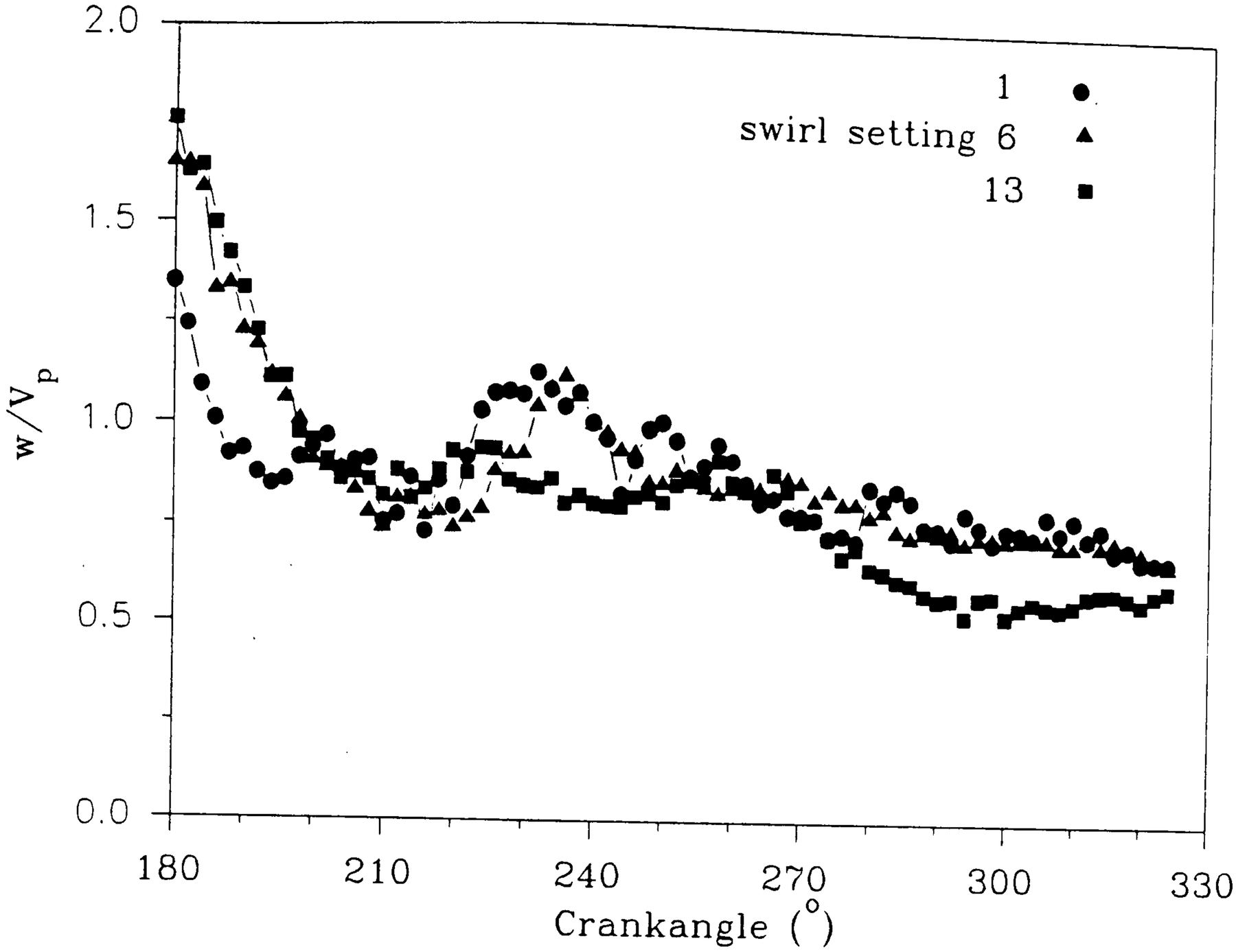


Figure 4.12 Temporal profiles of swirl rms velocities at different swirl levels (r=20mm, 2000rpm).

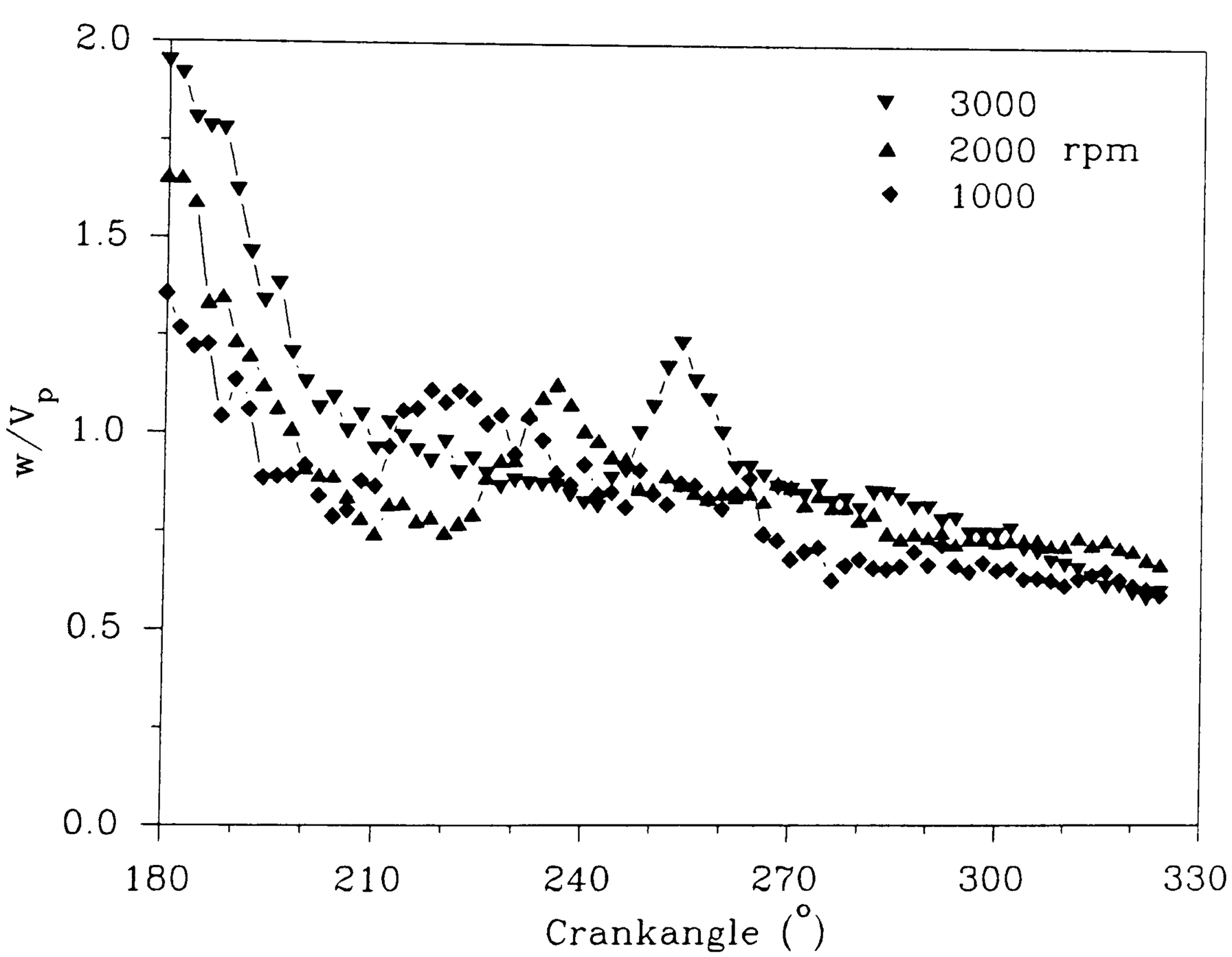


Figure 4.13 Temporal profiles of swirl rms velocities at different engine speeds (r=20mm, medium swirl).

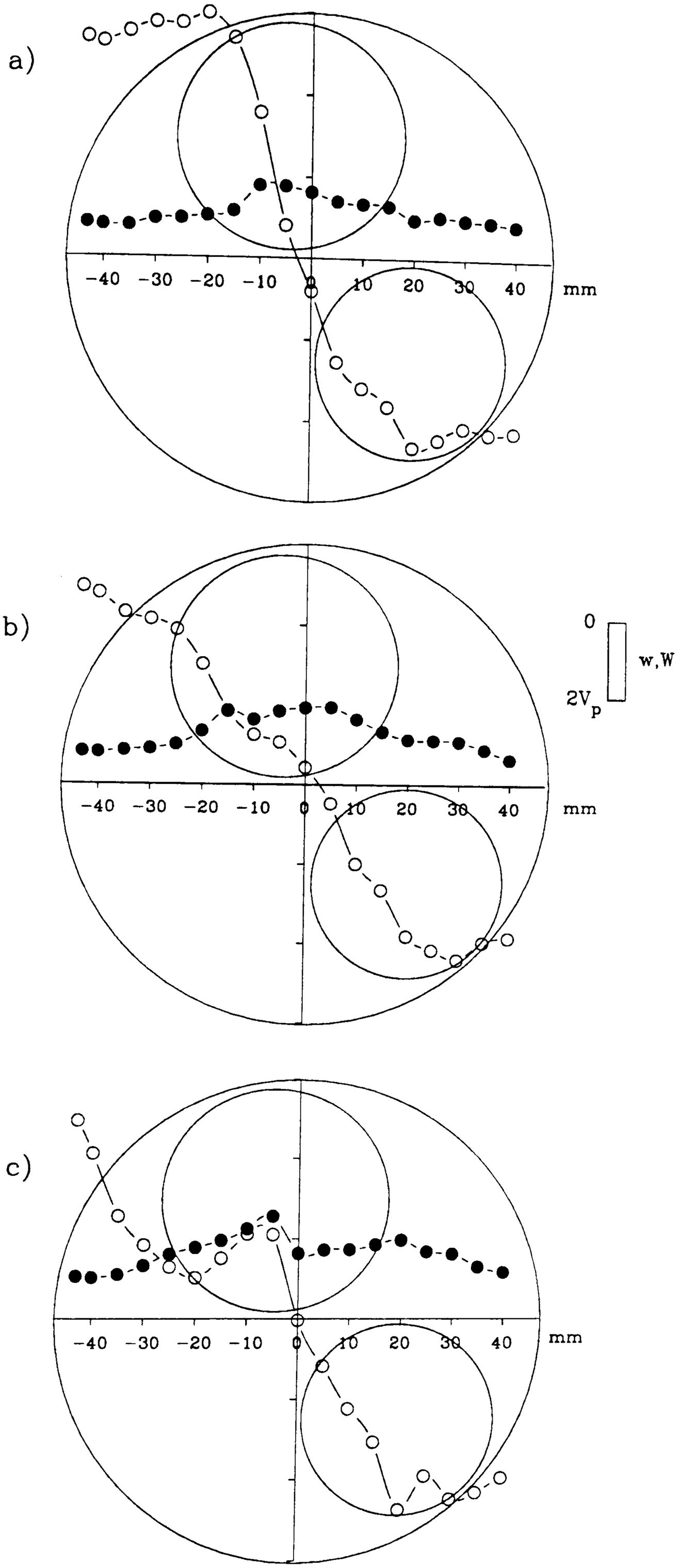


Figure 4.14 Spatial profiles of swirl mean and rms velocities at (a)1000 (b)2000 and (c)3000rpm ($\theta = 180^{o}$ CA, high swirl)

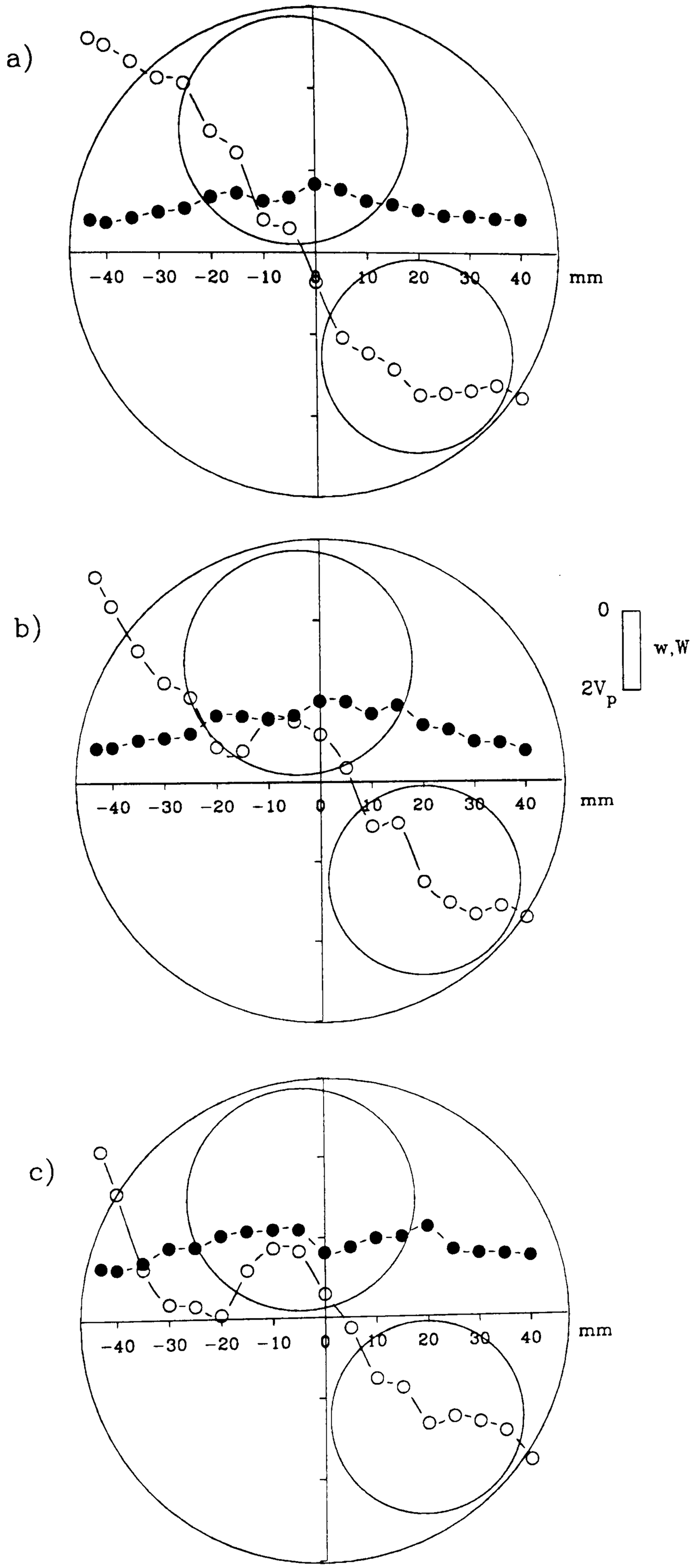


Figure 4.15 Spatial profiles of swirl mean and rms velocities at (a)1000 (b)2000 and (c)3000rpm ($\theta = 180^{o}$ CA, medium swirl)

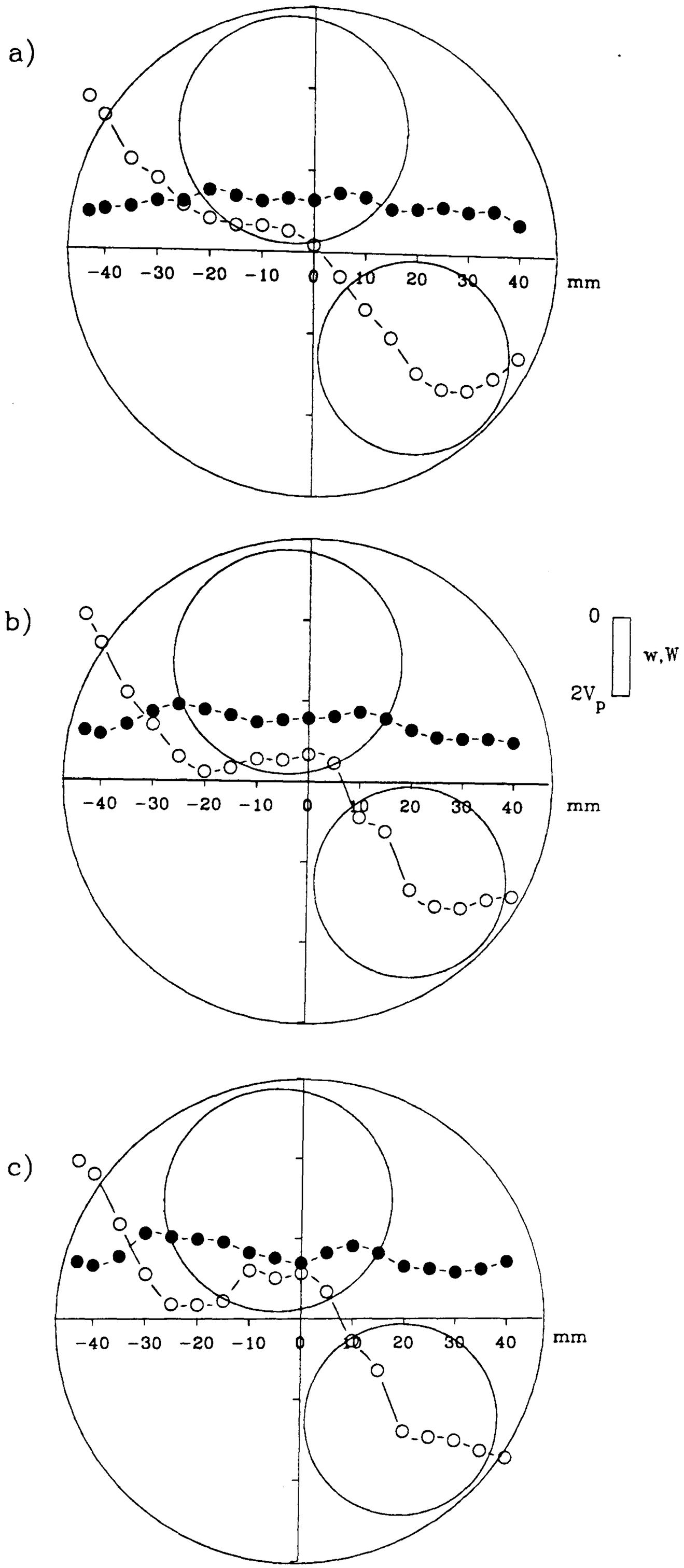


Figure 4.16 Spatial profiles of swirl mean and rms velocities at (a)1000 (b)2000 and (c)3000rpm ($\theta = 180^{o}$ CA, low swirl)

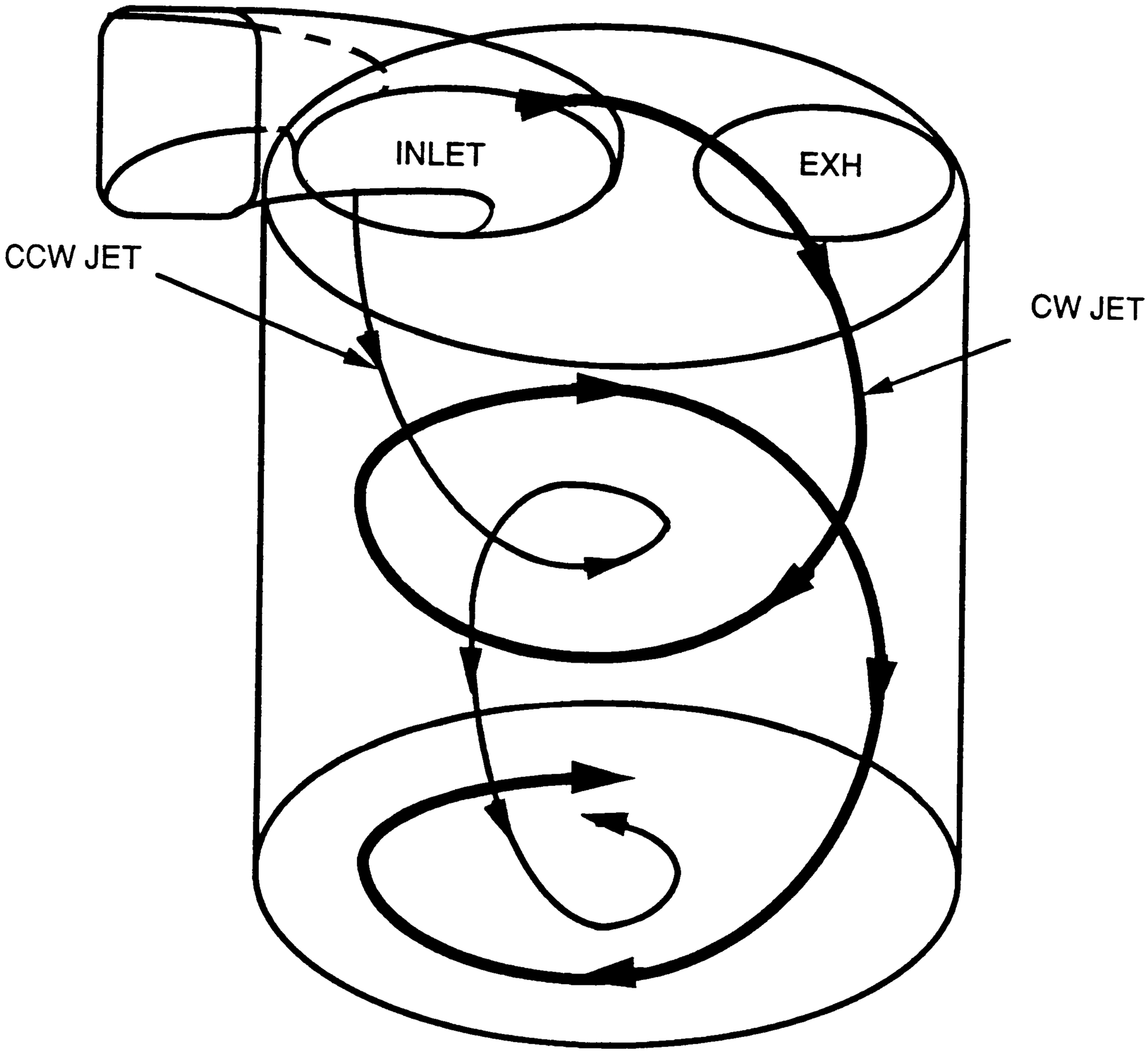


Figure 4.17 Schematic of the engine cylinder showing swirling air flow during induction.

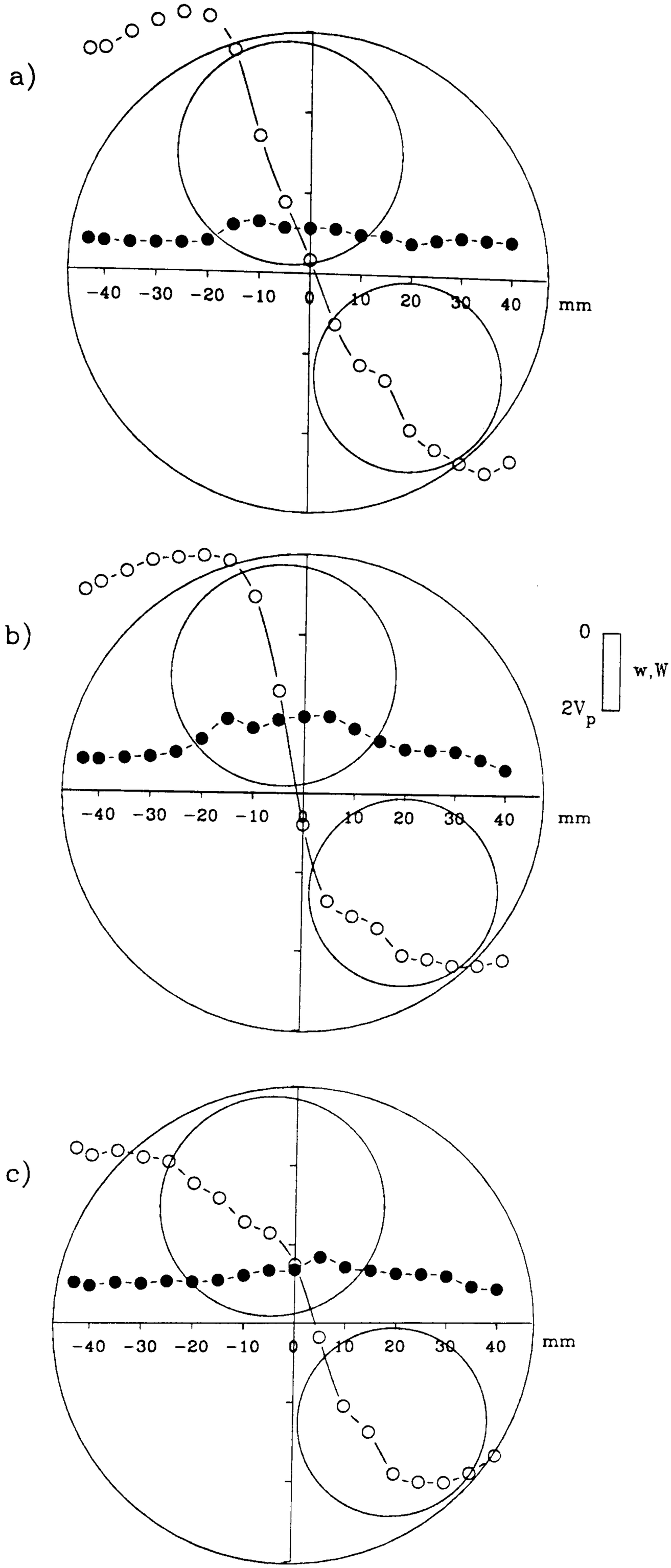


Figure 4.18 Spatial profiles of swirl mean and rms velocities at (a)1000 (b)2000 and (c)3000rpm (θ=200° CA, high swirl)

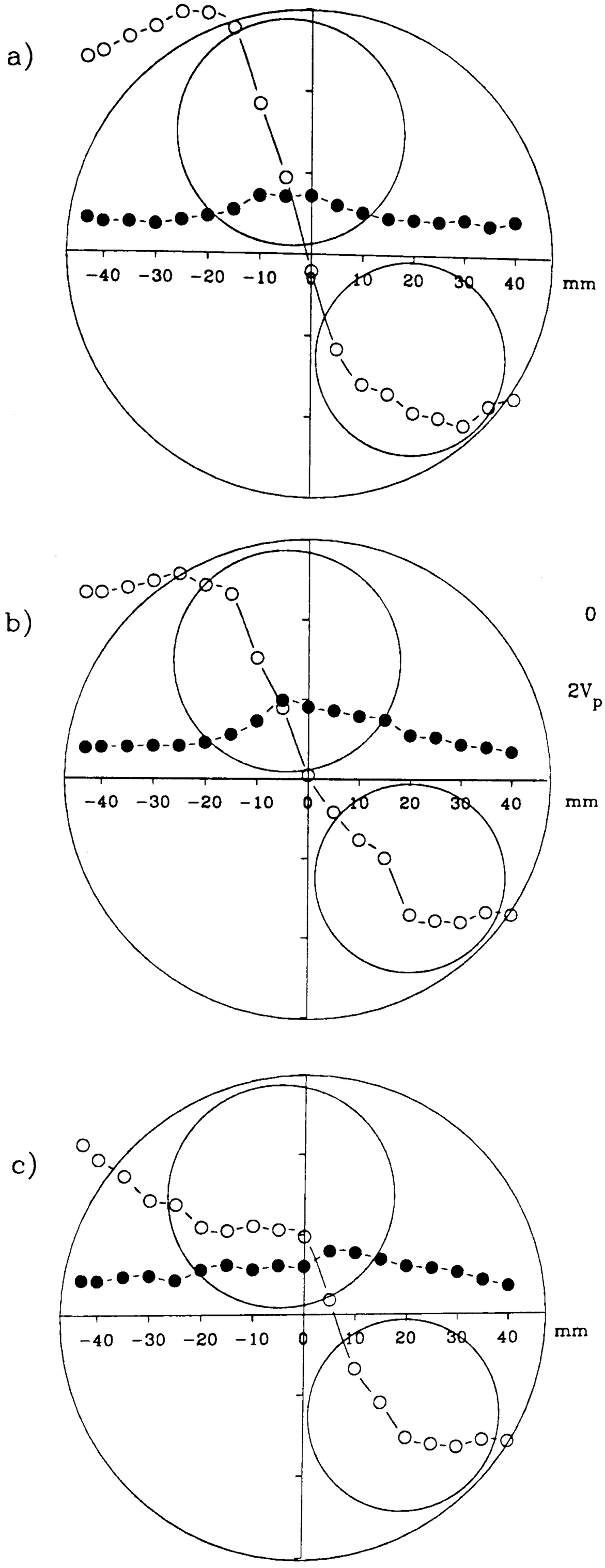


Figure 4.19 Spatial profiles of swirl mean and rms velocities at (a)1000 (b)2000 and (c)3000rpm (θ=200° CA, medium swirl)

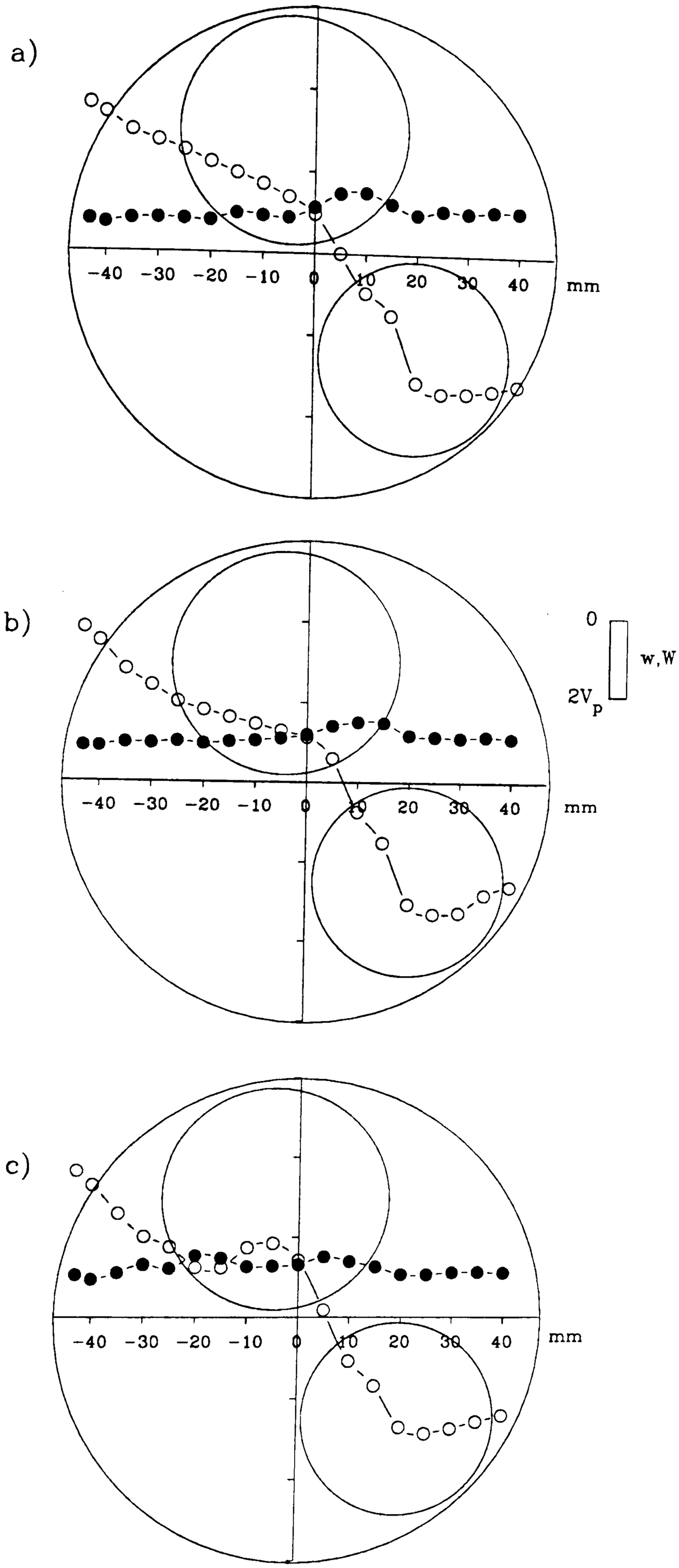


Figure 4.20 Spatial profiles of swirl mean and rms velocities at (a)1000 (b)2000 and (c)3000rpm (θ=200° CA, low swirl)

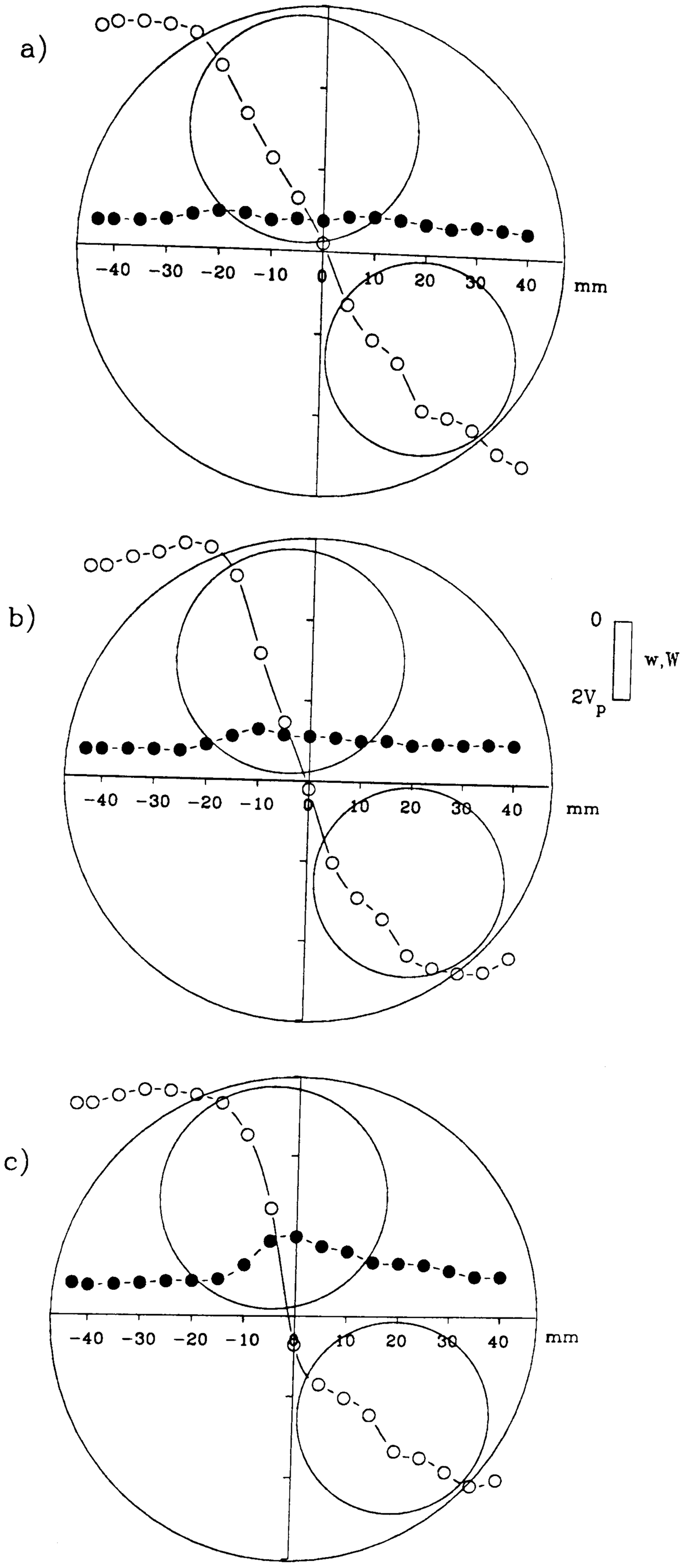


Figure 4.21 Spatial profiles of swirl mean and rms velocities at (a)1000 (b)2000 and (c)3000rpm (θ=218° CA, high swirl)

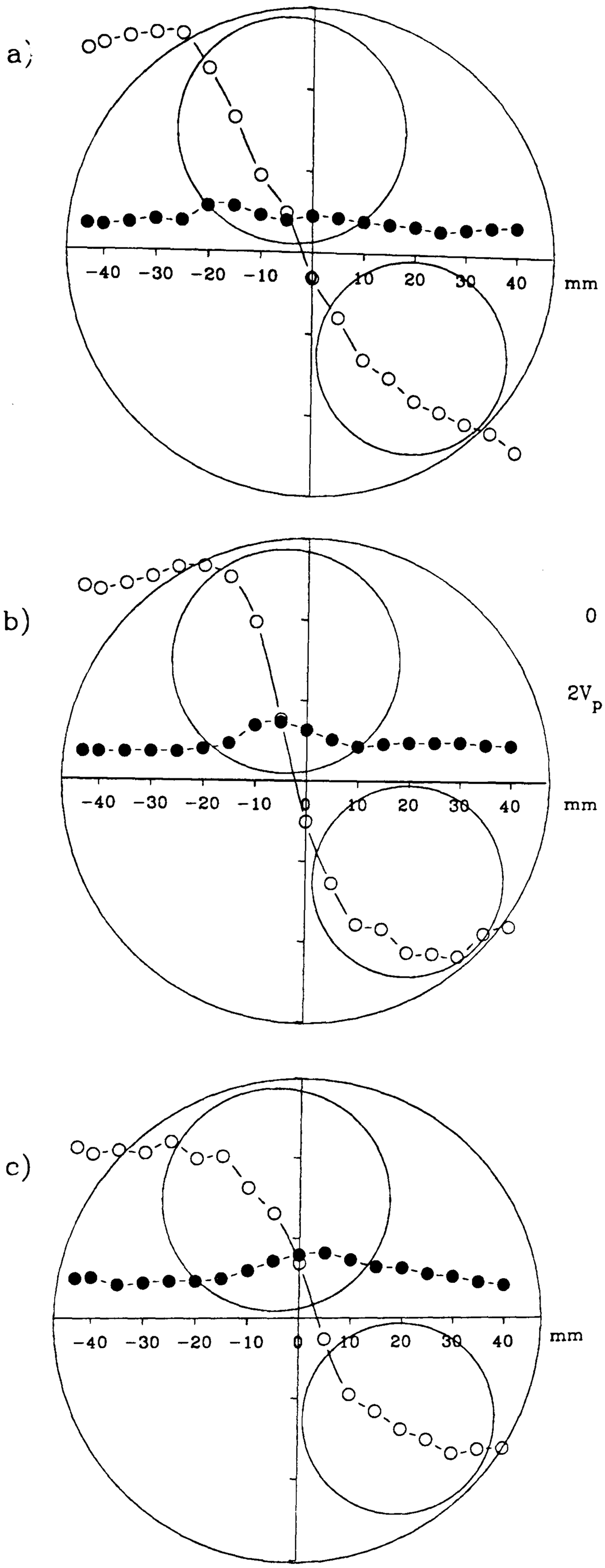


Figure 4.22 Spatial profiles of swirl mean and rms velocities at (a)1000 (b)2000 and (c)3000rpm (θ=218° CA, medium swirl)

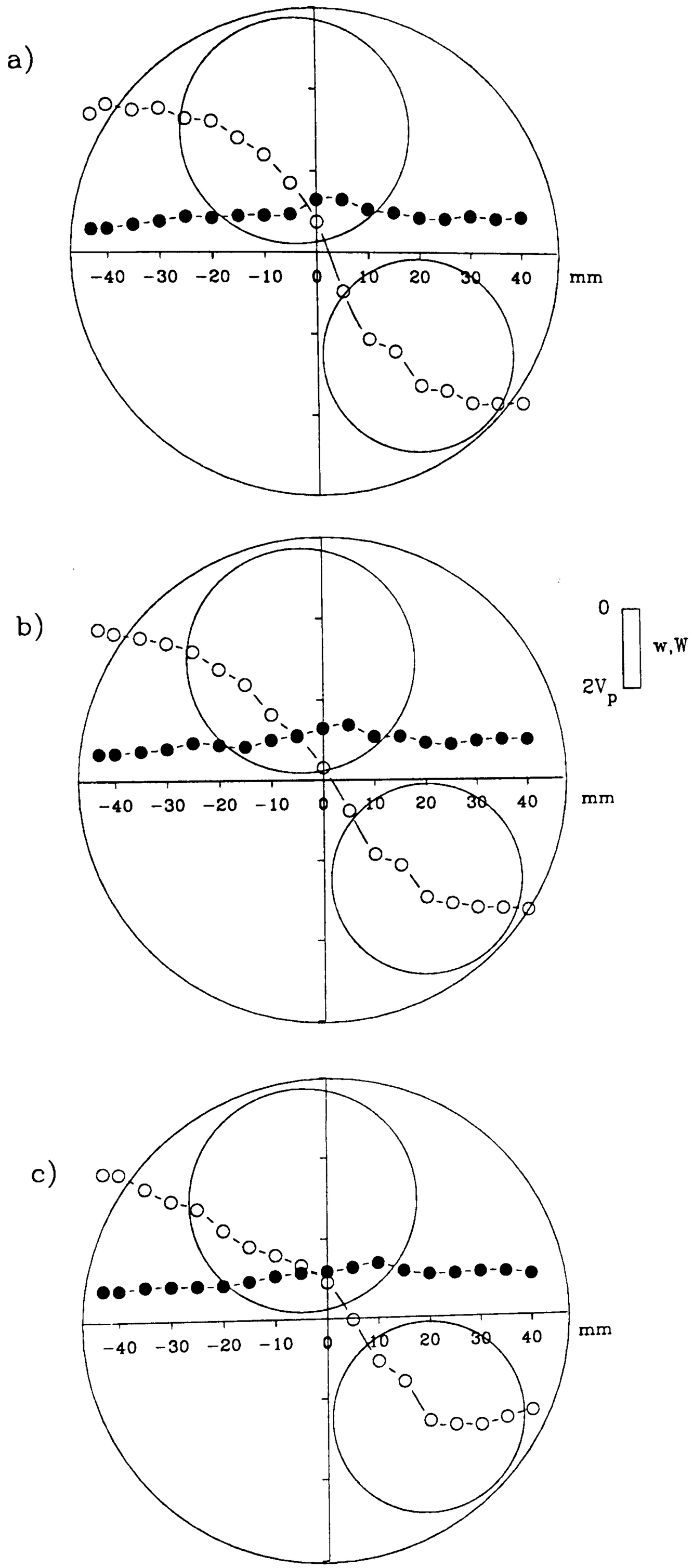


Figure 4.23 Spatial profiles of swirl mean and rms velocities at (a)1000 (b)2000 and (c)3000rpm (θ=218° CA, low swirl)

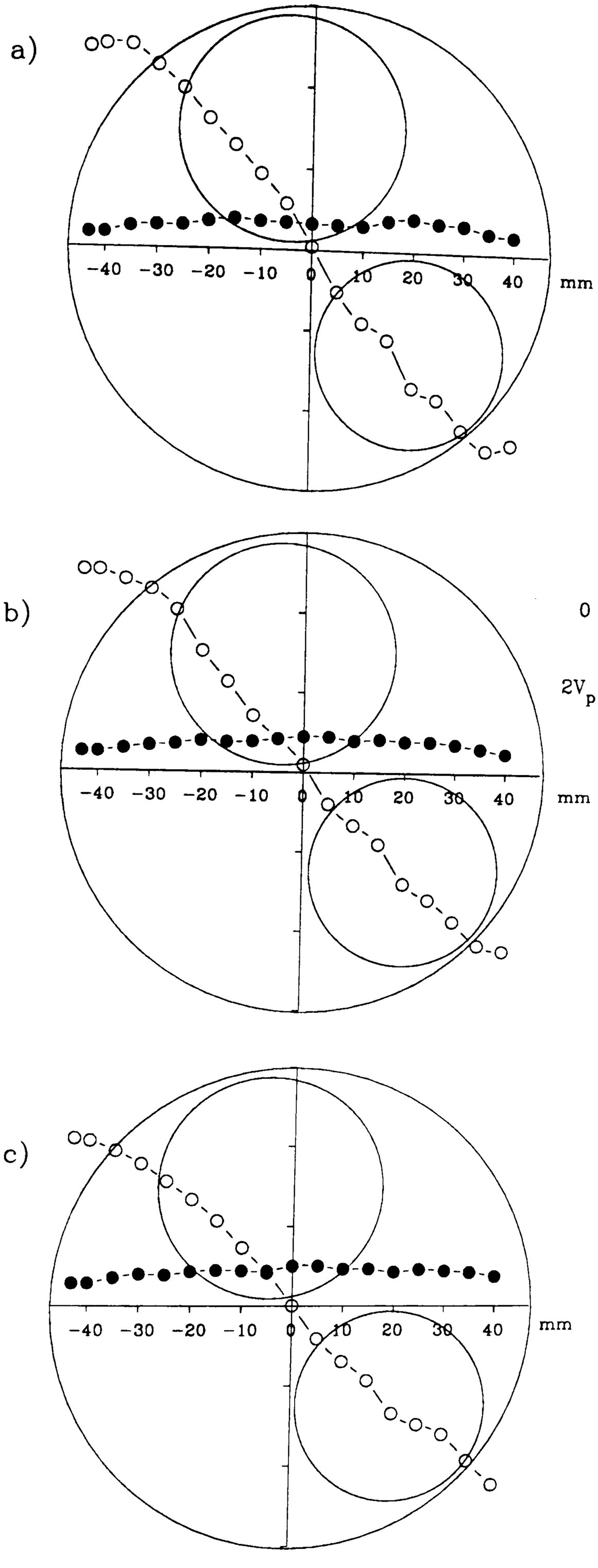


Figure 4.24 Spatial profiles of swirl mean and rms velocities at (a)1000 (b)2000 and (c)3000rpm (θ=270° CA, high swirl)

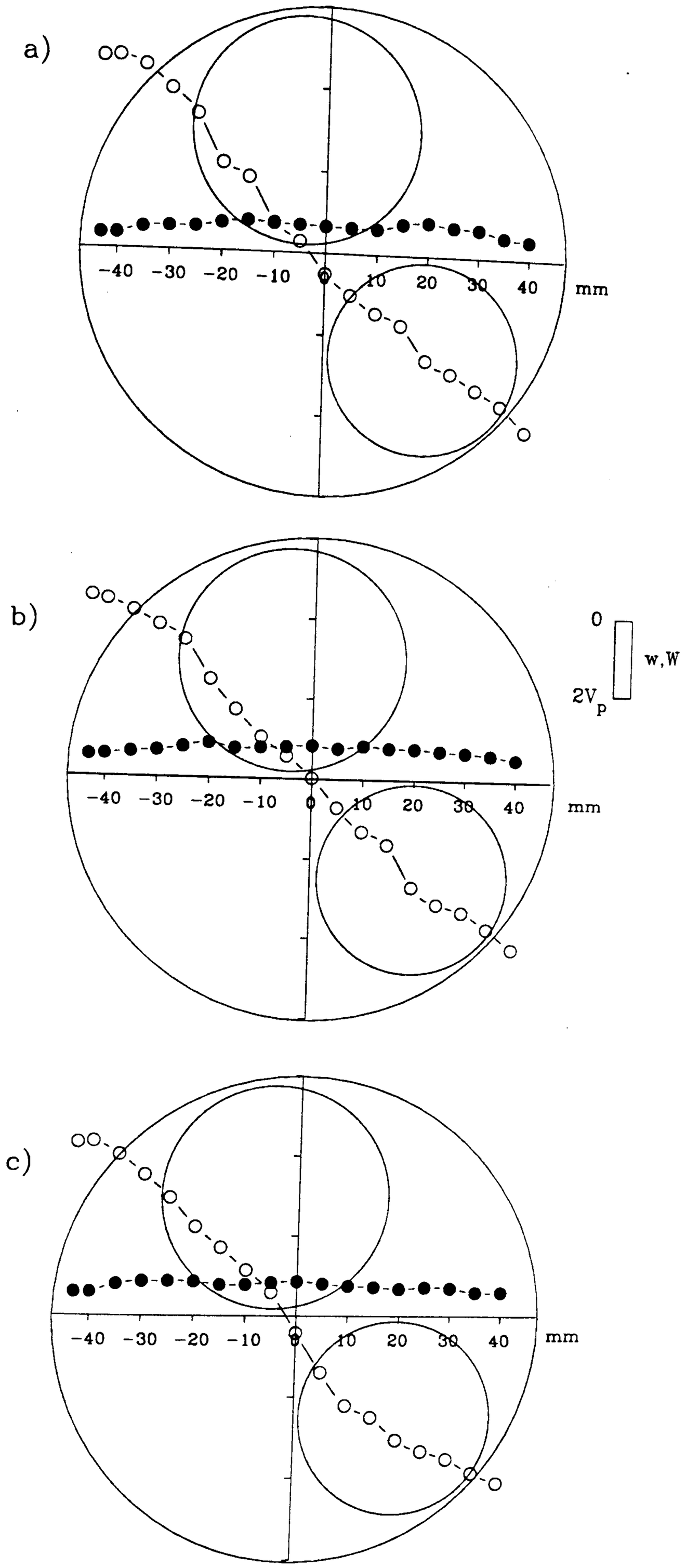


Figure 4.25 Spatial profiles of swirl mean and rms velocities at (a)1000 (b)2000 and (c)3000rpm (θ=270° CA, medium swirl)

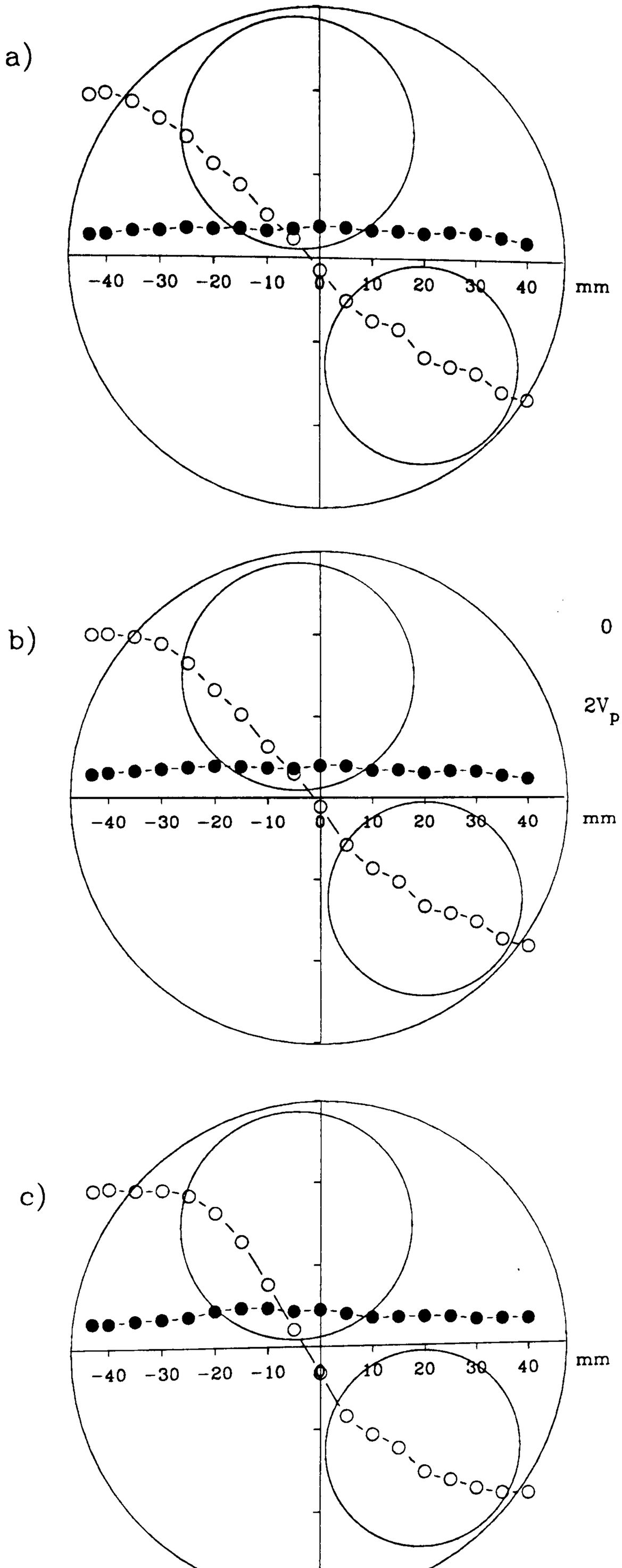


Figure 4.26 Spatial profiles of swirl mean and rms velocities at (a)1000 (b)2000 and (c)3000rpm (θ=270° CA, low swirl)

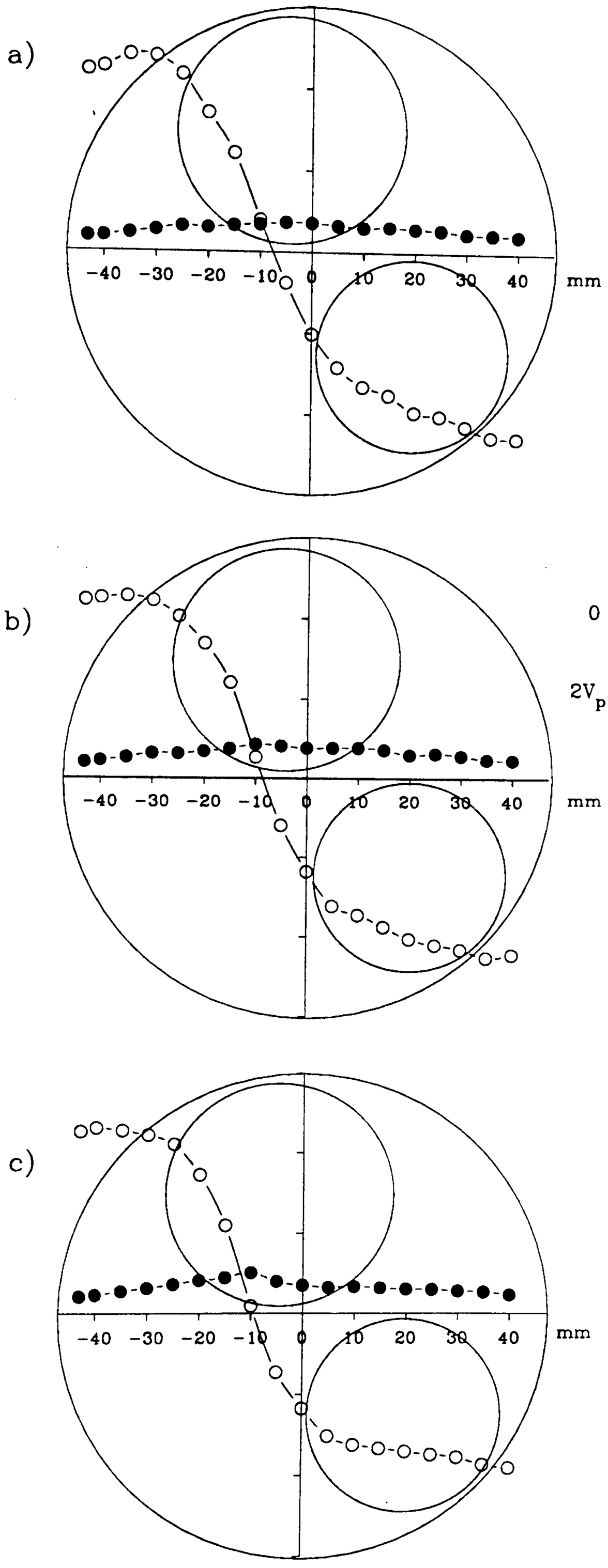


Figure 4.27 Spatial profiles of swirl mean and rms velocities at (a)1000 (b)2000 and (c)3000rpm (θ=320° CA, high swirl)

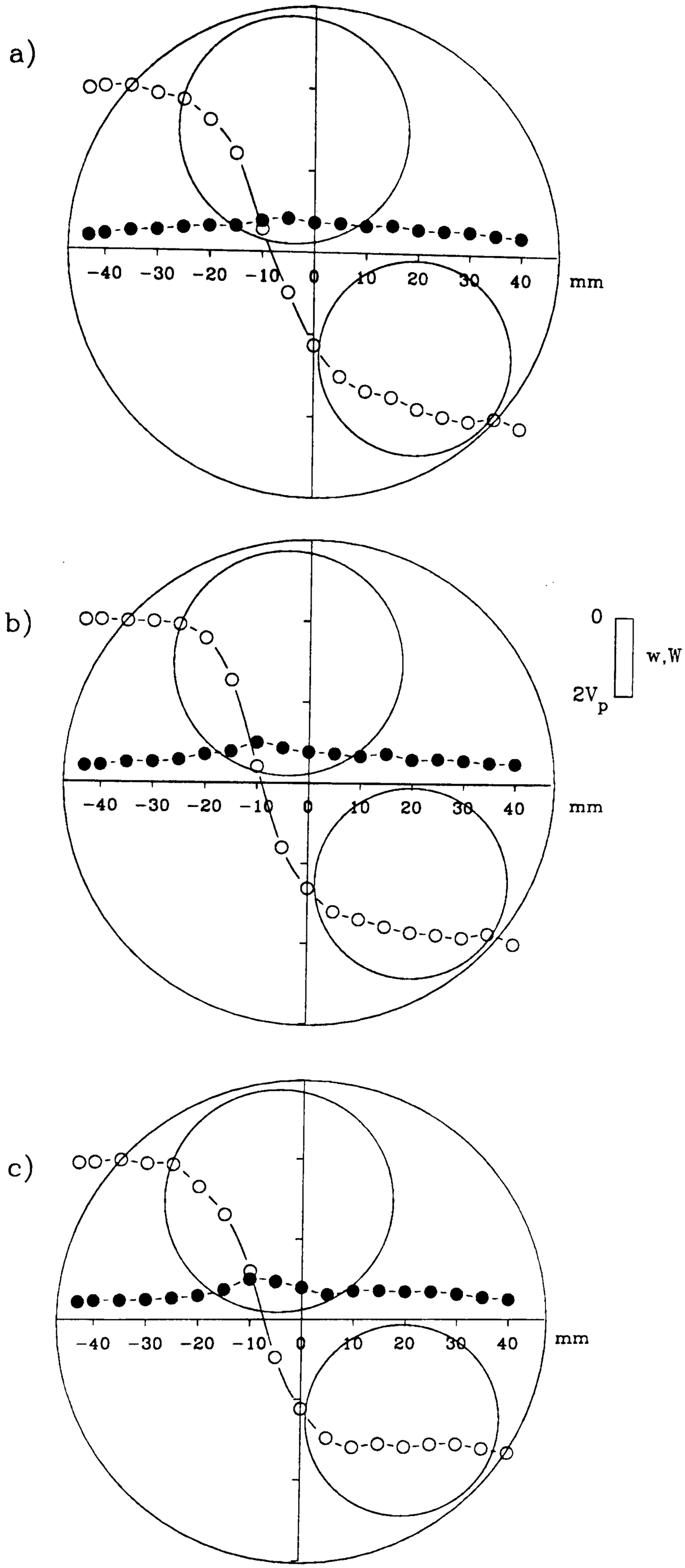


Figure 4.28 Spatial profiles of swirl mean and rms velocities at (a)1000 (b)2000 and (c)3000rpm (θ=320° CA, medium swirl)

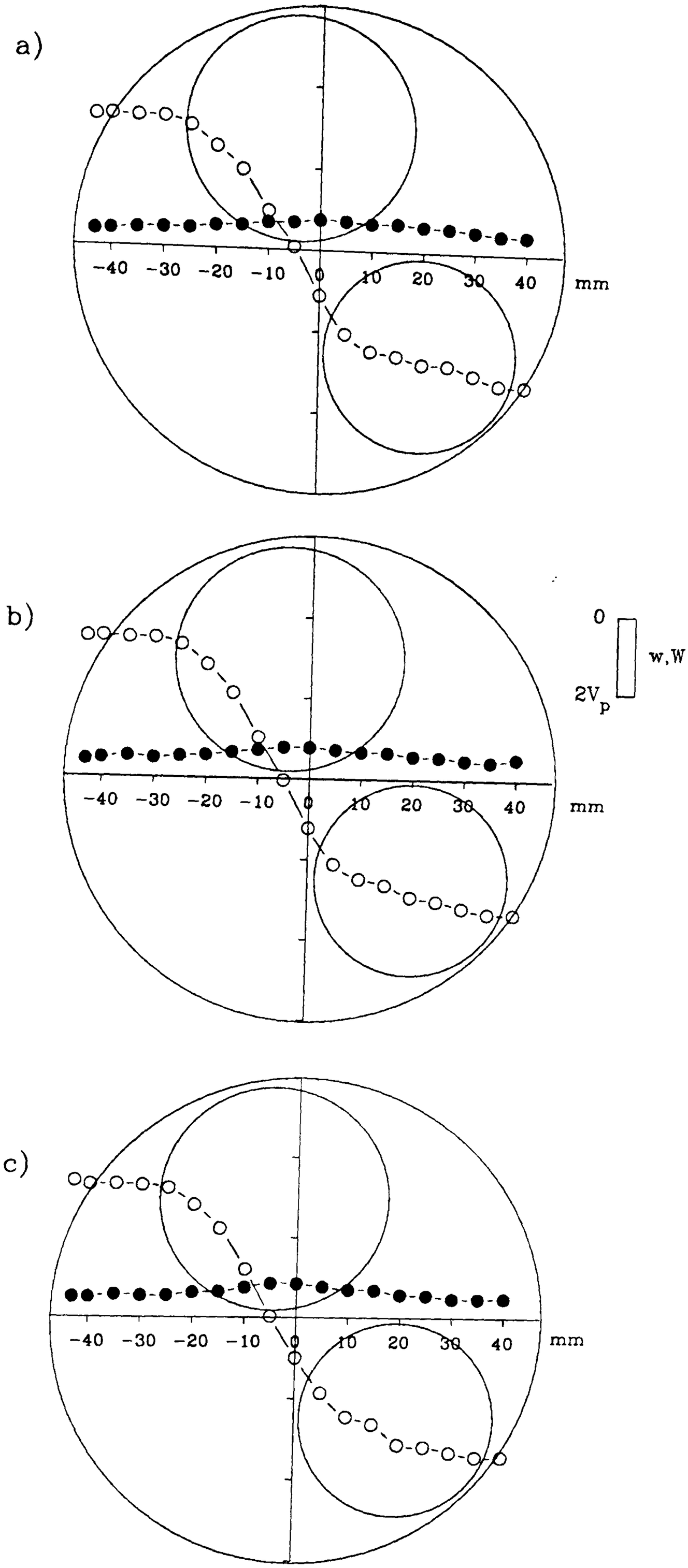


Figure 4.29 Spatial profiles of swirl mean and rms velocities at (a)1000 (b)2000 and (c)3000rpm ($\theta = 320^{o}$ CA, low swirl)

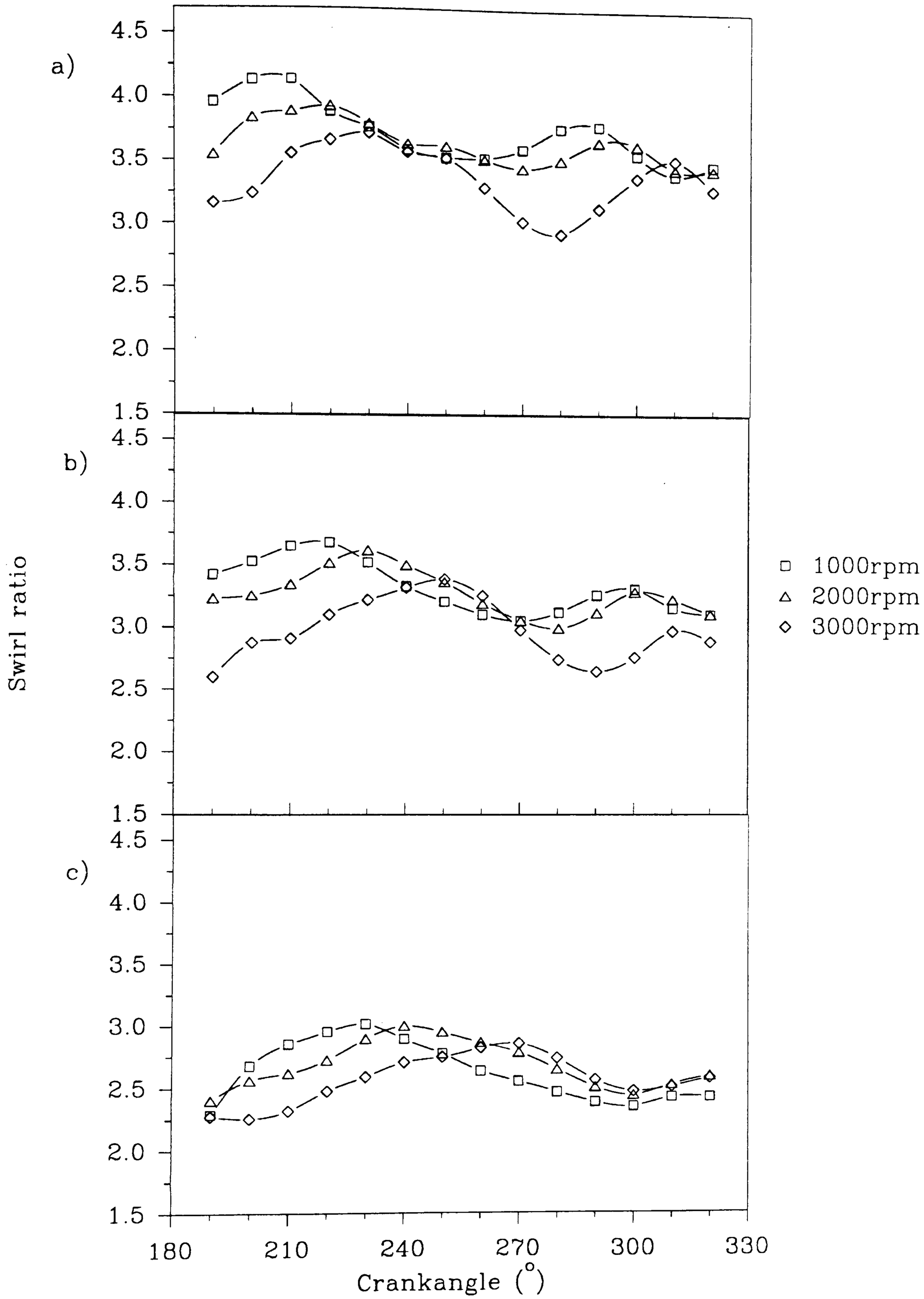


Figure 4.30 Temporal variation of equivalent swirl ratios at different engine speeds for (a) high, (b) medium and (c) low swirl.

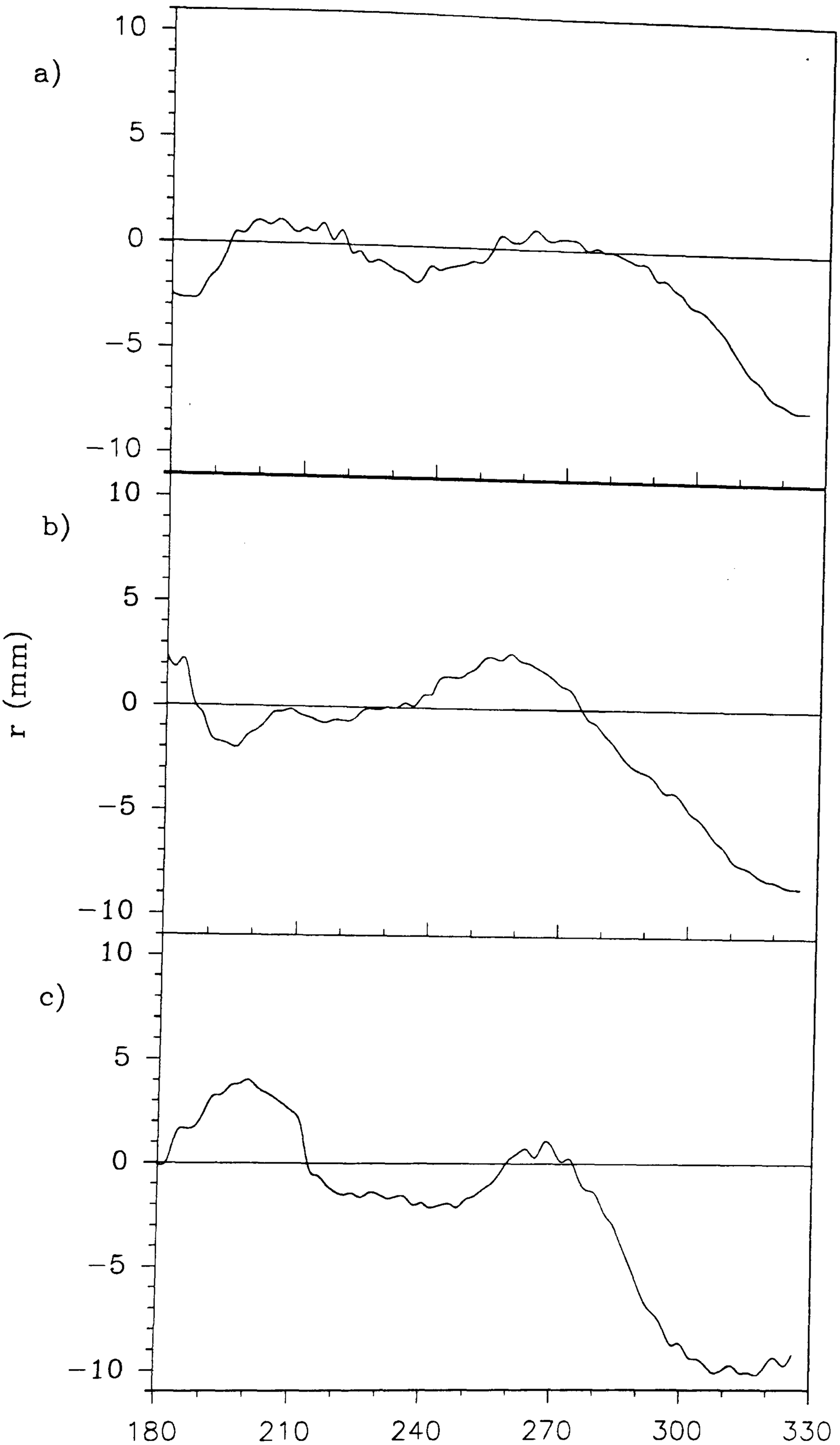


Figure 4.31 Temporal variation of the zero swirl velocity position on the measurements axis at (a)1000 (b)2000 and (c)3000rpm (high swirl).

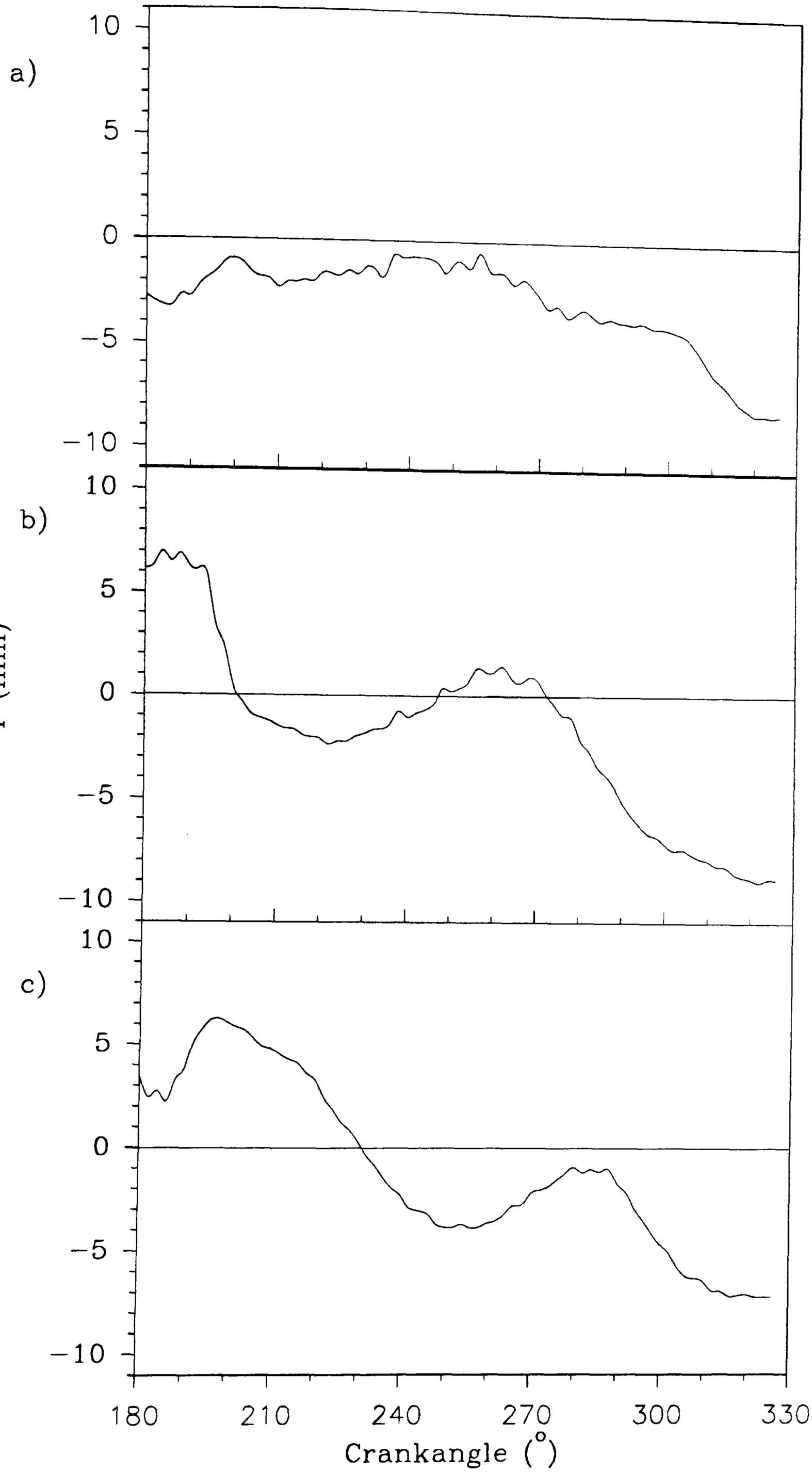


Figure 4.32 Temporal variation of the zero swirl velocity position on the measurements axis at (a)1000 (b)2000 and (c)3000rpm (medium swirl).

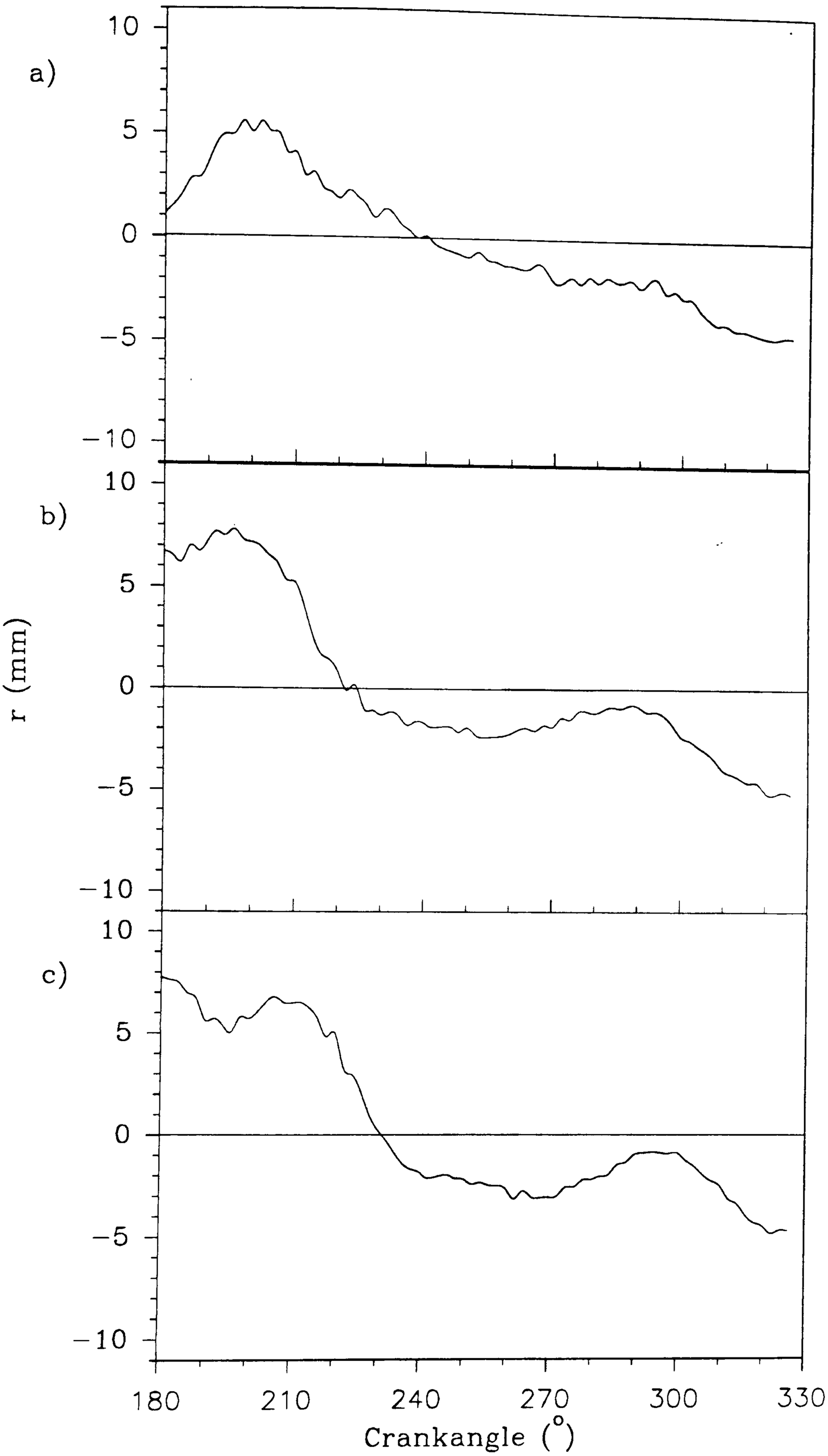


Figure 4.33 Temporal variation of the zero swirl velocity position on the measurements axis at (a)1000 (b)2000 and (c)3000rpm (low swirl).

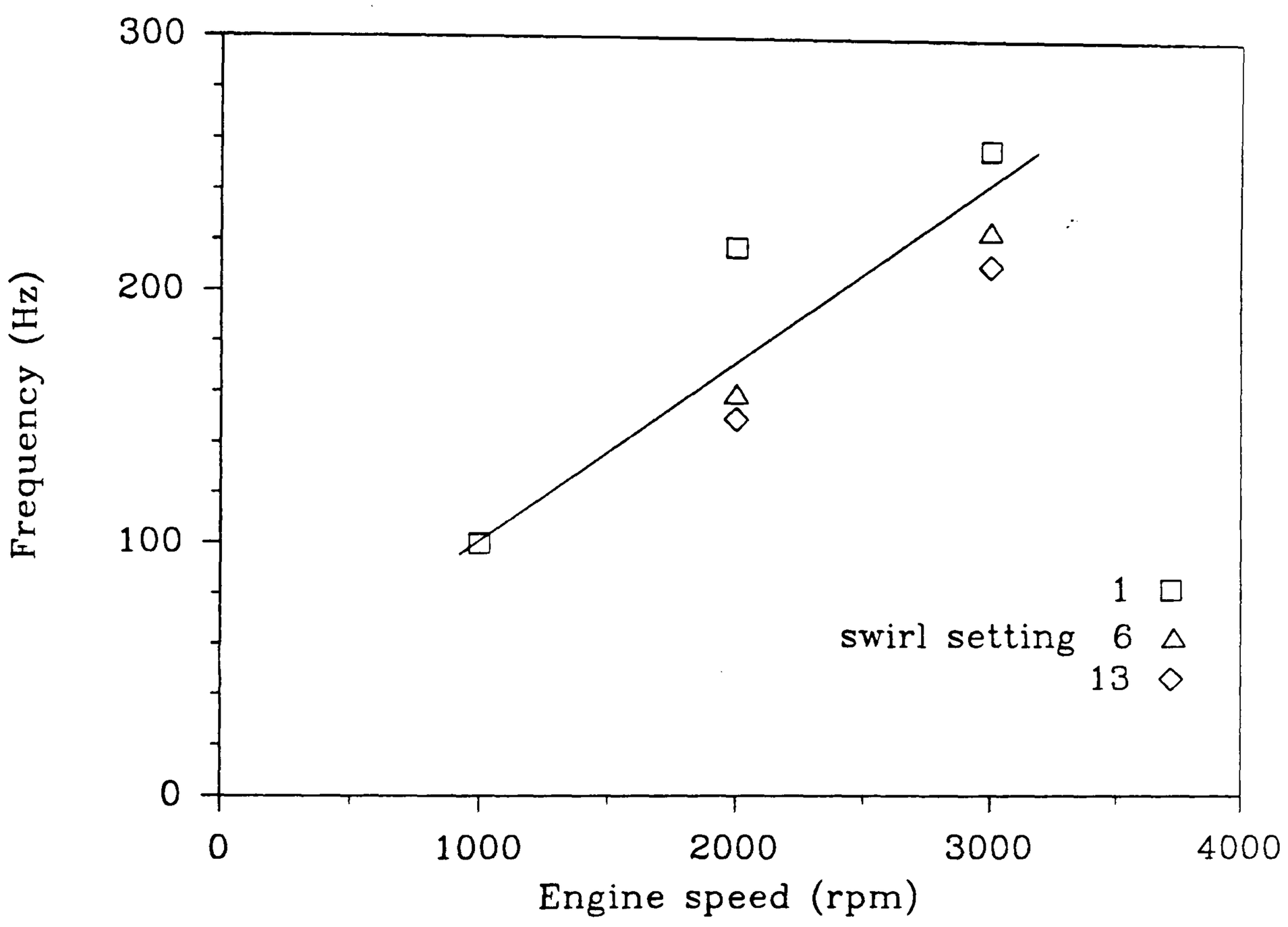


Figure 4.34 Variation of the characteristic frequency derived from Figs.4.31-4.33 with engine speed.

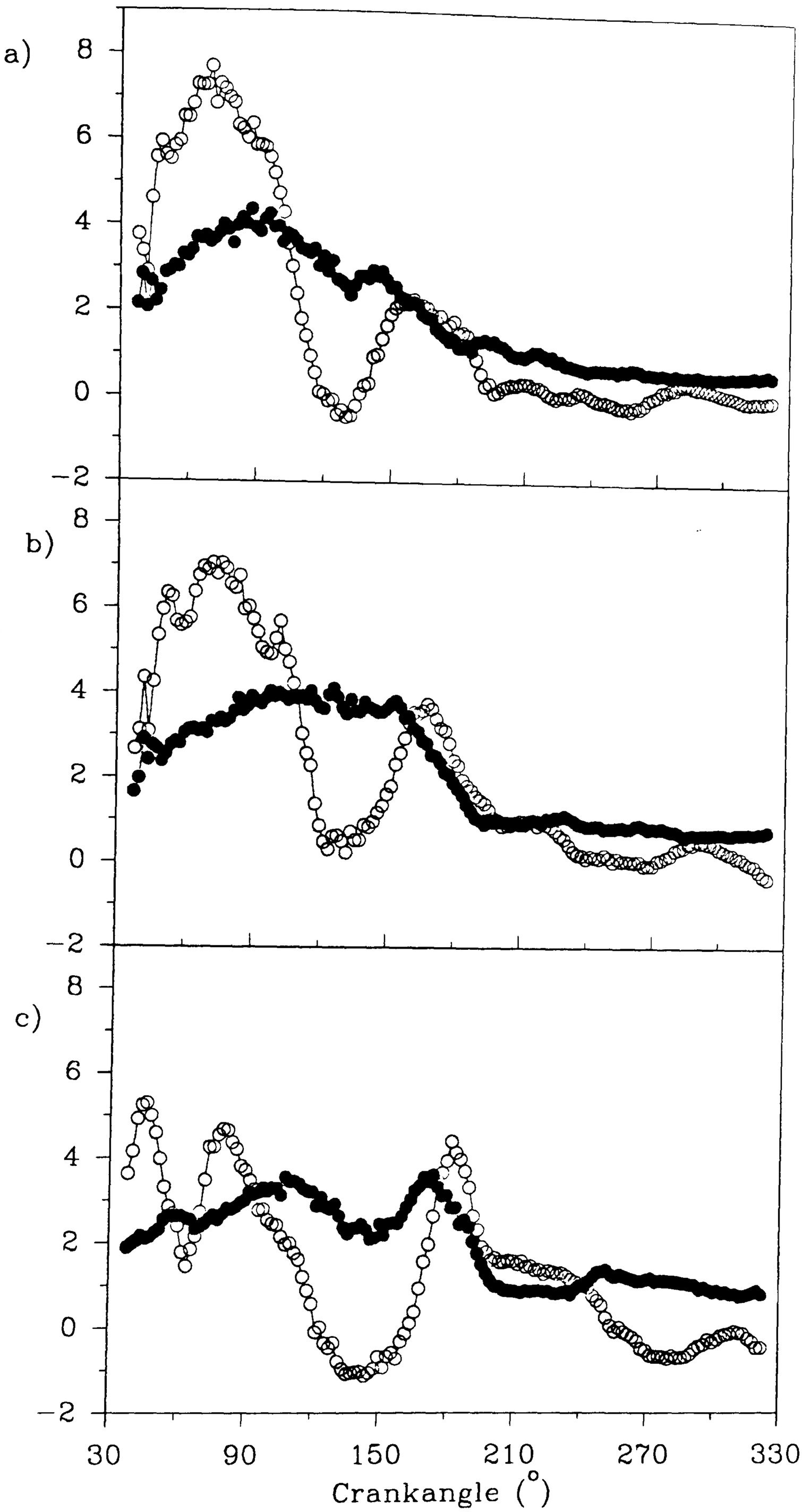


Figure 4.35 Temporal profiles of axial mean and rms velocities at (a)1000 (b)2000 (c)3000rpm (r=15mm, medium swirl).

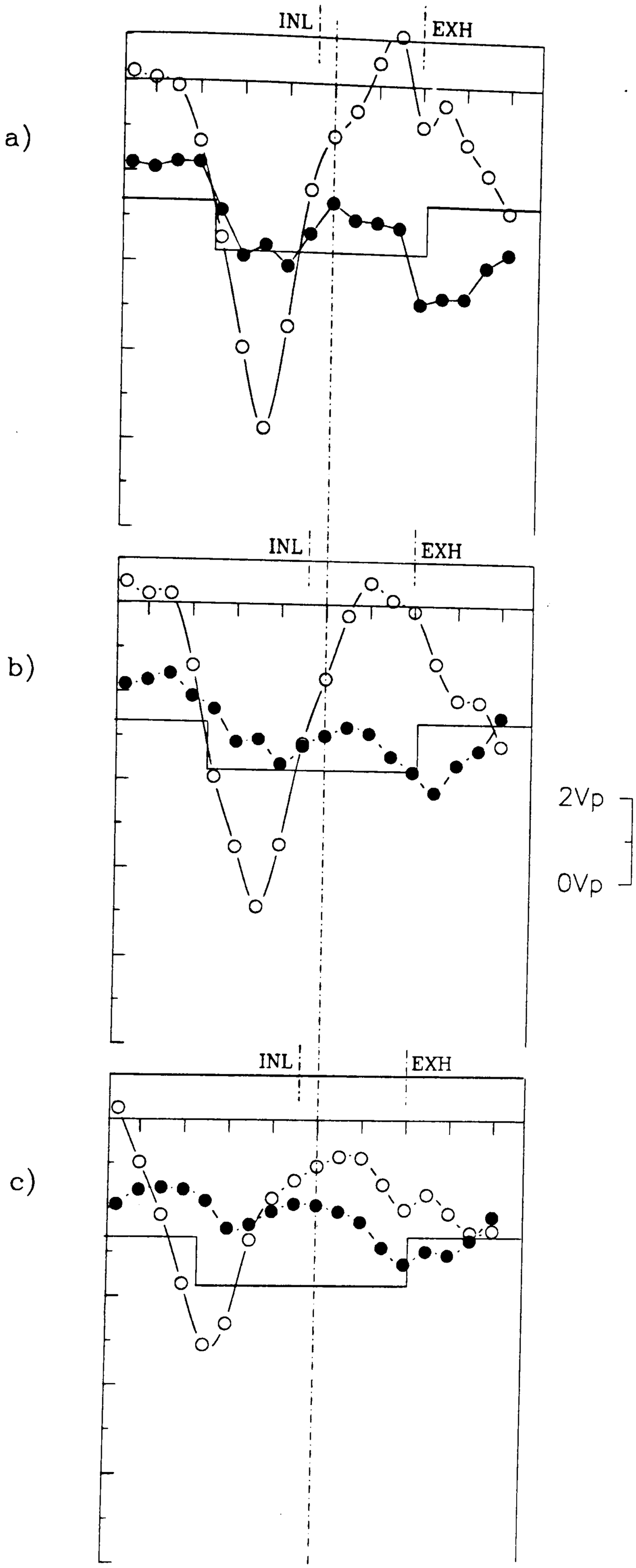


Figure 4.36 Spatial profiles of axial mean and rms velocities at (a)1000 (b)2000 and (c)3000rpm ($\theta = 70^{o}$ CA, medium swirl)

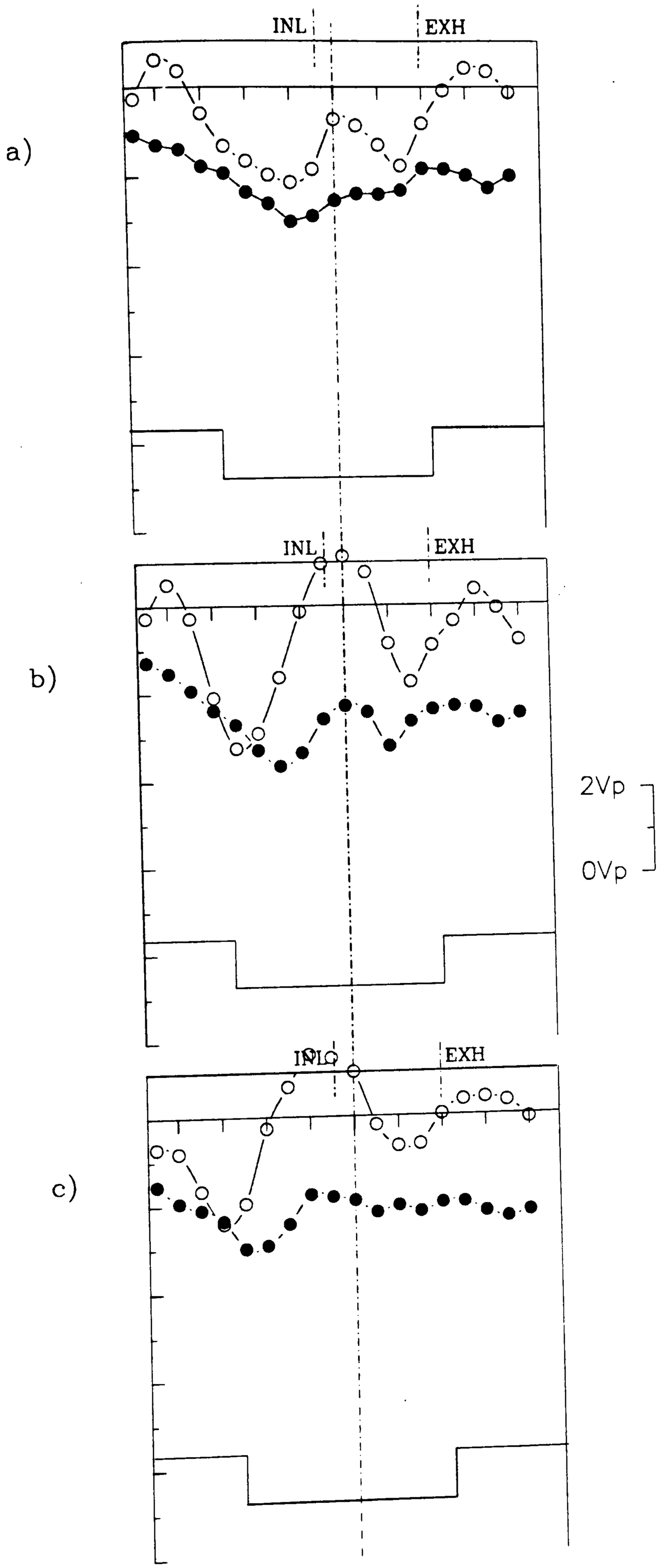


Figure 4.37 Spatial profiles of axial mean and rms velocities at (a)1000 (b)2000 and (c)3000rpm ($\theta = 150^{o}$ CA, medium swirl)

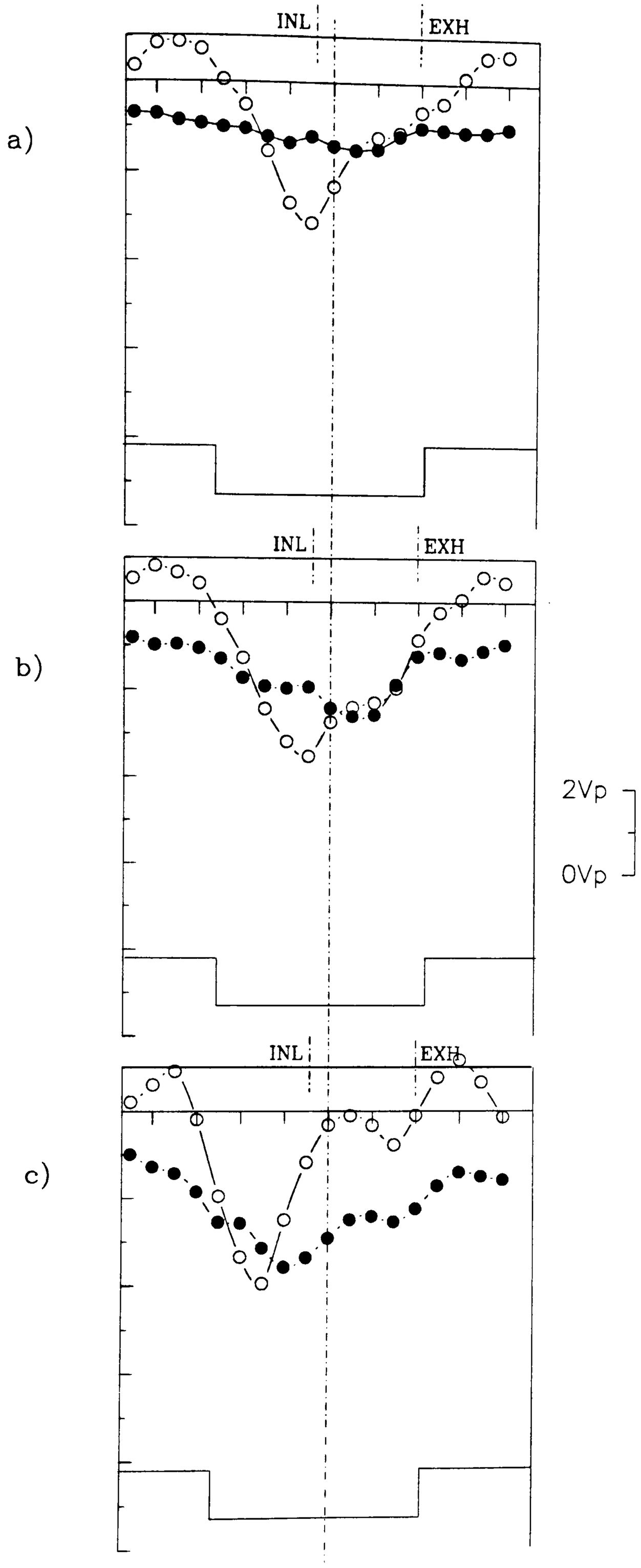


Figure 4.38 Spatial profiles of axial mean and rms velocities at (a)1000 (b)2000 and (c)3000rpm ($\theta = 180^{o}$ CA, medium swirl)

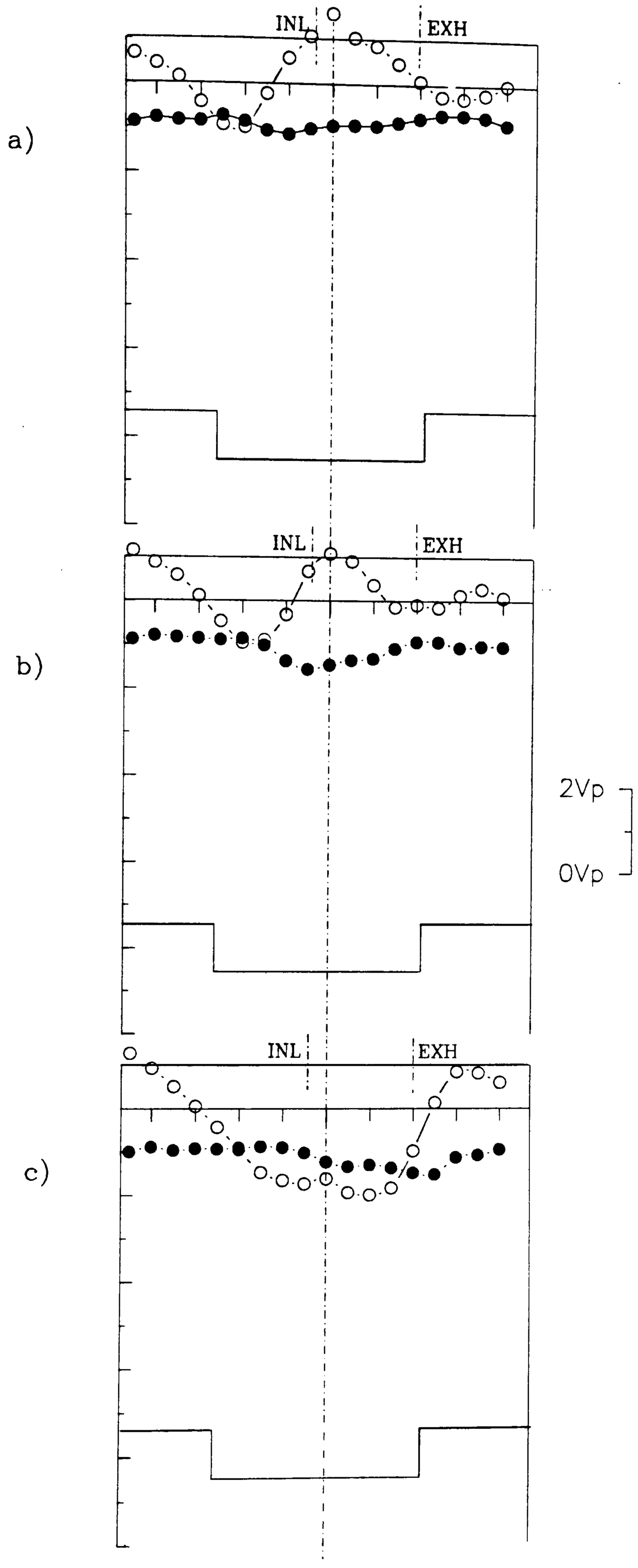


Figure 4.39 Spatial profiles of axial mean and rms velocities at (a)1000 (b)2000 and (c)3000rpm (θ=218° CA, medium swirl)

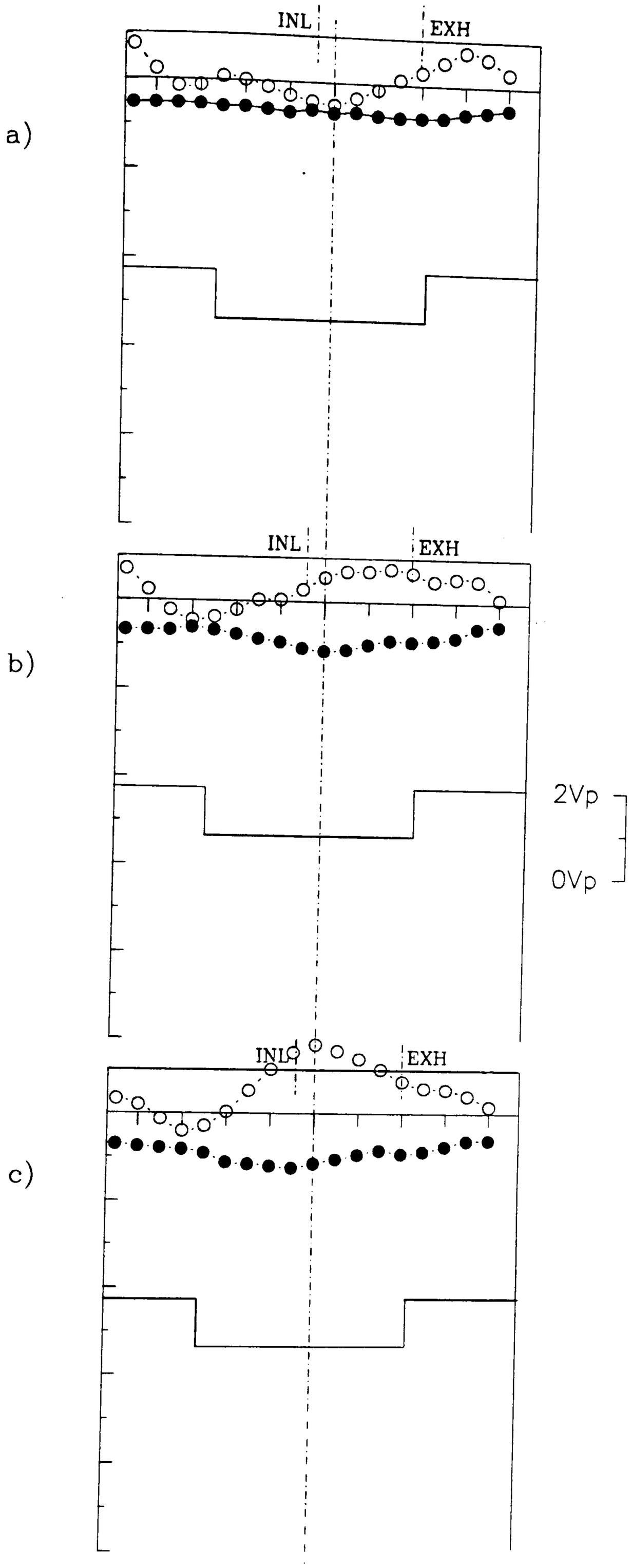


Figure 4.40 Spatial profiles of axial mean and rms velocities at (a)1000 (b)2000 and (c)3000rpm ($\theta = 270^{o}$ CA, medium swirl)

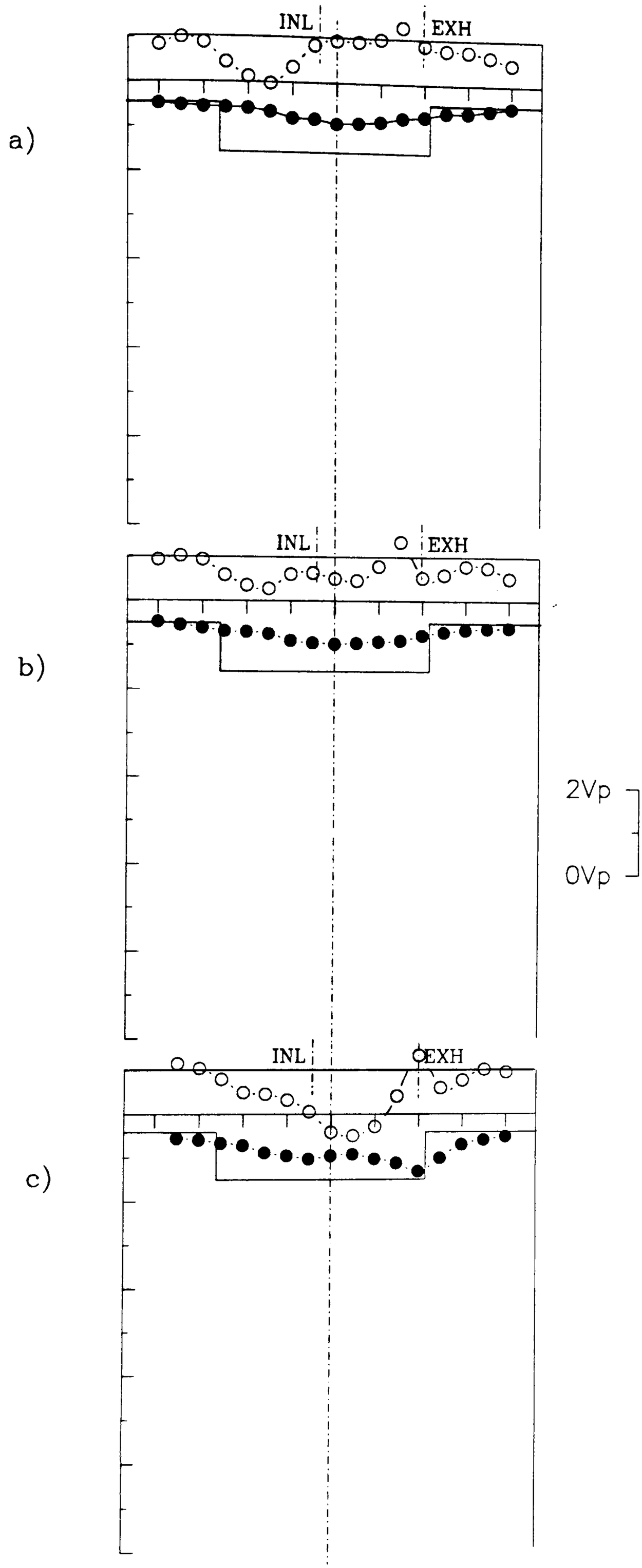


Figure 4.41 Spatial profiles of axial mean and rms velocities at (a)1000 (b)2000 and (c)3000rpm ($\theta = 320^{o}$ CA, medium swirl)

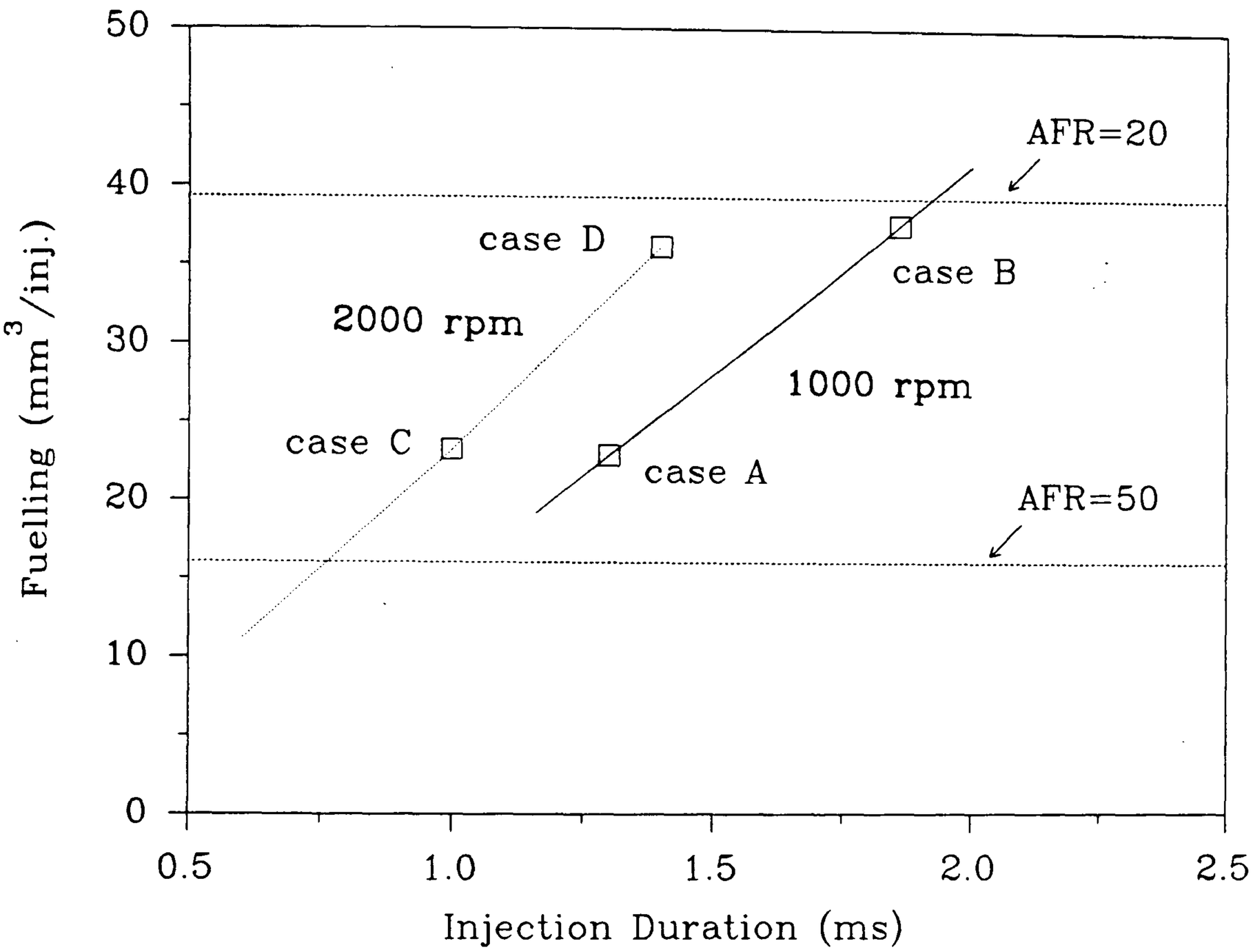


Figure 4.42 Variation of fuel injected volume at different engine speeds with injection duration.

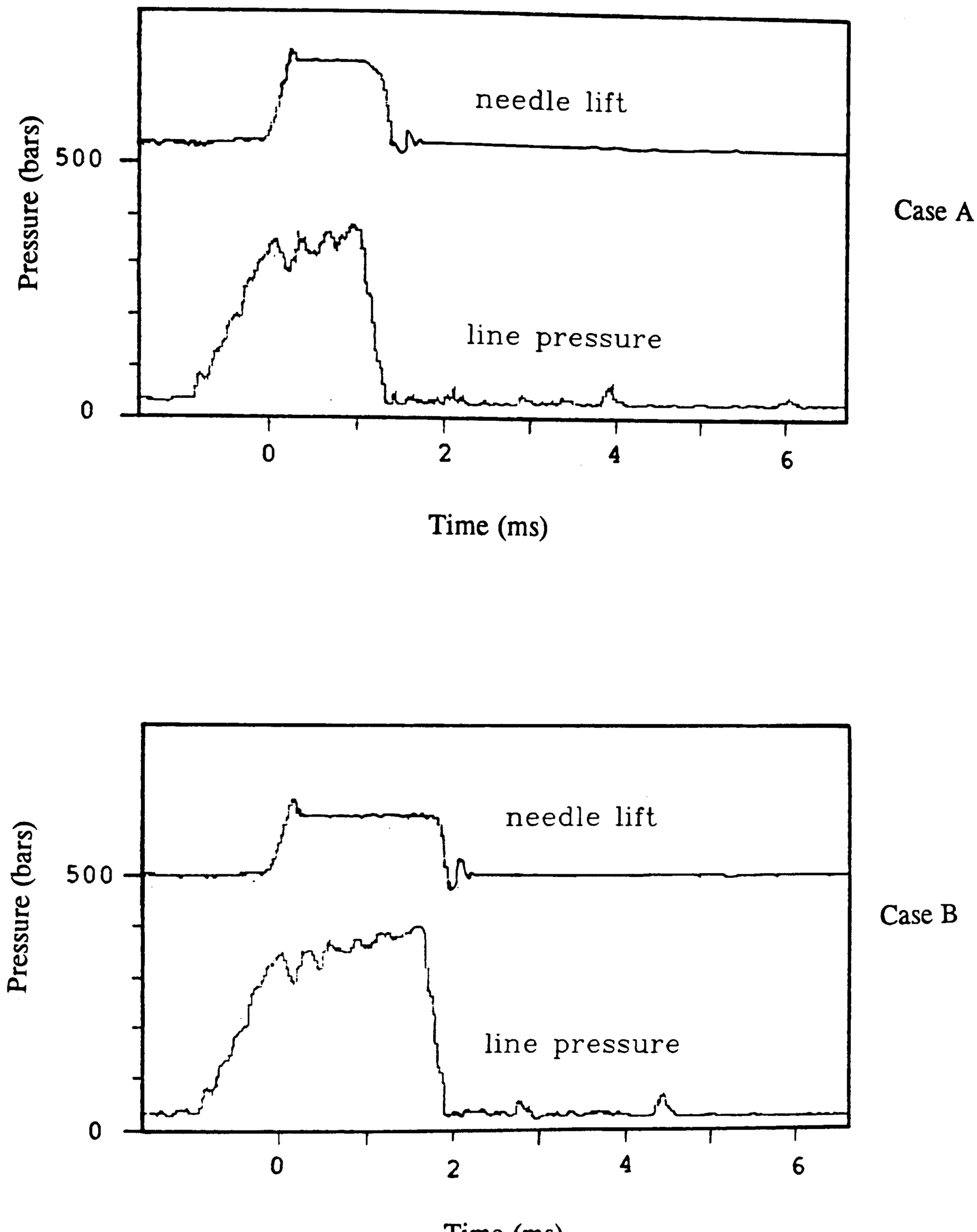
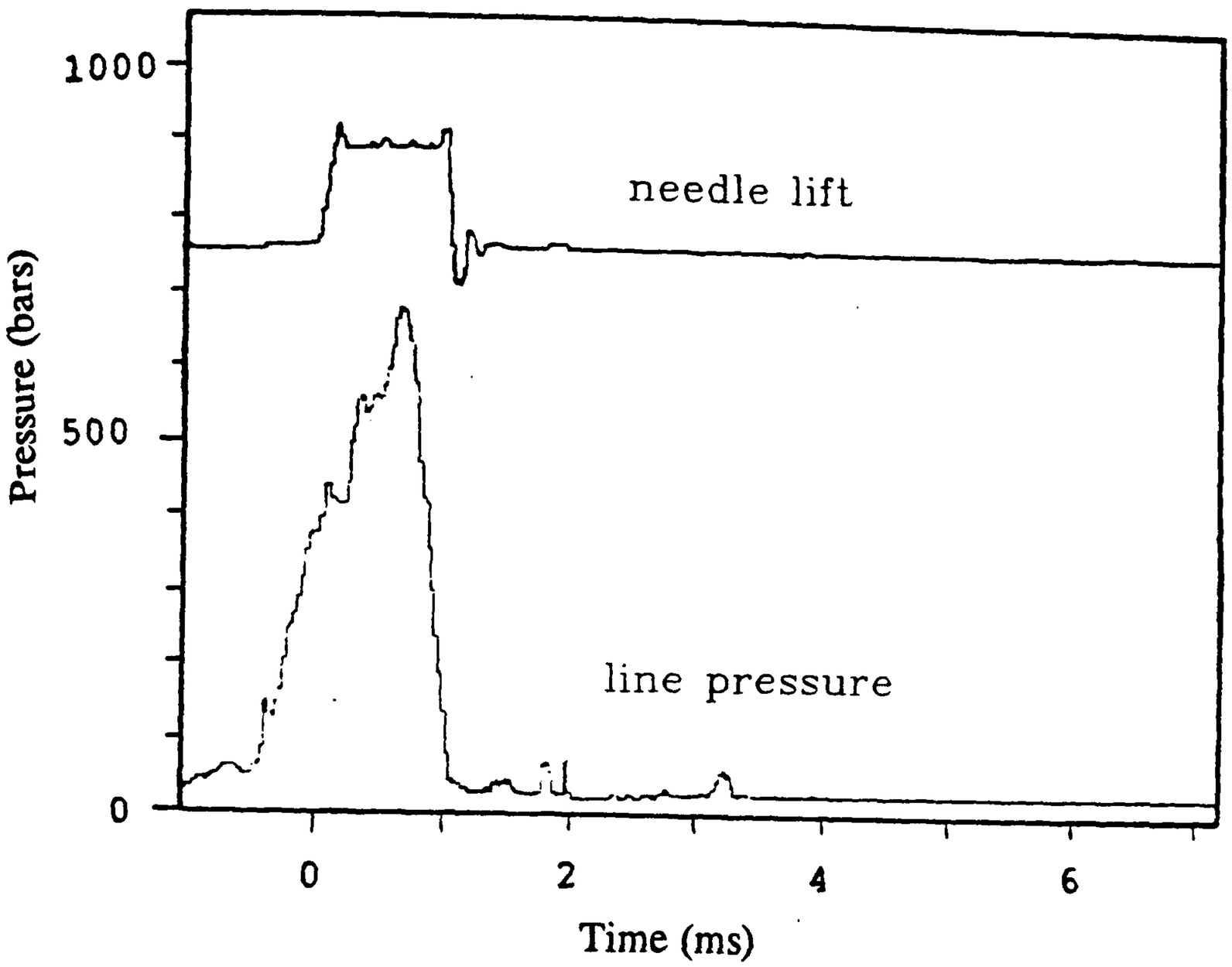


Figure 4.43 Temporal variations of instantaneous fuel line pressure and needle lift at the four different cases.



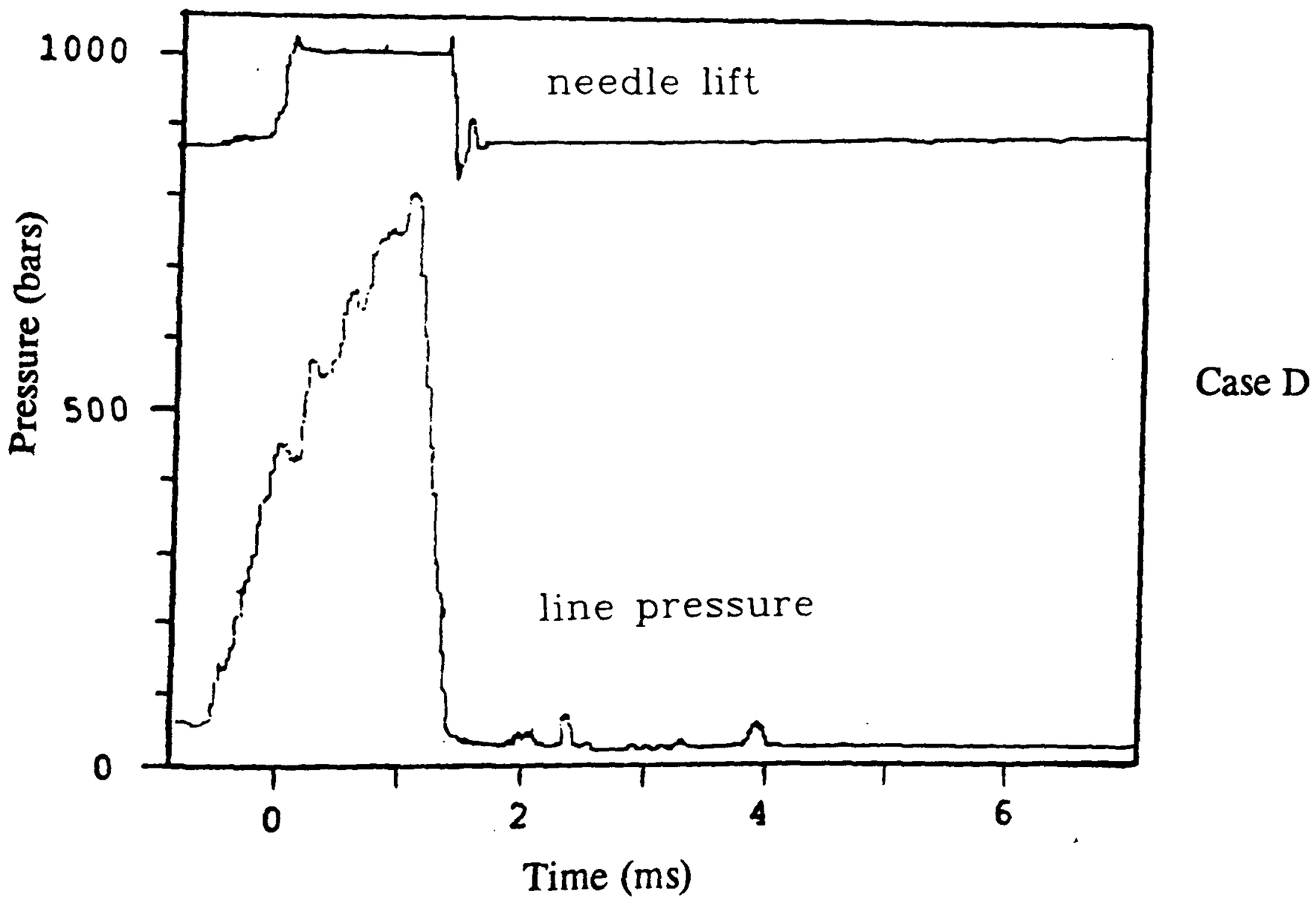


Figure 4.43 Continued

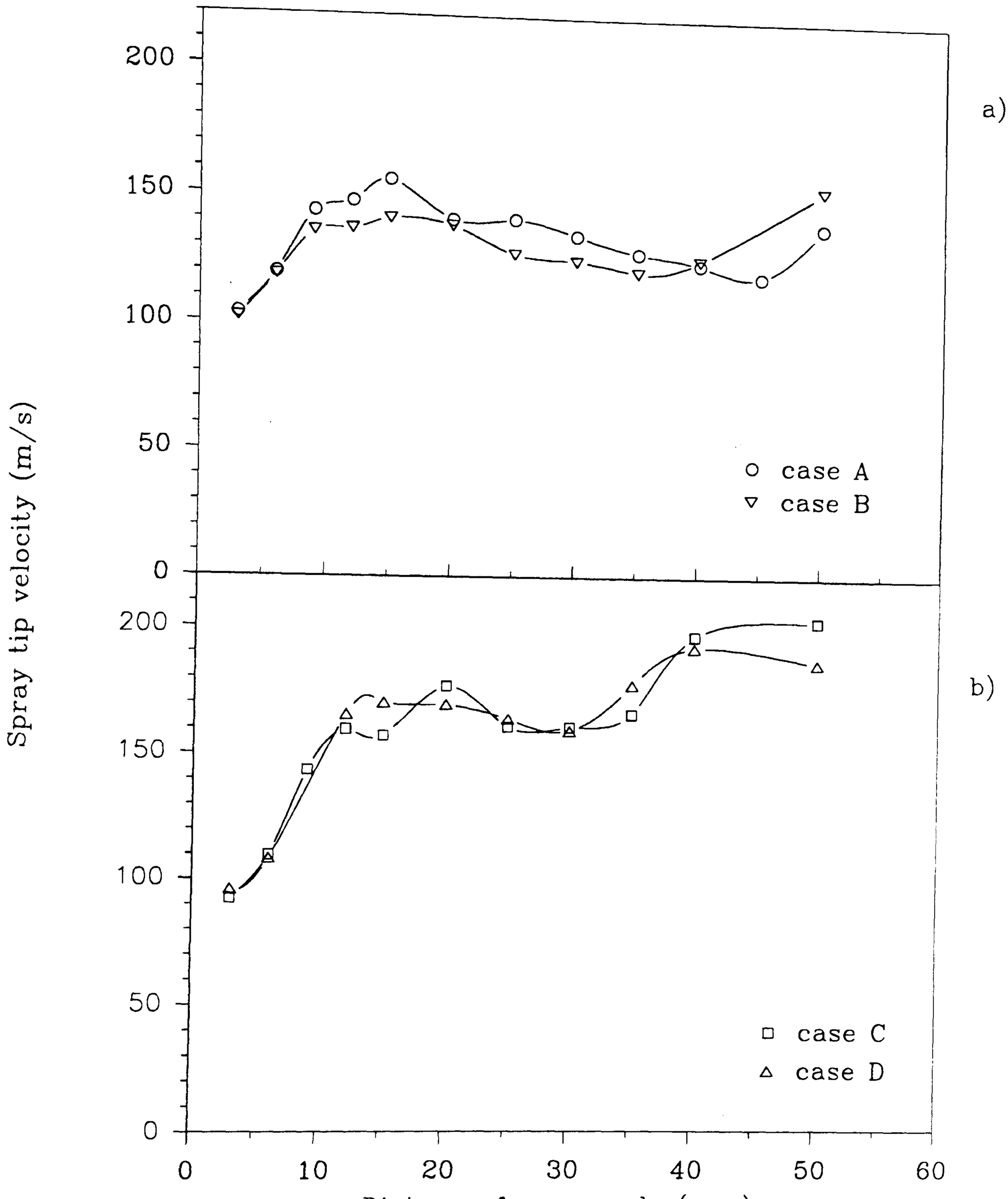


Figure 4.44 Variation of spray-tip velocity at (a)1000 and (b)2000 rpm with distance from the unit injector nozzle tip.

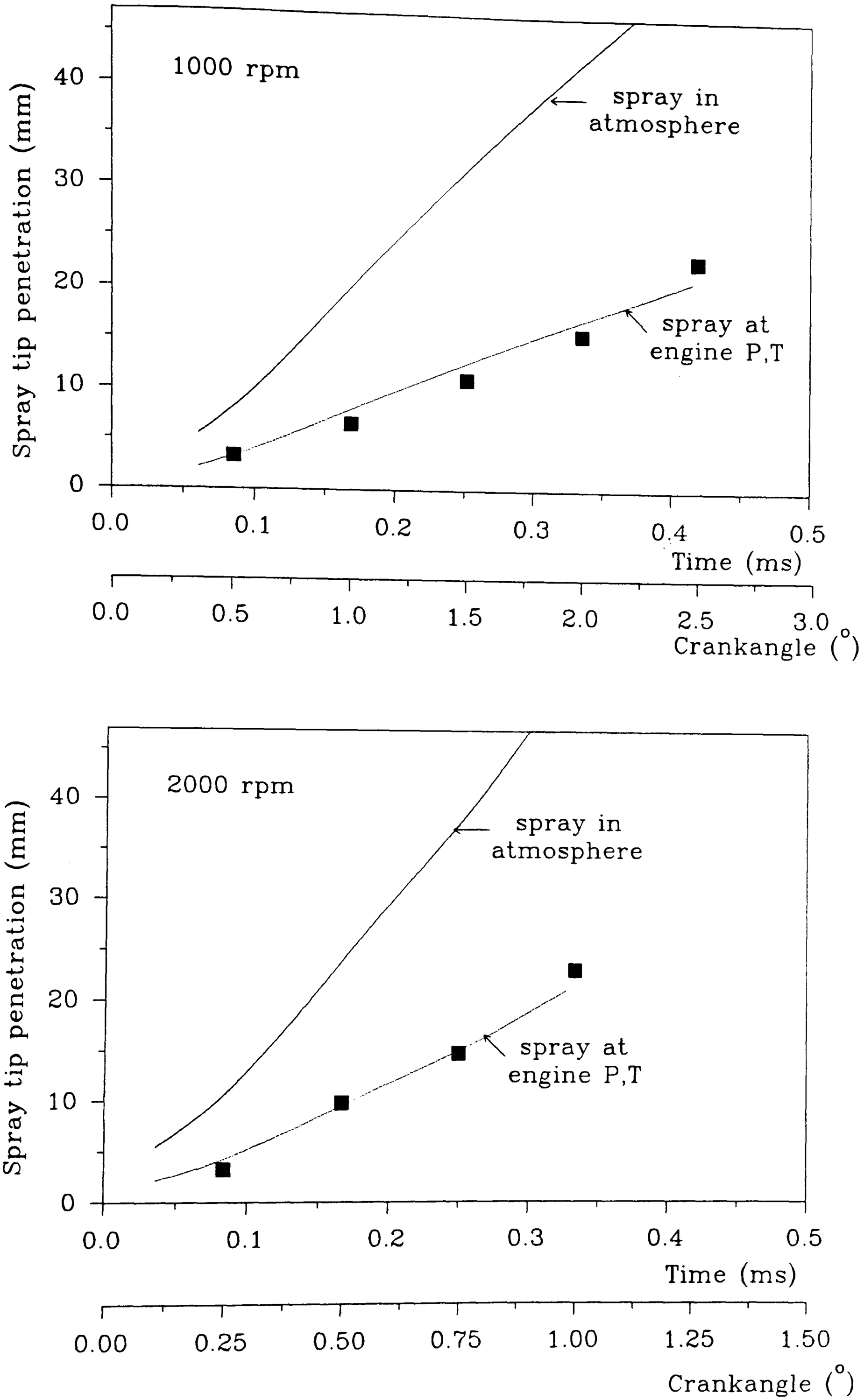


Figure 4.45 Variation of spray penetration at (a)1000 and (b)2000 rpm with time (ms/°CA) from the start of the injection under both atmospheric and engine conditions (using equation from Dent, 1971), compared with high speed photography data.

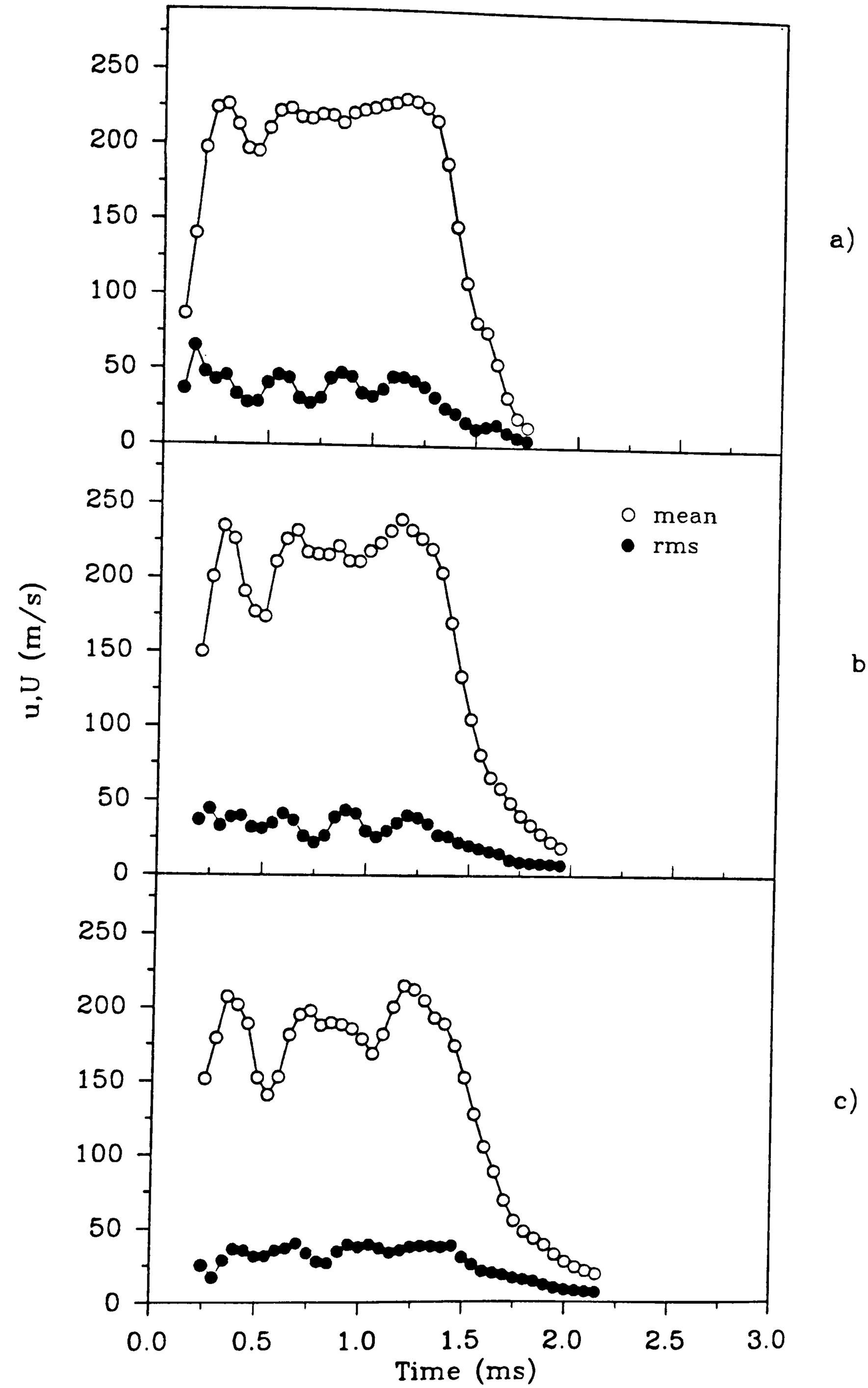


Figure 4.46 Temporal profiles of axial droplet velocities along the centreline at (a)r=10mm (b)r=20mm and (c)r=30mm (case A)

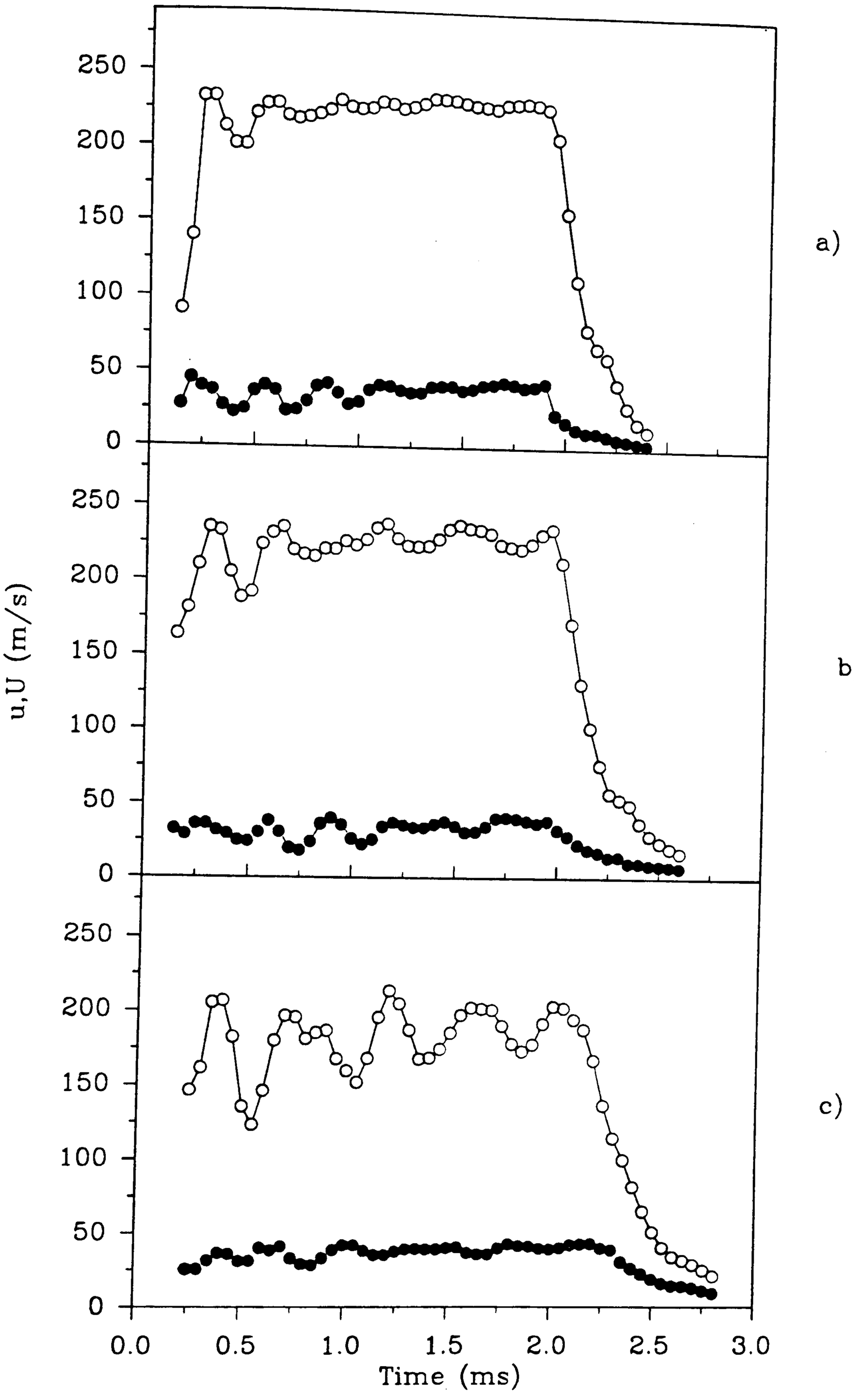


Figure 4.47 Temporal profiles of axial droplet velocities along the centreline at (a)r=10mm (b)r=20mm and (c)r=30mm (case B)

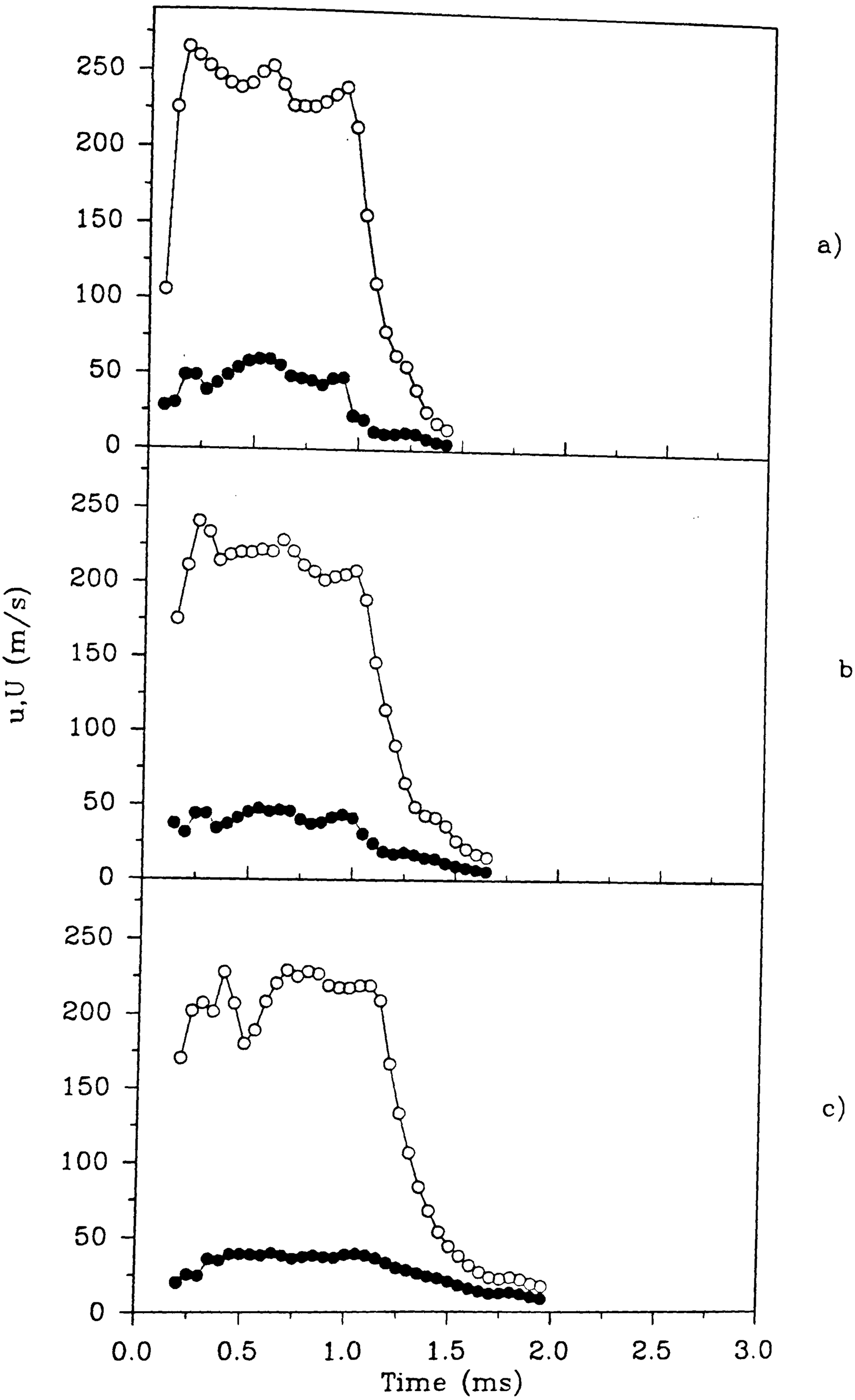


Figure 4.48 Temporal profiles of axial droplet velocities along the centreline at (a)r=10mm (b)r=20mm and (c)r=30mm (case C)

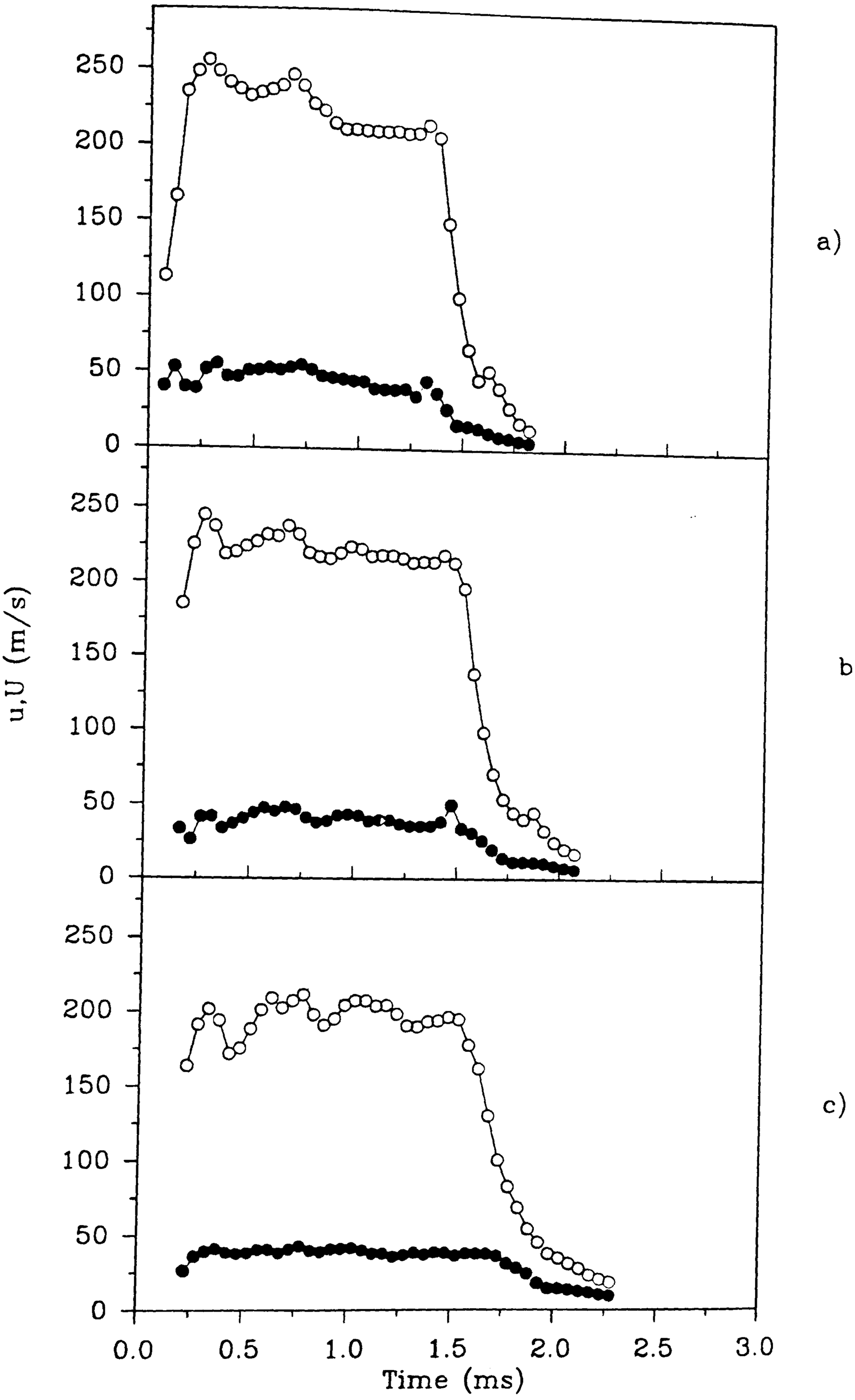


Figure 4.49 Temporal profiles of axial droplet velocities along the centreline at (a)r=10mm (b)r=20mm and (c)r=30mm (case D)

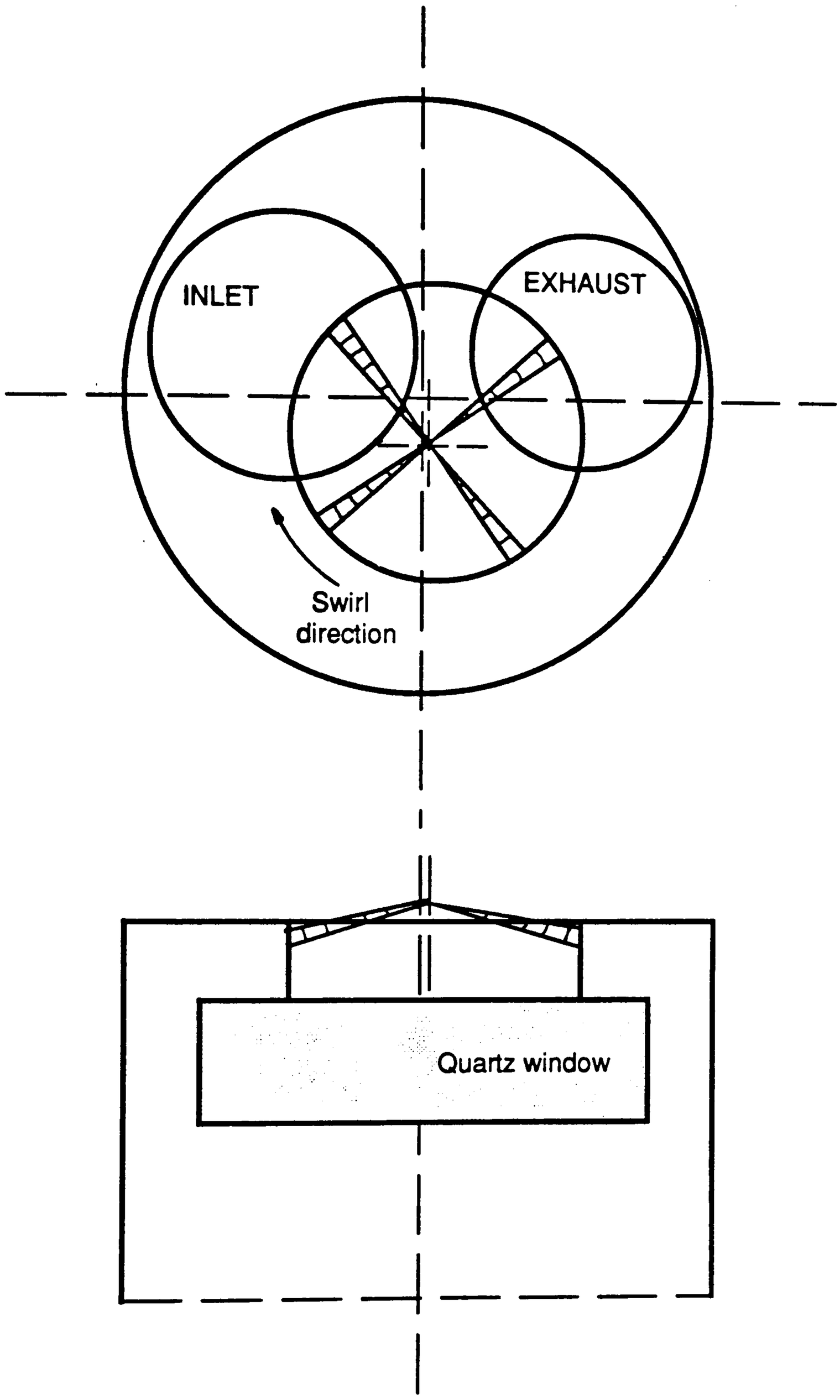


Figure 4.50 In-cylinder view of the Hydra combustion chamber





Figure 4.51 Sequence from high-speed film case A_1

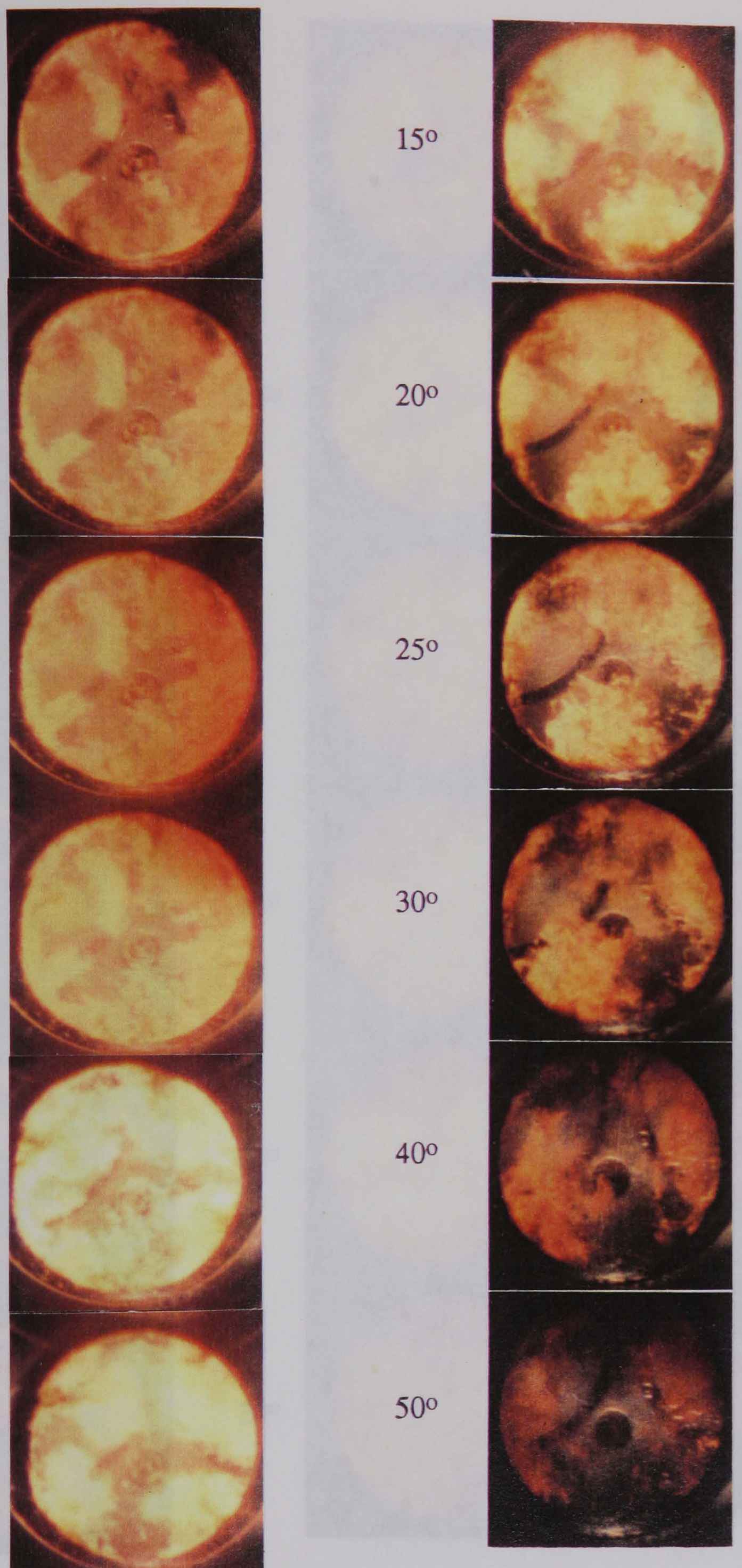


Figure 4.51 Continued

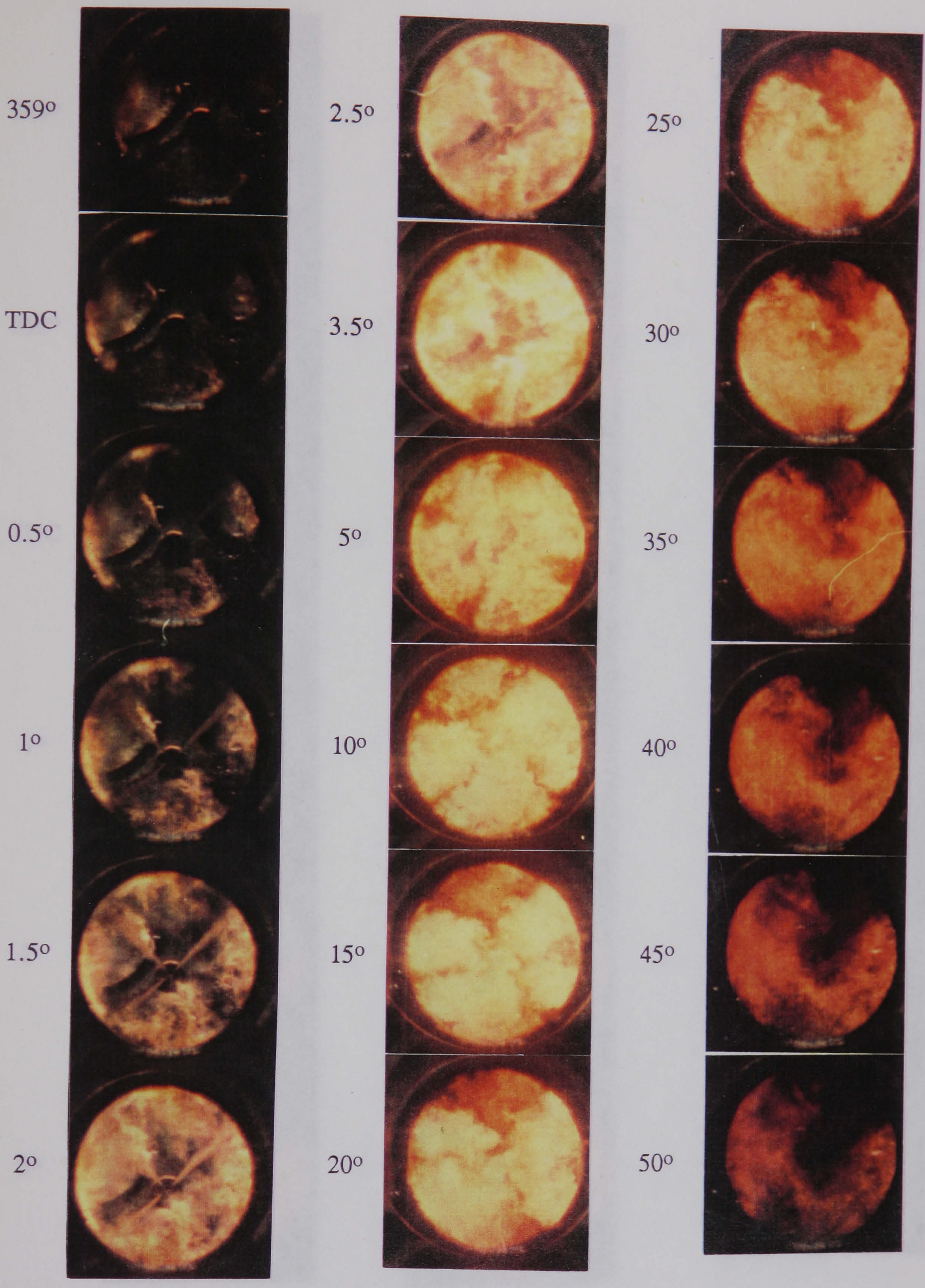


Figure 4.52 Sequence from high-speed film case B_1

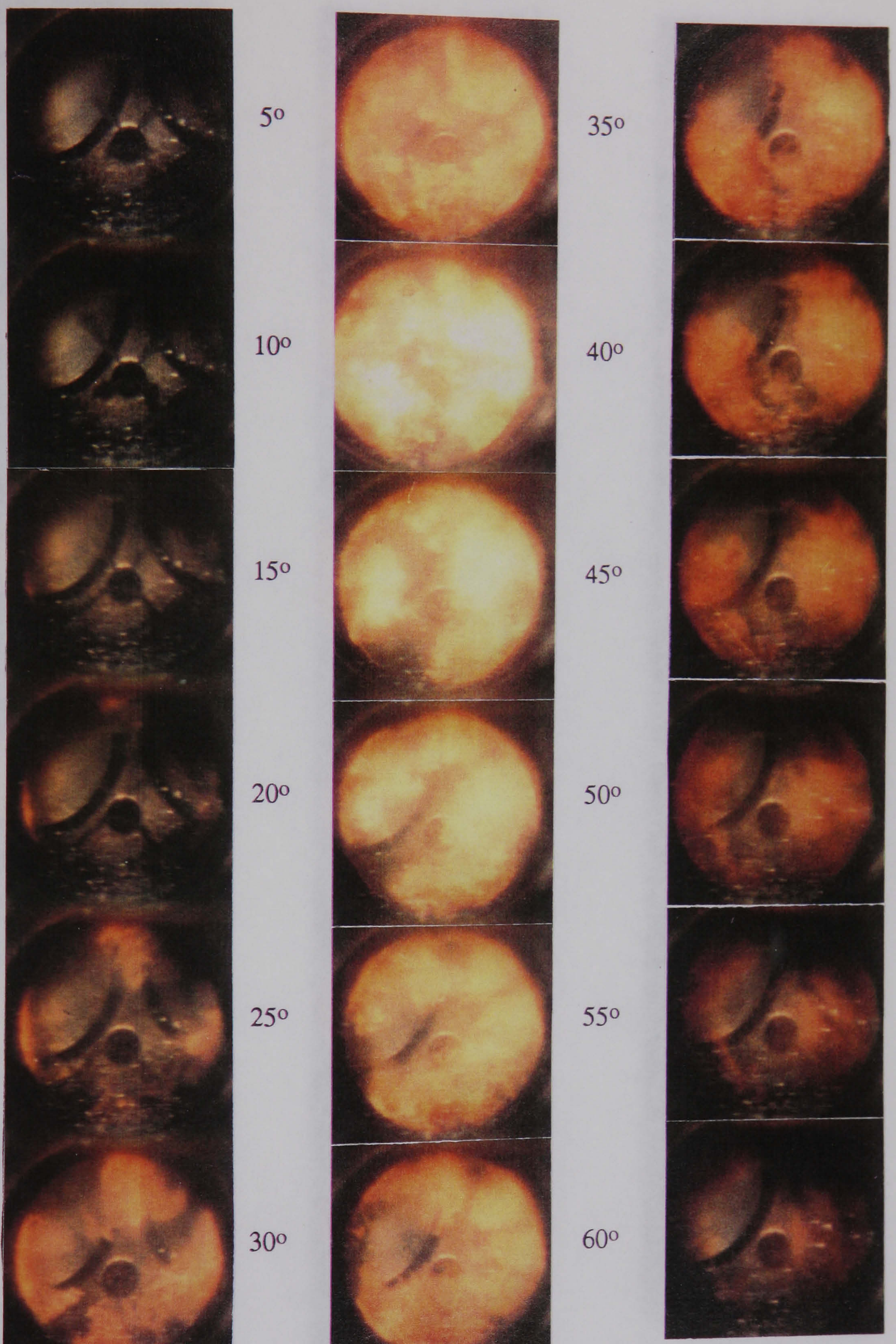


Figure 4.53 Sequence from high-speed film case C_1

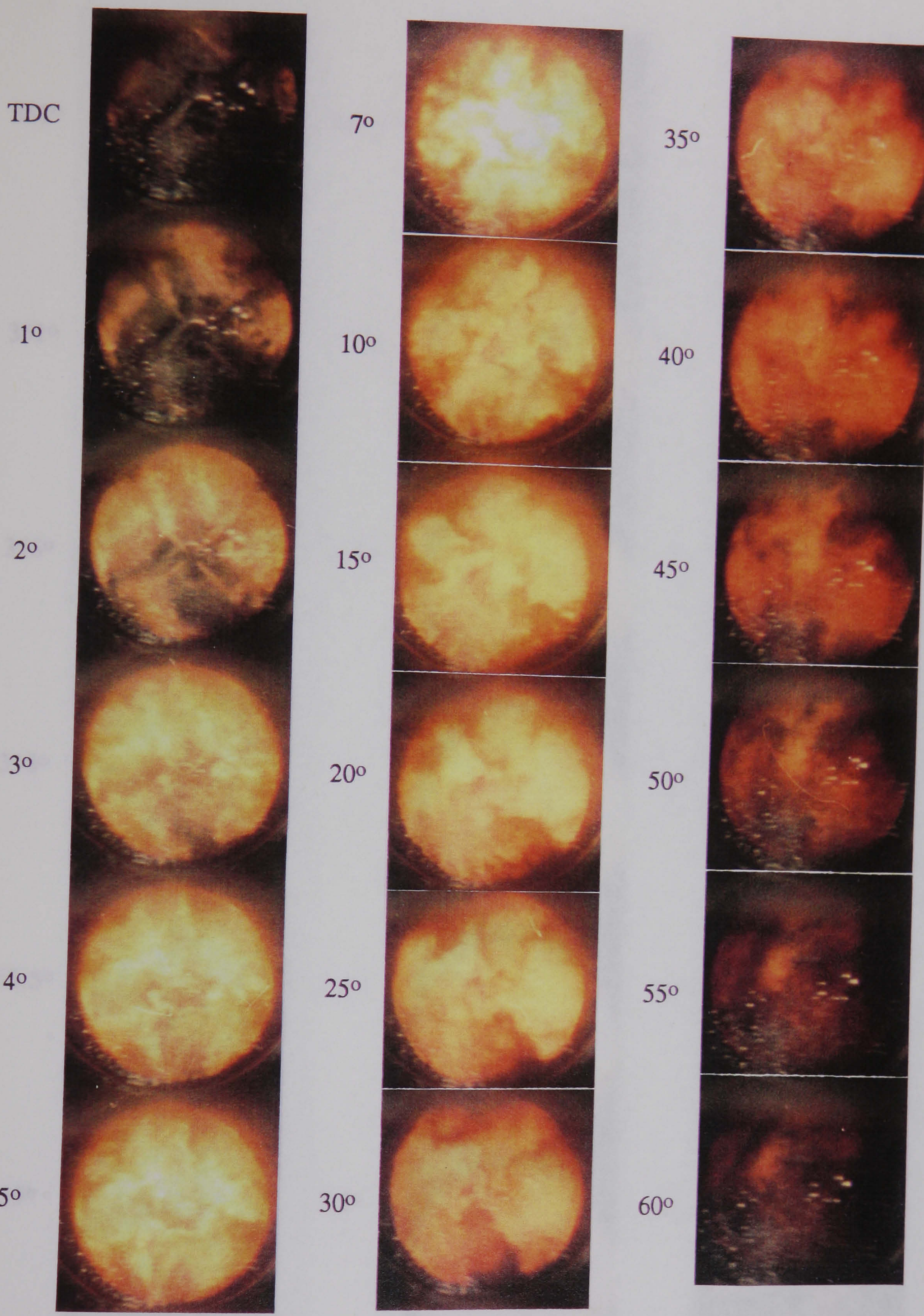


Figure 4.54 Sequence from high-speed film case D_1

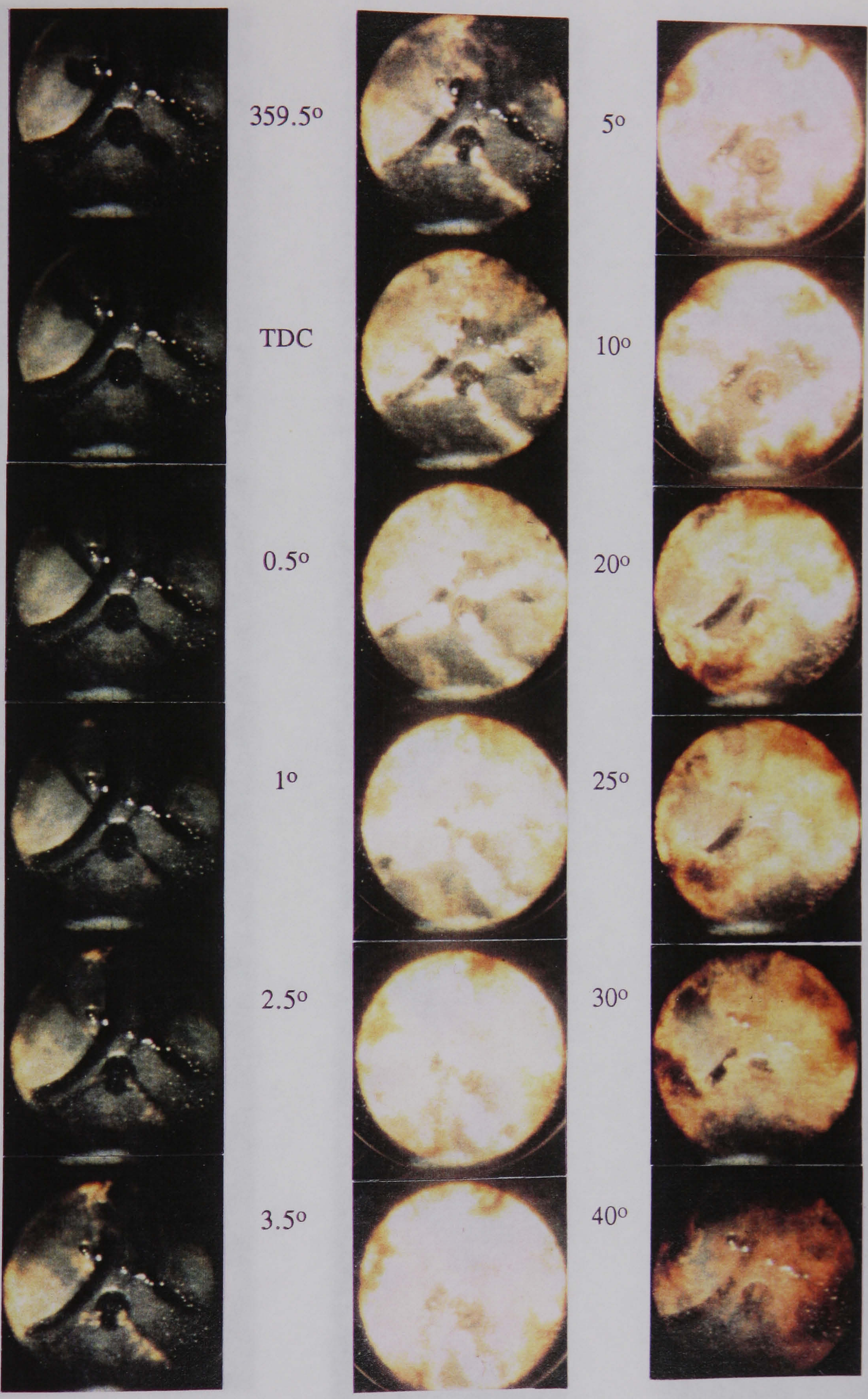


Figure 4.55 Sequence from high-speed film case A_2

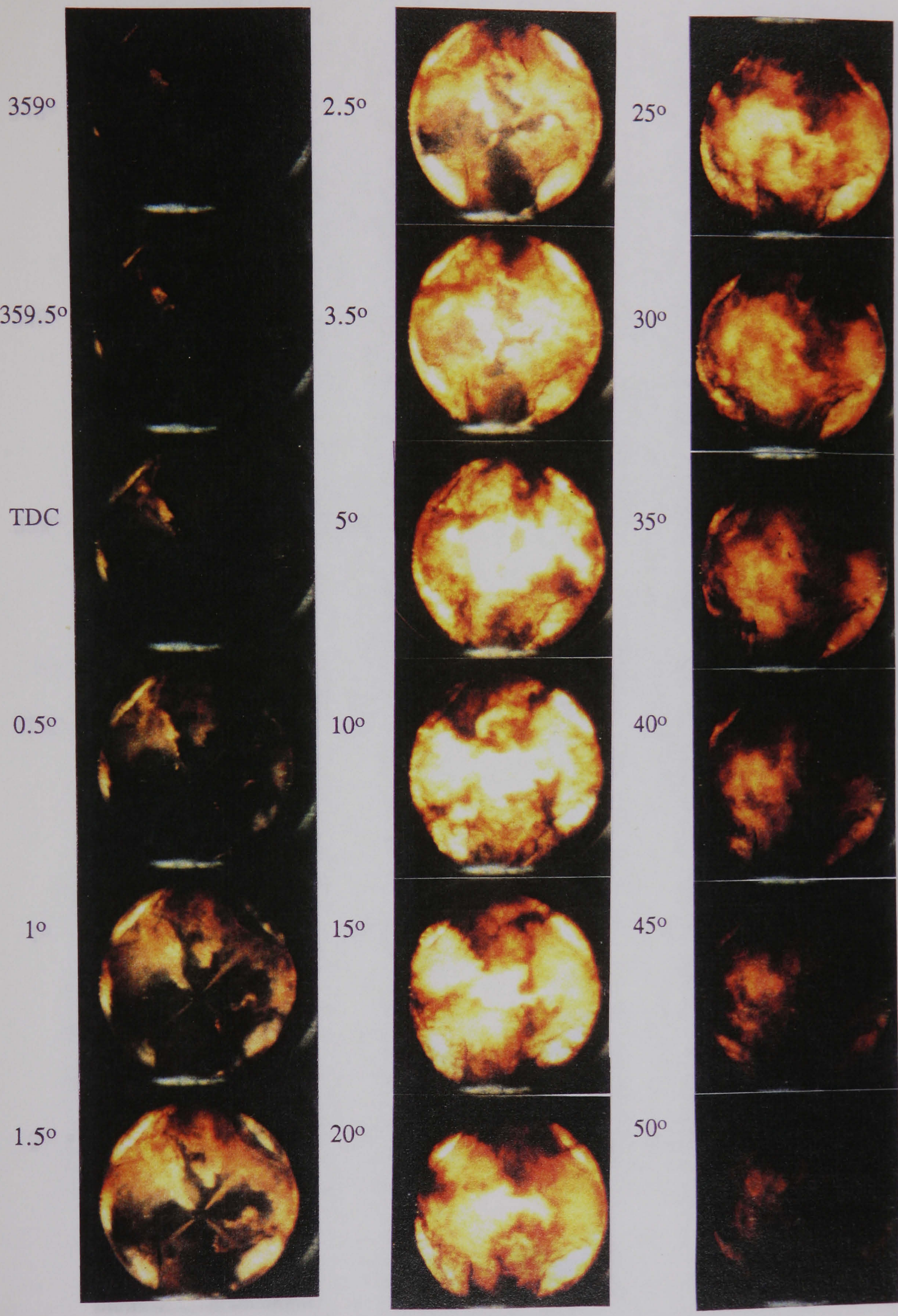


Figure 4.56 Sequence from high-speed film case B_2

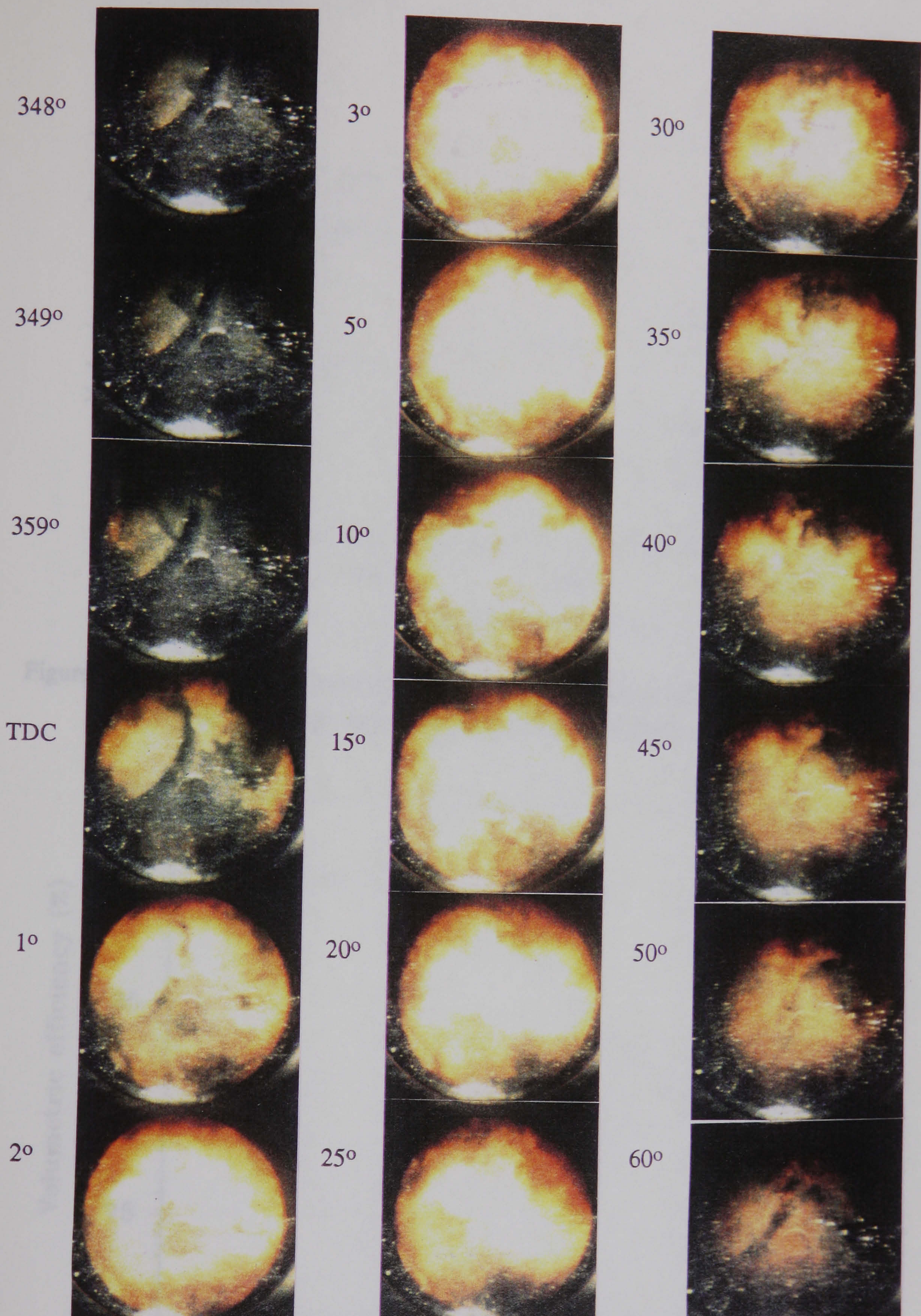


Figure 4.57 Sequence from high-speed film case C_2

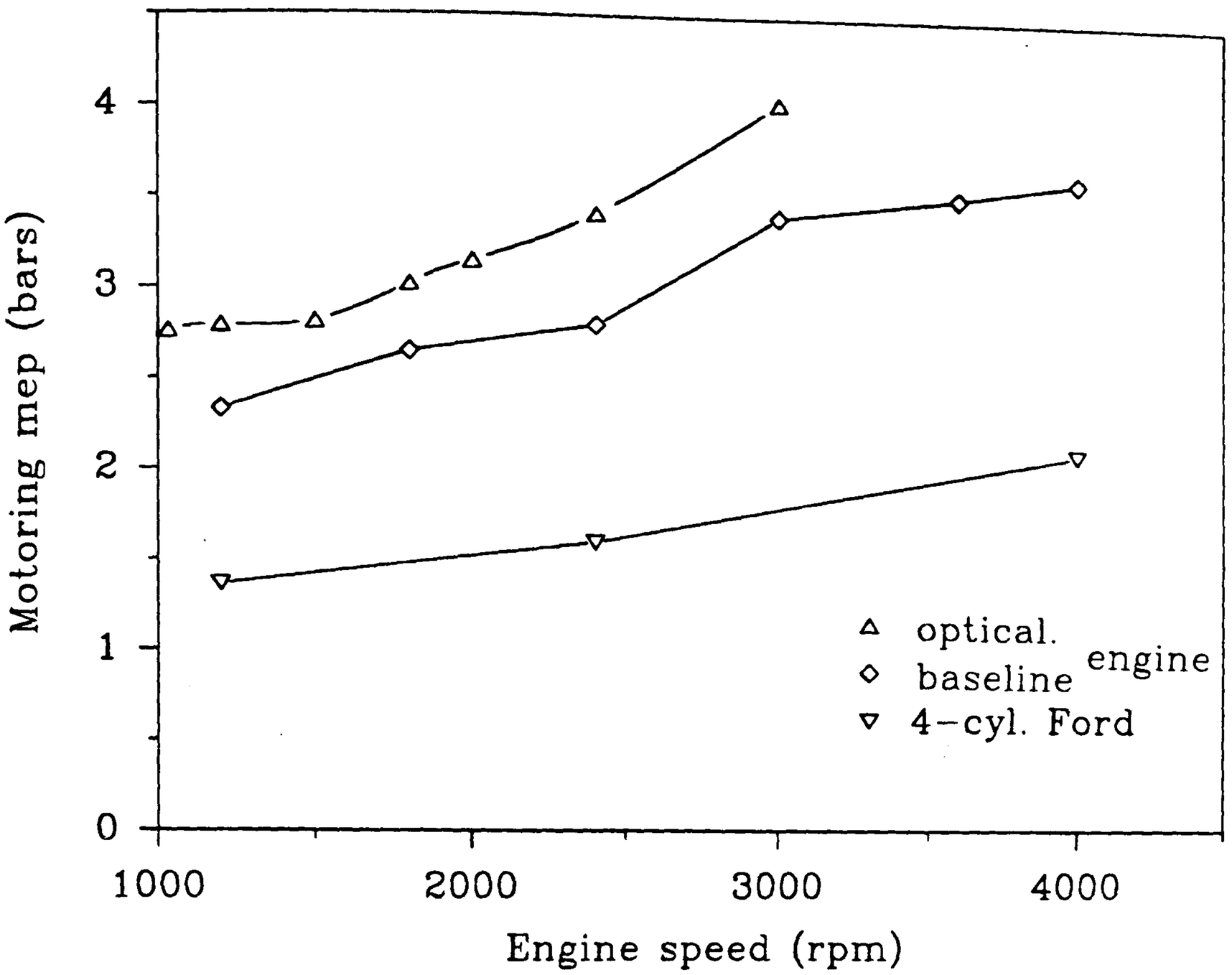


Figure 4.58 Variation of motoring mean effective pressure of the 4-cylinder Ford and Hydra engines (in both versions) with engine speed.

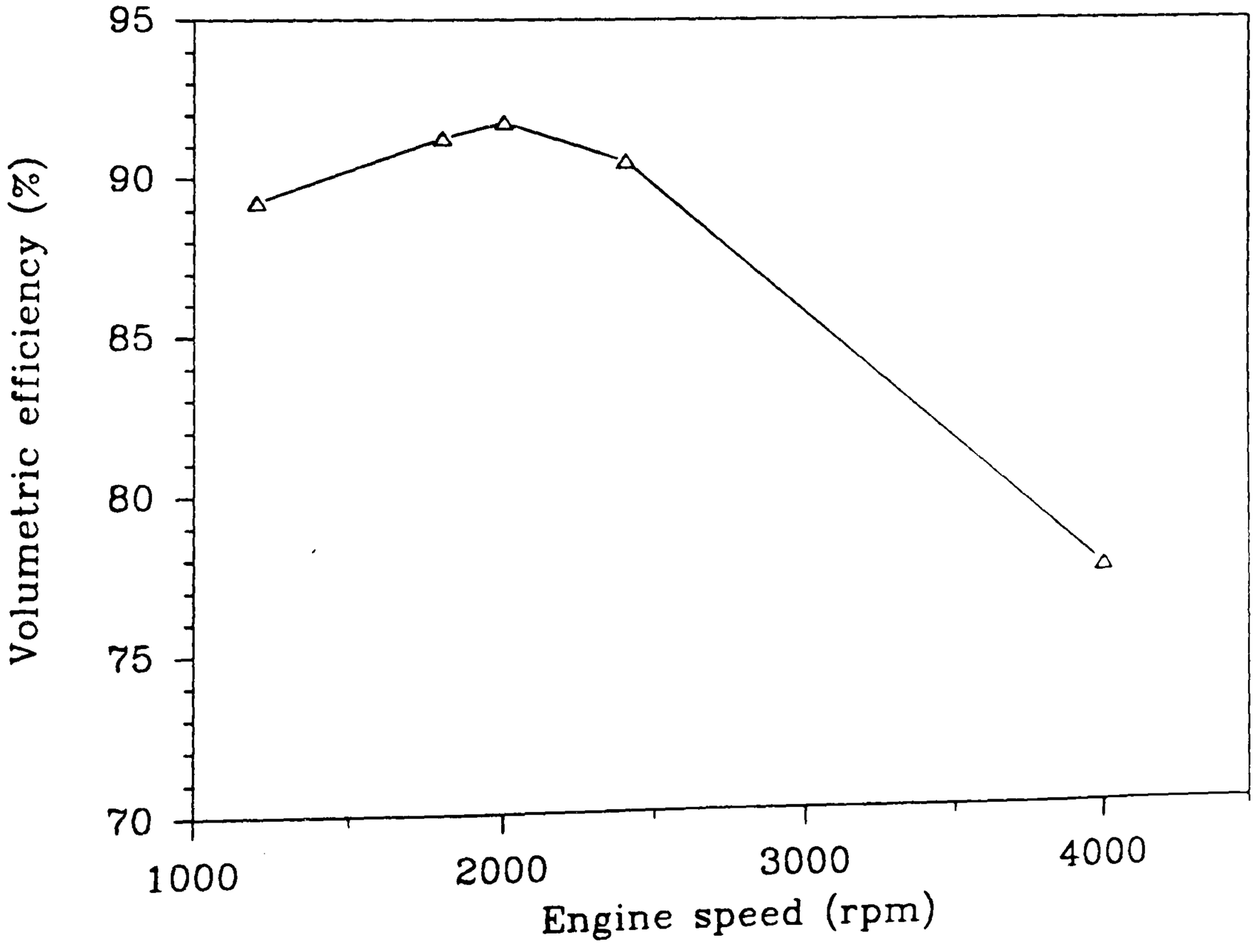


Figure 4.59 Variation of volumetric efficiency of the Hydra engine with engine speed

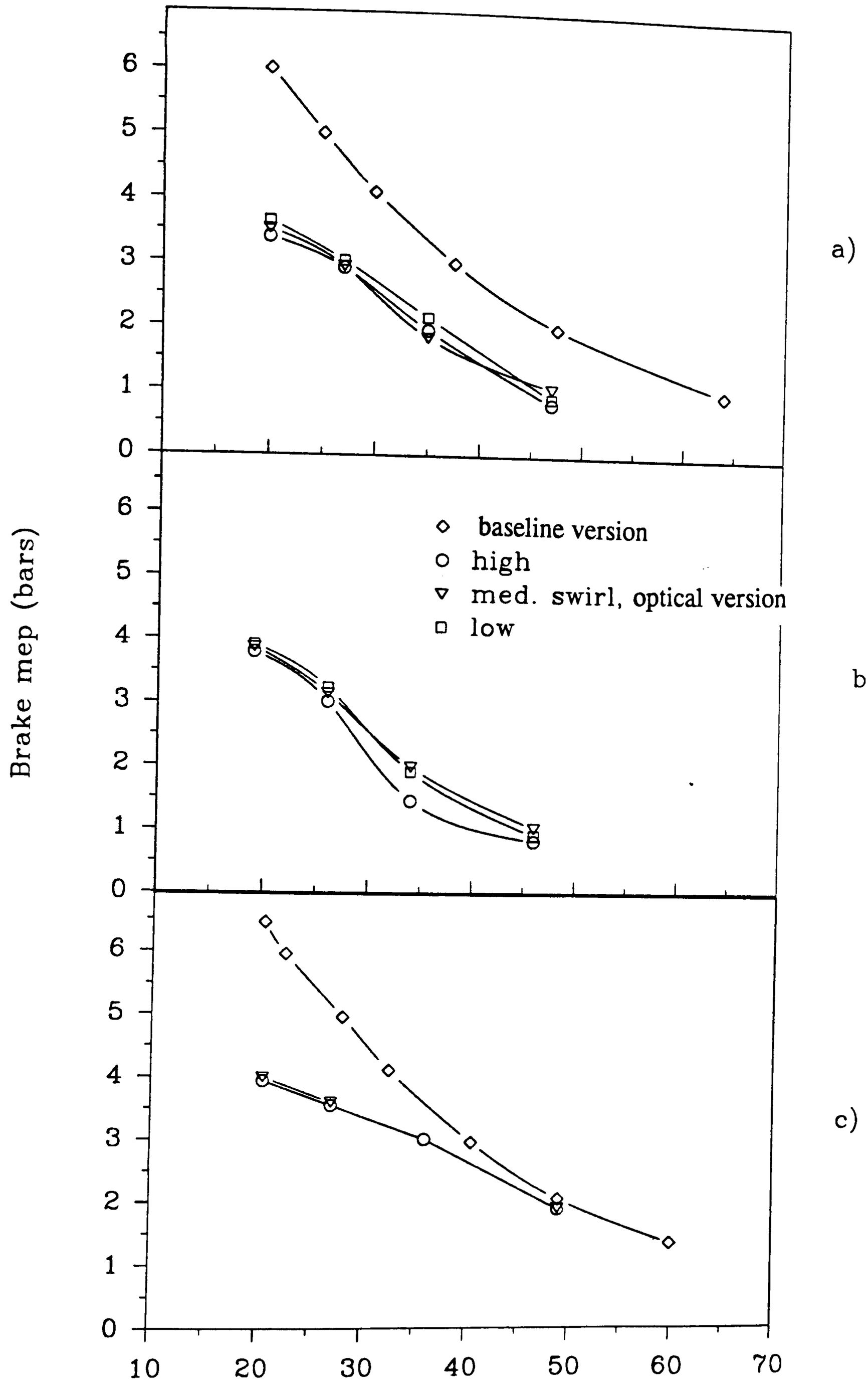


Figure 4.60 Variation of brake mean effective pressure of the Hydra engine in both versions with air-to-fuel ratio at (a)1200 (b)2000 and (c)2400rpm

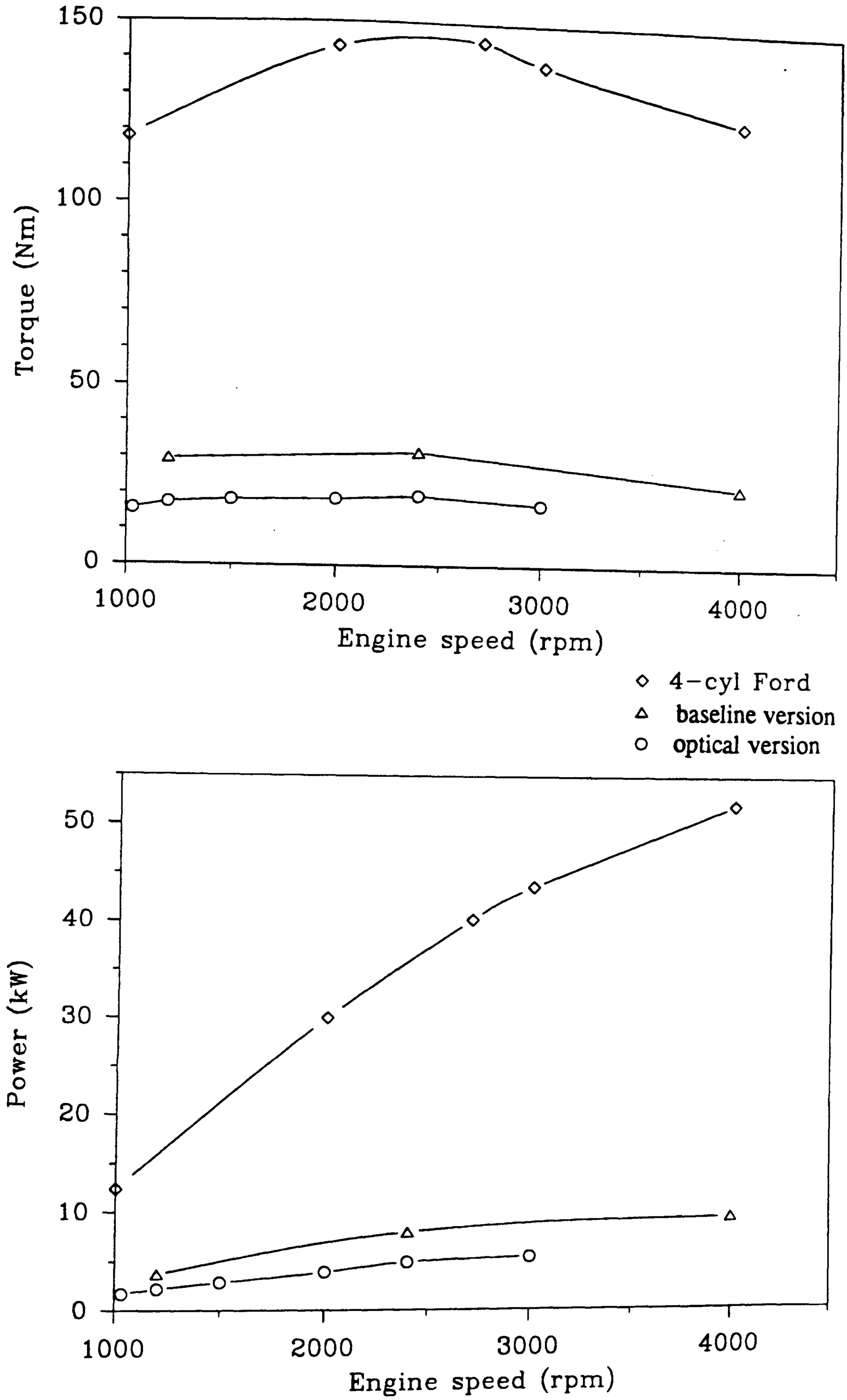


Figure 4.61 Variation of (a) torque and (b) power of the 4-cylinder Ford and Hydra engines (in both versions) with engine speed.

CHAPTER 5

CLOSURE TO THE THESIS

In this last chapter an overview of only the most important findings of the thesis is presented since the detailed information has been summarised at the end of the previous chapters. Based on the experience acquired from this work combined with conclusions from similar studies, areas in which further research is needed are identified and recommendations are made for the way in which future work should proceed. The chapter also discusses the implications of the findings on the design and operating variables of high-speed direct-injection diesel engines.

The presented data in this thesis were obtained by laser Doppler velocimetry, beam deflection and high speed photography in a steady flow rig and a variety of research engines with increasing geometrical complexity from idealised towards production engine geometries. In terms of the swirl generating mechanism three methods were examined; swirl vanes placed in an axisymmetric port, a production helical port and a variable swirl port mechanism producing swirl levels equivalent to those of production engine heads. Piston geometries under investigation included flat piston-crowns, elongated piston-bowls and cylindrical piston bowls corresponding to geometrical compression ratios of 3.5-18 and for engine speeds between 200 and 3000rpm.

Two research tools are proposed for the simulation of engine flows using widely available and easily machinable transparent acrylic material for optical access into the cylinder. In steady flow experiments a porous plate positioned at the open end of the acrylic cylinder can be used to simulate adequately the moving piston in terms of ensemble-averaged mean velocities. Throttling the induction air and, thus, reducing the maximum in-cylinder pressure allows the use of fully transparent acrylic liners and piston-bowls, identical to production geometries and at realistic diesel compression ratios, thus providing maximum optical access near TDC of compression for velocity measurements.

The effect of inlet manifold geometry on the TDC flowfield for a

cylinder head equipped with a helical port was negligible which shows that observed differences in engine performance with and without an inlet manifold are rather due to variations in volumetric efficiency caused by gas dynamics phenomena.

Swirl centre precession was identified in both the axisymmetric low speed (200rpm) model engine and in the Hydra engine incorporating a helical-type port and operating within the range 1000-3000rpm. The frequency of precession was found in both cases to scale with the rotational speed of the crankshaft while the increased rms values observed around the cylinder axis of the model engine are less pronounced in the more realistic geometry and higher speed range of the Hydra engine.

The investigation of the in-cylinder flow during induction and compression under different speeds and swirl levels, comparable to production engines, revealed that the initial relative strength of the two counteracting vortices generated by the variable-swirl port during the induction stroke and the time available for flow development, being inversely proportional to engine speed, shape the swirl profiles during compression. The axial velocity field around IVC is influenced by the magnitude of the reverse flow towards the inlet port, which, in turn, varies with engine speed for a given timing of the inlet valve closure. The detailed velocity measurements in the Hydra engine provide a data bank which is currently used to validate multi-dimensional computer codes under realistic production engine geometries and speeds; they also provide information about the temporal evolution of the flow throughout most of the compression stroke which allow improved understanding of the angular momentum decay mechanism as a function of initial swirl levels, bowl geometry and engine speed.

Due to difficulties to quantify the transient spray development inside the engine cylinder, the multi-hole spray from the electronic unit injector was characterised under atmospheric conditions in terms of spray tip penetration and droplet velocities which were correlated to those under engine conditions using data obtained by high speed photography. During the ignition delay period the sprays remained unaffected by the swirling air within the piston bowl at the range of load and swirl levels examined and, as a result,

considerable wall wetting occurred. The observed overpenetration of the fuel sprays seems to outweigh the major advantage offered by the higher injection pressures of the unit injector in improving fuel atomisation; this was confirmed by comparing the performance of the baseline version of the Hydra engine with the multi-cylinder Ford engine of nearly identical geometry and equipped with a pump-pipe-nozzle injection system.

Ignition was initiated at the spray boundaries where high velocity gradients and the associated strong shear stresses result in vaporisation of the smaller fuel droplets which are carried downwind by the swirling air to form a combustible mixture; at low-to-medium load ignition sites were observed midway along the bowl radius contrary to higher loads where ignition was initiated near the piston walls. During the mixing-controlled or 'diffusion' phase swirl affected the combustion development by transporting low momentum fuel clouds which had already impinged on the wall, and thus promoted the spreading of the flame; this was confirmed by the shorter duration of combustion at higher swirl levels, as revealed by the last visible light in the high speed photographs. The implication of this feature is that combustion development can be improved if swirl levels are maintained during early expansion and this can only be achieved by the particular design of the piston-bowl especially in the entrance area. Another important characteristic of the piston geometry is its base; the flat piston-bowl base dictated by the requirement for optical access was shown to contribute to the poor performance of the Hydra engine by not enhancing mixing in the central region of the bowl. At medium-to-high loads, fuel injection continues after the combustion starts and droplets ignite as soon as they emerge from the nozzle; it is during this period that high injection pressures and the associated finer atomisation can improve the burning rate of the fuel droplets during the expansion stroke and thus reduce the amount of partially burnt carbon particles which are the major cause of particulate emissions. It follows that the fuel injection rate should be decreased during the ignition delay period and increased during the main phase or alternatively, fuel injection should be divided into two-stages to minimise wall wetting. This can simultaneously reduce the rate of heat release during the 'premixed' phase resulting in lower NO_x emissions and noise levels. Current developments in this field such as the two-spring injectors attempt to achieve this situation with some degree of success. The best method seems to be the unit injector where, by employing

an electronic control of the solenoid valve, the injection timing and the injection rate temporal profile can be adjusted to suit the specific demands of the engine according to speed and load. Technical difficulties and cost have prevented until now the use of unit injectors in small HSDI diesel engines but in view of the more stringent emission regulations they may be considered as viable solution for production engines.

The Hydra engine which was specially manufactured as a research single-cylinder research engine based on a well tested multi-cylinder production engine, has proved to be a useful research tool where results from optical techniques as well as a limited number of conventional methods were combined in order to understand the combustion process and the associated mechanisms of pollutant formation. Further work is needed towards this direction either by improving the existing measurement techniques or developing new ones. In particular, detailed velocity measurements inside the piston-bowl and the clearance volume of realistic engine geometries should be obtained under both motored and firing conditions which may exceed the capabilities of current LDV systems. Typical TDC clearances are similar to the probe volume length and the presence of carbon particles and combustion emitted light together with the undesirable surface reflections result in poor signal-to-noise ratios. Smaller probe volumes with high frequency shift to compensate for the decreased number of fringes, and signal processing equipment based on hardware fast Fourier transform analysis are possible methods of overcoming these problems. High speed photography or shadowgraphy can only give qualitative information about the fuel distribution inside the piston-bowl and laser-induced fluorescence is currently under development to provide two-dimensional information about vapour and liquid fuel distribution in the combustion chamber. Phase Doppler velocimetry which can measure simultaneously size and velocity of fuel droplets, requires extended optical access and its use may be limited in production engines.

An area which has not been examined in this thesis is heat transfer between injected fuel and piston walls. This is particularly relevant to small HSDI diesel engines where a certain portion of the injected fuel impinges on the wall and vaporises as a result of secondary atomisation or forms a liquid film which evaporates later in the expansion stroke. Another area worth

investigating is the variations of flow, combustion and emissions between the individual cylinders of multi-cylinder production engines and this requires multi-cylinder optical research engines which were introduced in the research community very recently.

It is expected that the results of systematic experimental studies, supported by parallel theoretical investigations based on multi-dimensional computer codes, will further assist the understanding of the flow, combustion and emission formation inside the cylinders of HSDI diesel engines and thus contribute to the design of more efficient and clean engines at reduced development times.

APPENDIX A

DEFINITION OF SWIRL RATIO

The swirl ratio (SR) of the in-cylinder contents is defined as the angular velocity of a solid-body rotating flow (ω_{sb}) having equal angular momentum to the actual flow, divided by the crankshaft rotational speed.

$$SR=\frac{\omega_{sb}}{2\pi N}$$

It is usually calculated at IVC and during the compression stroke, when the mass of the cylinder contents remains constant; it is a dimensionless number and a function of crankangle, i.e.

$$SR=SR(\theta) \quad IVC<\theta<TDC$$

The value at IVC is a characteristic quantity representing the swirl capacity of the inlet port. It can be estimated approximately from steady-flow rig data or, more accurately, from swirl velocity profiles obtained at different levels inside the cylinder.

Monaghan and Pettifer (1981) used steady-flow impulse torque (T) meter data obtained at different valve lifts. Assuming that the valve flow is the same under the transient engine conditions as on the steady flow rig for the equivalent valve lifts (and corresponding crankangles), the equivalent solid-body angular velocity can be estimated by:

$$\omega_{sb}(IVC) = \frac{2}{R_c^2} \left(\int_{\theta_o}^{\theta_c} T d\theta\right) \Big/ \left(\int_{\theta_o}^{\theta_c} \dot{m} d\theta\right)$$

where θ_o, θ_c are the crankangles at IVO and IVC, respectively, and the torque T and mass flow rate $\dot{m}$ are evaluated at the valve lift corresponding to the particular crankangle. The resulting swirl ratio is better known as Ricardo swirl ratio (R_s).

When mean profiles of the tangential velocity component are available at different axial distances, a direct and more precise method can be applied. If Ω_{tot} is the total angular momentum of the cylinder contents with respect to the cylinder axis then, for a given crankangle, it can be shown that

$$\Omega_{tot} = \rho \int_0^{z_P} \int_0^{R_c} \int_0^{2\pi} W\, r^2\, d\phi\, dr\, dz$$

By definition

$$\omega_{sb} = \frac{\Omega_{tot}}{\frac{1}{2} m_c R_c^2}$$

Thus the swirl ratio becomes

$$SR = \frac{1}{R_c^4\, \pi^2\, z_p\, N} \int_0^{z_P} \int_0^{R_c} \int_0^{2\pi} W\, r^2\, d\phi\, dr\, dz$$

An equivalent swirl ratio (SR_e) can be defined for a given profile, representing the swirl level at the measurement plane. Assuming that the flow is axisymmetric (W=W(ϕ) only)

$$SR_e = \frac{2}{R_c^4\, \pi\, N} \int_0^{R_c} W\, r^2\, dr$$

For each swirl velocity profile, the SR_e is the average of the values calculated for the two halfs of the velocity distribution; the integration is performed using the trapezium rule and for the near-wall region a 1/7th power law is assumed.

Another characteristic quantity of the in-cylinder contents, similar to the swirl ratio, is the specific angular momentum (Ω_s in m^2/s) given by

$$\Omega_s = \frac{2}{R_c^2} \int_0^{R_c} W\, r^2\, dr$$

REFERENCES

ABDEL-GAYED, R.G., BRADLEY, D. and LAWES, M. (1987), "Turbulent Burning Velocities, a General Correlation in Terms of Straining Rates", Proc. R. Soc. Lond., A 414, pp. 389-413.

ALCOCK, J.F. and SCOTT, W.M. (1963), "Some More Light on Diesel Combustion", Proc. I. Mech. E., (AD), No.5, pp. 179-200.

ALKIDAS, A.C. (1984), "Relationships Between Smoke Measurements and Particulate Measurements", SAE Paper 840412.

AMANN, C.A., (1985), "Classical Combustion Diagnostics for Engine Research", SAE Paper 850395.

ANNAND, W.J.D. (1969), "Engine Breathing-Aerodynamics of Low Speed Flow Through Inlet Valves", Automobile Engineer, Vol. 59.

ARAI, M., TABATA, M., HIROYASU, H. and SHIMIZU, M. (1984), "Disintegrating Process and Spray Characterisation of Fuel Jet Injected by a Diesel Nozzle", SAE Paper 840275.

ARCOUMANIS, C. (1983), "Velocity and Concentration Fields in Reciprocating Model Engines", PhD Thesis, University of London.

ARCOUMANIS, C., BICEN, A.F. and WHITELAW, J.H. (1983), "Squish and Swirl-Squish Interaction in Motored Model Engines", J. Fluids Engng., Vol. 105, pp. 105-112.

ARCOUMANIS, C., BEGLERIS, P., GOSMAN, A.D. and WHITELAW, J.H. (1986), "Measurements and Calculations of the Flow in a Research Diesel Engine", SAE Paper 861563.

ARCOUMANIS, C., VAFIDIS, C. and WHITELAW, J.H. (1987a), "Valve and In-Cylinder Flow Generated by a Helical Port in a Production Diesel Engine", J. Fluids Engng., Vol. 109, (4).

ARCOUMANIS, C. and WHITELAW, J.H. (1987b), "Are Steady Flow Inlet Boundary Conditions Valid for Engine Cylinder Calculations?", Proc. Congress on Modelling of Internal Combustion Engines, Valencia.

ARCOUMANIS, C., VAFIDIS, C., VORROPOULOS, G. and WHITELAW, J.H. (1987c), "Correlation between Valve and In-Cylinder Flow in a Motored Reciprocating Engine, ASME FED, Vol. 62, pp.9-15.

ARCOUMANIS, C., COSSALI, E., VORROPOULOS, G. and WHITELAW, J.H. (1988a), "Steady Flow Characteristics through the Inlet Valve of a Ricardo Hydra Cylinder Head with a Variable Swirl Port", Imperial College, Mech. Eng. Dept., Report FS/88/06.

ARCOUMANIS, C., COSSALI, E. and WHITELAW, J.H. (1988b), "Measurements of Tip Penetration Velocity of Confined High Density Transient Jets by Laser Beam Deflection", Experiments in Fluids, Vol. 6.

ARCOUMANIS, C. and TANABE, S. (1989), "Swirl Generation by Helical Ports", SAE Paper 890790.

ARCOUMANIS, C., COSSALI, E., PAAL, G., and WHITELAW, J.H. (1990), "Transient Characteristics of Multi-hole Diesel Sprays", SAE Paper 900480.

AROLD, M.L., ESPEY, T.A., LITZINGER, T.A., SANTAVICCA, D.A. and SANTORO, R.J. (1990), "A Study of Non-swirling and Swirling and Their Effects on Spray Flow Fields and Combustion in an Optically-Accessible, DI Diesel Engine", SAE Paper 900396.

AUSTEN, A.E.W. and LYN, W.-T. (1963), "Relation Between Fuel Injection and Heat Release in a Direct-Injection Engine and the Nature of the Combustion Processes", Proc. I. Mech. E., No.1, pp. 47-62.

BALLES, E.N. and HEYWOOD, J.B. (1988), "Fuel-Air Mixing and Diesel Combustion in a Rapid Compression Machine", SAE Paper 880206.

BATCHELOR, G.K. (1967) *"An Introduction to Fluid Mechanics"*, Ch.7, Cambridge University Press.

BATES, S.C. (1988), "A Transparent Engine for Flow and Combustion Visualisation Studies", SAE Paper 880520.

BEER, J.M. and CHIGIER, N.A. (1974), *"Combustion Aerodynamics"*, Ch.5, Applied Science Publishers.

BEGLERIS, P. and GOSMAN, A.D. (1987), "Analysis of In-Cylinder Flow Generation by Helical Ports", Proc. Symp. on Fluid Flow and Heat Transfer in Reciprocating Engines, ASME Winter Meeting.

BELARDINI, P., BERTOLI, C., CORCIONE, F.E., POLICE, G. and VALENTINO, G., "The Role of Mean Motion and Turbulence Structure on Gaseous and Particulate Emissions of DI Diesel Combustion System", SAE Paper 890839.

BIRD, G.L., "The Ford 2.5 Litre High Speed Direct Injection Diesel Engine-Its Performance and Future Possibilities", SAE Paper 850262.

BOPP, S., VAFIDIS, C. and WHITELAW, J.H. (1986), "The Effect of Engine Speed on the TDC Flowfield in a Motored Reciprocating Engine", SAE Paper 860023.

BOSCH (1986), "Automotive Handbook", 2nd English Edition, Robert Bosch GmbH.

BRADLEY, D. and SHEPPARD, C.G.W. (1988), "Limitations to Turbulence-Enhanced Burning Rates in Lean Burn Engines", Proc. I. Mech. I., Paper C46/88.

BRANDL, F., REVERENCIC, I., CARTELLIERI, W. and DENT, J.C. (1979), "Turbulent Air-Flow in the Combustion Bowl of a DI Diesel Engine and its Effect on Engine Performance", SAE Paper 790040.

BRANDSTATTER, W., JOHNS, R.J.R. and WIGLEY, G. (1985), "The Effect of Inlet Port Geometry on In-cylinder Flow Structure", SAE Paper 850499.

CARTELLIERI, W.P and WACHTER, H. F. (1987), "Status Report on a Preliminary Survey of Strategies to Meet US-1991 HD Diesel Emission Standards without Exhaust Gas Aftertreatment", SAE Paper No 870342.

CARTELLIERI, W.P and HERZOG, P.L. (1988), "Swirl Supported or Quiescent Combustion for 1990's Heavy-Duty DI Diesel Engines-An Analysis", SAE Paper 880342.

CHANAUD, R.C. (1965), "Observations of Oscillatory Motion in Certain Swirling Flows", J. Fluid Mech., Vol. 21, Part 1, pp. 111-127.

CIPOLLA, G., PUGLISI, A. and VAFIDIS, C. (1987), "In-cylinder Velocity Field Measurements in a Motored Diesel Engine", SAE Paper 870373.

CLAYPOLE, T.C., EVANS, P., HODGE, J. and SYRED, N. (1986), "The Influence of the Precessing Vortex Core on Velocity Measurements in Swirling Flows" Proc. 3rd Int. Symposium on Applications of Laser Anemometry to Fluid Mechanics, Lisbon.

COGHE, A., BRUNELLO, G. and TASSI, E. (1988), "Effects of Intake Ports on the In-Cylinder Air Motion under Steady Flow Conditions", SAE Paper 880384.

COLE, J.B., and SWORDS, M.D. (1980), "An Investigation of the Ignition Process in a Lean-Burning Engine Using Conditionally Sampled Laser-Doppler Anemometry", SAE Paper 800043.

DENT,J.C. (1971), "A Basis for the Comparison of Various Experimental Methods for Studying Spray Penetration", SAE Paper 710571

DENT, J.C. and SALAMA, N.S. (1975), "The Measurement of the Turbulence Characteristics in an Internal Combustion Engine Cylinder", SAE Paper 750886.

DICKSIE, C.B. (1940), *"The High-Speed Compression-Ignition Engine"*, First Edition, Blackie and Son, London.

DIMOTAKIS, P. (1976), "Single Scattering Particle Laser Doppler Measurements of Turbulence", Paper 10, AGARD Conference No. 193, Applications of Non-Intrusive Instrumentation in Fluid Flow Research.

DUNN-RANKIN, D. and SAWYER, R.F. (1986), "LDA Study of the Unburnt Gas Motion Induced by Non-Steady Flame Propagation in a Constant Volume Duct", Lawrence Berkeley Laboratory, Report No. 19165.

DUNN-RANKIN, D., BARR, P.K. and SAWYER, R.F. (1986), "Numerical and Experimental Study of 'Tulip' Flame Formation in a Closed Vessel", 21st Int. Symp. on Combustion, Munich.

DURAO, D.F.G., LAKER, J. and WHITELAW, J.H. (1980), "Bias Effect in Laser Doppler Anemometry", J. Phys. E.,Sci. Instrum., Vol. 13, p. 442.

DURRET, R.P., OREN, D.C. and FERGUSON, C.R. (1987), "A Multidimentional Data Set for Diesel Combustion Model Validation, I-Initial Conditions, Pressure History and Spray Shapes", SAE Paper 872087.

DURST, F., MELLING, A. and WHITELAW, J.H. (1981), *"Principles and Practice of Laser Doppler Anemometry"*, Second Edition, Academic Press, London.

DYER, T.M. and WITZE, P.O. (1978), "Laser Velocimeter Measurements in a Constant Volume Internal Combustion Simulator", 3rd Int. Workshop on Laser Velocimetry, Purdue.

El TAHRY, S.H. (1982), "A Numerical Study on the Effects of Fluid Motion at Inlet-Valve Closure on Subsequent Fluid Motion in a Motored Engine", SAE Paper 820035.

El TAHRY, S.H., KHALIGHI, B., and KUZIAK, Jr.W.R., (1987), "Unsteady Flow Velocity Measurements Around an Intake Valve of a Reciprocating Engine", SAE Paper 870593.

ENOTIADIS, A.C., VAFIDIS, C. and WHITELAW, J.H. (1990), "Interpretation of Cyclic Flow Variations in Motored Internal Combustion Engines", Exp. Fluids, Vol. 10, pp. 77-86.

ESCUDIER, M.P. and KELLER, J.J. (1985), "Recirculation in Swirling Flow: A Manifestation of Vortex Breakdown", AIAA J., Vol. 23, No. 1, pp. 111-116.

ESPEY, C., PINSON, J.A. and LITZINGER, T.A. (1990), "Swirl Effects on Mixing and Flame Evolution in a Research DI Diesel Engine", SAE Paper 902076.

FANSLER, T.D. and FRENCH, D.T. (1987), "Swirl, Squish and Turbulence in Stratified-Charge Engines, Laser-Velocimetry Measurements and Implications for Combustion", SAE Paper 870371.

FISHER, G.L. (1983), "Through-the-piston Combustion Photography on a DI Diesel Engine", Ricardo Consulting Engineers, DP83/1367.

FITZGEORGE, D., and ALLISON, J.L. (1962), "Air Swirl in a Road Vehicle Diesel Engine", Proc. I. Mech. E., (AD), No4.

FRENCH, C.C.J. (1983), "A Universal Test Engine for Combustion Research", SAE Paper 830453.

FUKUTANI, I. and WATANABE, E. (1982), "Air Flow Through Poppet Inlet Valves-Analysis of Static and Dynamic Flow Coefficients", SAE Paper 820154.

GATOWSKI, J.A., BALLES, E.N., CHUN, K.M., NELSON, F.E., EKCHIAN, J.A. and HEYWOOD, J.B. (1984), "Heat Release Analysis of Engine Pressure Data", SAE Paper 841359.

GEORGE, W.K. (1975), "Limitations to Measuring Accuracy Inherent in the Laser Doppler signal", Proc. LDA-Symposium, Copenhagen.

GOSMAN, A.D. (1986), "Flow Processes in Cylinders", Chapter 11 in *Thermodynamics and Gas Dynamics of Internal Combustion Engines*, Vol. II, Horlock, J.H. and Winterbone, D.E. (Eds.), Clarendon Press, Oxford.

GRAY, C. (1988), "A Review of Variable Engine Valve Timing", SAE Paper 880386.

GREEVES, G., KHAN, I.M., WANG, C.H.T. and FENNE, I. (1977), "Origins of Hydrocarbon Emissions from Diesel Engines", SAE Paper 770259.

HAGHGOOIE, M. and KENT, J.C. (1987), "The Effect of Maximum Valve Lift on TDC Flow Field in a High Swirl Piston Engine", in Instrumentation for Combustion and Flow in Engines, D.F.G. Durao, J.H. Whitelaw and P.O. Witze (Eds.), Vol. 154, p.p. 365-374.

HAGIWARA, A. and BORTZ, S. (1984), "Studies on the Near Field Aerodynamics of Swirl Burners", IFRF, Research Report F 259/a/1.

HALL, M.J. and BRACO, F.V. (1987), "A Study of Velocities and Turbulence Intensities Measured in Firing and Motored Engines", SAE Paper 870453.

HARDALUPAS, Y., TAYLOR, A.M.K.P. and WHITELAW J.H. (1989), "Characteristics of Unsteady Sprays", Imperial College, Mech. Eng. Dept., Report FS/89/21.

HARVEY, P.S. and GOSMAN, A.D. (1982), "Computer Analysis of Fuel-Air Mixing and Combustion in an Axisymmetric DI Diesel", SAE Paper 820036.

HASHIMOTO, M., HAMAMOTO, Y., OHKAWA, H. and SATO, O. (1983), "Effect of Refractive Index Change at Flame Front", Bulletin of the JSME., Vol. 26, No.221-10.

HAY, N. and JONES, P.L. (1972), "Comparisons of the Various Correlations for Spray Penetration", SAE Paper 720776.

HERZOG, P., (1989), "The Ideal Rate of Injection For Swirl Supported Diesel Engines", Proc. I. Mech. I., Seminar on Diesel Fuel Injection System, pp. 11-18, London.

HEYWOOD ,J.B. (1988), *"Internal Combustion Engine Fundamentals"*, McGraw-Hill Book Company.

HIROYASU, H., (1985), "Diesel Engine Combustion and Its Modeling", Proc. Symposium on Diagnostics and Modelling of Combustion in Reciprocating Engines, pp. 53-75, COMODIA 85, Tokyo.

HIROYASU, H. and NISHIDA, K. (1989), "Fuel Spray Trajectory and Dispersion in a DI Diesel Combustion Chamber", SAE Paper 890462.

HIROYASU, H., NISHIDA, K., ARAI, M. and YOSHIKAWA, S. (1986), "A Visual Study of DI Diesel Combustion from the Under and Lateral Sides of an Engine", SAE Paper 861182.

HOLDER, D.W. and NORTH, R.J. (1963), "Schlieren Methods", Notes on Applied Science No. 31, National Physical Laboratory, London.

IIJIMA, T. and BRACCO, F.V. (1987), "LDV Measurements in an Engine with Square and Circular Piston Cups", SAE Paper 872073.

IKEGAMI , M. (1990), "Role of Flows and Turbulent Mixing in Combustion and Pollutant Formation in Diesel Engines", Proc. Int. Symposium, pp. 49-58, COMODIA 90, Tokyo.

JOHNS, R.J.R. (1985), "The Effect of Piston Bowl Offset on the Compression-Induced Air Motion in DI Diesel Engine Combustion Chambers", Proc. Symposium on Diagnostics and Modelling of Combustion in Reciprocating Engines, pp. 489-502, COMODIA 85, Tokyo.

KAJIYAMA, K., NISHIDA, K., MURAKAMI, A., ARAI, M.N and HIROYASU, H. (1984), "An Analysis of Swirling Flow in Cylinder for Predicting DI Diesel Engine Performance", SAE Paper 840518.

KARIMI, E.R. (1989), "High-Speed Photography of Fuel Spray and Combustion Events in a Production diesel engine and Combustion Bomb", Paper C372/012, Proc. Int. Conf. on the Small Internal Combustion Engine, I. Mech. E., London.

KASTNER, L.S., WILLIAMS, T.J. and WHITE, J.B. (1963), "Poppet Inlet Valve Characteristics and Their Influence on the Induction Process", Proc. I. Mech. E., Vol. 178, pp. 955-975.

KATO, T., TSUJIMURA, K., SHINTANI, M., MINAMI, T. and YAMAGUCHI, I. (1989), "Spray Characteristics and Combustion Improvement of DI Diesel Engine with High Pressure Fuel Injection", SAE Paper 890265.

KHAN, I.M., WANG, C.H.T. and LANGRIDGE, B.E. (1972), "Effect of Air Swirl on Smoke and Gaseous Emissions from DI Diesel Engines", SAE Paper 720102.

KHAN, I.M., GREEVES, G. and WANG, C.H.T. (1973), "Factors Affecting Smoke and Gaseous Emissions from DI Engines and a Method of Calculation", SAE Paper 730169.

KITO, O. (1984), "Axi-Asymmetric Character of Turbulent Swirling Flow in a Straight Circular Pipe", Bulletin of JSME, Vol. 27, No. 226, p. 683.

KOBAYASI, H., KAMIMOTO, T. and MATSUOKA, S. (1982), "A Photographic and Thermodynamic Study of Diesel Combustion in a Rapid Compression Machine", Trans. of JSME., 48-426, 389.

KOO, J-Y and MARTIN, J.K. (1990), "Droplet Sizes and Velocities in a Transient Diesel Fuel Spray", SAE Paper 900397.

LANCASTER, D.R., (1976), "Effects of Engine Variables on Turbulence in a Spark-Ignition Engine", SAE Paper 760159.

LANCASTER D.R., KRIEGER R.B. and LIENESCH, J.H. (1975), "Measurement and Analysis of Engine Pressure Data", SAE Paper 750026.

LIOY, T.-M and SANTAVICCA, D.A. (1983), "Cycle-Resolved Turbulence Measurements in a Ported Engine With and Without Swirl", SAE Paper 830419.

LIOY, T.-M and SANTAVICCA, D.A. (1985), "Cycle-Resolved LDV Measurements in a Motored IC Engine", Trans. ASME, J.Fluids Engng.,Vol. 107, pp. 232-240.

LYN, W.-T (1962), "Study of Burning Rate and Nature of Combustion in Diesel Engines", Proc. of Ninth International Symposium on Combustion, pp. 1069-1082, The Combustion Institute.

MACDONALD, J.S., PLEE, S.L., D'ARCY, J.B. and SCHRECK, R.M. (1980), "Experimental Measurements of the Independent Effects of Dilution Ratio and Filter Temperature on Diesel Exhaust Particulate Samples", SAE Paper 800185.

MACDONALD, J.S., BARSIC, N.J., GROSS, G.P., SHAHED, S.P. and JOHNSON, J.H. (1984), "Status of Diesel Particulate Measurement Methods", SAE Paper 840345.

MARGARY, R., NINO, E. and VAFIDIS, C. (1990), "The Effect of Intake Duct Length on the In-Cylinder Air-Motion in a Motored Diesel Engine", SAE Paper 900057.

MARKSTEIN, G.H. (1964) "Flame Propagation in Tubes and in Closed Vessels" in *Non-Steady Flame Propagation*, Pergamon Press, 1964.

McLAUGHLIN, D.K. and TIEDERMAN (1973), "Biasing Correction for Individual Realisation of Laser Anemometer Measurements in Turbulent Flows", Phys. Fluids, Vol.16, p. 2082.

MELLING, A. and WHITELAW, J.H. (1975), "Optical and Flow Aspects of Particles", Proc. LDA Symposium, Copenhagen.

METGHALCHI, M. and KECK, J.C. (1980), "Laminar Burning Velocity of Propane-Air Mixtures at High Temperature and Pressure", *Comb. Flame*,Vol. 38, pp.143-154.

MONAGHAN, M.L. and PETTIFER, H.F. (1981), "Air Motion and Its Effect on Diesel Performance and Combustion", SAE Paper 810255.

MONAGHAN, M.L. (1990), "The Diesel Passenger Car in a Green World", Ricardo Consulting Engineers, Report DP90/0390.

MORSE, A.P., WHITELAW, J.H. and YIANNESKIS (1980), "The Influence of Swirl on the Flow Characteristics of a Reciprocating Piston-Cylinder Assembly", J. Fluids Engng., Vol. 102, p. 478.

MURAKAMI, A., HIROYASU, H. and ARAI, M. (1986), "Time and Space Resolved Measurements in a Cylinder of DI Diesel Engine", SAE Paper 861229

MURAKAMI, A., ARAI, M. and HIROYASU, H. (1988), "Swirl Measurements and Modelling in DI Diesel Engines", SAE Paper 880385.

NABER, J.D. and REITZ, R.D. (1988), "Modelling Engine Spray/Wall Impingement", SAE Paper 880107.

NADARAJAH, TINDAL, M.J. and YIANNESKIS, M. (1991), "Swirl Centre Precession Under Steady Flow Conditions", Proc. Eurotech Direct Conference, Birmingham.

NAKANISHI, K., HIRANO, T., INOUE, T. and Ohigashi S. (1975), "The Effects of Charge Dilution on Combustion and Its Improvement-Flame Photography Study", SAE Paper 750054.

NAMAZIAN, M., HANSEN, S., LYFORD-PIKE, E., SANCHEZ-BARSSE, J., HEYWOOD, J. and RIFE ,J. (1980), "Schlieren Visualisation of the Flow and Density Fields in the Cylinder of a Spark-Ignition Engine", SAE Paper 800044.

NORRIS-JONES, S.R., HOLLIS, T. and WATERHOUSE, C.N.F. (1984), "A Study of the Formation of Particulates in the Cylinder of a DI Diesel Engine", SAE Paper 840419.

OBERT, E.F. (1973), *"Internal Combustion Engines and Air Pollution"*, Harper and Row Publishers.

OBLANDER, K., KOLLMANN, K., KRAMER, M. and KUTSCERA, I. (1989), "The Influence of High Pressure Fuel Injection on Performance and Exhaust Emissions of a High Speed DI Diesel Engine", SAE Paper 890438.

OBOKATA, T., INABA, K. and TAKAHASHI, H. (1988), "LDA Measurements of Diesel Spray and Entrainment Air Flow", Proc. Fourth International Symposium on Applications of Laser Anemometry to Fluid Mechanics, Lisbon.

OLDENGRAM, J., VAN KRIEKEN, A.H. and PATERINK, H.J. (1976), "Development of a Rotating Grating and Its Use in Laser Velocimetry", Proc. ISL/AGARD Workshop on Laser Anemometry, p.603, St. Louis, France.

OREN, D.C., DURRETT, R.P., FERGUSON, C.R., TIMAR, J., TREE, D.R. and DEWITT, D.P. (1987), "A Multidimensional Data Set for Diesel Model Validation:II-Fuel Injection Rate and Boundary Conditions", SAE Paper 872088.

PENWARDEN, D.P.A. (1987), "Ricardo Hydra No. 45 for Imperial College; Unit Injector DI Diesel Pass Off Tests", Ricardo Consulting Engineers, DP 87/1552.

PENWARDEN, D.P.A. and CLARKE (1987), "Ricardo Unit Injector Direct Injection Diesel Hydra Injection System Instruction Manual", Ricardo Consulting Engineers, DP87/2070.

PETTIFER, H.F. (1982), "Interaction of Port Design and Injection Rate for a DI Diesel Engine", SAE Paper 820358.

PRESS, W.H., FLANNERG, B.P., TECKOLSKY, S. and VETTERLING, W.T. (1986), *"Numerical Recipes"*, Ch. 12, Cambridge University Press.

RASK, R.B. (1981), "Comparison of Window, Smoothed-Ensemble and Cycle-by-cycle Data Reduction Techniques for Laser Doppler Anenometer Measurements of In-Cylinder Velocity", in Fluid Mechanics of Combustion Systems, Morel, T., Lohman, R.P. and Rackley, J.M. (Eds.), New York, ASME.

RICHMAN, R.M. and REYNOLDS, W.C. (1984), "The Development of a Transparent Cylinder for Piston Engine Fluid Mechanics Research", SAE Paper 840379.

SAXENA, V. and RASK, R.B., (1987), "Influence of Inlet Flows on the Flow Field in an Engine", SAE Paper 870369.

SCOTT, W.M. (1969), "Looking in on Diesel Combustion", SAE Paper 690002.

SHIMADA, T., SAKAI, K. and KURIHARA, S. "Variable Swirl Inlet System and Its Effect on Diesel Performance and Emissions", SAE Paper 861185.

SPICHER, U., VELJI, A., HUYNH, N.H. and KRUSE, F. (1987), "An Experimental Study of Combustion and Fluid Flow in Diesel Engines", SAE Paper 872060.

STEPHENSON, J.A. and HOOD, B.A. (1987), "A High Speed Diesel Engine for Passenger Cars", Proc. I. Mech. E., London.

SYRED, N. and BEER, J.M. (1972), "The Damping of Precessing Vortex Cores by Combustion in Swirl Generators", Astronautica Acta, Vol. 17, pp. 783-801, Pergamon Press.

TAKAHASHI, M., ISHIDA, T. and SATO, K. (1987), "Improvement of Diesel Engine Performance by Variable Swirl Systems", SAE Paper 871618.

TANABE, S., HAMAMOTO, Y. and OHIGASHI, S. "Swirl in a Four-Stroke Cycle Engine Cylinder", Bulletin of the JSME, Vol. 21, No. 152, p. 287.

TAYLOR, C.F. (1985), *"The Internal-Combustion Engine in Theory and Practice"*, VOL I, Second Edition, The MIT Press.

TINDAL, M.J. and WILLIAMS, T.J. (1977), "An Investigation of Cylinder Gas Motion in th DI Diesel Engine", SAE Paper 770405.

TINDAL, M.J., WILLIAMS, T.J. and HARCOMBE, A.T. (1987), "Fuel Spray Formation in an Experimental Swirl Chamber", SAE Paper 870451.

TINDAL, M.J., SUEN, K.O. and YIANNESKIS, M. (1989), "The Variation of Flow Pattern in a Diesel Engine Cylinder with Speed", SAE Paper 890791.

TIPPELMANN, G. (1977), "A New Method of Investigation of Swirl Ports", SAE Paper 770405.

UZKAN, T., BORGNAKKE, C. and MOREL, T. (1983), "Characterization of Flow Produced by a High-Swirl Inlet Port", SAE Paper 830266.

VAFIDIS, C. (1984), "Influence of Induction Swirl and Piston Configuration on Air Flow in a Four-Stroke Model Engine", Proc. I. Mech., Vol. 198c, p.71.

VAFIDIS, C. (1985), "Aerodynamics of Reciprocating Engines", PhD Thesis, University of London.

VAFIDIS, C., VORROPOULOS, G. and WHITELAW, J.H. (1987), Effects of Intake Port and Combustion Chamber Geometry on In-Cylinder Turbulence in a Motored Reciprocating Engine", Proc. Symposium on Fluid Flow and Heat Transfer in Reciprocating Machinery, ASME Winter Meeting, Boston.

VAN GERPEN, J.H., HUANG, C-W, BORMAN, G.L. (1985), "The Effects of Swirl and Injection Parameters on Diesel Combustion and Heat Transfer", SAE Paper 850265.

WATTS, R. and SCOTT, W.M. (1969), "Air Motion and Fuel Distribution Requirements in High-Speed DI engines", Proc. I. Mech. E., Vol. 184, Paper 17.

WERLBERGER, P. and CARTELLIERI, W.P. (1987), "Fuel Injection and Combustion Phenomena on a High Speed DI Diesel Engine Observed by Means of Endoscopic High Speed Photography", SAE Paper 870097.

WIGLEY, G. and HAWKINS, M.G. (1978), "Three Dimensional Velocity Measurements by Laser Anemometry in a Diesel Engine Cylinder Under Steady Inlet Flow Conditions.", SAE Paper 780060.

WIGLEY, G. (1990) Personal Communication.

WINSOR, R.E. and PATTERSON, D.J. (1973), "Mixture Turbulence-A Key to Cyclic Combustion Variation", SAE Paper 730086.

WINTERBONE, D.E. (1989), "A comparison of Synthesis and Analysis models for Wave Action Manifolds", Proc. I. Mech. E., Paper No C372/037.

WITZE, P.O. (1980), "Influence of Air Motion Variation on the Performance of a DI Stratified-Charge Engine", Proc. I. Mech. E., Paper C394/80

WITZE, P.O. and VILCHIS, F.R. (1981), "Stroboscopic Laser Shadowgraph Study of the Effect of Swirl on Homogeneous Combustion in a Spark-Ignition Engine", SAE Paper 810226.

WITZE, P.O., MARTIN J.K. and BORGNAKKE, C. (1984), "Conditionally-Sampled Velocity and Turbulence Measurements in a Spark-Ignition Engine", Comb. Sci. Tech., Vol.36, p.301.

WITZE, P.O. and BARITAUD T.A. (1986), "Particle Seeding for Mie Scattering Measurements in Combusting Flows" in Laser Anemometry in Fluid Mechanics-III, Adrian R.J. et al (Eds.), Ladoan, Lisbon.

WOJIK, K. (1989), "Improvement of Combustion Systems of High Speed Diesel Engines with Respect to Pollution", ASME International Symposium on Flows in Internal Combustion Engines, T. Uzkan et al (Eds.), pp. 33-43.

YANTA, W.J. (1973), "Turbulence Measurements with a Laser Doppler Velocimeter", Naval Ordinance Labs., White Oak, Silver Spring, Report NOLTR 73-94.

YOSHIKAWA, S., FURUSAWA, R., ARAI, M. and HIROYASU, H. (1989), "Optimizing Spray Behaviour to Improve Engine Performance and to Reduce Exhaust Emissions in a Small DI Diesel Engine", SAE Paper 890463.

YULE, A.J. and AVAL, S.M. (1989), "A Technique for Velocity Measurements in Diesel Sprays", Combustion and Flame, Vol. 77, pp.385-394.